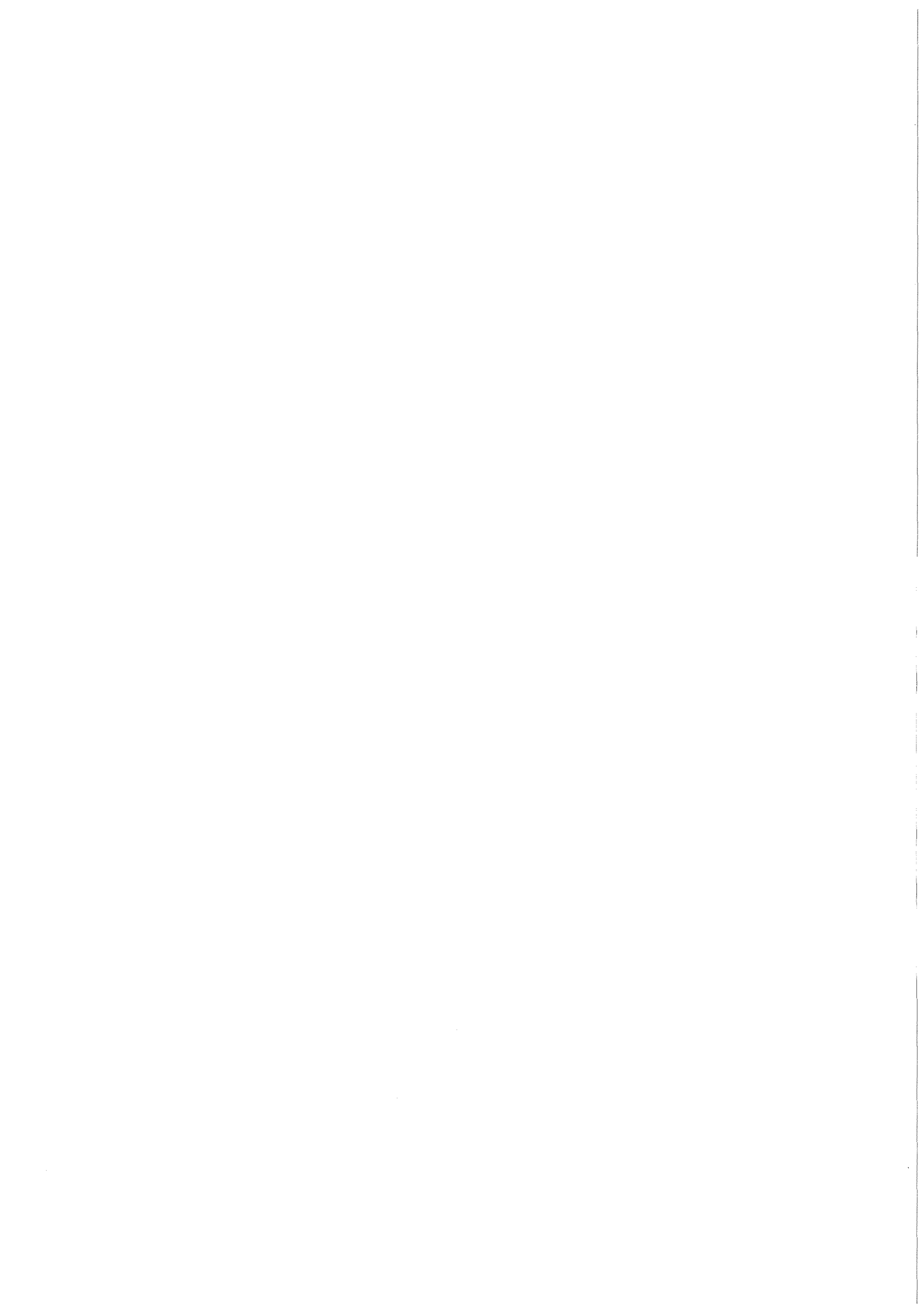


KfK 3317
Dezember 1982

BLOW-3A
A Theoretical Model to
Describe Transient Two-Phase
Flow Conditions in
LMFBR Coolant Channels

M. Bottoni, D. Struwe
Institut für Reaktorentwicklung
Projekt Schneller Brüter

Kernforschungszentrum Karlsruhe



KERNFORSCHUNGSZENTRUM KARLSRUHE
Institut für Reaktorentwicklung
Projekt Schneller Brüter

KfK 3317

BLOW-3A
A Theoretical Model to Describe Transient
Two-Phase Flow Conditions in LMFBR Coolant Channels

M. Bottoni, D. Struwe

Kernforschungszentrum Karlsruhe GmbH, Karlsruhe

Als Manuskript vervielfältigt
Für diesen Bericht behalten wir uns alle Rechte vor

Kernforschungszentrum Karlsruhe GmbH
ISSN 0303-4003

Summary

The computer programme BLOW-3A describes sodium boiling phenomena in sub-assemblies of fast breeder reactors as well as in in-pile or out-of-pile experiments simulating different failure conditions. This report presents a complete documentation of the code from three main viewpoints: the theoretical foundations of the programme are first described with particular reference to the most recent developments; the structure of the programme is then explained in all details necessary for the user to get a rapid acquaintance with it; eventually several examples of the programme validation are discussed thus enabling the reader to acquire a full picture of the possible applications of the code and at the same time to know its validity range.

BLOW-3A, ein theoretisches Modell zur Beschreibung transienter Zweiphasenbedingungen in Kühlkanälen natriumgekühlter schneller Brutreaktoren

Zusammenfassung

Das Rechenprogramm BLOW-3A beschreibt Natriumsiedephänomene sowohl in Brennelementen von schnellen Brutreaktoren als auch in Experimenten, in denen in Testreaktoren oder Versuchsständen unterschiedliche Fehlerursachen der Kühlung simuliert werden. Der vorliegende Bericht stellt eine vollständige Dokumentation des Rechenprogramms dar. Drei Bereiche werden hervorgehoben: Darstellung der theoretischen Grundlagen des Rechenprogramms unter besonderer Berücksichtigung neuerer Entwicklungsarbeiten; Detaillierte Erklärung der Programmstruktur, um den Benutzer mit BLOW-3A bekannt zu machen; Diskussion einiger Anwendungsbeispiele des Programms, die zur Programmvalidierung herangezogen wurden. Dadurch kann der Leser einen vollen Überblick über den möglichen Anwendungsbereich des Programms und seine Grenzen bekommen.

Content

	<u>Page</u>
List of Tables	V
List of Figures	VII
<u>Introduction</u>	1
 PART I - Summary of the main topics implemented in the BLOW-3A programme with respect to the BLOW-3 version documented in Reference /1/.	 4
 PART II - The physical model and its application	 10
A - Description of the test section	10
B - The basic equations	12
1. Fuel	12
2. Cladding	14
3. Coolant	14
4. Structural Material	19
C - Numerical treatment of the basic equations and programming details	20
1. The stationary calculation	20
1.1. Calculation of further channel geometrical data	22
1.2. Power normalization	25
1.3. Calculation of total power generation in the channel	28
1.4. Calculation of mass flow	28
1.5. Calculation of coolant temperature distribution	30
1.6. Calculation of coolant pressure distribution	31
1.7. Calculation of temperature distributions in fuel, clad, structure	34
a) First evaluation of temperature distributions in fuel and clad	34
b) Refined temperature distributions in fuel and clad and calculation of structure temperature with the Gauss-Seidel iteration method	36
1.8. Calculation of gap width in the stationary hot state	41
2. Transient calculation	43
2.1. The numerical treatment of the differential equations describing the transient temperature distributions in fuel, clad and structure	43

	<u>Page</u>
a) Fuel	44
b) Cladding	48
c) Structure	51
d) The Gauss-Seidel solution method	52
e) Programming details	53
2.2. Single phase flow calculation	58
2.2.1. - Basic numerical scheme and preliminary considerations for stability analysis	58
2.2.2. - Detailed solution of the momentum equation with a two-steps formula ("Predictor-Corrector" scheme)	63
2.2.3. - Solution of the continuity equation	66
2.2.4. - Solution of the energy equation	72
2.2.5. - Stability analysis of the system of basic equations	74
2.3. Two-phase flow calculation	80
2.3.1. - General information about bubbles initialisation coalescence, growth and collapse	81
2.3.2. - Remarks about the solution of the basic equations for the vapour phase and the application of the "Reynold-flux" concept to the two-phase flow.	83
a) Theoretical analysis	83
b) Programming details	91
2.3.3. - Solution of the basic equations for the liquid slug	93
a) Continuity equation	93
b) Momentum equation	93
c) Energy equation	95
d) Remark on the calculation of the terms QQ1 to QQ6	96
e) Definition of the Lagrangian meshes in the liquid slug	98
2.3.4. - Time and space variation of liquid film thickness	100
a) Theoretical analysis	101
b) Comparison with previous model of static film	103

2.3.5. - Calculation of liquid film velocity and of interfacial shear stress between liquid and vapour	105
a) Statement of the problem	105
b) Theoretical formulation and assumptions	106
c) Iterative calculation scheme	108
d) Numerical results	111
2.3.6. - Some considerations about turbulent heat transfer through liquid film	118
2.4 - Calculation of temperature distribution in fuel and clad during melting or solidification	122
3. Further Programme details	125
3.1. Time step control	126
3.2. Heat and mass exchange between upper liquid slug and coolant in upper plenum	128
3.3. Simulation of a typical experimental test rig and calculation of the heat transfer coefficient from the structure outer wall to a by-pass flow	131
3.4. Leakage flow representation	135
3.5. Definition of one-dimensional channels equi- valent to several subchannels of a pin bundle	136
PART III - Code structure	145
1. General Structure of the computer programme	145
1.1. Main Organisation	145
1.2. List of Subroutines and Functions	145
1.3. Organisation in Members	148
1.4. Overlay Structure	148
1.5. Remarks for the user	149
2. Description of Subroutines	150
2.1. - Basic Subroutines	150
2.2. - Problem oriented Subroutines	198
2.3. - Functions	204
3. List of FORTRAN symbols	209
4. Input and output descriptions	239
5. Auxiliary data sets and plotting facilities	248

	<u>Page</u>
PART IV Status of the experimental validation of the BLOW-3A programme and code application for LMFBR safety analysis	249
1. Theoretical interpretation of single-pin in-pile SCARABEE experiments	250
1.1 General	250
1.2 Main characteristics of the SCARABEE experiments	251
1.3 Analysis of SCARABEE IV experiments	255
1.3.1 Experiment 3064-2	259
1.3.2 Experiment 3068-2	264
1.4 Conclusion	273
2. Theoretical interpretation of 7-pin bundle out of pile sodium experiments of the NSK series.	275
2.1 General	275
2.2 Test section and instrumentation of the 7-pin bundles.	275
2.3 Simulation of the electrical heaters and definition of equivalent channels.	278
2.4 Calculations and comparison with experimental data	282
2.4.1 The computed experiments	282
2.4.1.1 Experiment 7-2/16	288
2.4.1.2 Experiment 7-2/24	293
2.4.1.3 Experiment 7-2/28	298
2.5 Conclusion	302
3. Application of the BLOW-3A code for consequence evaluation of an unprotected loss-of-flow accident in the core of SNR-2000	304
3.1 Characteristic data of the reactor core	304
3.2 Transient behaviour of the SNR-2000 reactor core	312
3.3 Influence of a slow mass flow reduction on the power evolution during the initiation phase	317
List of Symbols	322
References	324

<u>List of Tables</u>	<u>Page</u>
Table I - Summary of the possible cases illustrating the dependence of the vapour pressure drop due to "equivalent" shear stress (DPR 4 + 5) on the algebraic sign of G_v (vapour axial mass flux) and m (coolant mass flux by phase change)	90
Table II - Comparison of interfacial friction factors obtained with application of the Peplér, Lockhart-Martinelli and Wallis correlations	114
Table III - Comparison between heat transfer coefficient across the liquid film based on the conduction approximation and based on the separate contributions of laminar and turbulent sublayers	121
Table IV - Symbols defining the physical state of a bubble stretching over at least three Eulerian meshes	193
Table V - Summary of SCARABEE single pin experiments	256
Table VI - Data of SCARABEE IV test pin	257
Table VII - Comparison between experimental and calculated data for SCARABEE IV 3064-2 and 3068-2 referring to steady state and boiling inception	260
Table VIII - Input data for SCARABEE IV 3068-2	267
Table IX - Axial zone structure of electrical heaters of the NSK 7-2 experiments.	279
Table X - Dimensions of the coolant channel representation for the NSK 7-2 experiments.	282
Table XI - Characterization of the computed NSK 7-2 experiments	283

VI

	<u>Page</u>
Table XII - Input data of experiment NSK 7-2/16	284
Table XIII - Input data of experiment NSK 7-2/24	285
Table XIV - Input data of experiment NSK 7-2/28	286
Table XV - Comparison of experimental data obtained in the NSK loop with calculational results for the different equivalent channels	287
Table XVI - Characteristic data of the SNR-2000 reactor core	305
Table XVII - Characteristic nuclear data of the SNR-2000 reactor core	306
Table XVIII - Characteristic data of the ULOF-accident in the SNR-2000	316
Table XIX - Characteristic data of the ULOF-accident in the SNR-2000 dependent on different mass flow reduction curves	319

<u>List of figures</u>	<u>Page</u>
Fig. 1: Geometrical configuration of the test section modeled in the BLOW-3A programme	11
Fig. 2: Sketch showing the definition of radial meshes in fuel and cladding	24
Fig. 3: Sketch showing qualitatively the stationary pressure distribution in the coolant versus axial length	33
Fig. 4: Local deviation of mass flux from mean value versus axial length	70
Fig. 5: Scheme of the iteration method used to solve the single phase flow continuity equation	71
Fig. 6: Sketch showing qualitatively the dependence of the sum $A_4 + A_5$ of terms defined by Equations (19d) and (19e) of section II.C.2.3.2 on the coolant mass flux m by phase change	89
Fig. 7: Iteration scheme for calculation of liquid film velocity	112
Fig. 8: Comparison between interfacial friction coefficients calculated with the Wallis formula and with the Lockhart-Martinelli correlation versus liquid film thickness	115
Fig. 9: Interfacial friction coefficients between liquid film and vapour versus liquid film thickness (for vapour mass flux $G_v = 10 \text{ kg/m}^2 \text{ sec}$)	115
Fig. 10: As above with $G_v = 50 \text{ kg/m}^2 \text{ sec}$	116
Fig. 11: Ratio vapour to liquid film mean velocity versus liquid film thickness (Results obtained with the Lockhart-Martinelli correlation)	116
Fig. 12: As above (Results obtained with the Peppler correlation)	117

VIII

	<u>Page</u>
Fig. 13: Control volume for heat and mass exchange in upper plenum	129
Fig. 14: Sketch showing a typical experimental test rig to be simulated for the calculation of the heat transfer coefficient from structure to a by-pass flow	131
Fig. 15: General block diagram of the computer programme	144
Fig. 16: Sketch showing the possible configurations of coalescing bubbles as programmed in the subroutine ATØM	154
Fig. 17: Symbols characterizing a bubble initialized in the subroutine SETUP	191
Fig. 18: Symbols characterizing the configuration of a bubble stretching over at least three Eulerian meshes	192
Fig. 19: Cross section of the test rig for single-pin SCARABEE experiments	258
Fig. 20: Scheme of fuel pin used in the SCARABEE experiments with position of some thermocouples for SCARABEE IV	258
Fig. 21: Time variation of reactor power during the experiment SCARABEE IV 3064-2	261
Fig. 22: Experiment SCARABEE IV 3064-2. Experimental and calculated flow rate versus time	261
Fig. 23: Experiment SCARABEE IV 3064-2. Calculated and experimental coolant temperatures (thermocouple TC9, at axial level 30.5 mm; see Fig. 20)	262
Fig. 24: Experiment SCARABEE IV 3064-2. Calculated and experimental coolant temperatures (thermocouple TC11, at axial level 95.5 mm; see Fig. 20)	262
Fig. 25: Experiment SCARABEE IV 3064-2. Calculated and experimental coolant temperatures (thermocouple TC12, situated at axial level 180.5 mm, above the top end of the heated section; see Fig. 20)	263

	<u>Page</u>
Fig. 26: Experiment SCARABEE IV 3068-2. Experimental and calculated flow rate versus time	268
Fig. 27: Experiment SCARABEE IV 3068-2. Leakage to channel flow rate versus time	268
Fig. 28: Experiment SCARABEE IV 3068-2. Normalized leakage flow versus the flow rate through the inlet valve	269
Fig. 29: Experiment SCARABEE IV 3068-2. Development of voided region, dry-out and clad melting versus time	269
Fig. 30: Experiment SCARABEE IV 3068-2. Calculated and experimental coolant temperatures (thermocouple TC09 at axial level 30.5 mm; see Fig. 20)	270
Fig. 31: Experiment SCARABEE IV 3068-2. Calculated and experimental coolant temperatures (thermocouple TC11 at axial level 95.5 mm; see Fig. 20)	270
Fig. 32: Experiment SCARABEE IV 3068-2. Calculated and experimental coolant temperatures (thermocouple TC12 at axial level 180.5 mm; see Fig. 20)	271
Fig. 33: Experiment SCARABEE IV 3068-2. Calculated and measured coolant temperatures at axial level 497.5 mm above fuel mid-plane	271
Fig. 34: Experiment SCARABEE IV 3068-2. Axial distribution of coolant pressure with time as parameter. The distribution at $t = 5.4$ sec corresponds to boiling inception	272
Fig. 35: Experiment SCARABEE IV 3068-2. Normalized fuel-clad gap versus time	272
Fig. 36: Test section and measuring planes of the 7-pin bundle Nr. 2276	
Fig. 37: Experiment 7-2/16. Inlet pressure boundary condition and comparison between experimental and calculated inlet velocities versus time	290

	<u>Page</u>
Fig. 38: Experiment 7-2/16. Experimental and calculated peak coolant temperatures versus time	290
Fig. 39: Experiment 7-2/16. Experimental and calculated voided regions versus time	291
Fig. 40: Experiment 7-2/16. Calculated liquid film thickness at cladding in the axial mesh zone $M=11$ versus time, for equivalent channel $KKN=1$	291
Fig. 41: Experiment 7-2/16. Calculated liquid film thickness at the structural material in the axial mesh zone $M=11$ versus time, for equivalent channel $KKN=1$	292
Fig. 42: Experiment 7-2/24. Inlet pressure boundary condition and comparison between experimental and calculated inlet velocities versus time	292
Fig. 43: Experiment 7-2/24. Experimental and calculated peak coolant temperatures versus time	294
Fig. 44: Experiment 7-2/24. Experimental and calculated voided regions versus time	294
Fig. 45: Experiment 7-2/24. Experimental and calculated heater temperatures versus time at axial level $z = 400$ mm ($z = 0$ at the bottom of heated section)	296
Fig. 46: Experiment 7-2/24. Experimental and calculated heater temperatures versus time at axial level $z = 580$ mm ($z = 0$ at the bottom of heated section)	296
Fig. 47: Experiment 7-2/24. Calculated liquid film thickness at cladding in the axial mesh zone $M=11$ versus time, for equivalent channel $KKN=1$	297
Fig. 48: Experiment 7-2/24. Calculated liquid film thickness at the structural material in the axial mesh zone $M=11$ versus time, for equivalent channel $KKN=1$	297

	<u>Page</u>
Fig. 49: Experiment 7-2/28. Comparison between experimental and calculated inlet velocities versus time	299
Fig. 50: Experiment 7-2/28. Experimental and calculated peak coolant temperatures versus time	299
Fig. 51: Experiment 7-2/28. Experimental and calculated voided regions versus time	300
Fig. 52: Experiment 7-2/28. Experimental and calculated peak cladding temperatures (outer surface) versus time	300
Fig. 53: Experiment 7-2/28. Calculated liquid film thickness at cladding in the axial mesh zone M=11 versus time, for equivalent channel KKN=1	301
Fig. 54: Experiment 7-2/28. Calculated liquid film thickness at the structural material in the axial mesh zone M=11 versus time, for equivalent channel KKN=1	301
Fig. 55: Core cross section of the SNR-2000	307
Fig. 56: Grouping scheme of core elements for characteristic coolant channels	309
Fig. 57: Geometrical mesh of SNR-2000 with radial positions of control rods and the second safety system	310
Fig. 58: Normalized axial profiles of linear rating for the BEC-A and EEC-B core configurations	311
Fig. 59: Transient void front evolution in the coolant channel with the highest linear rating as consequence of a ULOF-accident	313
Fig. 60: Reactivity and power evolution in the BEC-A and EEC-B core configurations as consequence of a ULOF-accident	314
Fig. 61: Transient void front evolution in the coolant channel with the highest linear rating dependent on different mass flow reduction curves for the ULOF-accident	320

Fig. 62: Reactivity and power evolution in the BEC-A core configuration dependent on different mass flow reduction curves for the ULOF-accident

Introduction

The computer programme BLOW-3A aims at describing sodium boiling phenomena in fast breeder reactor subassemblies as consequence of different failure conditions. These concern especially integral mass flow reduction, single subassembly inlet blockages and mild or rapid reactivity transients. The programme is based on a theoretical approach assuming a multiple bubble slug ejection model as documented in /1/. Originally the BLOW-3 programme concentrated on the theoretical description of boiling initiated after achievement of moderate up to large superheat of single phase sodium. The current version BLOW-3A preserves this feature but has been improved with regard to several aspects. These are:

- allowance of negligible superheat prior to boiling onset,
- calculation of the behaviour of liquid film remaining on structure surfaces after boiling initialization,
- modified calculation of vapour pressure distribution inside large continuous two phase flow regions,
- application of different approximations for the determination of the two-phase friction coefficient at the liquid-vapour interface,
- calculation of single phase compressibility effects in case of extreme rapid coolant heat-up,
- calculation of heat and mass exchange between upper liquid slugs or vapour regions with an upper plenum,
- allowance for clad melting phenomena after dry-out.

The new code version has been used extensively for theoretical interpretation of in-pile and out-of-pile experiments /3,5,19,26,30/. These required special extensions of the programme to simulate various experimental conditions appropriately. Examples are capabilities to simulate heat losses from test sections to outer structures as well as leakage flows parallel to the main mass flow through the test section.

To allow for easy comparison of calculated and experimental results of the various experiments investigated in detail, special plotting capabilities were linked to the programme as well as an independent function library for material data.

This report gives a detailed documentation of the theoretical model upon which the code BLOW-3A is based as well as programming details. It should enable potential users to get acquainted with the code and serves as well as a basis for introduction of modifications if found to be necessary. For the sake of completeness, the full set of equations describing the temperature distributions in fuel, clad, coolant and structure is given as well as the equations describing the transient single-phase and two-phase flow behaviour. The numerical treatment as well as programming details are given. References /1/ and /4/ nevertheless still serve as the basic documentation of the theoretical background of the model.

In part II of this report details about specific aspects of the theoretical approximation of the code are presented. Special attention has been given to topics which have been either basically revised or newly implemented in the BLOW-3A version if compared to the BLOW-3 code. Part III affords to the user a description of the overall structure of the BLOW-3A programme and detailed explanations of individual subroutines. A list of all FORTRAN-symbols used in the code can be found in section III-3. Several examples of applications of the BLOW-3A code are given in part IV.

Though extensive effort has been put into the theoretical development and the experimental validation of the current code version, application of the code still has some limitations. First of all successful application needs careful determination of input variables according to the use of these data for approximation of real conditions in reactor subassemblies or test sections. Second, verification of experimental results can only be expected, if the flow regime in the two-phase flow zone quickly approaches a churn-turbulent, an annular or dispersed annular flow. Quickly in this sense means in time periods which are short if compared to the overall boiling time sequence of interest. Due to our experience this is fulfilled in all cases in which bulk coolant temperatures cross saturation conditions of the coolant quickly and in which radial coolant temperature distributions inside the simulated test sections or subassemblies are small or moderate. Difficulties might arise when transient conditions are investigated in which saturation of the bulk coolant is just reached and kept constant. Beyond that it is

prudent to list some deficiencies of the current model. These are:

- sodium vapour superheat cannot be taken into account,
- radiative heat transfer from dried-out regions to enclosing structures is not modelled,
- heat transfer from dried-out regions to the vapour flow is only crudely approximated,
- in cases of fuel pins no fission gas release as consequence of potential clad failures is simulated,
- hydraulic coupling of the two-phase flow phenomena to neighbouring coolant flow paths (by-pass flow, subassemblies etc.) can only be taken into account by appropriate specification of input data.

These items limit to some extent the application of the BLOW-3A programme. Nevertheless, if proper care is taken on these limitations, BLOW-3A has been proven to be an excellent tool for the investigation of two-phase flow phenomena either for predictive analysis or to support interpretation of experimental results.

Part I) Summary of the main topics implemented in the BLOW-3A programme with respect to the BLOW-3 version documented in /1/

The main programme improvements with respect to the previous BLOW-3 programme version, concern the following topics:

i) Applicability to reactor or experimental conditions characterized by small superheat at boiling inception

The BLOW-3 version worked optimally in case of large superheat when at boiling inception a long vapour bubble is generated. In case of small superheat a short vapour bubble is produced at the top end of the heated zone of the coolant channel and rapidly drawn upwards into the upper cooler region where it may totally recondense. The code structure had therefore to be revised by allowing the calculation to switch from two-phase to single phase flow with subsequent re-initialization of respective subroutines. Moreover, setting on of boiling with small superheat is characterized by the formation of a number of small bubbles (in a flow regime modelled as slug flow) which may either collapse or coalesce in a great variety of cases which are not normally described by modelling an annular flow. A number of subroutines have therefore been revised to describe all possible cases of interactions among small bubbles in the same or adjacent axial mesh zones. The initial boiling sequence is dealt with by the new code version with greater accuracy.

ii) Correct solution of continuity equation for coolant single phase flow

In a loss of flow experiment simulating rapid mass flow reduction temperature gradients along the coolant may change rapidly. In these cases an exact solution of the continuity equation for the coolant $\partial\rho(z,t)/\partial t + \partial G(z,t)/\partial z = 0$ is necessary. The space-time dependent density variation leads to an axial mass flow redistribution. For relative slow mass flow variations the influence of time dependent density variations on single phase mass flow distributions can be neglected. On the contrary, with quick coolant temperature and density variations the exact solution of the continuity equation leads to a mass flow axial distribution which differs locally some percents from the worth obtained by simply assuming $G = \text{const}$. This difference might be not negligible if very great accuracy should be reached in the single phase flow domain to simulate the proper initiating conditions for boiling. In the

theoretical interpretation of experiments where the ratio power to coolant mass flow is very close to the critical worth which allows boiling the correct solution of the coolant continuity equation may be compulsory to meet the conditions for boiling initialization.

The subprogram ITCl, which solves the continuity equation for the coolant in the single phase flow domain, as explained in section II-C-2.2.3 has been improved to afford its exact solution. The modified version of this subprogramme introduces the computed value of the mass flux G into the momentum equation on the basis of an iteration process which will is explained in detail in section II-C.2.2.2. In case the coolant temperature varies slowly with time, the iteration scheme provides very quickly the solution of the approximate equation $\partial G/\partial t=0$, without a remarkable increase of the required computing time.

iii) Determination of heat losses in radial direction

One of the most salient characteristic of experiments, which distinguish them from a typical reactor channel, is the presence of heat losses beyond the outer structure wall to the bounding medium. Taking into account in the code BLOW-3 the power losses, implied dropping the limiting assumption of adiabatic structure and implementing the subprogrammes dealing with the stationary and transient temperature distributions. Moreover, in practical cases, an overall heat transfer coefficient from the structure to the outer medium must be either estimated or calculated taking into account the physical characteristics of the experimental rig. A typical example of such a calculation for an experiment where the pin structure loses power to a by-pass flow through a series of intermediate layers comprising a vacuum gap is presented in section II-C-3.3.3.

iv) Representation of a leakage flow in parallel to the main coolant flow through the test section

Some experimental test sections are characterized by an undesired leakage flow in parallel to the channel flow. The leakage is normally negligible under single phase flow conditions but rises after boiling inception due to the increased frictional pressure drops in the two phase flow region. The leakage flow has a destabilizing effect on the coolant mass flux inducing large amplitude variations which superimpose on the slug oscilla-

tions due to boiling phenomena. These effects have been taken into account by introducing a variable pressure drop coefficient for the inlet valve under the assumption that friction pressure gradients in the leakage path dominate the acceleration pressure drops. Details of this calculation are presented in section II-C-3.4. The programme provides an option for the user to calculate either with the standard version or with the simulation of the leakage path.

v) Clad temperature distribution during melting or solidification

The discrete approach used to calculate the temperature distribution in the fuel pin during fusion or solidification has been applied to the clad material. If a calculated node temperature exceeds the fusion temperature by ΔT the amount of energy $\Delta Q = c_p \Delta T$ is assumed as part of the latent heat necessary to melt the clad material associated to the node. A correction of the node temperature is applied which resets it back to the fusion temperature as long as the sum of the latent heat made available over consecutive calculations does not exceed the heat necessary to melt the mass of material associated to the node. Similar considerations apply obviously in case the clad temperature decreases below the fusion temperature, the latent heat being in this case liberated during the solidifying process. Programming details about this mechanism are given in section II-C-2.4.

The above computation model is essentially discontinuous, as it assumes time and space discretization. An alternative calculation method, based on an analytical treatment of the problem of the temperature distribution in a melting clad has been presented in /6/.

vi) Calculation of two phase pressure drop multipliers for low quality sodium vapour flow

In a well developed annular flow regime, the thickness of the liquid film separating clad or structure surfaces from the flowing vapour increases in the upper non heated section of the test channel, due to vapour condensation on the cold surfaces. The resulting void fraction is small. A new calculation of two phase pressure drop has been performed which applies the concept of two phase multipliers, normally introduced for homogeneous flow, to the multiple bubbles model upon which the BLOW code is based. The application

of the Lockhart-Martinelli correlation /7/ has afforded in case of low quality better fitting of theoretical pressure distribution with experimental data.

Details of the above calculation are given in section II-C-2.3.5.

vii) Calculation of liquid film velocity

The above mentioned calculation of two phase pressure drop multipliers has been carried out applying an iterative scheme which computes at the same time the interfacial shear stresses between liquid film and vapour and the velocity distribution across the liquid film. The latter calculation is based upon the application of the relationships of the boundary layer theory under the assumptions that the two phase flow can be represented by the separate cylinders model.

Details of this calculation are given in section II-C-2.3.5. The knowledge of the velocity distribution across the liquid film, hence of the mean liquid film velocity has allowed the correct solution of the continuity equation for the liquid phase in the two phase flow region and the

viii) Calculation of liquid film thickness taking into account the liquid film velocity

The calculation of liquid film thickness was based, in the BLOW-3 code, on the model of "static" film, in which the film velocity is considered to be negligible. Actually, the film velocity was not computed.

The calculation of two phase multipliers, explained in section II-C-2.3.5, affords also the axial distribution of liquid film velocity. This allowed a new computation of space and time distribution of film thickness which takes into account the film velocity and therefore replaces the "static" film model. The new model of moving liquid film has been coupled to BLOW-3A and can be used as a new option.

ix) Revision of the numerical scheme to solve the coupled energy and momentum equations for the vapour phase

The numerical solution of the coupled energy and momentum equations which determine the time and space distributions of vapour pressure and temperature in the vapour bubbles represents the most arduous task of all numerical procedures used in the code. Numerical instabilities may arise when bubbles ex-

tend over a large section of the channel, from the hot central region with high vapour production rate to colder upper regions where strong vapour condensation occurs. Another source of instabilities may be the passage of a liquid slug through dried out clad regions with large vapour production rate.

As the rate of mass exchange by vaporization or condensation depends strongly on the temperature, small numerical fluctuation of the temperature may have large effects on the mass exchange between the phases, thus amplifying small numerical inaccuracies which otherwise would be negligible. These difficulties are enhanced when the exchange of mass varies rapidly with time as it may occur when the phase boundaries moving in axial direction pass an eulerian mesh boundary and reach a new mesh zone with structure or clad temperature which differ considerably from those of the adjacent zone.

The numerical scheme used to solve the energy and momentum equation for the vapour phase has been revised. An automatic procedure has been set up which allows a more refined calculation (with three axial nodes within every mesh zone) in case the axial pressure gradients in the vapour exceed a given threshold. Furthermore the Reynolds flux concept /8/ to describe the momentum exchange between the vapour and liquid phases by vaporization and condensation has been revised from the viewpoint of its applicability in the momentum equation.

Details about this improved numerical scheme are given in section II-C-2.3.2.

x) Calculation of heat and mass exchange between upper liquid slug and coolant in upper plenum

The coolant temperature in the uppermost cells of the test section depends on the upper plenum temperature when flow oscillations determine the re-entry of the uppermost liquid slug. The assumption of constant plenum temperature has been dropped and replaced by a calculation model which takes into account the heat and mass exchange between a properly defined control volume laying above the uppermost liquid slug and the bulk of the liquid in the plenum itself. Details of this calculation are given in section II-C-3.2.

xi) Radial power distribution in the fuel

With respect to the BLOW-3 version, a new representation of radial power distribution in the fuel has been introduced. It is compulsory in case of theoretical interpretation of electrically heated experiments where the power

generation is normally concentrated on a fraction of the heaters radius. Details are given in the input description.

xii) Evaluation of numerical results by means of a plotting facility

An optional automatic plotting facility has been linked to the BLOW-3A code. It allows to produce on request three sets of plots referred to as "standard", "bubbly" and "optional" plots. The standard set of plots, which is quite independent on the particular calculation performed includes inlet mass flow and fuel, clad, coolant, structure temperatures against time. All temperatures are plotted for the node with the stationary top power generation (referred to as NMP) and the node with the stationary largest coolant temperature (MPEAK).

The bubbly plot produces one large scale plot showing the bubble boundaries against time. It allows following with large accuracy the bubble generation and evolution.

The optional plot has to be programmed by the user for its particular problem. It may be used for instance to plot the precise temperature corresponding to the positions of the thermocouples which do not coincide in general with the nodes locations. Further application can be made to plot channel characteristics as pressure drops against channel flow (and similar plots) assuming time as parameter.

xiii) Independent functions library

A small library for materials physical properties has been built up including the only functions of interest for BLOW-3 calculations. The program has therefore been made independent from the large library called MAPLIB /9/ which was organized with several levels of calling subprograms. Fast access to the new small library has increased the program speed of calculation by a factor 2. Information about the functions available in the standard BLOW-3A version are given in section III-2.3.

Part II) The physical model and its application

A) Description of the test section

For applications of the calculation model to reactor conditions, the reactor core is ideally divided in concentric annular regions, where, for symmetry reasons, the temperature fields are equal for all pin elements and coolant subchannels. An annular region can therefore be represented by a single fuel pin with an equivalent annular coolant flow area bounded by a cylindrical layer of structural material. The symmetry around the axis lets dropping the azimuthal coordinate. As the temperature gradients in radial directions are far stronger than those in axial directions, only heat diffusion in radial direction is considered. The channel length is divided in a number of axial segments for which one-dimensional (in the r-coordinate) equations of heat diffusion are applied. In the coolant neither radial nor axial heat conduction are taken into consideration as this energy transfer is negligible with respect to the transport due to the coolant flow. The energy transfer from coolant to clad and structure affords therefore the coupling between the axial meshes of the channels.

Application of the model to different conditions, for instance in pile or out of pile experiments, is straightforward in case of single pin experiments with powered central pin (electrically heated or with nuclear fuel) and annular flow channel for the coolant. Otherwise, when the experimental geometry is different, as in the case of pin bundles, the programme user must first define an equivalent cylindrical channel where the masses of the materials involved (fuel, clad, coolant and structure) and the surfaces for heat exchange are representative of the real experimental conditions. An example of definition of an equivalent channel from a bundle geometry is given in section II-C-3.5.

A typical equivalent channel configuration is shown in the scheme of Fig. 1, with reference to the geometry of SNR type reactor having a lower fission gas plenum. As shown in this figure, a mixing chamber at pin outlet with a different flow area and surface to volume ratio for the structure can be modelled.

The channel is divided in up to 30 meshes in axial direction. Radial heat conduction is considered in fuel, clad and structure. In the coolant heat conduction is negligible with respect to convective heat transfer which affords the coupling between the axial meshes of the channel. Within an axial mesh up to 11 nodes are considered in radial direction in the fuel,

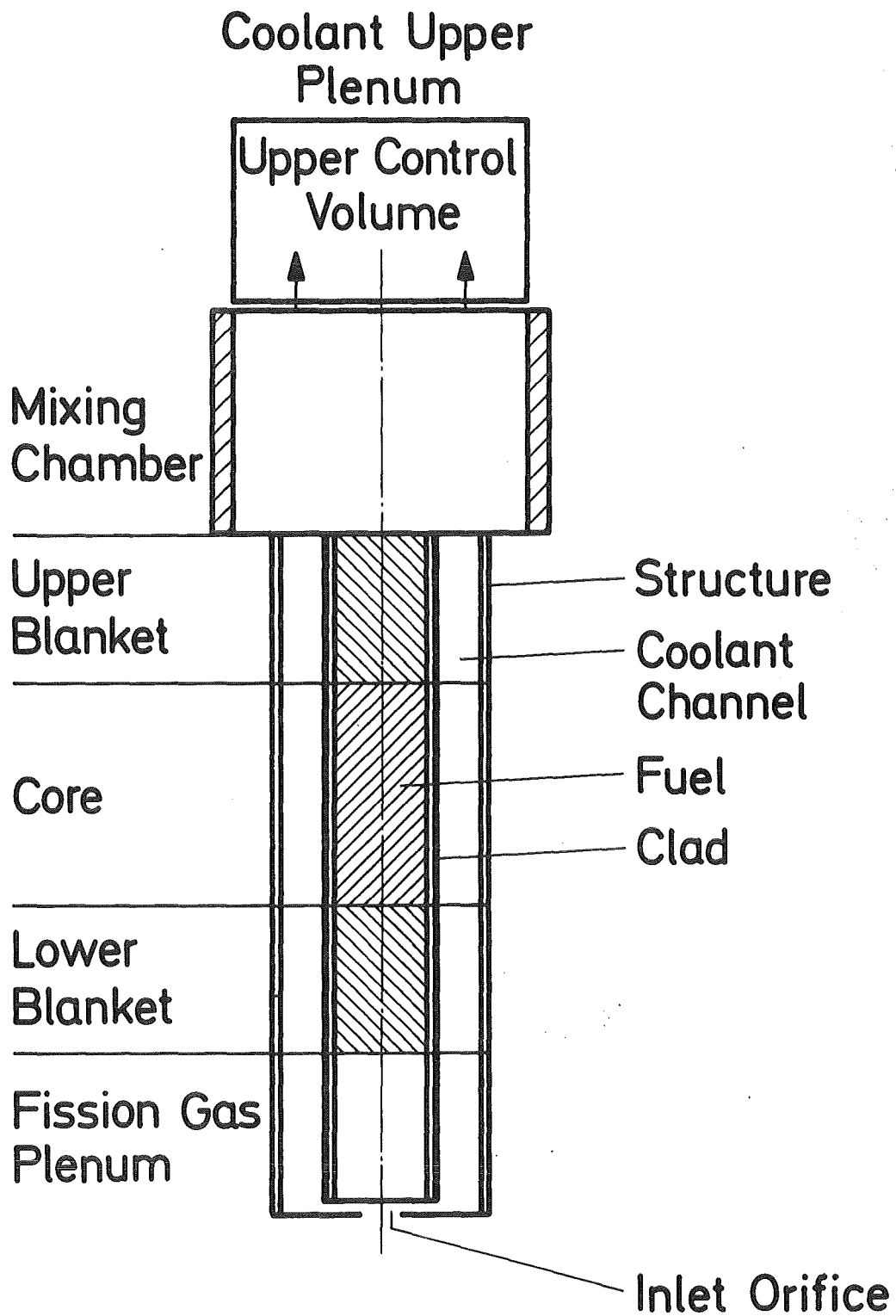


Fig. 1: Geometrical configuration of the test section modelled in the BLOW-3A programme.

3 nodes in the clad, 1 for the coolant and 1 for the structural material. The one-dimensional heat diffusion equations are solved rigorously for fuel and clad while the assumption of a linear temperature profile in the structure is made.

In case of coolant reentry, the calculation of the temperature in the uppermost axial mesh requires the knowledge of coolant temperature in the region above it. This is computed modelling the heat and mass exchange between the upper liquid slug and the coolant in a suitable control volume in the upper plenum.

The up to ten equivalent channels are coupled by the pressure boundary conditions at inlet and outlet and by the common inlet temperature and steady state outlet temperature. Radial interaction of the channels cannot be simulated. The coupling between the channels and the coolant primary loop is provided by the consideration of upper and lower inertial reduced lengths.

The main accident conditions which can be modelled by appropriate choice of the boundary conditions are loss of flow (LOF), simulating pump failure or pipe rupture, or a whole core power perturbation resulting from reactivity insertion. Partial flow blockage can be simulated by increasing the coefficient for the calculation of the pressure drop in the inlet orifice.

B) The basic equations

The complete set of equations describing the temperature distributions in the fuel, clad, coolant and structure material as well as the dynamic of the coolant are reported in this section. The reader is remanded to /1/ for details and their derivation.

1) Fuel

The equation describing the space and time temperature distribution in the fuel is (without taking into account heat conduction in axial direc-

tion):

$$\frac{\partial}{\partial r} \left(\lambda_B \frac{\partial T_B}{\partial r} \right) + \frac{1}{r} \lambda_B \frac{\partial T_B}{\partial r} + q_B = \rho_B c_{p_B} \frac{\partial T_B}{\partial t} \quad (r \neq 0) \quad (1)$$

where $T_B = T_B(r, t)$

$\lambda_B = \lambda_B(r, t)$

$\rho_B = \rho_B(r, t)$

$c_{p_B} = c_{p_B}(r, t)$

and $q_B = q_B(r, t)$ is a given input function

with the boundary condition

$$-\left(\lambda_B \frac{\partial T_B}{\partial r} \right)_{R_B} = \alpha_{BH} [T_B(t, R_B) - T_H(t, R_{Hi})] \quad (2)$$

and the initial condition

$$T_B(r, 0) = T_{Bo}(r) \quad (3)$$

On the fuel axis it holds:

$$2\lambda_B \frac{\partial^2 T_B}{\partial r^2} + q_B = \rho_B c_{p_B} \frac{\partial T_B}{\partial t} \quad (r=0) \quad (4)$$

with a symmetry condition

$$\left(\frac{\partial T_B}{\partial r} \right)_{r=0} = 0 \quad (5)$$

In the above equations symbols are defined as follows:

c_{p_B} = fuel specific heat (J/kg °C)

q_B = specific power generated in the fuel (W/m³)

r = radial coordinate (m)

R_B = fuel outer radius

R_{Hi} = radius of the inner clad surface

t = time (s)

T_B = fuel temperature (°C)

T_H = clad temperature (°C)

α_{BH} = fuel-clad heat transfer coefficient (W/m² °C)

λ_B = fuel thermal conductivity (W/m °C)

ρ_B = fuel density (kg/m³)

2) Cladding

The equation describing space and time temperature distribution in the clad is

$$\frac{\partial}{\partial r} \left(\lambda_H \frac{\partial T_H}{\partial r} \right) + \frac{1}{r} \lambda_H \frac{\partial T_H}{\partial r} + q_H = \rho_H c_{pH} \frac{\partial T_H}{\partial t} \quad (6)$$

with the boundary conditions

$$\alpha_{BH} \left[T_B(t, R_B) - T_H(t, R_{Hi}) \right] = - \left(\lambda_H \frac{\partial T_H}{\partial r} \right)_{R_{Hi}} \quad (7)$$

$$- \left(\lambda_H \frac{\partial T_H}{\partial r} \right)_{R_{Ha}} = \alpha_{HK} \left[T_H(t, R_{Ha}) - T_K(t) \right] \quad (8)$$

and the initial condition

$$T_H(r, 0) = T_{Ho}(r) \quad (9)$$

Symbols are defined as follows:

- c_{pH} = specific heat of clad material (J/kg°C)
- q_H = specific power generated in the clad (W/m³)
- R_B = fuel outer radius (m)
- R_{Hi} = radius of inner clad surface (m)
- R_{Ha} = radius of outer clad surface (m)
- T_B = fuel temperature (°C)
- T_H = clad temperature (°C)
- T_K = coolant temperature (°C)
- α_{BH} = fuel-clad heat transfer coefficient (W/m²°C)
- λ_H = thermal conductivity of clad material (W/m°C)
- ρ_H = density of clad material (kg/m³)

3) Coolant

a) Single phase flow

The continuity, momentum and energy equations for the coolant single phase flow are:

$$\frac{\partial \rho_K(z, t)}{\partial t} + \frac{\partial G_K(z, t)}{\partial z} = 0 \quad (10)$$

$$\frac{\partial G_K}{\partial t} + \frac{\partial}{\partial z} \left(\frac{G_K^2}{\rho_K} \right) = - \frac{\partial p}{\partial z} - \frac{f}{2 D_h} \frac{|G_K| G_K}{\rho_K} - g \rho_K \quad (11)$$

$$\rho_K \frac{\partial H_K}{\partial t} + G_K \frac{\partial H_K}{\partial z} = \Phi_K \quad (12)$$

with

$$\Phi_K = \frac{2\pi R_{Ha}}{A} \alpha_{HK} \left[\bar{T}_H(t, R_{Ha}) - T_K(t) \right] + q_K - \frac{2\pi R_{si}}{A} \alpha_{KS} \left[\bar{T}_K(t) - T_S(t) \right] \quad (13)$$

The above set of equations (10) to (12) is closed by the equation of state

$$i_K(z, t) = f \left[\bar{\rho}_K(z, t), p_K(z, t) \right] \quad (14)$$

Boundary conditions are the inlet and outlet pressures

$$\begin{aligned} p_{ei}(z = 0, t) \\ p_a(z = L, t) \end{aligned} \quad (15)$$

while the initial conditions

$$\begin{aligned} \rho_K(z, 0) \\ p_K(z, 0) \\ u_K(z, 0) \\ H_K(z, 0) \end{aligned} \quad (16)$$

are supplied by the solution of the stationary equation (see section II-C-1)

The coolant transient temperature distribution $T_K(z, t)$ is known from $i_K(z, t)$ and $p_K(z, t)$.

b) Two phase flow

For a liquid slug between two vapour bubbles of index $K, K + 1$ the above equations (10) to (13) hold.

The continuity equation is anyway always solved under the approximating

assumption that the time derivative of the coolant density in the slugs is negligible, hence:

$$\frac{dG_K}{dz} = 0 \quad (17)$$

Integration of the momentum equation over the slug length L_K gives

$$L_K \frac{dG_K}{dt} = p_{v2,K} - p_{v1,K+1} - G_K^2 \left[\frac{1}{\rho_{K1,K+1}} - \frac{1}{\rho_{K2,K}} \right] - \frac{G_K^2}{2 D_h} - \int_0^{L_K} \frac{f}{\rho_K} dz - g \int_0^{L_K} \rho_K dz \quad (18)$$

where p_v is the vapour pressure and the indexes 1,2 refer to the lower and upper phase interface respectively.

Similar equations yield for the inlet and outlet slugs where obviously inlet and outlet pressures are involved in the boundary conditions, and the reduced upper and lower lengths are taken into consideration.

The energy equation referred to Lagrangian meshes simplifies to:

$$\rho_K \frac{dH_K}{dt} = \phi_K \quad (19)$$

where the energy transfer ϕ_K is calculated taking into account that the Lagrangian mesh may face different Eulerian (fixed) meshes (see section II-C. 2.3.3)

The continuity equations for the liquid film and the vapour phase are

$$\frac{\partial(1-\alpha) \rho_l}{\partial t} + \frac{\partial(1-\alpha) \rho_l u_l}{\partial z} = - \frac{U}{A} \sqrt{\alpha} m \quad (20)$$

$$\frac{\partial \alpha \rho_v}{\partial t} + \frac{\partial \alpha \rho_v u_v}{\partial z} = \frac{U}{A} \sqrt{\alpha} m \quad (21)$$

where m , considered positive by vaporization, is the mass of coolant transferred from one phase to the other through the unit surface in the unit time by vaporization or condensation.

The momentum equations for the liquid and vapour phases are:

$$\rho_1 \frac{\partial u_1}{\partial t} + \rho_1 u_1 \frac{\partial u_1}{\partial z} = - \frac{\partial p}{\partial z} - \rho_1 g - \frac{U \psi_w}{A(1-\alpha)} \frac{\rho_1}{2} |u_1| u_1 + \frac{U}{A(1-\alpha)} \left[\psi_1 \frac{\rho_v}{2} |u_v| u_v + \frac{v^m}{2} \right] \quad (22)$$

$$\frac{U}{A(1-\alpha)} \left[\psi_1 \frac{\rho_v}{2} |u_v| u_v + \frac{v^m}{2} \right]$$

$$\rho_v \frac{\partial u_v}{\partial t} + \rho_v u_v \frac{\partial u_v}{\partial z} = - \frac{\partial p}{\partial z} - \rho_v g - \frac{U}{A} \frac{\psi_i}{2} \rho_v |u_v| u_v - \frac{U}{A} u_v \frac{m}{2} \quad (23)$$

The energy equations for both phases are:

$$\frac{\partial}{\partial t} \int (1-\alpha) \rho_1 H_1 \bar{\cdot} + \frac{\partial}{\partial z} \int (1-\alpha) \rho_1 u_1 H_1 \bar{\cdot} = \phi_1 \quad (24)$$

$$\frac{\partial}{\partial t} (\alpha \rho_v H_v) + \frac{\partial}{\partial z} \int \alpha \rho_v u_v H_v \bar{\cdot} = \phi_v \quad (25)$$

when ϕ_1, ϕ_v are the amounts of energy transferred to either phase for unit volume and time.

Combining the continuity and energy equation for the liquid phase one derives an equation for the mass transfer between the phases:

$$-m = - \frac{q_w}{h_{fg}} + \frac{S \rho_1}{h_{fg}} \frac{\partial H_1}{\partial t} + \frac{S u_1 \rho_1}{h_{fg}} \frac{\partial H_1}{\partial z} \quad (26)$$

which inserted into (20) yields the basic equation describing the space and time distribution of the liquid film thickness:

$$\frac{\partial S}{\partial t} + \frac{\partial (u_1 S)}{\partial z} = - \frac{q_w}{\rho_1 h_{fg}} + \frac{S}{h_{fg}} \frac{\partial H_1}{\partial t} + \frac{S u_1}{h_{fg}} \frac{\partial H_1}{\partial z} \quad (27)$$

In the above equations symbols are defined as follows:

A	Area of coolant channel cross section (m^2)
D_h	Hydraulic diameter (m)
f	friction coefficient for single phase flow
g	gravity acceleration (m/sec^2)
G_K	coolant (single phase) mass flux (kg/m^2sec)
h_{fg}	vaporization enthalpy (J/kg)
H_K	enthalpy of coolant (single phase) (J/kg)
H_l	enthalpy of liquid film (J/kg)
H_v	enthalpy of vapour (J/kg)
L	channel length
L_k	length of liquid slug above bubble k
m	mass flux by phase change (vaporization) or condensation (kg/m^2sec)
P_K	coolant pressure (= p, equal in either phase) (N/m^2)
p_a	channel outlet pressure (N/m^2)
p_{ei}	channel inlet pressure ahead of the inlet valve (N/m^2)
q_K	specific power generated in the coolant (single phase) (W/m^3)
q_w	power flux released by the clad outer surface (W/m^2)
r	radial coordinate (m)
R_{Ha}	radius of clad outer surface (m)
R_{Si}	radius of structure inner radius (m)
S	liquid film thickness (m)
t	time (sec)
T_H	clad temperature ($^{\circ}C$)
T_K	coolant temperature (single phase) ($^{\circ}C$)
T_S	structure temperature ($^{\circ}C$)
u_K	coolant velocity (single phase) (m/sec)
u_l	liquid film velocity (m/sec)
u_v	vapour velocity (m/sec)
U	perimeter of clad outer surface or of structure inner surface (m)
z	axial coordinate (m)
α	void fraction
α_{HK}	clad-coolant heat transfer coefficient ($W/m^2\ ^{\circ}C$)
α_{KS}	coolant-structure heat transfer coefficient ($W/m^2\ ^{\circ}C$)
ρ_K	coolant density (single phase) (kg/m^3)
ρ_l	liquid film density (kg/m^3)

- ρ_v vapour density (kg/m³)
- Φ_K power transferred to the coolant (single phase) for unit volume (W/m³)
- Φ_l specific power transferred to the liquid film (W/m³)
- Φ_v specific power transferred to the vapour (W/m³)
- Ψ_i interfacial liquid-vapour friction coefficient
- Ψ_w friction coefficient at the channel wall (clad or structure) for single phase flow.

4. Structural material

Assuming the structural material of an axial mesh zone concentrated into one node, the equation describing the time dependence of its temperature is

$$\alpha_{KS} \frac{F_S}{V_S} \overline{[T_K(t) - T_S(t)]} + \alpha_w \frac{F_w}{V_S} \overline{[T_S(t) - T_w(t)]} + q_S(t) = \rho_S c_{pS} \frac{dT_S(t)}{dt} \quad (28)$$

where the first two terms at the left side represent the boundary conditions, i.e. the energy transfer from coolant to the structure and from the structure surface to a surrounding medium (for instance to a by-pass flow with temperature $T_w(t)$).

In the above equation symbols are defined as follows:

- c_{pS} specific heat of structure material (J/kg °C)
- F_S inner surface of structure per unit axial length (m)
- F_w outer surface of structure per unit axial length (m)
- q_S energy produced in structural material per unit volume and time (W/m³)
- t time (sec)
- T_K coolant temperature (°C)
- T_S structure temperature (°C)
- T_w surrounding medium temperature (°C)
- V_S volume of structural material per unit axial length (m²)
- α_{KS} heat transfer coefficient coolant-structure (W/m² °C)
- α_w heat transfer coefficient structure-surrounding medium (W/m² °C)
- ρ_S density of structural material (kg/m³)

C) Numerical treatment of the basic equations and programming details

1) The stationary calculation

A summary description of the subroutine STATO, which performs the stationary calculations, is given in section III-2 with particular reference to some marginal tasks like reading input data, editing results and selecting information for the use of the plotting facilities.

In this section the solution of the basic equations describing the stationary situation is explained together with numerical and programming details which concern the following topics:

- 1.1 calculation of further geometrical data
- 1.2 power normalization
- 1.3 calculation of total power generation in the channel
- 1.4 calculation of mass flow
- 1.5 calculation of coolant temperature distribution
- 1.6 calculation of coolant pressure distribution
- 1.7 calculation of temperature distribution in fuel, clad, structure
- 1.8 calculation of gap width in the stationary hot state.

The basic equations describing the stationary temperature distribution in fuel, clad, coolant, structure and the coolant flow are straightly derived by the equations of section B:

i) Fuel

$$\frac{\partial}{\partial r} \lambda_B \frac{\partial T_B}{\partial r} + \frac{1}{r} \lambda_B \frac{\partial T_B}{\partial r} + q_B = 0 \quad r \neq 0 \quad (1)$$

with the boundary condition

$$-\lambda_B \left(\frac{\partial T_B}{\partial r} \right)_{R_B} = \alpha_{BH} [T_B(0, R_B) - T_H(0, R_{Hi})] \quad (2)$$

and

$$2 \lambda_B \frac{\partial^2 T_B}{\partial r^2} + q_B = 0 \quad r=0 \quad (3)$$

with the symmetry condition

$$\left(\frac{\partial T_B}{\partial r} \right)_{r=0} = 0 \quad (4)$$

ii) Cladding

$$\frac{\partial}{\partial r} \left(\lambda_H \frac{\partial T_H}{\partial r} \right) + \frac{1}{r} \lambda_H \frac{\partial T_H}{\partial r} + q_H = 0 \quad (5)$$

with the boundary conditions:

$$\alpha_{BH} [\bar{T}_B(0, R_B) - T_H(0, R_{Hi})] = - \left(\lambda_H \frac{\partial T_H}{\partial r} \right)_{R_{Hi}} \quad (6)$$

$$- \left(\lambda_H \frac{\partial T_H}{\partial r} \right)_{R_{Ha}} = \alpha_{HK} [\bar{T}_H(0, R_a) - T_K(0)]$$

iii) Coolant

Continuity equation

$$\frac{\partial G_K(z, 0)}{\partial z} = 0 \quad (7)$$

Momentum equation

$$\frac{\partial}{\partial z} \left(\frac{G_K^2}{\rho_K} \right) = - \frac{\partial p}{\partial z} - \frac{f}{2D_h} \frac{|G_K| G_K}{\rho_K} - g \rho_K \quad (8)$$

Energy equation

$$G_K \frac{\partial i_K}{\partial z} = \phi_K \quad (9)$$

Equation of state

$$i_K(z, 0) = f / [\rho_K(z, 0), p_K(z, 0)] \quad (10)$$

The boundary conditions are

$$p(\bar{z}, 0) = p_{ei} \text{ (ahead of the inlet valve, } z = \bar{z})$$

$$p(z = L, 0) = p_a$$

$$T_K(0, 0) = T_{ei} \quad (11)$$

$$T_K(z = L, 0) = T_a$$

iv) Structure

$$\alpha_{KS} \frac{F_S}{V_S} [\bar{T}_K(0) - T_S(0)] - \alpha_w \frac{F_w}{V_S} [\bar{T}_S(0) - T_w(0)] + q_s = 0 \quad (12)$$

Beyond the inlet and outlet coolant pressures and temperatures main input data for the stationary calculation are:

- power generation in fuel, clad, coolant and structure material, the latter owing (if any) to irradiation.
- the inlet and outlet reduced lengths which provide the coupling of the test section to the primary circuit.

The above listed topics are explained hereafter in detail.

1.1 Calculation of further channel geometrical data, namely:

- HSPALT = Length of lower fission gas section (length of axial mesh zones from 1 to NMO-1)
- HKUEKA = Length of the axial breeder zone (section between axial zones NMO and NM1 inclusive)
- HTOP = Length of upper coolant mixing section (axial zones from NM1+1 to NM2)
- HCORE = HSPALT + HKUEKA = length of test section from inlet to mesh zone NM1 inclusive
- AR(M) = Area of flow cross section in the axial mesh zone M.
 $AR(M) = \pi(RKUE(M)^2 - (RBR(M) + DCAN(M))^2)$ in the mesh zones without grid.
- XBRKT(M) = $2\pi (RBR(M) + DCAN(M))/AR(M)$ = ratio of pin circumference to area of flow cross section for axial mesh zone M
- XSTKT(M) = $VSTRUK(M)/(VDUF(M) * AR(M))$ = ratio of structure inner circumference to area of flow cross section
- DH(M) = $4/(XBRKT(M) + XSTKT(M))$ = hydraulic diameter of flow cross section

The above formula for the calculation of the hydraulic diameter is equivalent to (dropping the mesh index M)

$$DH = \begin{cases} \frac{4 \cdot AR}{2\pi(RBR+DCAN) + \frac{VSTRUK}{VDUF}} = \frac{4AR}{2\pi \sqrt{(RBR+DCAN)+RKUE}} & NMO \leq M \leq NM1 \\ \frac{4AR}{VSTRUK} & M < NMO \\ \frac{VSTRUK}{VDUF} & M > NM1 \end{cases}$$

The different definition of DH in the lower fission gas section and in the upper coolant mixing section depends on the fact that in this zones XBRKT(M) = 0 and the values of VDUF, VSTRUK are calculated by taking into account, beyond the structural material, also the volume and surface of the can. Hence in these zones

$$VSTRUK^* = (VSTRUK + \pi(RBR + DCAN)^2)$$

$$VDUF^* = \frac{VSTRUK^*}{2\pi(RBR + DCAN) + RKUE}$$

where the star is used to distinguish between these equivalent worths and the real volume of structure alone.

With reference to the sketch of Fig. 2 one defines the following geometry values for the fuel and cladding:

- DRBR = R_B / NN
- DRBR2 = DRBR**2
- R(N) = r_n (N=1, NN) = radial coordinate of fuel nodes (except fuel axial node)
- RMIN(N) = $r_{n-1/2} = r_n - DRBR/2$
- QRMIN(N) = $r_{n-1/2} / r_n$
- QRPL(N) = $r_{n+1/2} / r_n$
- QRMIV = $(R_B - DRBR/4) / R_B$
- DRC = $r_m - r_i = DCAN/2$
- DRC2 = DRC**2
- RCI = r_i
- RCM = $r_m = r_i + DRC$
- RCA = $r_a = r_i + DCAN$
- QRPLV = $(r_i + DRC/4) / r_i$

$$QRPLH = (r_i + DRC/2)/r_i$$

$$QRCA = (r_a - DRC/4)/r_a$$

$$QRCH = (r_a - DRC/2)/r_a$$

$$QRCMS = (r_m - DRC/2)/r_m$$

$$QRCPL = (r_m + DRC/2)/r_m$$

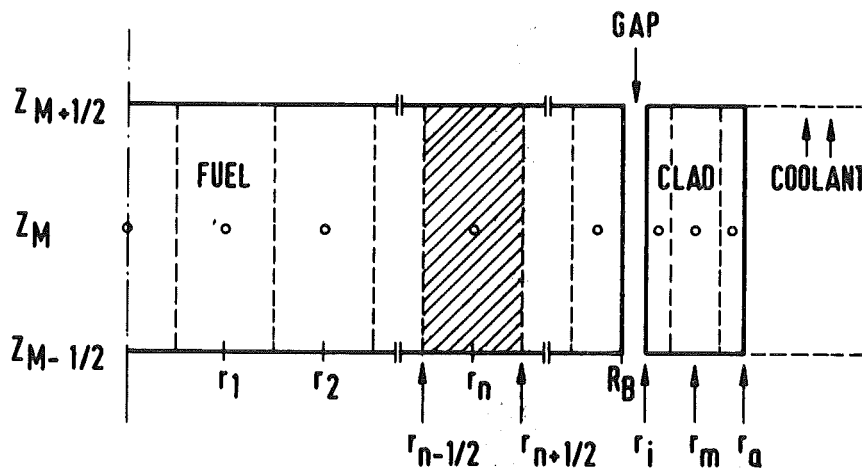


Fig. 2: Sketch showing the definition of radial meshes in fuel and clad.

1.2 Power normalization (axial distribution)

These are four possible ways of defining the pin power according to the four possible combinations of the input parameters $ML = 1/2$ and $MAX = -1/1$ (See Input Description, Section III.4) The normalization of the axial power distribution is accordingly performed in one of four distinct branches.

a) Case I

ML = 1 Total power generation QSUM is defined for the full channel (W)
MAX = -1 Node-wise power distribution is given (W) in the array FAX(M),
 $M=1,2,\dots,NM2$. That means: FAX(M) contains the total power, in
 Watts, generated in the volume of the mesh M, of length DELTZ(M)

The total power generation in the channel is (see also Section 1.3.)

$$\begin{aligned} QSUM &= \sum_M^{NM2} QGESO(M) \cdot \sum_i^4 ANT_i(M) V_i(M) = \\ &= \pi \sum_M^{NM2} QGESO(M) \cdot XKK(M) \cdot DELTZ(M) \quad (W) \end{aligned}$$

with

$$XKK(M) = \frac{\sum_i^4 ANT_i(M) V_i(M)}{\pi DELTZ(M)} \quad (m^2)$$

where the index i refers to the fuel, clad, coolant and structural materials of volume V_i (in the mesh M) and ANT_i defines the distribution of power in the four materials.

Defining a form factor

$$FAK = \frac{QSUM}{\sum_M^{NM2} FAX(M)}$$

the normalized specific power distribution is

$$\begin{aligned} QGESO(M) &= \frac{QSUM \cdot FAX(M)}{\sum_M FAX(M) \cdot \pi XKK(M) DELTZ(M)} = \\ &= FAK \cdot \frac{FAX(M)}{\sum_i ANT_i(M) V_i(M)} \quad (W/m^3) \end{aligned}$$

b) Case II

ML = 1 Total power generation QSUM is defined for the full channel (W)
MAX = 1 Node-wise specific power distribution (W/m³) is given in the
array FAX(M), M = 1, 2, ... NM2.

Defining the form factor

$$FAK = \frac{QSUM}{\pi \sum_{M=1}^{NM2} FAX(M) \cdot XKK(M) \cdot DELTZ(M)}$$

the axial specific power distribution is

$$QGESO(M) = FAK \cdot FAX(M) \quad (W/m^3)$$

c) Case III

ML = 2 Peak power density QQSO (W/m³) is given
MAX = -1 Node-wise power distribution is given (W) in the array FAX(M),
M = 1, 2, ... NM2.

Defining MAX(FQS) the maximum for every M of

$$FQS(M) = \frac{FAX(M)}{\pi \cdot XKK(M) \cdot DELTZ(M)} = \frac{FAX(M)}{\sum_i ANT_i(M) V_i(M)} \quad (W/m^3)$$

and

$$FAK = \frac{QQSO}{MAX(FQS)}$$

the axial specific power distribution is

$$\begin{aligned} QGESO(M) &= \frac{QQSO}{MAX(FQS)} \cdot \frac{FAX(M)}{\sum_i ANT_i(M) V_i(M)} = \\ &= FAK \cdot FQS(M) \quad (W/m^3) \end{aligned}$$

d) Case IV

ML = 2 Peak power density QQSO (W/m³) is given.
MAX = 1 Node-wise specific power distribution is given (W/m³) in the
array FAX(M), M = 1, 2, ... NM2.

Defining

$$FAK = \frac{QQSO}{\text{MAX}_M(FAX(M))}$$

the axial specific power distribution is

$$QGESO(M) = FAK \cdot FAX(M) \quad (W/m^3)$$

1.3 Calculation of total power generation in the channel $\overline{QSUM(KKN)}$

$$\begin{aligned}
 QSUM &= \sum_1^{NM2} M \text{ (Power generated in fuel + clad + coolant + structure)}_M \\
 &= \sum_1^{NM2} M \text{ QGESO}(M) \sum_1^4 \text{ ANT}_i V_i \quad \overline{W} \quad (13)
 \end{aligned}$$

where the index i refers to the four materials of volume V_i among which the specific power generation (QGESO) is distributed according to the values of ANT_i .

Letting

$$\begin{aligned}
 XKK(M) &= \text{ANTB}(M) \cdot \text{RBR}(M)^2 \\
 &+ \text{ANTC}(M) \cdot \overline{(\text{RBR}(M) + \text{DCAN}(M))^2 - \text{RBR}(M)^2} \\
 &+ \text{ANTK}(M) \cdot \overline{\text{RKUE}(M)^2 - (\text{RBR}(M) + \text{DCAN}(M))^2} \\
 &+ \text{ANTS}(M) \cdot \text{VSTRUK}(M) / \pi = \frac{\sum_1^4 \text{ ANT}_i(M) V_i(M)}{\pi \text{ DELTZ}(M)} \quad \overline{m}^2 \quad (14)
 \end{aligned}$$

one has

$$\begin{aligned}
 QSUM &= \pi \sum_1^{NM2} M \text{ QGESO}(M) \cdot XKK(M) \cdot \text{DELTZ}(M) \quad \overline{W} \\
 &= \sum_1^{NM2} M Q_c(M) \cdot \text{DELTZ}(M) \quad (15)
 \end{aligned}$$

letting $Q_c(M)$ denote the total power generated per unit length in the channel mesh zone M .

1.4 Calculation of mass flow

Applying the first equation of thermodynamic in the form

$$dq = di - Av dp \quad (16)$$

(where A is the transformation factor from mechanical to thermal units) to the mass flow G_K (kg/sec) and assuming that the coolant undergoes a transformation at constant pressure one has

$$dQ = dI = G_K di = G_K \left(\frac{\partial i}{\partial T} \right)_p dT = G_K c_p dT \quad (17)$$

hence

$$G_K = \frac{dQ}{di} = \frac{dQ}{c_p dT} \quad (18)$$

In the programme

$$XMAST = \frac{QSUM}{DXIG} \quad \underline{[kg/sec]} \quad (19)$$

where the enthalpy difference between outlet and inlet DXIG is calculated from the known pressures and temperatures. This first evaluation of the mass flow is later refined by taking into account the power losses beyond the structure outer surface which can be calculated when the temperature distribution is known. The stationary power losses are

$$Q_w = \sum_{1}^{NM2} (T_S(M) - T_w) \alpha_w(M) F_w(M) \Delta z(M) \quad \underline{[W]} \quad (20)$$

where

T_S = structure temperature

T_w = temperature of surrounding medium (for instance by-pass flow temperature)

α_w = heat transfer coefficient from the structure outer surface to the surrounding medium

F_w = outer structure surface per unit axial length

Δz = length of axial mesh zone

The refined value of the mass flow is:

$$XMAST = \frac{QSUM - \sum_{1}^{NM2} (T_S(M) - T_w) \alpha_w(M) F_w(M) \Delta z(M)}{DXIG} \quad (21)$$

Equation (19) could have been obtained straightly integrating the stationary equation

$$G_K \frac{\partial i_K}{\partial z} = \phi_K$$

over the channel length, keeping in mind that in stationary conditions

the full power generated (detracted the thermal losses) is supplied to the coolant, hence

$$\int_{\text{Channel length}} \phi_K dz = Q_{\text{SUM}} P_w$$

1.5 Calculation of coolant temperature distribution

The temperature distribution of the coolant is calculated starting from the known inlet value T_{ei} and applying to every mesh zone M in upwards direction the relationship

$$TK_{\text{out}} = TK_{\text{inn}} + \Delta T_K(M) \quad (22)$$

where

$$\Delta T_K(M) = \frac{Q_K(M)}{c_{pK} G_K} \quad (23)$$

Q_K is the energy transferred to the coolant in the unit time (in the mesh zone M), given by the difference between the total power generated in the channel $Q_c(M)$ and power lost beyond the structure $\alpha_w(M)$. Dropping the index M one has

$$Q_K = (Q_c - Q_w) \Delta z \quad (24)$$

with

$$Q_w = \alpha_w F_w (T_S - T_w) \quad (25)$$

From the equation (12) determining the stationary structure temperature one derives

$$Q_w = \alpha_{KS} F_S (T_K - T_S) + Q_S \quad (26)$$

with $Q_S = q_S V_S$ hence

$$Q_K = (Q_c - \alpha_{KS} F_S (T_K - T_S) - Q_S) \Delta z \quad (27)$$

Introducing into (23) one derives for the coolant temperature increment over half mesh length

$$T_K - T_{K \text{ inn}} = \frac{Q_K}{2c_{pK} G_K} = \frac{Q_c - \alpha_{KS} F_S (T_K - T_S) - Q_S}{2c_{pK} G_K} \Delta z \quad (28)$$

from which the middle-point coolant temperature is derived:

$$T_K = \frac{2c_{pK} G_K T_{K \text{ inn}} + (Q_c - Q_S) \Delta z + \alpha_{KS} F_S T_S \Delta z}{2c_{pK} G_K + \alpha_{KS} F_S \Delta z} \quad (29)$$

Letting

$$\begin{aligned} c\phi 1 &= 2c_{pK} G_K \\ c\phi 2 &= \alpha_{KS} F_S \Delta z \\ c\phi 3 &= (Q_c - Q_S) \Delta z = QGESO \left(XKK - \frac{ANTS \cdot VSTRVK}{\pi} \right) \pi \Delta z \end{aligned} \quad (30)$$

one has

$$T_K = \frac{c\phi 1 T_{K \text{ inn}} + c\phi 3 + c\phi 2 T_S}{c\phi 1 + c\phi 2} \quad (31)$$

The ratio of power lost in the axial mesh zone to the power generated in the same zone is

$$\xi_w(M) = \frac{Q_w(M)}{Q_c(M)} = \frac{Q_c - Q_K/\Delta z}{Q_c} = \frac{Q_c \Delta z - 2c_{pK} G_K (T_K - T_{K \text{ inn}})}{Q_c \Delta z} \quad (32)$$

The ratio of power losses over the full channel length to total power generation

$$L_w = \frac{\sum_M^{NM2} Q_w(M)}{QSUM} \quad (33)$$

1.6 Calculation of coolant pressure distribution

Integrating equation (8) over the channel length with the boundary conditions $p = p_{ei}$ ahead of the inlet valve and $p = p_a$ at channel outlet one derives the pressure drop in the channel:

$$\begin{aligned} \Delta p_c &= G_K^2 \left(\frac{1}{\rho_a} - \frac{1}{\rho_{ei}} \right) + \sum_1^{NM2} M \frac{f(M)}{2D_h(M)} \left| \frac{G_K}{\rho_K(M)} \right| + \rho_K(M) g \Delta z(M) \\ &+ \Delta p_A \end{aligned} \quad (34)$$

where ρ_a , ρ_{ei} are the coolant densities at channel outlet and inlet respectively, f the wall friction coefficient, g the gravity acceleration, and Δp_A is the pressure difference due (if any) to enlargement of cross section in the upper mixing region.

The coefficient f takes into account the power losses due to friction and an additional contribution due to the grid spacers, homogenized over the channel length. It is calculated by

$$f = a \text{Re}^b + \psi \frac{D_h}{D_{ABST}} \quad (35)$$

where default values of the coefficient are $a = 0.183$, $b = -0.25$, $\psi = 1.15$ and D_{ABST} is the distance between two consecutive spacers (see also Input Description, section III-4).

The pressure difference due to variation of the cross flow area is given, taking into account the irreversible pressure drop, by /1/

$$\Delta p_A = \frac{G_K}{2\rho_K} \left[-|G_K| K_1 \left(1 - \frac{AR_1}{AR_2} \right)^2 + G_K \left(1 - \frac{AR_1^2}{AR_2^2} \right) \right] \quad (36)$$

$$\begin{aligned} \text{where } K_1 &= 1 & \text{if } G_K \geq 0 \\ K_1 &= 0.5 & \text{if } G_K < 0 \end{aligned}$$

and AR_1 is the flow area upstream, AR_2 downstream the cross section enlargement.

Subtracting the pressure drops in the channel from the (input) driving pressure ($p_{ei} - p_a$) one has the pressure drop in the inlet valve

$$\Delta p_{B1} = (p_{ei} - p_a) - \Delta p_c \quad (37)$$

Application of equation (34) or integration of equation (8) over every axial mesh, from the top downwards to the bottom of the channel, yields the coolant pressure distribution, as shown in the following sketch:

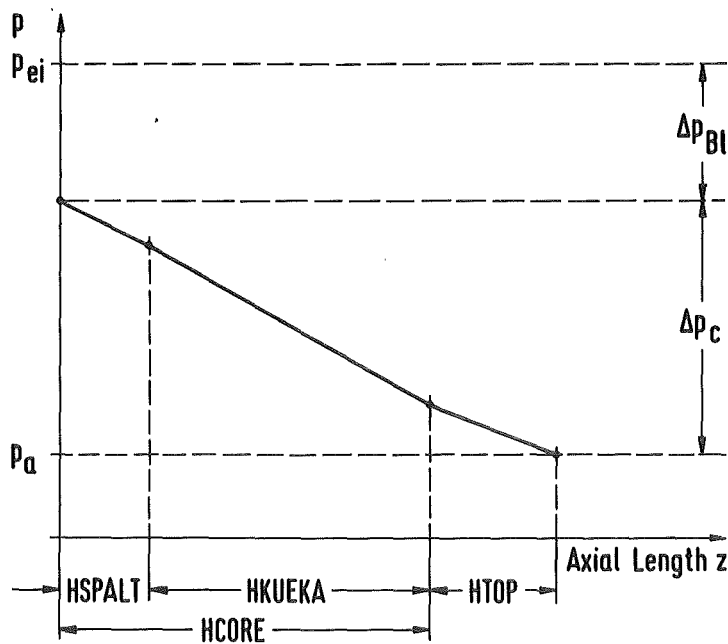


Fig. 3 Sketch showing qualitatively the stationary pressure distribution in the coolant versus axial length.

The pressure drop in the inlet valve being also given by

$$\Delta p_{B1} = \zeta_o \frac{G_K^2}{2\rho} \quad (38)$$

one derives the coefficient ζ_o (= ZETADO) as output of the stationary calculation and initial value for a time variation of the type $\zeta = \zeta_o f(t)$ which lets simulating a transient mass flow reduction (see description of subroutine FZETAD).

Calculation steps 1.4 - 1.6 (mass flow, coolant temperature and pressure distribution) are carried out simultaneously with an iteration procedure which stops when a temperature distribution has been found which is consistent with the power and the given boundary conditions.

1.7 Calculation of temperature distributions in fuel, clad, structure

a) First evaluation of temperature distributions in fuel and clad

The calculated temperature distribution in the coolant is assumed as boundary condition for a first estimation of temperature in clad and fuel. This occurs by integrating equations (1) and (5) assuming the thermal conductivity constant. The integration constants are determined imposing the boundary condition that the heat flux through any cylindrical surface in fuel and clad is equal (in stationary condition) to the total power generated inside that surface.

Proceeding from the clad outer surface, where the boundary condition given by the coolant temperature is known, inwards, one has for the clad outer node temperature

$$\alpha_{HK}^0 (T_{H,r_a}^0 - T_K^0) S_{r_a} = Q_B^0 + Q_H^0 \quad (39)$$

where S_{r_a} is the clad outer surface per unit axial length and Q_b , Q_H are the powers generated in fuel and clad respectively. This boundary condition yields T_{H,r_a}^0 .

Writing equation (5) in the form

$$\frac{1}{r} \frac{d}{dr} \left(r \frac{dT_H}{dr} \right) - \frac{q_H}{\lambda_H} = 0 \quad (40)$$

under the assumption that the thermal conductivity is constant, and integrating one has (for an hollow cylinder)

$$T_H(r) = a + b \ln r - \frac{q_H r^2}{4\lambda_H} \quad (41)$$

where a,b are integration constants.

Assuming that the influence of the power generation in the clad onto the temperature distribution is negligible (hence neglecting the term $q_H r^2/4\lambda$), the temperature of the clad middle node is derived from the above equation imposing the boundary conditions:

$$T_H(r_a) = T_{Ha} - 2\pi\lambda_H r_a \left(\frac{dT_H}{dr} \right)_{r_a} = Q_B^o + Q_H^o \quad (42)$$

which determines the constants a, b and yields:

$$T_H^o(r_m) = T_{Hr_a}^o + \frac{Q_B^o + Q_H^o}{2\pi\lambda_H} \ln \frac{r_a}{r_m} \quad (43)$$

where the thermal conductivity is calculated with reference to the known temperature $T_H(r_a)$.

The temperature of the clad inner node is derived imposing the boundary conditions :

$$T_H(r_m) = T_{Hm} - 2\pi\lambda_H r_m \left(\frac{dT_H}{dr} \right)_{r_m} = Q_B^o + Q_H^o/2 \quad (44)$$

which yields

$$T_H^o(r_i) = T_{Hm}^o + \frac{Q_B^o + \frac{Q_H^o}{2}}{2\pi\lambda_H} \ln \frac{r_m}{r_i} \quad (45)$$

The temperature of the outermost fuel is given by the boundary condition

$$q_{BH}^o (T_{BNN}^o - T_{Hr_i}^o) = Q_B^o \quad (46)$$

The temperature distribution in the fuel is described under the assumption of constant thermal conductivity by the equation

$$\frac{1}{r} \frac{d}{dr} \left(r \frac{dT_B}{dr} \right) - \frac{q_B}{\lambda_B} = 0 \quad (47)$$

Integrating one has

$$T_B(r) = a - \frac{q_B r^2}{4\lambda_B} \quad (48)$$

The integration constant a represents the fuel axial temperature ($a = T_{B0}$) and is determined by imposing the boundary condition

$$T_B^o(r_{NN}) = T_{BNN}^o \quad (49)$$

which yields

$$T_{BO}^{\circ} = T_{BNN}^{\circ} + \frac{q_B^{\circ} r_{NN}}{4\lambda_B} \quad (50)$$

The fuel temperature in any internal node N (N = 1, 2, ..., NN-1) is then given by

$$T_B^{\circ}(r_n) = T_{BNN}^{\circ} + \frac{(T_{BO}^{\circ} - T_{BNN}^{\circ})(r_{NN}^2 - r_n^2)}{r_{NN}^2} \quad (51)$$

This estimation of the temperature distribution in clad and fuel is not definite because the thermal conductivities were calculated with reference to a temperature different from the yet unknown temperatures of the respective nodes. This temperature distribution is therefore used only as first approximation to start the refined calculation performed iteratively by means of the Gauss-Seidel iteration scheme, as explained hereafter.

b) Refined temperature distributions in fuel and clad and calculation of structure temperature with the Gauss-Seidel iteration method.

i) Fuel

Taking the annulus delimited by the cylindrical surfaces

$S_{n-1/2}$, $S_{n+1/2}$ with radii $r_{n-1/2}$, $r_{n+1/2}$ as control volume, and integrating equation (1) over the outer surfaces of this control volume one has

$$- \int_{S_{n-1/2}} \lambda_B^{\circ} \frac{\partial T_B^{\circ}}{\partial r} ds + \int_{S_{n+1/2}} \lambda_B^{\circ} \frac{\partial T_B^{\circ}}{\partial r} ds + q_n^{\circ} V_n = 0 \quad (52)$$

or

$$-\lambda_{B,r_{n-1/2}} \left(\frac{\partial T_B^{\circ}}{\partial r} \right)_{r_{n-1/2}} S_{n-1/2} + \lambda_{B,r_{n+1/2}} \left(\frac{\partial T_B^{\circ}}{\partial r} \right)_{r_{n+1/2}} S_{n+1/2} + q_n^{\circ} V_n = 0 \quad (53)$$

where V_n is the volume of the annular section belonging to the considered axial mesh zone. Space discretisation of this equation yields the algebraic equation

$$A_n^o T_{B,n}^o + B_n^o T_{B,n-1}^o + C_n^o T_{B,n+1}^o = Q_n^o \quad (54)$$

with

$$A_n^o = \lambda_{B,r_{n-1/2}} \frac{r_{n-1/2}}{r_n} + \lambda_{B,r_{n+1/2}} \frac{r_{n+1/2}}{r_n} \quad (55a)$$

$$B_n^o = - \lambda_{B,r_{n-1/2}} \frac{r_{n-1/2}}{r_n} \quad (55b)$$

$$C_n^o = - \lambda_{B,r_{n+1/2}} \frac{r_{n+1/2}}{r_n} \quad (55c)$$

$$Q_n^o = q_n^o \Delta r_B^2 \quad (55d)$$

and
$$\Delta r_B = r_{n+1/2} - r_{n-1/2} \quad (55e)$$

The above equation is applicable to all fuel internal nodes ($n = 1, 2, \dots, NN-1$).

For the fuel outermost node, taking as control volume the annulus delimited by the cylindrical surfaces with radii $r_{NN-1/2}$, r_{NN} , one has

$$- \int_{S_{NN-1/2}} \lambda_B \frac{\partial T_B}{\partial r} ds - \alpha_{BH} S_{NN} (T_{B,NN} - T_{Hi}) + q_{NN} V_{NN} = 0 \quad (56)$$

which yields the algebraic equation

$$A_{NN}^o T_{B,NN}^o + B_{NN}^o T_{B,NN-1}^o + C_{NN}^o T_{Hi}^o = Q_{NN}^o \quad (57)$$

with

$$A_{NN}^o = \lambda_{r_{NN-1/2}} \frac{r_{NN-1/2}}{r_{NN}} + \alpha_{BH} \Delta r_B \quad (58a)$$

$$B_{NN}^o = -\lambda r_{NN-1/2} \frac{r_{NN-1/2}}{r_{NN}} \quad (58b)$$

$$C_{NN}^o = -\alpha_{BH} \Delta r_B \quad (58c)$$

$$Q_{NN}^o = \frac{\Delta r_B^2}{2} \frac{r_{NN-1/4}}{r_{NN}} q_{NN} \quad (58d)$$

For the fuel central node, taking as control volume the cylinder of radius $r_{1/2}$, one has

$$- \int_{S_{1/2}} \left(- \frac{\lambda \partial T_B}{\partial r} \right) ds + q_o V_o = 0 \quad (59)$$

which yields the algebraic equation (the superscript "o" refers to the stationary calculation, the subscript to the axial fuel node)

$$A_o^o T_{B,o}^o + C_o^o T_{B,1}^o = Q_o^o \quad (60)$$

with:

$$A_o^o = \lambda r_{1/2} \quad (61a)$$

$$C_o^o = -\lambda r_{1/2} \quad (61b)$$

$$Q_o^o = q_o \frac{\Delta r_B^2}{4} \quad (61c)$$

ii) Cladding

For the clad inner node, taking as control volume the annulus delimited by the cylindrical surfaces with radii r_i , $r_{i+1/2}$, one has

$$\alpha_{BH} (T_{B,NN} - T_{Hi}) S_i - \int_{S_{i+1/2}} \left(-\lambda_H \frac{\partial T_H}{\partial r} \right) ds + q_{Hi} V_{Hi} = 0 \quad (62)$$

which yields the algebraic equation

$$A_{Hi}^{\circ} T_{Hi}^{\circ} + B_{Hi}^{\circ} T_{B,NN}^{\circ} + C_{Hi}^{\circ} T_{Hm}^{\circ} = Q_{Hi}^{\circ} \quad (63)$$

with

$$A_{Hi}^{\circ} = \alpha_{BH}^{\circ} \Delta r_H + \lambda_{H,r_{i+1/2}}^{\circ} \frac{r_{i+1/2}}{r_i} \quad (64a)$$

$$B_{Hi}^{\circ} = -\alpha_{BH}^{\circ} \Delta r_H \quad (64b)$$

$$C_{Hi}^{\circ} = -\lambda_{H,r_{i+1/2}}^{\circ} \frac{r_{i+1/2}}{r_i} \quad (64c)$$

$$Q_{Hi}^{\circ} = \frac{r_{i+1/4}}{r_i} \frac{\Delta r_H^2}{2} q_{Hi} \quad (64d)$$

For the clad middle node, taking as control volume the annulus delimited by the cylindrical surfaces with radii $r_{m-1/2}$, $r_{m+1/2}$ one has

$$- \int_{S_{m-1/2}} \lambda_H \frac{\partial T_H}{\partial r} ds + \int_{S_{m+1/2}} \lambda_H \frac{\partial T_H}{\partial r} ds + q_{Hm} V_{Hm} = 0 \quad (65)$$

which yields the algebraic equation

$$A_{Hm}^{\circ} T_{Hm}^{\circ} + B_{Hm}^{\circ} T_{Hi}^{\circ} + C_{Hm}^{\circ} T_{Ha}^{\circ} = Q_{Hm}^{\circ} \quad (66)$$

with

$$A_{Hm}^{\circ} = \lambda_{H,m-1/2}^{\circ} \frac{r_{m-1/2}}{r_m} + \lambda_{H,m+1/2}^{\circ} \frac{r_{m+1/2}}{r_m} \quad (67a)$$

$$B_{Hm}^{\circ} = -\lambda_{H,m-1/2}^{\circ} \frac{r_{m-1/2}}{r_m} \quad (67b)$$

$$C_{Hm}^{\circ} = -\lambda_{H,m+1/2}^{\circ} \frac{r_{m+1/2}}{r_m} \quad (67c)$$

$$Q_{Hm}^{\circ} = q_{Hm}^{\circ} \Delta r_H^2 \quad (67d)$$

For the clad outer node, taking as control volume the annulus delimited by the cylindrical surfaces with radii $r_{m+1/2}$, r_a one has

$$-\int_{S_{m+1/2}} \lambda_H \frac{\partial T_H}{\partial r} ds - \alpha_{HK} (T_{Ha} - T_K) S_{ra} + q_{Ha} V_{Ha} = 0 \quad (68)$$

which yields the algebraic equation

$$A_{Ha}^{\circ} T_{Ha}^{\circ} + B_{Ha}^{\circ} T_{Hm}^{\circ} + C_{Ha}^{\circ} T_K^{\circ} = Q_{Ha}^{\circ} \quad (69)$$

With

$$A_{Ha}^{\circ} = \lambda_{H,r_{a-1/2}} \frac{r_{a-1/2}}{r_a} + \alpha_{HK} \Delta r_H \quad (70a)$$

$$B_{Ha}^{\circ} = -\lambda_{H,r_{a-1/2}} \frac{r_{a-1/2}}{r_a} \quad (70b)$$

$$C_{Ha}^{\circ} = -\alpha_{HK} \Delta r_H \quad (70c)$$

$$Q_{Ha}^{\circ} = \frac{\Delta r_H}{2} \frac{r_{a-1/4}}{r_a} q_{Ha}^{\circ} \quad (70d)$$

iii) Structure

Equation (12) can be straightforward written in the form

$$A_S^{\circ} T_S^{\circ} + B_S^{\circ} T_K^{\circ} + C_S^{\circ} T_W^{\circ} = Q_S^{\circ} \quad (71)$$

with

$$A_S^{\circ} = \alpha_{KS}^{\circ} + \alpha_W^{\circ} \frac{F_W}{F_S} \quad (72a)$$

$$B_S^{\circ} = -\alpha_{KS}^{\circ} \quad (72b)$$

$$C_S^{\circ} = -\alpha_W^{\circ} \frac{F_W}{F_S} \quad (72c)$$

$$Q_S^{\circ} = q_S^{\circ} \frac{V_S}{F_S} \quad (72d)$$

The above equations form a system of NN+5 linear algebraic equations which can be written in matrix form as

$$AT = Q \quad (73)$$

where A is a tridiagonal square matrix formed by the A, B, C 's coefficients. T is a column vector containing the unknown node temperatures and Q a column vector with the power generation terms.

The solution of this linear system yields the stationary temperature distribution. It is carried out with the iterative Gauss-Seidel method assuming as initial distribution in fuel and clad that supplied by the analytical solution of the respective equations under the assumption of constant material properties, as explained in the first part of this section.

A detailed description of the Gauss-Seidel iteration scheme is given in section II-C-2.1d, where the same problem is dealt with under transient conditions introducing both space and time discretizations.

1.8 Calculation of gap width in the stationary hot state (a simplified gap conductance model)

A simple calculation of the gap width, which takes into account only thermal strains, is available in the BLOW-3A programme. Accordingly, the fuel-clad heat transfer coefficient can be calculated in dependence on the gap width, making use of the results supplied by the SATURN-1 programme /10/.

The simplified gap width calculation is split into a stationary and a transient part. The stationary one is based on the following algorithm:

Let $\bar{\delta}$ be the input worth of the gap width in the cold state and ΔT_B , ΔT_{Hi} the temperature increments of fuel outer surface and clad inner surface respectively corresponding to the transition from the cold state to the stationary state which precedes the initiation of a simulated accident. The fuel and clad inner radii in the (hot) stationary state are, for the axial mesh m:

$$R_B^m = \bar{R}_B^m (1 + \lambda_B \Delta T_B^m) \quad (74)$$

$$R_{Hi}^m = \bar{R}_{Hi}^m (1 + \lambda_{Hi} \Delta T_{Hi}^m) \quad (75)$$

where, in the cold state,

$$\bar{\delta} = \bar{R}_B - \bar{R}_{Hi} \quad (76)$$

The axial dependent gap width is then in the stationary state:

$$\delta^m = R_{Hi}^m - R_B^m \quad (77)$$

and its deviation from the mean value over the full axial length $\sum_m \Delta Z^m$ is:

$$\Delta \delta^m = \delta^m - \frac{\sum_m \delta^m \Delta Z^m}{\sum_m \Delta Z^m} \quad (78)$$

Let \bar{h} be the input worth of the fuel-clad heat transfer coefficient which corresponds to the input gap width. It is used for the iterative calculation to determine fuel and coolant stationary temperature fields. One has therefore to find a value of the gap width consistent with the input worth \bar{h} of the heat transfer coefficient. To this purpose the above calculated deviation $\Delta \delta^m$ from the mean value is assumed to hold with respect to the input worth. The stationary gap width is therefore assumed as:

$$\delta_0^m = \bar{\delta} + \Delta \delta^m = \bar{\delta} + \delta^m - \frac{\sum_m \delta^m \Delta Z^m}{\sum_m \Delta Z^m} \quad (79)$$

Thermal strains during the transient calculation are then derived taking the stationary (hot) temperature as reference.

2. Transient calculation

The methods used for the solution of the basic equations describing the transient temperature distribution and the transient coolant behaviour are illustrated, in this section.

Two focal points are considered, according to the single-phase or two-phase flow conditions of the coolant, and are described separately in sections two and three respectively. The first section deals with the numerical solution of the heat diffusion equations in fuel, clad and structural material. This is essentially the same for the single phase flow and for the two phase flow calculations and therefore treated in a single section. As far as the calculation of temperature distribution in the solid materials is concerned, the main difference between single and two-phase flow computation consists in the calculation of the clad (or structure) to coolant heat transfer coefficients which is straightforward in one case but rather complicated in the other, because the location of the vapour bubbles must be considered. Accordingly, the solution of the energy equation for the coolant in the single phase flow is treated together with the heat diffusion equations for fuel, clad and structure in the same subroutine FBRT, while it is treated separately for the two phase flow and does not therefore appear in the subroutine FBRTB. Apart from this the two subroutines are equal. A fourth section explains the calculation of temperature distribution in fuel and clad during melting.

2.1 The numerical treatment of the differential equations describing the transient temperature distributions in fuel, clad and structure.

Numerical solution of the set of equations (II-B-10) to (12) for the coolant single phase flow or of equations (II-B-17) to (27) for the two phase flow is performed first at the beginning of every time step and yields the mass flow, the axial pressure and temperature distribution in the coolant. The latter is assumed as boundary condition for the subsequent numerical solution of the equations (II-B-1) to (9) and (II-B-28) describing the transient temperature distributions in fuel, clad and structural material.

Referring to a given axial mesh zone with index M ($M=1, \dots, NM2$) space and time discretisation of the above equations is done as follows. With reference to sketch shown in Fig. 2, the fuel radius R_B is divided into NN segments

of length $\Delta r_B = R_{BNN}$, defining the position of $NN+1$ radial nodes: $r_0 = 0$, r_n ($n=1, NN$) with $r_{NN} = R_B$. To every internal node is associated the mass of fuel material comprised in the annulus of radii $r_{n-1/2}$, $r_{n+1/2}$, represented by the shaded area around the node of coordinates $(z_{M+1/2}, r_n)$ in the sketch. To the axial node is associated the mass within the cylinder of radius $r_{1/2}$; to the outermost node the mass in the annulus with radii $r_{n-1/2}$, R_B . The clad material is associated to three nodes of radial coordinates r_i , r_m , r_a (inner, middle, outer node) (with $r_m = (r_i + r_a)/2$). Let $\Delta r_H = (r_a - r_i)/2$. The mass of clad material associated to the middle node is therefore roughly twice the masses associated to the lateral nodes. The problem time is discretized in a sequence of macroscopic time steps $\Delta t_n = t_n - t_{n-1}$. Time discretisation may be grafically represented in the above sketch by a set of horizontal lines thus giving a lattice of rectangular cells. Let refer with indexes $h, h-1$ to the symbols of physical magnitudes calculated at the time points t_n, t_{n-1} respectively.

a) Fuel

i) Inner node

With reference to the annulus $(r_{n-1/2}, r_{n+1/2})$ of unit axial length as control volume, equation (II-B-1) may be written:

$$-\int_{S_n} \lambda \frac{\partial T_B(r, t)}{\partial r} ds + q_n V_n = \rho_n c_p V_n \frac{\partial T_B}{\partial t} \quad (1)$$

where V_n denotes the volume of the annulus and the integral is calculated for both lateral surfaces $(S_n = S_{n-1/2} \cup S_{n+1/2})$.

Hence:

$$-\lambda_{r_{n-1/2}} \left(\frac{\partial T_B}{\partial r} \right)_{r_{n-1/2}} 2\pi r_{n-1/2} + \lambda_{r_{n+1/2}} \left(\frac{\partial T_B}{\partial r} \right)_{r_{n+1/2}} 2\pi r_{n+1/2} + q_n 2\pi r_n \Delta r = \rho_n c_p 2\pi r_n \Delta r \frac{\partial T_B}{\partial t} \quad (2)$$

Terms of this equation are approximated by

$$\begin{aligned} \lambda_{r_{n-1/2}} \left(\frac{\partial T_B}{\partial r} \right)_{r_{n-1/2}} &= \theta \left[\lambda_{r_{n-1/2}} \left(\frac{\partial T_B}{\partial r} \right)_{r_{n-1/2}} \right]^h + (1-\theta) \left[\lambda_{r_{n-1/2}} \left(\frac{\partial T_B}{\partial r} \right)_{r_{n-1/2}} \right]^{h-1} \\ &= \theta \left[\lambda_{r_{n-1/2}}^h \frac{T_{B,n}^h - T_{B,n-1}^h}{\Delta r} \right] + (1-\theta) \left[\lambda_{r_{n-1/2}}^{h-1} \frac{T_{B,n}^{h-1} - T_{B,n-1}^{h-1}}{\Delta r} \right] \end{aligned} \quad (3)$$

$$\begin{aligned} \lambda_{r_{n+1/2}} \left(\frac{\partial T_B}{\partial r} \right)_{r_{n+1/2}} &= \theta \left[\lambda_{r_{n+1/2}} \left(\frac{\partial T_B}{\partial r} \right)_{r_{n+1/2}} \right]^h + (1-\theta) \left[\lambda_{r_{n+1/2}} \left(\frac{\partial T_B}{\partial r} \right)_{r_{n+1/2}} \right]^{h-1} \\ &= \theta \left[\lambda_{r_{n+1/2}}^h \frac{T_{B,n+1}^h - T_{B,n}^h}{\Delta r} \right] + (1-\theta) \left[\lambda_{r_{n+1/2}}^{h-1} \frac{T_{B,n+1}^{h-1} - T_{B,n}^{h-1}}{\Delta r} \right] \end{aligned} \quad (4)$$

$$q_n = \theta q_n^h + (1-\theta)q_n^{h-1} \quad (5)$$

$$\frac{\partial T_B}{\partial t} = \frac{T_{B,n}^h - T_{B,n}^{h-1}}{\Delta t_h} \quad (6)$$

where θ is a parameter. For $\theta = 0$ one has the ordinary explicit scheme, and for $\theta=1$ a fully implicit scheme. $\theta = 1/2$ was first used by Crank and Nicolson /11/ and yields an half-implicit scheme.

Introducing equations (3) to (6) in (2) one has:

$$\begin{aligned} A_n^h T_B^h + B_n^h T_{B_{n-1}}^h + C_n^h T_{B_{n+1}}^h &= \\ = A_n^{h-1} T_B^{h-1} + B_n^{h-1} T_{B_{n-1}}^{h-1} + C_n^{h-1} T_{B_{n+1}}^{h-1} + Q_n \end{aligned} \quad (7)$$

with

$$A_n^h = \theta \left(\lambda_{B, r_{n-1/2}}^h \frac{r_{n-1/2}}{r_n} + \lambda_{B, r_{n+1/2}}^h \frac{r_{n+1/2}}{r_n} \right) +$$

$$+ \frac{\Delta r_B^2}{\Delta t} \left(\theta \rho_{B,n}^h c_{p_{B,n}}^h + (1-\theta) \rho_{B,n}^{h-1} c_{p_{B,n}}^{h-1} \right) \quad (8a)$$

$$B_n^h = -\theta \lambda_{B,r_{n-1/2}}^h \frac{r_{n-1/2}}{r_n} \quad (8b)$$

$$C_n^h = -\theta \lambda_{B,r_{n+1/2}}^h \frac{r_{n+1/2}}{r_n} \quad (8c)$$

$$A_n^{h-1} = -(1-\theta) \left(\lambda_{B,r_{n-1/2}}^{h-1} \frac{r_{n-1/2}}{r_n} + \lambda_{B,r_{n+1/2}}^{h-1} \frac{r_{n+1/2}}{r_n} \right) + \frac{\Delta r_B^2}{\Delta t} \left(\theta \rho_{B,n}^h c_{p_{B,n}}^h + (1-\theta) \rho_{B,n}^{h-1} c_{p_{B,n}}^{h-1} \right) \quad (8d)$$

$$B_n^{h-1} = (1-\theta) \lambda_{B,r_{n-1/2}}^{h-1} \frac{r_{n-1/2}}{r_n} \quad (8e)$$

$$C_n^{h-1} = (1-\theta) \lambda_{B,r_{n+1/2}}^{h-1} \frac{r_{n+1/2}}{r_n} \quad (8f)$$

$$Q_n = \Delta r_B^2 (\theta q_n^h + (1-\theta) q_n^{h-1}) \quad (8g)$$

ii) Outermost node

Applied to the outermost fuel node NN; making a thermal balance for the annulus ($r_{NN-1/2}$, $r_{NN} = R_B$), taking into account the boundary condition for the heat transfer to the clad, equation (II-B-1) yields

$$-\int_{S_{NN-1/2}} \lambda_B \frac{\partial T_B}{\partial r} ds - \alpha_{BH} S_{NN} (T_{B,NN} - T_{Hi}) + q_{NN} V_{NN} = \rho_{NN} c_{p_{NN}} V_{NN} \frac{\partial T_B}{\partial t} \quad (9)$$

with the same space and time discretization as above, the following algebraic equation is obtained

$$A_{NN}^h T_{B,NN}^h + B_{NN}^h T_{B,NN-1}^h + C_{NN}^h T_{Hi}^h = A_{NN}^{h-1} T_{B,NN}^{h-1} + B_{NN}^{h-1} T_{B,NN-1}^{h-1} + C_{NN}^{h-1} T_{Hi}^{h-1} + Q_{NN} \quad (10)$$

with

$$A_{NN}^h = \theta \lambda_{r_{NN-1/2}}^h \frac{r_{NN-1/2}}{r_{NN}} + \theta \alpha_{BH}^h \Delta r_B + \frac{\Delta r_B^2}{2\Delta t_n} \frac{r_{NN-1/4}}{r_{NN}} \left(\theta \rho_{NN}^h c_{P_{NN}}^h + (1-\theta) \rho_{NN}^{h-1} c_{P_{NN}}^{h-1} \right) \quad (11a)$$

$$B_{NN}^h = - \theta \lambda_{r_{NN-1/2}}^h \frac{r_{NN-1/2}}{r_{NN}} \quad (11b)$$

$$C_{NN}^h = - \theta \alpha_{BH}^h \Delta r_B \quad (11c)$$

$$A_{NN}^{h-1} = - (1-\theta) \lambda_{r_{NN-1/2}}^h \frac{r_{NN-1/2}}{r_{NN}} - (1-\theta) \alpha_{BH}^{h-1} \Delta r_B + \frac{\Delta r_B^2}{2\Delta t_n} \frac{r_{NN-1/4}}{r_{NN}} \left(\theta \rho_{NN}^h c_{P_{NN}}^h + (1-\theta) \rho_{NN}^{h-1} c_{P_{NN}}^{h-1} \right) \quad (11d)$$

$$B_{NN}^{h-1} = (1-\theta) \lambda_{r_{NN-1/2}}^{h-1} \frac{r_{NN-1/2}}{r_{NN}} \quad (11e)$$

$$C_{NN}^{h-1} = (1-\theta) \alpha_{BH}^{h-1} \Delta r_B \quad (11f)$$

$$Q_{NN} = \frac{\Delta r_B^2}{2} \frac{r_{NN-1/4}}{r_{NN}} \left(\theta q_{NN}^h + (1-\theta) q_{NN}^{h-1} \right) \quad (11g)$$

iii) Central node

Similarly, for the fuel central node one derives the algebraic equation

$$A_o^h T_{Bo}^h + C_o^h T_{B1}^h = A_o^{h-1} T_{Bo}^{h-1} + C_o^{h-1} T_{B1}^{h-1} + Q_o \quad (12)$$

with

$$A_o^h = 4\theta \lambda_{r_{1/2}}^h + \frac{1}{\Delta t_n} \left(\theta \rho_o^h c_{p_o}^h + (1-\theta) \rho_o^{h-1} c_{p_o}^{h-1} \right) \quad (13a)$$

$$C_o^h = -4\theta \lambda_{r_{1/2}}^h \quad (13b)$$

$$A_o^{h-1} = -4(1-\theta) \lambda_{r_{1/2}}^{h-1} + \frac{1}{\Delta t_n} \left(\theta \rho_o^h c_{p_o}^h + (1-\theta) \rho_o^{h-1} c_{p_o}^{h-1} \right) \quad (13c)$$

$$C_o^{h-1} = 4(1-\theta) \lambda_{r_{1/2}}^{h-1} \quad (13d)$$

$$Q_o = (\theta q_o^h + (1-\theta) q_o^{h-1}) \Delta r_B^2 \quad (13e)$$

b) Cladding

i) Inner node

Application of the heat diffusion equation to the clad inner node yields, with the same space and time discretization as above, the algebraic equation

$$\begin{aligned} A_{Hi}^h T_{Hi}^h + B_{Hi}^h T_{B,NN}^h + C_{Hi}^h T_{Hm}^h &= \\ &= A_{Hi}^{h-1} T_{Hi}^{h-1} + B_{Hi}^{h-1} T_{B,NN}^{h-1} + C_{Hi}^{h-1} T_{Hm}^{h-1} + Q_{Hi} \end{aligned} \quad (14)$$

with

$$\begin{aligned} A_{Hi}^h &= \theta \alpha_{BH}^h \Delta r_H + \theta \lambda_{r_{i+1/2}}^h \frac{r_{i+1/2}}{r_i} \\ &+ \frac{1}{\Delta t_n} \frac{r_{i+1/4}}{r_i} \frac{\Delta r_H^2}{2} \left(\theta \rho_{Hi}^h c_{p_{Hi}}^h + (1-\theta) \rho_{Hi}^{h-1} c_{p_{Hi}}^{h-1} \right) \end{aligned} \quad (15a)$$

$$B_{Hi}^h = -\theta \alpha_{BH}^h \Delta r_H \quad (15b)$$

$$C_{Hi}^h = -\theta \lambda_{Hr_{i+1/2}}^h \frac{r_{i+1/2}}{r_i} \quad (15c)$$

$$A_{Hi}^{h-1} = -(1-\theta) \alpha_{BH}^{h-1} \Delta r_H - (1-\theta) \lambda_{Hr_{i+1/2}}^{h-1} \frac{r_{i+1/2}}{r_i} + \frac{1}{\Delta t_n} \frac{r_{i+1/4}}{r_i} \frac{\Delta r_H^2}{2} \left(\theta \rho_{Hi}^h c_{P_{Hi}}^h + (1-\theta) \rho_{Hi}^{h-1} c_{P_{Hi}}^{h-1} \right) \quad (15d)$$

$$B_{Hi}^{h-1} = (1-\theta) \alpha_{BH}^{h-1} \Delta r_H \quad (15e)$$

$$C_{Hi}^{h-1} = (1-\theta) \lambda_{Hr_{i+1/2}}^{h-1} \frac{r_{i+1/2}}{r_i} \quad (15f)$$

$$Q_{Hi} = \frac{r_{i+1/4}}{r_i} \frac{\Delta r_H^2}{2} \left(\theta q_{Hi}^h + (1-\theta) q_{Hi}^{h-1} \right) \quad (15g)$$

ii) Middle node

For the middle clad node one has:

$$A_{Hm}^h T_{Hm}^h + B_{Hm}^h T_{Hi}^h + C_{Hm}^h T_{Ha}^h = \quad (16)$$

$$= A_{Hm}^{h-1} T_{Hm}^{h-1} + B_{Hm}^{h-1} T_{Hi}^{h-1} + C_{Hm}^{h-1} T_{Ha}^{h-1} + Q_{Hm}$$

with

$$A_{Hm}^h = \theta \left(\lambda_{Hr_{m-1/2}}^h \frac{r_{m-1/2}}{r_m} + \lambda_{Hr_{m+1/2}}^h \frac{r_{m+1/2}}{r_m} \right) + \frac{1}{\Delta t_n} \left(\theta \rho_{Hm}^h c_{P_{Hm}}^h + (1-\theta) \rho_{Hm}^{h-1} c_{P_{Hm}}^{h-1} \right) \Delta r_H^2 \quad (17a)$$

$$B_{Hm}^h = -\theta \lambda_{Hr_{m-1/2}}^h \frac{r_{m-1/2}}{r_m} \quad (17b)$$

$$C_{Hm}^h = -\theta \lambda_{Hr_{m+1/2}}^h \frac{r_{m+1/2}}{r_m} \quad (17c)$$

$$A_{Hm}^{h-1} = - (1-\theta) \left(\lambda_{Hr_{m-1/2}}^{h-1} \frac{r_{m-1/2}}{r_m} + \lambda_{Hr_{m+1/2}}^{h-1} \frac{r_{m+1/2}}{r_m} \right) + \frac{1}{\Delta t_n} \left(\theta \rho_{Hm}^h c_{PHm}^h + (1-\theta) \rho_{Hm}^{h-1} c_{PHm}^{h-1} \right) \Delta r_H^2 \quad (17d)$$

$$B_{Hm}^{h-1} = (1-\theta) \lambda_{Hr_{m-1/2}}^{h-1} \frac{r_{m-1/2}}{r_m} \quad (17e)$$

$$C_{Hm}^{h-1} = (1-\theta) \lambda_{Hr_{m+1/2}}^{h-1} \frac{r_{m+1/2}}{r_m} \quad (17f)$$

$$Q_{Hm} = (\theta q_{Hm}^h + (1-\theta) q_{Hm}^{h-1}) \Delta r_H^2 \quad (17g)$$

iii) Outer Node

For the outer clad node one has:

$$\begin{aligned} A_{Ha}^h T_{Ha}^h + B_{Ha}^h T_{Hm}^h + C_{Ha}^h T_K^h &= \\ &= A_{Ha}^{h-1} T_{Ha}^{h-1} + B_{Ha}^{h-1} T_{Hm}^{h-1} + C_{Ha}^{h-1} T_K^{h-1} + Q_{Ha} \end{aligned} \quad (18)$$

with

$$A_{Ha}^h = \theta \lambda_{Hr_{a-1/2}}^h \frac{r_{a-1/2}}{r_a} + \theta \alpha_{HK}^h \Delta r_H + \frac{1}{\Delta t_h} \frac{\Delta r_H^2}{2} \frac{r_{a-1/4}}{r_a} \left(\theta \rho_{Ha}^h c_{PHa}^h + (1-\theta) \rho_{Ha}^{h-1} c_{PHa}^{h-1} \right) \quad (19a)$$

$$B_{Ha}^h = -\theta \lambda_{Hr_{a-1/2}}^h \frac{r_{a-1/2}}{r_a} \quad (19b)$$

$$C_{Ha}^h = -\theta \alpha_{HK}^h \Delta r_H \quad (19c)$$

$$A_{Ha}^{h-1} = -(1-\theta) \alpha_{HK}^{h-1} \Delta r_H - (1-\theta) \lambda_{Hr}^{h-1} \frac{r_{a-1/2}}{r_a} + \frac{1}{\Delta t_h} \frac{\Delta r_H^2}{2} \frac{r_{a-1/4}}{r_a} \left(\theta \rho_{Ha}^h c_{pHa}^h + (1-\theta) \rho_{Ha}^{h-1} c_{pHa}^{h-1} \right) \quad (19d)$$

$$B_{Ha}^{h-1} = (1-\theta) \lambda_{Hr}^{h-1} \frac{r_{a-1/2}}{r_a} \quad (19e)$$

$$C_{Ha}^{h-1} = (1-\theta) \alpha_{HK}^{h-1} \Delta r_H \quad (19f)$$

$$Q_{Ha} = \frac{\Delta r_H}{2} \frac{r_{a-1/4}}{r_a} \left(\theta q_{Ha}^h + (1-\theta) q_{Ha}^{h-1} \right) \quad (19g)$$

c) Structure

Similarly, discretization of equation (II-B-27) for the structure node yields

$$\begin{aligned} & \frac{F_S}{V_S} \left[\theta \alpha_{KS}^h (T_K^h - T_S^h) + (1-\theta) \alpha_{KS}^{h-1} (T_K^{h-1} - T_S^{h-1}) \right] + \\ & - \frac{F_w}{V_S} \left[\theta \alpha_w^h (T_S^h - T_w^h) + (1-\theta) \alpha_w^{h-1} (T_S^{h-1} - T_w^{h-1}) \right] + \\ & + \theta q_S^h + (1-\theta) q_S^{h-1} = (\theta \rho_S^h c_{pS}^h + (1-\theta) \rho_S^{h-1} c_{pS}^{h-1}) \frac{T_S^h - T_S^{h-1}}{\Delta t_h} \end{aligned}$$

which can be written:

$$\begin{aligned} A_S^h T_S^h + B_S^h T_K^h + C_S^h T_w^h &= \\ &= A_S^{h-1} T_S^{h-1} + B_S^{h-1} T_K^{h-1} + C_S^{h-1} T_w^{h-1} + Q_S \end{aligned} \quad (21)$$

with:

$$A_S^h = \theta \left(\alpha_{KS}^h + \frac{F_w}{F_S} \alpha_w^h \right) + \frac{1}{\Delta t_h} \frac{V_S}{F_S} \left(\theta \rho_S^h c_{p_S}^h + (1-\theta) \rho_S^{h-1} c_{p_S}^{h-1} \right) \quad (22a)$$

$$B_S^h = -\theta \alpha_{KS}^h \quad (22b)$$

$$C_S^h = -\theta \frac{F_w}{F_S} \alpha_w^h \quad (22c)$$

$$A_S^{h-1} = -(1-\theta) \left(\alpha_{KS}^{h-1} + \frac{F_w}{F_S} \alpha_w^{h-1} \right) + \frac{1}{\Delta t_h} \frac{V_S}{F_S} \left(\theta \rho_S^h c_{p_S}^h + (1-\theta) \rho_S^{h-1} c_{p_S}^{h-1} \right) \quad (22d)$$

$$B_S^{h-1} = (1-\theta) \alpha_{KS}^{h-1} \quad (22e)$$

$$C_S^{h-1} = (1-\theta) \frac{F_w}{F_S} \alpha_w^{h-1} \quad (22f)$$

$$Q_S = \frac{V_S}{F_S} \left(\theta q_S^h + (1-\theta) q_S^{h-1} \right) \quad (22g)$$

In the above equations, the coefficient A always refers to the node under consideration, the coefficient B refers to the adjacent node at the fuel axis side, C refers to the adjacent node in the outward direction.

d) The Gauss-Seidel solution method

The above difference equations may be written in matricial form as

$$AT = B \quad (23)$$

where A is a tridiagonal matrix containing the coefficients A_o^h, C_o^h up to $A_{Ha}^h, B_{Ha}^h, C_{Ha}^h$ and A_S^h, B_S^h, C_S^h all calculated at time t_n . Taking NN+1 nodes in the fuel, 3 in the clad and 1 in the structure A becomes a square matrix with NN+5 rows. T is a column vector containing the unknown temperatures at time t_n . B is a column vector formed by the right hand side of the above discretized equations. It is not completely known because, beyond all temperatures

and physical quantities at time t_{n-1} (with index $h-1$) it also contains the unknown terms $\rho^h c_p^h$. A direct solution of the above matrix equation by inversion of the matrix A yielding

$$T = A^{-1} B \quad (24)$$

is not therefore possible unless the unknown terms $\rho^h c_p^h$ are replaced by some extrapolated worths. Extrapolation is avoided by solving the above system of difference equations with the Gauss-Seidel iteration scheme. To this purpose, the unknown terms containing $\rho^h c_p^h$, which are multiplied by the temperature of the node under consideration at time t_{n-1} , are brought to the left side of the above equations and treated as the other terms with index h . (Let refer to this term with the symbol D_i , for the node i). Let r be a running index of the iteration scheme which allows to derive the temperatures at time t_n (index h) from the known temperature at the end of the previous time step t_{n-1} (index $h-1$). Letting $i-1, i, i+1$ denote any three consecutive nodes in radial direction, the Gauss-Seidel iteration is based on a scheme of the type:

$$A_i^r T_i^{r+1} = - B_i^{r+1} T_{i-1}^{r+1} - C_i^r T_{i+1}^r + D_i^r + \bar{R}_i \quad (25)$$

where A_i, B_i, C_i have the same meaning as in the above algebraic equations, D_i contains the $\rho^h c_p^h$ term, and \bar{R}_i indicates all known quantities at time t_{n-1} .

Equation (25) is applied consecutively for all nodes from the fuel axis to the clad outer node. The already determined $(r+1)$ estimation of the temperature of the inner node $(i-1)$ is thus used for the new estimation $(r+1)$ of node i , together with the previous value (r) of the outer node $(i+1)$. (This is the typical feature of the Gauss-Seidel iteration scheme.) For the first iteration step $(r=0)$ the temperature distribution at the end of the previous time step (t_{n-1}) is used to calculate the coefficients A_i^0, C_{i+1}^0, D_i^0 . One has further to remark that for the first node $i=1$ (fuel axial node) the term $(i-1)$ does not exist, according to equation (12). This allows triggering the iteration scheme with the above formula.

e) Programming details

To facilitate the comprehension of the use of the above equations in the numerical scheme of the subroutines FBRT (single phase flow calculation)

and FBRTB (two phase flow calculation), FORTRAN symbols are given hereafter, with reference to

- i) equation (7) for inner fuel nodes
- ii) equation (16) for the clad middle node
- iii) equation (21) for the structure node

For simplicity are omitted the axial dimensions of the FORTRAN symbols (like TBNR (M,N) or TCMNR (M) where the index N refers to the radial node considered and the index M to the axial mesh).

i) Fuel inner node

Letting:

DRBR = RBR/NN
 DRBR2 = DRBR**2
 QRMIN(N) = $r_{n-1}/2/r_n$
 QRPL(N) = $r_{n+1}/2/r_n$
 RØB = fuel density at node N
 CPB = fuel specific heat at node N
 XLBN1(N) = fuel thermal conductivity at node N
 DTKUE = Δt

and letting indexes h-1, r, r+1 indicate the time point at which the worths are calculated, equation (7) becomes

$$\begin{aligned} \text{QOT}^r \cdot \text{TBNR}^{r+1} = & \theta \left[\text{QRMIN}(N) \cdot (\text{XLBN1}(N) \cdot \text{TBNR}(N-1))^{r+1} + \right. \\ & \left. + \text{QRPL}(N) \cdot (\text{XLBN1}(N+1) \cdot \text{TBR2}(N+1))^r \right] \\ & + \text{DRBR2} \cdot \theta \cdot \left(\text{ROB} \cdot \text{C}_{\text{PB}} \right)^r \text{TBN1}(N)^{h-1} / \text{DTKUE} \\ & + \text{REB}(N)^{h-1} \end{aligned} \quad (26)$$

with

$$\begin{aligned} \text{QOT} = \text{A}_n^h = & \theta \left[\text{QRMIN}(N) \cdot \text{XLBN1}^r(N) + \text{QRPL}(N) \cdot \text{XLBN1}^r(N+1) \right] \\ & + \text{DRBR2} \left[\theta \cdot (\text{RØB} \cdot \text{CPB})^r + (1-\theta) \cdot (\text{RØB} \cdot \text{CPB})^{h-1} \right] / \text{DTKUE} \end{aligned} \quad (27a)$$

$$\begin{aligned}
 \text{REB}(N) &= \left\{ A_n^{h-1} - \frac{\theta \rho_{Bn}^r c_{pBn}^r}{\Delta t} T_{Bn}^{h-1} + B_n^{h-1} T_{B_{n-1}}^{h-1} + C_n^{h-1} T_{B_{n+1}}^{h-1} + \theta_n \right\} \Delta r_B^2 \\
 &= (1-\theta) \left[\text{QRMIN}(N) \cdot \text{XLBN1}(N) \cdot (\text{TBN1}(N-1) - \text{TBN1}(N)) \right. \\
 &\quad \left. + \text{QRPL}(N) \cdot \text{XLBN1}(N+1) \cdot (\text{TBN1}(N+1) - \text{TBN1}(N)) \right] \quad (27b) \\
 &\quad + (1-\theta) \cdot \text{DRBR2} \cdot (\text{R}\phi\text{B} \cdot \text{CPB})^{h-1} \cdot \text{TBN1}(N) / \text{DTKUE} + \\
 &\quad + \text{ANTB} \cdot \text{DRBR2} \cdot (\theta \cdot \text{QGMN} + (1-\theta) \cdot \text{QGMN1})
 \end{aligned}$$

ii) Clad middle node

Letting

$$\text{DCAN} = r_a - r_i$$

$$\text{DRC} = r_m - r_i = \text{DCAN}/2$$

$$\text{DRC2} = \text{DRC} \cdot 2$$

$$\text{QRPLV} = \frac{r_i + (r_m - r_i)/4}{r_i}$$

$$\text{QRPLH} = \frac{r_i + (r_m - r_i)/2}{r_i}$$

$$\text{QRCMI} = r_{m-1/2} / r_m$$

$$\text{QRCPL} = r_{m+1/2} / r_m$$

$\text{R}\phi\text{H}$ = middle node clad density

CPH = middle node clad specific heat

XLCIN1 = inner node clad thermal conductivity

XLCAN1 = outer node clad thermal conductivity

equation (16) becomes:

$$\begin{aligned}
 \text{QOT}^r \cdot \text{TCMNR}^{r+1} &= \theta \left[\text{QRCMI} \cdot (\text{XLCINI} \cdot \text{TCINR})^{r+1} + \right. \\
 &\quad \left. + \text{QRCPL} \cdot (\text{XLCAN1} \cdot \text{TCAR2})^r \right] \quad (28) \\
 &\quad + \theta \cdot \text{DRC2} \cdot (\text{R}\phi\text{H} \cdot \text{CPH})^r \cdot \text{TCMN1}^{h-1} / \text{DTKUE} + \text{REC2}^{h-1}
 \end{aligned}$$

with

$$QOT = \theta(QRCMI \cdot XLCINI^r + QRCPL \cdot XLCANI^r) + \quad (29a)$$

$$+ DRC2 \left[\theta \cdot R\phi H^r \cdot CPH^r + (1-\theta) R\phi H^{h-1} \cdot CPH^{h-1} \right] / DTKUE$$

$$REC2 = \left\{ \left(A_{Hm}^{h-1} - \frac{\theta \rho_{Hm}^r c_{pHm}^r}{\Delta t} \right) T_{Hm}^{h-1} + B_{Hm}^{h-1} T_{Hi}^{h-1} + C_{Hm}^{h-1} T_{ha}^{h-1} + \theta_{Hm} \right\} \Delta r_H^2$$

$$= (1-\theta) \left[QRCMI \cdot XLCINI \cdot (TCINI - TCMN1) + QRCPL \cdot XLCANI (TCANI - TCMN1) \right] + \quad (29b)$$

$$+ (1-\theta) \cdot DRC2 \cdot ROH^{h-1} \cdot CPH^{h-1} \cdot TCMN1 / DTKUE +$$

$$+ ANTC \cdot DRC2 \left(\theta \cdot QGMN^r + (1-\theta) QGMN1 \right)^{h-1}$$

iii) Structure node

Letting:

$$FWFS = F_W / F_S$$

$$VDUF = V_S / F_S$$

R ϕ S = density of structure material

CPS = specific heat of structure

WWSTR (WWST1) = α_W = heat transfer coefficient from the structure outer surface to the surrounding medium.

HKST = α_{KS} = heat transfer coefficient coolant-structure

equation (21) becomes:

$$QOT^r \cdot TSTNR^{r+1} = \theta \left[(HKST \cdot TKNR)^{r+1} + FWFS \cdot (WWSTR \cdot TBYPSTR)^r \right] / VDUF$$

$$+ \theta (R\phi S \cdot CPS)^r \cdot TSTN1^{h-1} / DTKUE + REST^{h-1} \quad (30)$$

with:

$$\begin{aligned}
 \text{QOT} &= \theta (\text{HKST}^r + \text{FWFS} \cdot \text{WWSTR}^r) / \text{VDUF} + \\
 &+ \left[\theta (\text{R}\emptyset\text{S} \cdot \text{CPS})^r + (1-\theta) (\text{R}\emptyset\text{S} \cdot \text{CPS})^{h-1} \right] / \text{DTKUE}
 \end{aligned} \tag{31a}$$

$$\begin{aligned}
 \text{REST} &= \left\{ \left(A_S^{h-1} - \frac{\theta \rho_S^h c_P^h}{\Delta t_h} \frac{V_S}{F_S} \right) T_S^{h-1} + B_S^{h-1} T_K^{h-1} + C_S^{h-1} T_W^{h-1} + Q_S \right\} \frac{F_S}{V_S} \\
 &= (1-\theta) \left[\text{HKST} \cdot (\text{TKN1} - \text{TSTN1}) + \text{FWFS} \cdot \text{WWST1} \cdot (\text{TBYS1} - \text{TSTN1}) \right] / \text{VDUF} \\
 &+ (1-\theta) (\text{ROS} \cdot \text{CPS})^{h-1} \text{TSTN1} / \text{DTKUE} + \\
 &+ \text{ANTS} (\theta \text{QGMN}^r + (1-\theta) \text{QGMN1})^{h-1}
 \end{aligned} \tag{31b}$$

At the end of the iteration scheme, which is carried out simultaneously for all radial nodes of the mesh zone M, worths with index r+1 yields the new "h" values at time t_n .

2.2 Single Phase Flow Calculation

The solution of the basic equations (II-B-10) to (12) is discussed in this chapter from both theoretical and numerical viewpoints. The subject is divided into five sections: in the first one the fundamental equations, written in the conservation-law form, are set-up in matrix form and dealt from a general aspect which allows stability considerations to be developed in a further section. Section two explains in details the numerical method adopted for the solution of the momentum equation. Sections three and four report about the numerical solution of the continuity and energy equations respectively. Obviously, the numerical procedure works out a contemporary solution of all basic equations at the time. The subdivision in four sections is therefore only adopted for sake of clarity. Section five presents an analysis of the stability of the hyperbolic system of basic equations based on the application of the Von Neumann (Fourier Transform) method.

2.2.1 Basic numerical scheme and preliminary considerations for stability analysis

Let us recall the system of basic equations describing the single phase flow coolant behaviour:

$$\frac{\partial \rho_K(z,t)}{\partial t} + \frac{\partial G_K(z,t)}{\partial z} = 0 \quad (1)$$

$$\frac{\partial G_K(z,t)}{\partial t} + \frac{\partial}{\partial z} \frac{G_K(z,t)^2}{\rho_K(z,t)} = - \frac{\partial p}{\partial z} - \frac{f}{2D_h} \frac{|G_K| G_K}{\rho_K} - g \rho_K(z,t) \quad (2)$$

$$\rho_K \frac{\partial H_K}{\partial t} + G_K \frac{\partial H_K}{\partial z} = \phi_K \quad (3)$$

Letting e be the coolant internal energy per unit of mass [$e = \text{J/kg}$], $E = \rho_K e$ the internal energy per unit of volume [$\rho e = \text{J/m}^3$], H the coolant enthalpy per unit of mass, it holds

$$e = H - pv = H - \frac{p}{\rho} \quad (4)$$

Equation (3) can be written in terms of internal energy:

$$\frac{\partial}{\partial t} E + \frac{G_K}{\rho_K} \frac{\partial}{\partial z} (E + p) = \Phi_K \quad (5)$$

where $\partial p / \partial t \approx 0$ is assumed.

Equations (1), (2) and (5) represent the "conservation-law" form of the (single phase flow) fluid dynamic. They can be written in vectorial form as

$$\frac{\partial}{\partial t} Y + \frac{\partial}{\partial z} F(Y) + R(Y) = 0 \quad (6)$$

where

$$Y = \begin{pmatrix} \rho_K \\ G_K \\ E \end{pmatrix} \quad (7)$$

is a vector having for components the three dependent variables,

$$F(Y) = \begin{pmatrix} G_K \\ G_K^2 / \rho_K + p \\ (E + p)G_K / \rho_K \end{pmatrix} \quad (8)$$

is a vector whose components are functions of the dependent variables and

$$R(Y) = \begin{pmatrix} 0 \\ \frac{f}{2D_h} \frac{|G_K| G_K}{\rho_K} + g \rho_K \\ -\Phi_K \end{pmatrix} \quad (9)$$

is the vector whose components do not contain time and space derivatives. The third component of the vector R [$\Phi_K = W/m^3$] is given by the boundary conditions (clad and structure surface temperature) while the second component contains only dependent variables and known coefficients.

The coolant pressure is not included as a component of the vector Y as it is given by the equation of state

$$p = f(e, \rho) \quad (10)$$

The stability analysis of the system of equations (6) is strictly connected to the behaviour of the relative characteristics which do not depend on the inhomogeneous term $R(Y)$. This does not therefore need to be taken into consideration and the homogeneous form

$$\frac{\partial Y}{\partial t} + \frac{\partial}{\partial z} F(Y) = 0 \quad (11)$$

can be analyzed. The vector $R(Y)$ contains a dissipative term, depending on the friction coefficient, and a source term, which takes into account the heat exchange between coolant and the channel wall surfaces. Dropping $R(Y)$ implies that the stability analysis of the system of homogeneous equations (11) can be performed under the simplifying assumption that the entropy s of the fluid remains constant, hence

$$ds = \frac{dq}{T} = \frac{1}{T} \left[de + p d\left(\frac{1}{\rho}\right) \right] = 0 \quad (12)$$

and the adiabatic sound speed

$$c^2 = \left(\frac{dp}{d\rho} \right)_s \quad (13)$$

may be used to simplify the energy conservation equation (see 2.2.5)

Let m be an index for discrete spatial meshes in the axial direction, and n for the time discretization. A Taylor expansion of the unknown vector Y with respect to time at the fixed point m yields:

$$Y_m^{n+1} = Y_m^n + \Delta t \left(\frac{\partial Y}{\partial t} \right)_m^n + \frac{1}{2} \Delta t^2 \left(\frac{\partial^2 Y}{\partial t^2} \right)_m^n + \dots \quad (14)$$

The first and second order time derivatives are given by

$$\frac{\partial Y}{\partial t} = - \frac{\partial}{\partial z} F(Y) \quad (15)$$

$$\begin{aligned} \frac{\partial^2 Y}{\partial t^2} &= - \frac{\partial}{\partial t} \left(\frac{\partial F(Y)}{\partial z} \right) = - \frac{\partial}{\partial z} \left(\frac{\partial}{\partial t} F(Y) \right) = - \frac{\partial}{\partial z} \left(A \frac{\partial Y}{\partial t} \right) \\ &= \frac{\partial}{\partial z} \left(A \frac{\partial F}{\partial z} \right) \end{aligned} \quad (16)$$

where the matrix

$$A = A(Y) = \left| a_{ij} \right| = \left| \frac{\partial F_i}{\partial Y_j} \right| \quad (17)$$

is the Jacobian of $F(Y)$ with respect to Y .

Inserting into (14) yields

$$\begin{aligned} Y_m^{n+1} &= Y_m^n - \Delta t \frac{F_{m+1}^n - F_{m-1}^n}{2\Delta z} + \\ &+ \frac{\Delta t^2}{2} \frac{A_{m+1/2}^n (F_{m+1}^n - F_m^n) - A_{m-1/2}^n (F_m^n - F_{m-1}^n)}{\Delta z^2} \end{aligned} \quad (18)$$

where $A_{m+1/2}^n$ for instance is calculated as

$$A \left(\frac{Y_{m+1}^n + Y_m^n}{2} \right).$$

In case the functional matrix $A(Y)$ can be assumed constant over the axial mesh m , the above equation simplifies to:

$$Y_m^{n+1} = Y_m^n - A \frac{\Delta t}{2\Delta z} (Y_{m+1}^n - Y_{m-1}^n) + \frac{1}{2} \left(A \frac{\Delta t}{\Delta z} \right)^2 (Y_{m+1}^n - 2 Y_m^n + Y_{m-1}^n) \quad (19)$$

Rearranging one has

$$\begin{aligned}
 Y_m^{n+1} &= \left(-\frac{A}{2} \frac{\Delta t}{\Delta z} + \frac{A^2}{2} \frac{\Delta t^2}{\Delta z^2} \right) Y_{m+1}^n + \left(I - A^2 \frac{\Delta t^2}{\Delta z^2} \right) Y_m^n + \\
 &+ \left(\frac{A}{2} \frac{\Delta t}{\Delta z} + \frac{A^2}{2} \frac{\Delta t^2}{\Delta z^2} \right) Y_{m-1}^n
 \end{aligned} \tag{20}$$

where I is the (3x3) identity matrix.

Equation (19) is used indirectly by means of a two-steps formula which makes it possible to avoid the direct calculation of the matrix A. In the first step a provisional value of the unknown Y is derived truncating the Taylor expansion (14) after the first two terms

$$Y_m^{n+1} = Y_m^n - \Delta t \frac{F_{m+1}^n - F_m^n}{\Delta z} \tag{21}$$

The second step refines these values by means of the formula

$$Y_m^{n+1} = Y_m^n - \frac{\Delta t}{2\Delta z} (F_m^{n+1} - F_{m-1}^{n+1}) \tag{22}$$

where $F_m^{n+1} = F(Y_m^{n+1})$ is calculated by using the preliminary values supplied by the first step (and similarly for F_{m-1}^{n+1}).

Under the assumption of constant matrix A, therefore letting $F(Y) = A \cdot Y$, insertion of (21) into (22) yields (19). This shows that, in spite of the truncation of the Taylor series after the first order term in the first step, the two steps formula is a second order one, the truncation error being of the order $O(\Delta t^3)$. The detailed application of the above numerical scheme in the computer programme is shown in the next section, with respect to the solution of the momentum equation.

2.2.2 Detailed solution of the momentum equation with a two-steps formula ("Predictor - Corrector" scheme)

The solution of the momentum equation (2) is based on the application of the two-steps formula (21) and (22) which is equivalent in the order of accuracy to (19). As the numerical treatment of the basic equations is presented in distinct sections, we refer here to the dependent variable under consideration with the symbol G (mass flux) (instead of using the vectorial notation Y as before).

Obviously, the non-homogeneous terms at the right side of equation (2) which were provisionally dropped in the previous section for introducing stability analysis considerations, must now be taken into consideration. The symbols F in equations (21), (22) is therefore replaced by say FF where it is meant that this takes also into account the non-homogeneous terms.

Moreover, following the "Integral-Momentum" model, the mean value of the mass flux over the channel length L is considered, thus eliminating the dependence from the spatial coordinate z

$$G(t) = \frac{1}{L_K} \int_0^L G_K(z,t) dz \quad (23)$$

and the momentum equation is integrated over the channel length, yielding

$$\begin{aligned} \frac{dG(t)}{dt} = \frac{1}{L} \{ & p_K(0,t) - p_K(L_K,t) - G(t)^2 \left(\frac{1}{\rho_a} - \frac{1}{\rho_{ei}} \right) + \\ & - \Delta p_{BL} - \Delta p_A - \int_0^{L_K} \left[\frac{f}{2D_h} \frac{G(z,t) |G(z,t)|}{\rho} - \rho g \right] dz \} \end{aligned} \quad (24)$$

where the pressure drops in the inlet valve (Δp_{B1}) and eventual pressure drop due to enlargement of the test section (Δp_A) are also taken into account. The integral is calculated summing up the contributions of the axial meshes m ($m = 1, 2 \dots NM2$).

$$\int_0^L \left[\frac{f}{2D_h} \frac{G(z,t) |G(z,t)|}{\rho} - \rho g \right] dz \approx \sum_{m=1}^{NM2} \left[\frac{f_m}{2D_{h_m}} \frac{G_m |G_m|}{\rho_m} - \rho_m g \right] \quad (25)$$

The right hand side of (24) represents the sum of the terms which have been previously indicated with the symbol FF, and, apart from the division by the channel length, it yields the time derivative of the integral mass flux. Hence, synthetically

$$\frac{dG}{dt} L \equiv FF \cdot L = \{\Delta p\} \quad (26)$$

where $\{\Delta p\}$ denotes the total pressure drop in the channel. With the simplification introduced by the integral momentum model, the application of the two-steps formula is carried out as follows:

a) First (predictor) step

$$\tilde{G}^{n+1} = G^n + \left(\frac{dG}{dt}\right)^n \cdot \Delta t = G^n + (FF)^n \Delta t \quad (27)$$

with

$$(FF)^n = \frac{1}{L_K} \left\{ p_{ei} - p_a - G^{n2} \left(\frac{1}{\rho_a} - \frac{1}{\rho_{ei}} \right) - \Delta p_{B1} - \Delta p_A - \sum_I^{NH2} \frac{f_m}{2D_{hm}} \frac{G_m^n |G_m^n|}{\rho_m} - \rho_m g \right\} \quad (28)$$

The tilde \sim indicates that the value of the mass flux G at time $n+1$ is a provisional one. The use of the index m , referring to the axial meshes, is justified by the fact that, beyond the integral mass flux G , there exist a spatial distribution of G along the axial coordinate z which is supplied by the contemporary solution of the continuity equation, as explained in next section.

It is important to remark that the space derivative $-(\Delta F/\Delta z)$ which appears in formula (21) of the previous section has been replaced in (27) by the time derivative (dG/dt) . The same is done for the second step. This is legitimate by equation (24).

b) Intermediate calculation

An intermediate step consists in the calculation of the time derivative of the mass flux at time $n+1$ using the provisional value of the mass

flux at the same time

$$\begin{aligned} \left(\frac{dG}{dt}\right)^{n+1} &= (FF)^{n+1} = \frac{1}{L_K} \left\{ p_{ei} - p_a - G^{n+1/2} \left(\frac{1}{\rho_a} - \frac{1}{\rho_{ei}} \right) - \Delta p_{B1} - \Delta p_A \right. \\ &\quad \left. - \sum_m^{NH2} \frac{f_m}{2D_{hm}} \frac{G_m^{n+1} |G_m^{n+1}|}{\rho_m} - \rho_m g \right\} \end{aligned} \quad (29)$$

c) Second (corrector) step

The final value of the mass flux is given by

$$\begin{aligned} G^{n+1} &= G^n + \left(\frac{dG}{dt}\right)^{n+1/2} \Delta t \\ &= G^n + \frac{1}{2} \left[\left(\frac{dG}{dt}\right)^n + \left(\frac{dG}{dt}\right)^{n+1} \right] \Delta t \\ &= G^n + \frac{1}{2} \left[FF^n + FF^{n+1} \right] \Delta t \end{aligned} \quad (30)$$

This represents the mean value of the mass flux over the axial length. Its axial distribution about the mean value is found by the solution of the continuity equation as explained in the next section.

Finally, application of (24) over every mesh length ($z, z + \Delta z$) proceeding from the top of the channel downwards to the bottom yields the axial pressure distribution. For a single mesh length one has, at time t_{n+1}

$$\begin{aligned} p(z) &= p(z+\Delta z) + \Delta z \left(\frac{dG(t)}{dt}\right)^{n+1} + G^2(t) \left(\frac{1}{\rho(z+\Delta z)} - \frac{1}{\rho(z)} \right) \\ &\quad + \left[\frac{f}{2Dh} \frac{G(t) |G(t)|}{\rho(z+\Delta z/2)} - \rho(z+\Delta z/2) g \right] \Delta z \end{aligned} \quad (31)$$

where the term Δp_A has been dropped, as it appears only for one mesh.

2.2.3 Solution of the continuity equation

An input flag allows the user to choose between an approximate solution of the continuity equation, carried out in the subroutines ITC1 and ITC11, and an exact solution which is performed in the subroutines ITC1R, ITC11R.

In the first case, neglecting the time derivative of the coolant density, the continuity equation yields $\partial G(z)/\partial z = 0$ hence $G(z) = \text{constant}$. This solution is acceptable in case of slow transient conditions.

In case of fast transient conditions the exact solution of the continuity equation (1) should be preferred. Numerical details of this solution are given hereafter.

The coolant mass flux $G(z,t)$ can be split into two terms; an average value

$$\hat{G}(t) = \frac{1}{L} \int_0^L G(z,t) dz \quad (32)$$

constant over the channel length L , and a space dependent term $\tilde{G}(z,t)$ representing local deviations of the actual mass flux from its mean value. Hence:

$$G(z,t) = \hat{G}(t) + \tilde{G}(z,t) \quad (33)$$

This formal representation of the mass flux offers the advantage that the continuity equation has to hold only for the component $\tilde{G}(z,t)$:

$$\frac{\partial \rho}{\partial t} + \frac{\partial \tilde{G}}{\partial z} = 0 \quad (34)$$

Introducing space and time discretization letting index m refer to a mesh of length Δz_m in the axial direction z and index n refer to the time step, (34) yields

$$\Delta_m \tilde{G}_m^n = \tilde{G}_{m+1/2}^n - \tilde{G}_{m-1/2}^n = -(\rho_m^n - \rho_m^{n-1}) \frac{\Delta z_m}{\Delta t_n} \quad (35)$$

The segmented curve (a) in Fig. 4 shows the consecutive increments $\Delta_m \tilde{G}_m^n$ as provided by equation (35). Let introduce an iteration index r

(whose meaning will be explained next) and denote \tilde{G}_r to the local deviation from the mean value \hat{G} at the inlet of the channel. The solution provided by (35) does not, in general, satisfy the physical condition that the mean value of the local variation \tilde{G} from \hat{G} is zero; it must therefore be shifted by an amount, say G_x allowing for

$$\int_0^L \tilde{G}(z,t) dz = 0 \quad (36)$$

Assuming a value G_x is known, the local deviations from \hat{G} are given by:

$$\begin{aligned} \tilde{G}_{m,r} &= \tilde{G}_{r-1} + G_{x,r-1} + \sum_1^{m-1} \Delta_i G_i + \frac{\Delta_m \tilde{G}_m}{2} \\ &= \tilde{G}_r + \sum_1^{m-1} \Delta_i \tilde{G}_i + \frac{\Delta_m \tilde{G}_m}{2} \end{aligned} \quad (37)$$

with

$$\tilde{G}_r = \tilde{G}_{r-1} + G_{x,r-1} \quad (38)$$

These values are represented by curve (b) in Fig. 4.

Imposing condition (36) onto equation (37), and iterating over r until Eq. (36) is satisfied within a chosen limit of accuracy, yields the required value G_x . For the iteration step r one has:

$$\sum_1^{NM2} \tilde{G}_{r-1} \Delta z_m + \sum_1^{NM2} G_{x,r-1} \Delta z_m + \sum_2^{NM2} \left[\sum_1^{m-1} \Delta_i \tilde{G}_i \right] \Delta z_m + \frac{1}{2} \sum_1^{NM2} \Delta_m \tilde{G}_m \Delta z_m = 0 \quad (39)$$

(NM2 is the number of meshes in the axial direction z), from which $G_{x,r-1}$ is derived:

$$G_{x,r-1} = \frac{-1}{L} \left[\tilde{G}_{r-1} + \sum_2^N \left(\sum_1^{m-1} \Delta_i \tilde{G}_i \right) \Delta z_m + \frac{1}{2} \sum_1^N \Delta_m \tilde{G}_m \Delta z_m \right] \quad (40)$$

Eq. (38) gives now \tilde{G}_F as \tilde{G}_{F-r-1} is known from the previous iteration (for G_e an arbitrary value can be assumed, for instance zero). Eq. (37) gives $\tilde{G}_{m,r}$ for every $m = 1, 2 \dots N$, and Eq. (33) gives $G_{m,r} = \hat{G}_{r-1}^n + \tilde{G}_{m,r}$. The value of \hat{G}_{r-1}^n is known from the previous iteration and for \hat{G}_0^n the approximate solution of the continuity equation is obtained without accounting for further mass flow variations with regard to further transient density variations.

The iteration scheme is coupled to the solution of the momentum equation. In fact time derivative of coolant mass flux is expressed in terms of $G_{m,r}$ by

$$FF_r^n = \frac{1}{L} \left\{ p_{ei} - p_a - \left(\frac{G_a^2}{\rho_a} \right)^n + \left(\frac{G_e^2}{\rho_e} \right)^n - \Delta p_{B1} - \Delta p_A \right. \\ \left. - \sum_{m=1}^N \left[\frac{f_{m,r}}{2D_h} \frac{|G_{m,r}| G_{m,r}}{\rho_m^n} \Delta z_m - \rho_{m,r}^n g \Delta z_m \right] \right\} \quad (41)$$

as explained in the previous section.

Eq.(26) allows to derive a new mean value

$$\hat{G}_r^n = \hat{G}^{n-1} + \frac{1}{2} \left[F^{n-1} + F_r^n \right] \Delta t_n \quad (42)$$

which yields a new value of $G_{m,r}$ consistent with both continuity and momentum equations:

$$G_{m,r} = \hat{G}_r^n + \tilde{G}_{m,r} \quad (43)$$

The iterative process is repeated from equation (37) to (43) as long as the "new" $G_{m,r}$ differs from the "old" value by less than a given figure. In practice, convergence is achieved quite rapidly after 5 to 10 iteration step. The iteration process represented by the formulas (37) to (43) is schematically shown in Fig. 5.

Symbols used in this section

- t = time (sec)
z = axial coordinate (m)
NM2 = number of meshes in z direction
L = channel length (m)
 ρ = density (kg/m³)
p = pressure (N/m²)
G = coolant mass flux (kg/m²sec)
 \hat{G} = mean value of G (kg/m²sec)
 \tilde{G} = local deviation of mass flux from its mean value (kg/m²sec)
G_x = correction to be applied to inlet mass flux according to equation (36) (kg/m²sec)
F = time derivative of mass flux (kg/m²sec²)
f = friction coefficient (dimensionless)
g = gravity acceleration (m/sec²)

Subscripts

- m refers to a mesh of the z axis
n refers to time step t_n
r iteration index
e refers to channel inlet
a refers to channel outlet

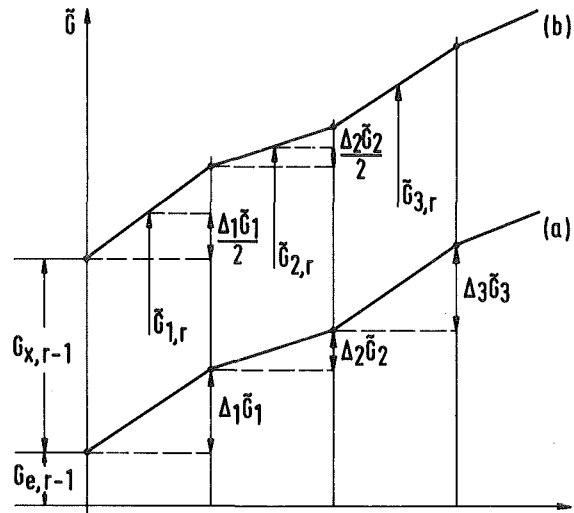
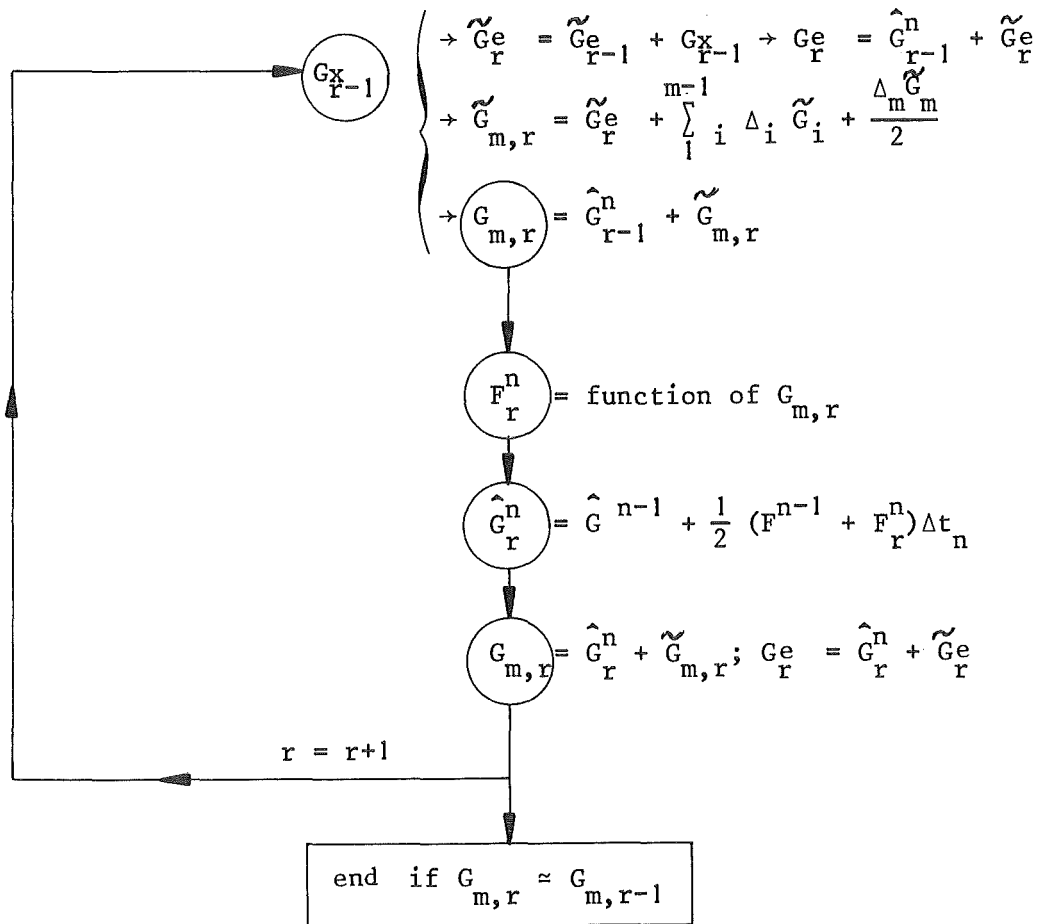


Fig. 4: Local deviation of mass flux from mean value versus axial length.

Fig. 5: Scheme of the iteration method used to solve the single phase flow continuity equation.

Input for iteration: $\left\{ \begin{array}{l} \hat{G}_0 = \text{solution of the continuity equation } \partial G / \partial z = 0 \\ \Delta_m G_m = \text{first solution of } \frac{\partial \rho}{\partial t} = - \frac{\partial G}{\partial z} \\ \tilde{G}_0^e = \text{initial value, for instance } \tilde{G}_0^e = 0. \end{array} \right.$

↓ r=1



2.2.4 Solution of the energy equation

The energy equation for the single phase flow is solved in the subroutine FBRT together with the heat diffusion equations describing the temperature distribution in fuel, clad and structure material. The solution is based on the Gauss-Seidel iteration method and follows the calculation scheme explained in section 2.1.

Inserting in the energy equation (3)

$$di_K = c_{pK} dT_K$$

and

$$\dot{\phi}_K = \frac{U_H}{A} \alpha_{HK} (T_{Ha} - T_K) - \frac{U_S}{A} \alpha_{KS} (T_K - T_S) + q_K$$

where q_K represents the intrinsic specific power generation in the coolant, and discretizing with respect to time one has with reference to a given axial mesh of length Δz and using the indexes $h, h-1$ to refer to time t_n, t_{n-1} for analogy with section 2.1:

$$\begin{aligned} (\rho c_p)^{h-1/2} \frac{T_K^h - T_K^{h-1}}{\Delta t} &= \frac{U_H}{A} \alpha_{HK} \theta (T_{Ha}^h - T_K^h) + \frac{U_S}{A} \alpha_{KS} \theta (T_S^h - T_K^h) \\ &- c_p^h G^h \theta \left(\frac{T_K^h - T_{K,e}^h}{\Delta z/2} \right) + \\ &+ \frac{U_H}{A} \alpha_{HK} (1-\theta) (T_{Ha}^{h-1} - T_K^{h-1}) \\ &+ \frac{U_S}{A} \alpha_{KS} (1-\theta) (T_S^{h-1} - T_K^{h-1}) \\ &- (1-\theta) c_p^{h-1} G^{h-1} \frac{T_{Ko}^{h-1} - T_{Ke}^{h-1}}{\Delta z} + \\ &+ \theta q_K^h + (1-\theta) q_K^{h-1} \end{aligned} \quad (44)$$

In this formula T_K represents the coolant temperature in the middle of the considered axial mesh, while $T_{K,e}$ and $T_{K,o}$ represents the coolant

temperatures at the mesh inlet and outlet respectively.

Calculating the term ρc_p at time $h-1/2$ and rearranging, the above equation can be written

$$A_K^h T_K^h + B_K^h T_{Ha}^h + C_K^h T_S^h + D_K^h T_{Ke}^h = \quad (45)$$

$$A_K^{h-1} T_K^{h-1} + B_K^{h-1} T_{Ha}^{h-1} + C_K^{h-1} T_S^{h-1} + D_K^{h-1} T_{Ke}^{h-1} + E_K^{h-1} T_{Ko}^{h-1} + Q_K$$

with:

$$A_K^h = \frac{1}{\Delta t} (\rho c_p)^{h-1/2} + \theta \left[\frac{U_H}{A} \alpha_{HK} + \frac{U_S}{A} \alpha_{KS} + \frac{2c_p^h G^h}{\Delta z} \right] \quad (46a)$$

$$B_K^h = -\theta \frac{U_H}{A} \alpha_{HK} \quad (46b)$$

$$C_K^h = -\theta \frac{U_S}{A} \alpha_{KS} \quad (46c)$$

$$D_K^h = -\frac{2\theta}{\Delta z} c_p^h G^h \quad (46d)$$

$$A_K^{h-1} = \frac{1}{\Delta t} (\rho c_p)^{h-1/2} - (1-\theta) \left[\frac{U_H}{A} \alpha_{HK} + \frac{U_S}{A} \alpha_{SK} \right] \quad (46e)$$

$$B_K^{h-1} = (1-\theta) \frac{U_H}{A} \alpha_{HK} \quad (46f)$$

$$C_K^{h-1} = (1-\theta) \frac{U_S}{A} \alpha_{KS} \quad (46g)$$

$$D_K^{h-1} = \frac{(1-\theta)}{\Delta z} c_p^{h-1} G^{h-1} \quad (46h)$$

$$E_K^{h-1} = -\frac{(1-\theta)}{\Delta z} c_p^{h-1} G^{h-1} \quad (46i)$$

$$Q_K = \theta q_K^h + (1-\theta) q_K^{h-1} \quad (46l)$$

This equation is similar to those derived by the equations describing the temperature distribution in fuel, clad and structure. The only difference consists in the presence of additional terms for the coolant temperature deriving from the discretization of the spatial derivative $\partial i_K / \partial z$.

The Gauss-Seidel method supplies the solution of the above equation by iterating according to the scheme

$$A_K^r T_K^{r+1} = - B_K^{r+1} T_{Ha}^{r+1} - C_K^r T_S^r - D_K^h T_{Ke}^h + R_K^{h-1} \quad (47)$$

when r is the iteration index, R_K^{h-1} contains all known terms at time $h-1$ and the term $D_K^h T_{Ke}^h$ is known from the solution for the previous axial mesh.

2.2.5 Stability analysis of the system of basic equations

The analysis of the stability of a numerical scheme based on the application of equation (19) can be performed by applying the Fourier integral to the vector of the dependent variable Y by letting

$$Y(z,t) = \frac{1}{2\pi} \int_0^\infty V(k,t) e^{+iKz} dK \quad (48)$$

which represents the solution vector by harmonics of wavenumber K ($0 < K < \infty$). In fact this is the inversion formula applied to the Fourier Transform $V(K,t)$. Although continuous in z , it only needs to be evaluated at the gitter nodes $m, m+1$ which yields the exponential terms $\exp(iKz)$ and $\exp(iK(z+\Delta z))$. After differentiation and elimination of the common factor $\exp(iKz)$ from all terms, equation (20) yields

$$\begin{aligned} V^{n+1}(k,t) = & \left(-\frac{A}{2} \frac{\Delta t}{\Delta z} + \frac{A^2}{2} \frac{\Delta t^2}{\Delta z^2} \right) V^n(k,t) e^{iK\Delta z} + \\ & + \left(I - A^2 \frac{\Delta t^2}{\Delta z^2} \right) V^n(k,t) + \left(\frac{A}{2} \frac{\Delta t}{\Delta z} + \frac{A^2}{2} \frac{\Delta t^2}{\Delta z^2} \right) V^n(k,t) e^{iK(-\Delta z)} \end{aligned} \quad (49)$$

which can be written

$$V^{n+1}(k,t) = Q(K,\Delta t) V^n(k,t) \quad (50)$$

with the "amplification matrix" given by

$$Q(K, \Delta t) = I - \left(A \frac{\Delta t}{\Delta z} \right)^2 (1 - \cos(K\Delta z)) - i A \frac{\Delta t}{\Delta z} \sin(K\Delta z) \quad (51)$$

By successive application of (50) to an initial value $V^0(K, t)$ one has

$$V^n(K, t) = Q^n(K, \Delta t) V^0(K, t) \quad (52)$$

and the stability condition requires that the matrices $Q^n(K, \Delta t)$ be uniformly bounded (for every wavenumber K) with increasing time steps n .

If $S(K, \Delta t)$ denotes the spectral radius of the matrix $Q(K, \Delta t)$, the spectral radius of $Q^n(K, \Delta t)$ is $S^n(K, \Delta t)$, since the eigenvalues of Q^n are the n -th powers of the eigenvalues of Q . Since the spectral radius of a matrix does not exceed its norms /12/ it holds

$$S(K, \Delta t)^n \leq \|Q^n(K, \Delta t)\| \leq \|Q(K, \Delta t)\|^n \quad (53)$$

This implies that a necessary condition for $Q^n(K, \Delta t)$ to be bounded is $S(K, \Delta t)^n$ to be bounded for every K , with increasing number of time steps n . For the eigenvalues q_1 ($l=1, 2, 3$) of the matrix $Q(K, \Delta t)$ it must therefore hold:

$$|q_1| \leq 1 \quad (\text{for every wavenumber } K) \quad (54)$$

As $Q(K, \Delta t)$ is a function of the matrix A , its eigenvalues q_1 are related to the eigenvalues λ_1 of the matrix A by the same functional expression.

$$q_1 = 1 - \left(\lambda_1 \frac{\Delta t}{\Delta z} \right)^2 (1 - \cos(K\Delta z)) - i \lambda_1 \frac{\Delta t}{\Delta z} \sin(K\Delta z) \quad l=1, 2, 3 \quad (55)$$

Letting $r_1 = \lambda_1 \cdot \Delta t / \Delta z$ one has

$$\begin{aligned} |q_1|^2 &= \left[1 - r_1^2 (1 - \cos(K\Delta z)) \right]^2 + r_1^2 \sin^2(K\Delta z) \\ &= 1 - 4 r_1^2 \sin^4\left(\frac{K\Delta z}{2}\right) \cdot (1 - r_1^2) \end{aligned} \quad (56)$$

which shows that (54) is satisfied when

$$|r_1| = |\lambda_1| \frac{\Delta t}{\Delta z} \leq 1 \quad (57)$$

Deriving the eigenvalues of the matrix A from its definition (17) would be quite a difficult task. They can anyway be found indirectly by writing the system of the homogeneous conservation equations in the alternative form

$$\frac{\partial \rho}{\partial t} + \rho \frac{\partial u}{\partial z} + u \frac{\partial \rho}{\partial z} = 0 \quad (58)$$

$$\frac{\partial u}{\partial t} + u \frac{\partial u}{\partial z} + \frac{1}{\rho} \frac{\partial p}{\partial z} = 0 \quad (59)$$

$$\frac{\partial}{\partial t} (\rho e) + \frac{\partial}{\partial z} (\rho e u) = 0 \quad (60)$$

with

$$e = e(p, \rho) \quad (61)$$

Differentiating further the equation (60) expressing $\partial \rho / \partial t$ by means of the continuity equation and introducing the adiabatic sound speed

$$c^2 = \left(\frac{dp}{d\rho} \right)_s = \frac{\frac{p}{\rho^2} - \frac{\partial e}{\partial \rho}}{\frac{\partial e}{\partial p}} \quad (62)$$

the energy equation reduces to

$$\frac{\partial p}{\partial t} + \rho c^2 \frac{\partial u}{\partial z} + u \frac{\partial p}{\partial z} = 0 \quad (63)$$

The system of equations (58), (59) and (63) can therefore be written as

$$\frac{dW}{dt} + B(W) \frac{dW}{dz} = 0 \quad (64)$$

with

$$B(W) = \begin{vmatrix} u & \rho & 0 \\ 0 & u & \frac{1}{\rho} \\ 0 & \rho c^2 & u \end{vmatrix} \quad W = \begin{vmatrix} \rho \\ u \\ p \end{vmatrix} \quad (65), (66)$$

The eigenvalues of the matrix $B(W)$ are the same as those of the above defined matrix $A(Y)$ because in both cases they are the reciprocal of the characteristic directions in the (t, z) plane.

By solving the third grade algebraic equation

$$\det (B - \lambda I) = 0 \quad (67)$$

one has

$$\begin{aligned} \lambda_1 &= u \\ \lambda_2 &= u+c \\ \lambda_3 &= u-c \end{aligned} \quad (68)$$

The fact that the eigenvalues of $B(W)$ are real and distinct reflects the hyperbolicity of the system of basic equations (58) to (60).

Alternatively, the characteristic directions of the above system are given by

$$\det (I - \mu B) = 0 \quad (69)$$

which yields

$$\begin{aligned} \mu_1 &= 1/u \\ \mu_2 &= 1/(u+c) \\ \mu_3 &= 1/(u-c) \end{aligned} \quad (70)$$

The differential equation of the characteristics in the (t, z) plane are

$$\frac{dt}{dz} = \mu_l \quad l = 1, 2, 3 \quad (71)$$

which represent three one-parameter families of curves. Inserting (68) into (57), the stability condition of the numerical scheme becomes

$$(|u| + c) \frac{\Delta t}{\Delta z} \leq 1 \quad (72)$$

This represent the Von Neumann necessary condition for stability. It can be proved that the condition $|q_1| \leq 1$ is also sufficient for the stability of the numerical scheme represented by equation (19).

In fact the matrix Q possesses three distinct eigenvalues, therefore a set of three linearly independent eigenvectors

$$v_1^1, v_1^2, v_1^3 \quad i = 1, 2, 3 \quad (73)$$

They are pairwise orthogonal and their Euclidean length

$$\left[\sum_{i=1}^3 (v_1^i)^2 \right]^{1/2} \quad (74)$$

can be normalized to 1.

These eigenvectors form the columns of a non-singular matrix P such that

$$P^{-1}QP = D \quad (75)$$

is a diagonal matrix whose main diagonal is formed by the eigenvalues of G. It holds

$$Q = PDP^{-1} \quad (76)$$

$$Q^n = PD^nP^{-1} \quad (77)$$

and for the norms

$$\|Q^n\| \leq \|P\| \cdot \|D^n\| \cdot \|P^{-1}\| \leq \|P\| \cdot \|D\|^n \cdot \|P^{-1}\| \quad (78)$$

To show that the matrix Q is uniformly bounded for every wavenumber K is therefore sufficient to show that the norms of the three matrices at the right side are bounded. The norm of P is bounded by the maximum norm of its columns which are the normalized eigenvectors with Euclidean length 1. The

elements of P^{-1} are

$$p_{ij}^{(-1)} = (-1)^{i+j} \frac{P_{ij}}{d} \quad i, j = 1, 2, 3 \quad (79)$$

when P_{ij} are the cofactors of the elements p_{ij} and d is the determinant of P . It holds

$$|p_{ij}^{(-1)}| \leq \frac{1}{d} \quad (d = \det P \neq 0) \quad (80)$$

because the absolute value of P_{ij} (as of any determinant) does not exceed the product of the Euclidean lengths of the vectors forming its columns/13/ and these are bounded by 1.

The norm of any $(n \times n)$ matrix is bounded by n times the absolute value of its largest element, therefore

$$||P^{-1}|| \leq 3/d \quad (81)$$

The elements of the matrix D^n are the n -th power of the eigenvalues of Q and tend to the limit zero with increasing number n of time steps if $|q_1| < 1$. The norm of D^n is in any case bounded by three times its largest element

$$||D^n|| \leq 3 (\max |q_1|)^n \leq 3 \quad (82)$$

The condition $|q_1| \leq 1$ ($1 = 1, 2, 3$) is therefore sufficient for Q^n to be bounded, hence sufficient for the stability of the numerical scheme.

2.3 Two phase flow calculation

The most difficult problem concerning the theoretical description of coolant behaviour during the two-phase flow regime consists in the solution of the coupled continuity and momentum equations for the vapour phase, which determine the space and time temperature and pressure distributions in the vapour bubbles. The method adopted for the solution of these equations has been described in detail in reference /1/ (Section 4.2.2.1 and Appendix A1). As the numerical scheme has not been basically changed, it will not be reported here extensively. Some additional information is given concerning the use of the basic equations from the programming viewpoint and the application of the "Reynolds-flux" concept /8/ for the calculation of pressure drops by vaporization or condensation.

Beyond some general information about bubbles initialization, coalescence, growth and collapse, given in section 2.3.1 and the above mentioned solution of the basic equations for the vapour and liquid phases, sections 2.3.2 and 2.3.3, two items are dealt with in detail, because they have been basically modified with respect to the BLOW-3 programme version documented in reference /1/. These items are: time and space variation of liquid film thickness, which may optionally take into account the film entrainment by flowing vapour (section 2.3.4) and the related calculation of liquid film velocity and of interfacial shear stresses between liquid and vapour (section 2.3.5).

The solution of the heat diffusion equations describing the temperature distribution in fuel, clad and structural material during the two-phase flow calculation, although performed in a separate subroutine (FBRTB), is based on the same numerical method (Gauss-Seidel iteration scheme) adopted for the calculation during single phase flow conditions and documented in section 2.1.

A general information about the sequence of the calculations performed during a time step in the two-phase flow analysis is given in the description of subroutine ITCB.

2.3.1 General information about bubbles initialization, coalescence, growth and collapse.

During the single phase flow calculation, at the end of every time step the programme checks whether the peak coolant temperature has exceeded the saturation temperature by the given (input specified) amount of superheat. In this case the precise time point is determined, within the previous time step, in which boiling inception occurred and the previous time step is correspondingly reduced.

Initialization of the first bubble occurs at the lower boundary of the mesh zone in which the boiling criterion was satisfied. The initial bubble length is assumed 0.5 mm.

The bubble is assumed to fill instantaneously the full cross section of the coolant channel, apart from an input specified film thickness on both clad and structure surfaces. Experimental investigations /14/ suggest to assume the initial film thickness to correspond to about 0.80 - 0.85 void fraction.

According to a theoretical investigation by Schlechtendahl /15/ the description of the bubble growth in spherical form up to the size which fills the cross section occurs in a very short time and its modelling can be skipped in the computer code without affecting the practical results.

The initial bubble temperature is the coolant temperature of the same mesh node; the pressure is assumed to be the saturation pressure corresponding to its temperature. The initialization of a bubble with large superheat thus implies a pressure peak in the node of the bubble formation. This expands rapidly pushing the inlet and outlet slugs away. The pressure peak broadens at the same time and drops in amplitude thus allowing a liquid film evaporation which sustains the pressure inside the bubble. Boiling inception with a large amount of superheat is therefore characterized by a formation of a large bubble which normally prevents for a while the formation of new ones. On the other side, boiling inception without or with negligible superheat is characterized by the nearly simultaneous formation of several bubbles over a relatively large section of the test channel.

As a programming rule, no more than one bubble can be initialized for every time step. A maximum of ten bubbles is allowed for every channel. Initialization of new bubbles after the first one occurs with a newly specified amount of superheat.

Bubbles displacement and growth or shrink is determined by the solution of the momentum equations for the liquid slugs between the bubbles, as well as for the inlet and outlet slugs. For this solution pressures at the phase interfaces are assumed as boundary conditions. When the new axial positions of the phase interfaces are known the energy and momentum equations for the vapour inside the bubbles are solved.

A bubble is considered to be "small" if it does not stretch over three axial mesh zones. It is "long" when it overlaps at least partially three axial mesh zones, thus containing at least two mesh zone boundaries. For short bubbles only integral values of vapour pressure and temperature are calculated. For long bubbles the programme switches to a module which allows a numerical solution of energy and momentum equations for the vapour. The phase boundaries and the internal mesh boundaries yield the nodes necessary for the numerical discretization of the above equations. In case a bubble shrinks, due to vapour condensation, from a long to a short one the programme resets the integral calculation.

Two consecutive bubbles coalesce when either of the following conditions is satisfied:

- the length of the intermediate liquid slug is less than 2 mm.
- the pressure gradient in the intermediate liquid slug exceeds a given threshold (depending on the length of the slug itself)
- the mass flow in the intermediate liquid slug exceeds a given threshold (depending on the pressure gradient).

A bubble is considered to vanish when its length shrinks below 0.4 mm. The programme switches from the two phase flow calculation back to the single phase flow calculation in case the very last bubble collapsed.

2.3.2 Remarks about the solution of the basic equations for the vapour phase and the application of the "Reynolds flux" concept to the two-phase flow.

As explained in the introduction to section 2.3 it is remanded to Reference /1/, section 4.2.2.1 for details about the numerical solution of the basic equations for the vapour in the two phase flow region. In this section a theoretical discussion is presented about a refinement of the numerical solution of the coupled momentum and continuity equations based on application of the Reynolds flux concept to calculate the liquid-vapour interfacial shear stresses in presence of phase change. The related programme modification has contributed to get rid of instability in the numerical scheme. Some programming details conclude this section.

a) Theoretical analysis

Let us introduce

$$G_v = \rho_v u_v \quad (1)$$

into the momentum equation for the vapour phase

$$\rho_v \frac{\partial u_v}{\partial t} + \rho_v u_v \frac{\partial u_v}{\partial z} = - \frac{\partial p_v}{\partial z} - \frac{U}{A} \frac{\psi_i}{2} \rho_v u_v |u_v| - \frac{U}{A} u_v \frac{m}{2} - \rho_v g. \quad (2)$$

The term $\frac{U}{A} u_v \frac{m}{2}$ represents the additional pressure drop due to mass transfer from one phase to the other with mass flux m (m is considered positive by vaporization).

One has

$$\frac{\partial G_v}{\partial t} = \rho_v \frac{\partial u_v}{\partial t} + u_v \frac{\partial \rho_v}{\partial t} \quad (3)$$

or by means of the continuity equation (assuming $\alpha \simeq 1$).

$$\frac{\partial G_v}{\partial t} = \rho_v \frac{\partial u_v}{\partial t} + u_v \left[- \frac{\partial G_v}{\partial z} + \frac{U}{A} m \right] \quad (4)$$

Combining (2) and (4) and taking into account that

$$\frac{\partial G_v}{\partial z} = \rho_v \frac{\partial u_v}{\partial z} + u_v \frac{\partial \rho_v}{\partial z} \quad (5)$$

$$\frac{\partial}{\partial z} \left(\frac{G_v^2}{\rho_v} \right) = 2 u_v \rho_v \frac{\partial u_v}{\partial z} + u_v^2 \frac{\partial \rho_v}{\partial z} \quad (6)$$

one derives a new momentum equation in the form

$$\frac{\partial G_v}{\partial t} + \frac{\partial}{\partial z} \left(\frac{G_v^2}{\rho_v} \right) = - \frac{\partial p_v}{\partial z} - \frac{U}{A} \frac{\psi_i}{2} \frac{G_v |G_v|}{\rho_v} - \frac{U}{A} \frac{G_v}{\rho_v} \frac{m}{2} + \frac{U}{A} \frac{G_v}{\rho_v} \frac{m}{2} - \rho_v g \quad (7)$$

The second and third terms at the right side represent (apart from the factor U/A) the real shear stresses at the liquid-vapour interface and an additional shear stress which results from the phase change. The fourth term, which must not be confused with the third one, derives simply by the use of the continuity equation for the change of dependent variable from $u_v(z,t)$ to $G_v(z,t)$.

The physical interpretation of the second and third terms, to which we refer as total "equivalent" shear stresses, can be illustrated by recalling the concept of "Reynolds-flux" /8/. This allows to represent in a one-dimensional flow a transversal mass and momentum transfer by means of a macroscopic representation which models the microscopic process of turbulent mixing.

In absence of phase change the shear stress at the liquid-vapour interface can be represented by a mass flux ϵ_0 from the main vapour stream striking the phase interface and bouncing back after transferring its momentum to the liquid. The shear stress at the interface can therefore be written

$$\tau_i = \frac{1}{2} \psi_i \rho_v u_v |u_v| = \epsilon_0 u_v \quad (8)$$

Letting u_o be the average transverse vapour flow velocity (from the main vapour flow to the interface and viceversa) occuring through 1/2 of the transverse flow area in each direction, the mass flux ϵ_o can be written

$$\epsilon_o = \frac{1}{2} u_o \rho_v \quad (9)$$

Consider now the mass transfer m due to vaporization or condensation and let u_N be the velocity component normal to the interface. It holds

$$m = u_N \rho_v \quad (10)$$

The velocities of vapour striking the interface and flowing back to the main stream are $u_o - u_N$ and $u_o + u_N$ respectively and the relative mass fluxes transferring momentum to the liquid and to the vapour are

$$\epsilon_m = \frac{1}{2} \rho_v (u_o \pm u_n) = \epsilon_o \pm \frac{m}{2} \quad (11)$$

when the minus sign can be suppressed with the conversion that $m < 0$ by condensation.

Hence

$$\frac{\epsilon_m}{\epsilon_o} = 1 + \frac{m}{2\epsilon_o} \quad (12)$$

represents the ratio of the mass fluxes with and without mass transfer due to phase change.

The equivalent shear stresses can be written

$$\begin{aligned} \frac{U}{A} \tau_e &= \frac{U}{A} \left(\frac{\psi_i}{2} \frac{G_v |G_v|}{\rho_v} + \frac{G_v}{\rho_v} \frac{m}{2} \right) = \frac{U}{A} (\tau_i + \tau_m) \\ &= \frac{U}{A} \bar{u}_v (\epsilon_o + \frac{m}{2}) = \frac{U}{A} \bar{u}_v \epsilon_m \end{aligned} \quad (13)$$

with

$$\tau_m = u_v \frac{m}{2} \quad (14)$$

According to the physical interpretation of the Reynolds flux concept, the equivalent shear stress

$$\tau_e = \tau_i (1 + \tau_m / \tau_i) = \frac{\epsilon_m}{\epsilon_o} \tau_i \quad (15)$$

must always take the same sign as G_v . Remarking that τ_i has always the same sign as G_v one must have

$$\tau_m \geq -\tau_i \quad \text{or} \quad m \geq -2\epsilon_o \quad \text{if } G_v \geq 0 \quad \begin{matrix} (\tau_i \geq 0) \\ (\epsilon_o \geq 0) \end{matrix} \quad (16a)$$

$$\tau_m \leq |\tau_i| \quad \text{or} \quad m \leq 2|\epsilon_o| \quad \text{if } G_v < 0 \quad \begin{matrix} (\tau_i < 0) \\ (\epsilon_o \leq 0) \end{matrix} \quad (16b)$$

The way in which this constraint is imposed in the numerical solution of the momentum equation (7) is shown hereafter. From the theoretical viewpoint it is worth to remark that the necessity to impose the above constraint arises from the assumption that u_o be the average transverse vapour velocity, which leads to the ratio ϵ_m / ϵ_o given by (12). In reality the transverse velocity has some probability distribution about a mean value u_o . This assumption would lead to replace (12) by a formula of the type

$$\frac{\epsilon_m}{\epsilon_o} = \exp(m/2\epsilon_o) \quad (17)$$

which shows that the ratio $\epsilon_m / \epsilon_o = 1 + \tau_m / \tau_i$ is always positive, therefore automatically satisfying the physical condition that τ_e has the same sign as the vapour mass flux G_v .

Space and time discretization of the momentum equation (7) yields the following relationship for the vapour pressure drop between two mesh nodes $j-1/2$, $j+1/2$ distant Δz_j (see reference /1/, section 4.2.2.1 for details)

$$P_{v,j-1/2} - P_{v,j+1/2} = A_1 + A_2 + A_3 + (A_4 + A_5) - 2A_5 \quad (18)$$

where

$$A_1 = \frac{\Delta z_j}{\Delta t_n} (G_{v,j}^{n+1} - G_{v,j}^n) \quad (19a)$$

$$A_2 = \frac{(G_{v,j+1/2}^{n+1})^2}{\rho_{v,j+1/2}^{n+1}} - \frac{(G_{v,j-1/2}^{n+1})^2}{\rho_{v,j-1/2}^{n+1}} \quad (19b)$$

$$A_3 = \rho_{v,j}^{n+1} g \Delta z_j \quad (19c)$$

$$A_4 = \frac{\psi_i}{3D_h} \Delta z_j \left[\frac{G_{v,j-1/2}^{n+1} |G_{v,j-1/2}^{n+1}|}{\rho_{v,j-1/2}^{n+1}} + 4 \frac{G_{v,j}^{n+1} |G_{v,j}^{n+1}|}{\rho_{v,j}^{n+1}} + \right. \quad (19d)$$

$$\left. + \frac{G_{v,j+1/2}^{n+1} |G_{v,j+1/2}^{n+1}|}{\rho_{v,j+1/2}^{n+1}} \right]$$

$$A_5 = \left(\frac{U}{A} \right)_j \frac{G_{v,j}^{n+1}}{\rho_{v,j}^{n+1}} \frac{1}{2} \Delta z_j (m_j^{n+1} + m_j^n) / 2 \quad (19e)$$

The sum $A_4 + A_5$ represents the pressure drop due to the equivalent shear stresses, while the term $-2A_5$ arises from the change of dependent variable and the application of the continuity equation. The physical condition imposed previously on τ_e , leading to (16a) and (16b) is equivalent to require that $A_4 + A_5$ be always of the same sign as G_v . Remark again that A_4 has always the same sign as G_v while the sign of A_5 depends on both the signs of G_v and m . With reference to the sketch of Fig. 6 showing qualitatively the dependence of $(A_4 + A_5)$ on m , with G_v as parameter, four possible cases can occur. They are summarized in Table I where $DPR_{4+5} = PVI - PV\emptyset$ represents the contribution to the vapour pressure drop over a given axial mesh due only to the above terms A_4 and A_5 . Considering, for instance, case III ($G_v > 0, m > 0$)

it is clear, that both terms A_4 and A_5 are positive, hence $A_4 + A_5 > 0$ and the required physical condition is always satisfied. In case I on the contrary ($G_v > 0$, $m < 0$) is $A_4 > 0$, but $A_5 < 0$ and the computer programme must avoid taking $A_4 + A_5$ negative, just imposing the sum to be zero, if it were negative. The table shows clearly that only in two of the four possible cases one has to take care whether the physical constraint must be applied.

Obviously, the physical constraint would be automatically satisfied if a formula like (17) were used.

To distinguish in equation (18) between the two terms containing m and having as above explained different physical meaning let denote the first, which takes into account the pressure drops due to phase change, with the symbol $A5D$ and write equation (18) as

$$P_{v,j-1/2} - P_{v,j+1/2} = A1 + A2 + A3 + A4 + A5D - 2A5 \quad (20)$$

The factor m contained in the term $A5$, which actually represents the mass continuity by phase change, may be positive (vaporization) or negative (condensation). The only constraint on it is that it cannot be positive in dry-out zones.

The above explained constraints on the term $A5D$ are complemented by imposing $A5D \leq 0$ if $m > 0$ and $G_v > 0$ (in practice summing up only negative contributions, if any, to $A5D$). Physically this means that, by vaporization, the vapour is assumed to be generated with zero velocity and no additional pressure drop is calculated at the time of generation. The lost of momentum due to acceleration of the vapour from zero to the bulk velocity follows then automatically by solving the momentum equation, due to the time and space variation of the term G_v^2 / ρ_v . If $m < 0$, $G_v > 0$, on the contrary, the momentum released by the condensing vapour is taken into account determining a diminution of the equivalent shear stresses. In practice it holds $A5D = 0$ (in case $m > 0$, $G_v > 0$) and this means that in Fig.6 the branch ABD is followed, instead of A'B'C'.

Conversely, if $m > 0$, $G_v < 0$ one must have $A5D \geq 0$ implying that the branch: A' B' D' is followed, instead of A'B'C'.

The above discussion can be summarized by stating that

- a) By evaporation ($m \geq 0$) the equivalent shear stress is equal to the real shear stress (no further contribution occurs because the vapour is assumed to be

generated with zero velocity).

- b) By condensation ($m < 0$) the absolute value of the equivalent shear stress is lower than the absolute value of the real shear stress but the sign of the equivalent shear stress must remain equal to the sign of the real shear stress.

Statement a) implies that no momentum is lost at the moment of vapour generation. Momentum is lost subsequently as vapour is accelerated in the mean stream. Statement b) implies that momentum is given back at the moment of vapour condensation.

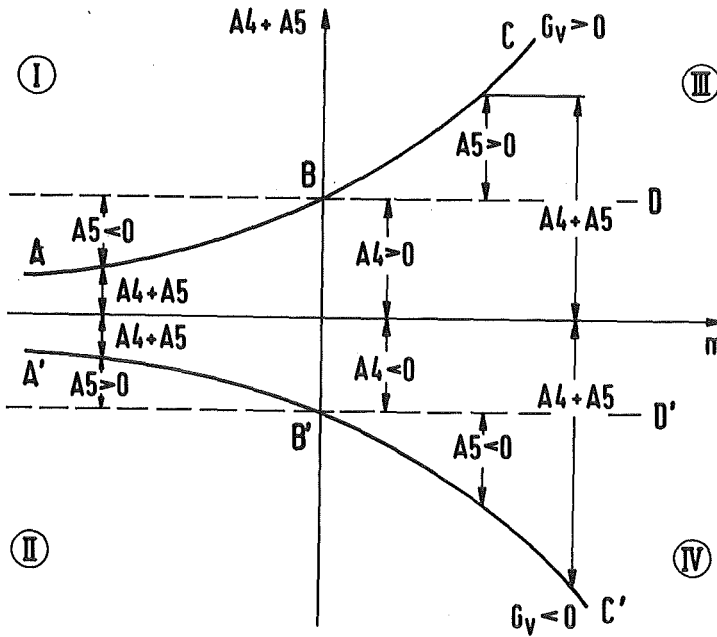


Fig. 6 Sketch showing qualitatively the dependence of the sum $A_4 + A_5$ of terms defined by equations (19d) and (19e) on the coolant mass flux m by phase change.

TABLE I

<u>CASE</u>				
I	$\left\{ \begin{array}{l} G_v > 0 \\ m < 0 \end{array} \right.$	$A_4 > 0$ $A_5 < 0$	$DPR_{4+5} = PVI - PV\phi \geq 0$	$A_4 + A_5 \geq 0$ *
II	$\left\{ \begin{array}{l} G_v < 0 \\ m < 0 \end{array} \right.$	$A_4 < 0$ $A_5 > 0$	$DPR_{4+5} = PVI - PV\phi \leq 0$	$A_4 + A_5 \leq 0$ *
III	$\left\{ \begin{array}{l} G_v > 0 \\ m > 0 \end{array} \right.$	$A_4 > 0$ $A_5 > 0$	$DPR_{4+5} = PVI - PV\phi > 0$	$A_4 + A_5 > 0$
IV	$\left\{ \begin{array}{l} G_v < 0 \\ m > 0 \end{array} \right.$	$A_4 < 0$ $A_5 < 0$	$DPR_{4+5} = PVI - PV\phi < 0$	$A_4 + A_5 < 0$

* Physical condition to be imposed in the programme.

Table I - Summary of the possible cases illustrating the dependence of vapour pressure drop due to "equivalent" shear stress (DPR_{4+5}) on the algebraic sign of G_v (vapour axial mass flux) and m (coolant mass flux by phase change).

b) Programming details

The coolant mass flux by phase change m is derived by combining the continuity and energy equations for the liquid phase as

$$m = \frac{q_w}{h_{fg}} - \frac{S\rho_1}{h_{fg}} \frac{dH_1}{dt} \quad (21)$$

with

$$q_w = \alpha_{HK} (T_{Ha} - T_v) + \alpha_{KS} (T_S - T_v) \quad (22)$$

where

h_{fg} = vaporization enthalpy (J/kg)

H_1 = liquid film enthalpy(J/kg)

S = liquid film thickness at either clad surface (S_H) or structure surface (S_S) (m)

T_{Ha} = clad surface temperature ($^{\circ}C$)

T_S = structure surface temperature($^{\circ}C$)

T_v = vapour temperature($^{\circ}C$)

α_{HK} = clad to coolant heat transfer coefficient ($W/m^2^{\circ}C$)

α_{SK} = structure to coolant heat transfer coefficient ($W/m^2^{\circ}C$)

ρ_1 = liquid density (kg/m^3)

Calculating the time derivative of the liquid enthalpy as

$$\frac{dH_1}{dt} = \frac{dH_1}{dT_1} \frac{dT_1}{dt} = \frac{dH_1}{dp} \frac{dp}{dT_1} \frac{dT_1}{dt} \quad (23)$$

where T_1 and p are liquid temperature and pressure, assumed equal to those of the vapour phase, one has

$$m = \frac{q_w}{h_{fg}} - \frac{S\rho_1}{h_{fg}} \frac{dH_1}{dp} \frac{dT_1}{dt} \quad (24)$$

The source term m is calculated for the time step t_n, t_{n+1} at node j as $(m_j^{n+1} + m_j^n)/2$.

Letting

$$XM_j = \left(\frac{U}{A} \right)_j \frac{m_j^{n+1} + m_j^n}{2} \Delta z_j \quad (25)$$

hence

$$A5 = \frac{G_{v,j}^{n+1}}{\rho_{v,j}^{n+1}} \frac{XM_j}{2} \quad (26)$$

XM is programmed as follows, with separate contributions from the liquid films at the clad and structure surfaces (dropping the index j for simplicity)

$$XM = \frac{1}{h_{fg}} \frac{XM1R + XM1}{2} + \frac{XM2R + XM2}{2} \frac{T_v^{n+1} - T_v^n}{h_{fg} \frac{dT_l}{dp} \Delta t_{n+1}} \frac{dH_1}{dp} \quad (27)$$

where

$$XM1R = \left[\frac{U_{Ha}^{n+1}}{AR} \alpha_{HK}^{n+1} (T_{Ha}^{n+1} - T_v^{n+1}) + \frac{U_S^{n+1}}{AR} \alpha_{SK}^{n+1} (T_S^{n+1} - T_v^{n+1}) \right] \Delta z \quad (28a)$$

$$XM1 = \text{as above with index } n \quad (28b)$$

$$XM2R = \left[\frac{U_H}{AR} S_H^{n+1} + \frac{U_S}{AR} S_S^{n+1} \right] \rho_1^{n+1} \Delta z \quad (28c)$$

$$XM2 = \text{as above with index } n \quad (28d)$$

and

$$\frac{U_H}{AR} = \text{XBRKT is the ratio of pin circumference to area of flow section}$$

$\frac{U_S}{AR}$ = XSTKT is the ratio of structure inner circumference to area of flow section

The two terms comparing in XM1R and XM1 within brackets are zeroed in case the respective film thickness S_H , S_S are zero (dry-out) because in this case no mass transfer can occur.

2.3.3 Solution of the basic equations for the liquid slug

a) Continuity equation

The simplified continuity equation for a liquid slug, above a bubble of index K, $\partial G_K / \partial z = 0$ yields $G_K = \text{const.}$

b) Momentum equation

The integral value of the mass flux is calculated in the subroutines IMGL and TRANS explicitly by means of

$$G_K^{n+1} = G_K^n + \left(\frac{dG_K}{dt} \right)^n \Delta t_n \quad (29)$$

with

$$\left(\frac{dG_K}{dt} \right)^n = \frac{1}{L_K} \left\{ p_{v2,K}^n - p_{v1,K+1}^n - G_K^{n2} \left(\frac{1}{\rho_{K1,K+1}^n} - \frac{1}{\rho_{K2,K}^n} \right) - \frac{G_K^n |G_K^n|}{2D_h} \int_0^{L_K} \frac{f}{\rho_K^n} dz - g \int_0^{L_K} \rho_K^n dz \right\} \quad (30)$$

when p_v is the vapour pressure, the indexes K, K+1 refer to the lower and upper bubbles bounding the liquid slug, and the indexes 1,2 refer to the lower, upper phase interfaces.

The vapour pressure at the phase interfaces which form the boundary conditions is supplied by the vapour pressure distribution calculation (subroutine DPDA for "long" bubbles and subroutine ENBL1 for "short" bubbles). The axial position ZL of the phase interfaces, hence the slug length L_K , is calculated by

$$ZL^{n+1} = ZL^n + \left(\frac{G_K}{\rho_K} \right)^{n+1/2} \Delta t_n . \quad (31)$$

For the inlet and outlet slug hold equations similar to (30), where the reduced inlet and outlet lengths and the inlet and outlet pressures are taken into consideration. Finally, application of the momentum equation to every Eulerian mesh within a liquid slug yields the pressure distribution in the liquid coolant. For a mesh between z , $z + \Delta z$ one has

$$p(z) = p(z+\Delta z) + \left(\frac{dG_K}{dt} \right)^n \Delta z + G_K^2 \left(\frac{1}{\rho(z+\Delta z)} - \frac{1}{\rho(z)} \right) + \left(\frac{f}{2D_h} \frac{G_K |G_K|}{\rho_K(z+\Delta z/2)} - \rho(z+\Delta z/2) g \right) \Delta z . \quad (32)$$

c) Energy equation

The solution of the energy equation, written for the liquid slugs with reference to a Lagrangian mesh of index i

$$\rho_{Ki} \frac{dH_{Ki}}{dt} = \dot{\Phi}_{Ki} \quad (33)$$

is carried out by means of the half-implicit time discretization scheme

$$\frac{T_{Ki}^{n+1} - T_{Ki}^n}{\Delta t_n} = \frac{1}{(\rho c_p)^{n+1/2}} \left[\theta \dot{\Phi}_{Ki}^{n+1} + (1-\theta) \dot{\Phi}_{Ki}^n \right] \quad (34)$$

with $0 < \theta < 1$ and

$$\dot{\Phi}_{Ki} = \frac{1}{\Delta z_{Ki}} \sum_j \left[\frac{U_H}{A} \alpha_{HK} (T_{Ha} - T_{Ki}) + \frac{U_S}{A} \alpha_{KS} (T_S - T_{Ki}) + q_K \right] \delta z_{Ki,j} = \left[\frac{W}{m^3} \right] \quad (35)$$

when Δz_{Ki} is the length of the i -th Lagrangian mesh, $\delta z_{Ki,j}$ is the length of the segment of Lagrangian mesh i overlapping the Eulerian mesh j and the sum extends to all Eulerian meshes facing the considered Lagrangian mesh.

q_K takes into account the heat generation in the coolant.

Letting

$$CC1 = \frac{U_H}{A} \alpha_{HK}^n (T_{Ha}^n - T_{Ki}^n) \quad (36a)$$

$$SS1 = \frac{U_S}{A} \alpha_{KS}^n (T_S^n - T_{Ki}^n) \quad (36b)$$

$$CCR = \frac{U_H}{A} \alpha_{HK}^{n+1} (T_{Ha}^{n+1} - \tilde{T}_{Ki}^{n+1}) \quad (36c)$$

$$SSR = \frac{U_S}{A} \alpha_{KS}^{n+1} (T_S^{n+1} - \tilde{T}_{Ki}^{n+1}) \quad (36d)$$

where the tilde \sim denotes provisional values at time t_{n+1} provided by the iteration scheme within the driving subroutine ITCB, one has

$$T_{Ki}^{n+1} = T_{Ki}^n + \frac{\Delta t_n}{(\rho c_p)^{n+1/2}} \frac{1}{\Delta z_{Ki}} \cdot \sum_j \left[\theta (CC1 + SS1) + (1-\theta) (CCR + SSR) + q_K \right] \delta z_{Ki,j} \quad (37)$$

d) Remark on the calculation of the terms QQ1(M) to QQ6(M) (1 < M < NM2)

The coupling between the thermal-hydraulic calculation for the coolant and the calculation of temperature distributions in fuel, clad and structure materials is provided, both for the single and two phase flows, by the terms QQ1 to QQ6 which are either heat fluxes (QQ1 to QQ4) or heat transfer coefficients used for calculating heat fluxes (QQ5 and QQ6).

Referring to the list of symbols given in section III.3 for their physical meaning, these terms are defined for every Eulerian mesh as

$$QQ1 = \alpha_{HK}^n (T_K^n - T_H^n) \quad (W/m^2) \quad (38)$$

$$QQ2 = \alpha_{KS}^n (T_K^n - T_S^n) \quad (W/m^2) \quad (39)$$

$$QQ3 = \alpha_{HK}^{n+1} T_K^{n+1} \quad (W/m^2) \quad (40)$$

$$QQ4 = \alpha_{KS}^{n+1} T_K^{n+1} \quad (W/m^2) \quad (41)$$

$$QQ5 = \alpha_{KS}^{n+1} \quad (W/m^2 \text{ } ^\circ C) \quad (42)$$

$$QQ6 = \alpha_{HK}^{n+1} \quad (W/m^2 \text{ } ^\circ C) \quad (43)$$

In the definition of QQ1 to QQ4 T_K may be either liquid or vapour temperature.

For the single phase flow calculation the terms QQ1 to QQ6 are computed in the subroutine ITC11 (or ITC11R).

In the two phase flow the calculation is done as follows:

- a) At the very first boiling initialization in subroutine SETUP the terms QQ1 and QQ2 are initialized.
- b) Terms QQ3 to QQ6 are calculated in subroutine TLKM, referring to the bubbles configuration at time t_{n+1} , only for the meshes partially or completely filled with liquid coolant.
- c) The calculation of terms QQ3 to QQ6 is completed in subroutine ITCB for the meshes partially or completely filled with vapour.

The calculation of temperature distributions in fuel, clad and structure occurs at this stage in subroutine FBRTB.

- d) Terms QQ1 and QQ2 are calculated in subroutine TLKMS using values at time t_{n+1} . After time step advancement they yield the "old" values referring to the beginning of the time step.

e) Definition of the Lagrangian meshes in the liquid slugs

Once a bubble is initialized the mass, momentum and energy equations for the liquid slugs above and below it are solved in a Lagrangian mesh. Definition of the Lagrangian meshes of liquid slugs are slightly modified dependent on whether boiling has already progressed and several vapour bubbles have been produced or only one single vapour bubble is initialized inside the coolant channel.

At boiling onset the Lagrangian mesh for the upper slug is initialized equivalent to the Eulerian mesh of the single phase coolant calculation. If boiling has already progressed, the Lagrangian meshes of the slug which is located between the upper boundary of the newly formed bubble and the lower boundary of the next bubble in upward direction define the Lagrangian mesh of the upper slug of the newly formed bubble. If the uppermost slug moves in downward direction and it happens that the sum of Lagrangian mesh sizes of this slug is less than the distance between the end of the coolant channel and the upper boundary of the sodium vapour interface a new Lagrangian mesh is generated. Its length is Z_{SLUG} and its initial values of coolant temperature and pressure correspond to the upper plenum mixing temperature and to the outlet pressure.

For the lower slug special measures are taken to define the Lagrangian meshes. At boiling onset firstly a reference mesh size is determined as follows:

$$\Delta Z_{ref}^L = (\Delta Z_{max}^E + \Delta Z_{min}^E) / 4$$

where ΔZ_{ref}^L - reference Lagrangian mesh size
 ΔZ_{max}^E - maximum Eulerian mesh size
 ΔZ_{min}^E - minimal Eulerian mesh size

If an Eulerian mesh size of the lower slug is larger than this reference mesh size the value of the respective mesh is subdivided into a number of NT Lagrangian meshes according to

$$NT = (\Delta Z^L / \Delta Z_{ref}^L) + 1$$

Initial values of coolant temperatures and pressures are set assuming a linear profile along the mesh to be subdivided.

The length of a Lagrangian mesh located just below a vapour bubble might be further modified. If its length is larger than Z_{SLUG} it is subdivided into NT Lagrangian meshes according to

$$NT = \Delta Z^L / Z_{SLUG} + 1$$

In this case initial values for coolant temperatures and pressures in the newly built-up Lagrangian meshes are set to the value of the original Lagrangian mesh located just below the new liquid-vapour interface. By this procedure calculation of coolant temperatures and pressures in the vicinity of a liquid-vapour interface is sufficiently detailed to allow for multiple bubble formation in case of flat temperature and pressure gradients in the vicinity of the boiling front.

If the lowermost slug moves upwards and the distance between the lower vapour boundary and the entrance into the coolant channel is larger than the sum of all Lagrangian meshes of the lowermost slug, a new Lagrangian mesh is defined. Its length normally is Z_{SLUG} , its coolant temperature and pressure correspond to the respective inlet input data.

Initialization and/or modifications of the Lagrangian meshes are performed in the subroutines SETUP and/or TRANS. Procedures for definition of Lagrangian meshes allow for proper simulation of slug ejection as well as total re-wetting of voided regions.

2.3.4 Time and space variation of liquid film thickness

The analytical and numerical treatment of the equations for the liquid phase in the two phase flow region are presented for the programme BLOW-3 in section 4.2.2.3 and Appendix A2 of reference /1/. For the sake of clarity these equations are hereafter rewritten and discussed together with other programme improvements which have been introduced in the BLOW-3A version. These are mainly:

- a) Drop the limiting assumption that the liquid film velocity is negligible with respect to the vapour velocity. The model of "static" film (applied in BLOW-3) may be optionally replaced by the model of moving film in BLOW-3A. (See section 2.3.5)
- b) The calculation of velocity distribution within the liquid film, which determines the interfacial shear stresses between film and vapour, has been carried out assuming a "universal velocity profile" through the film and applying to the heterogeneous multiple bubble slug ejection model the concept of two-phase multipliers and the correlations of Lockhart-Martinelli /7/. (See section 2.3.5)
- c) The calculation of heat transfer coefficient clad-vapour and vapour structure through the liquid film has been revised taking into account the contributions of a laminar sublayer and of a turbulent layer (see section 2.3.6).

a) Theoretical analysis

The basic equations for the calculation of the space and time variation of liquid film thickness at the clad and structure material are:

i) Continuity equation:

$$\frac{\partial}{\partial t} (1-\alpha) \rho_1 + \frac{\partial}{\partial z} (1-\alpha) \rho_1 u_1 = - \frac{U}{A} \sqrt{\alpha} m \quad (44)$$

ii) Energy equation:

$$\frac{\partial}{\partial t} (1-\alpha) \rho_1 H_1 + \frac{\partial}{\partial z} (1-\alpha) \rho_1 u_1 H_1 = \dot{\Phi}_1 \quad (45)$$

iii) Momentum equation:

$$\rho_1 \frac{\partial u_1}{\partial t} + \rho_1 u_1 \frac{\partial u_1}{\partial z} = - \frac{\partial p}{\partial z} - \rho_1 g - \frac{1}{S} \psi_w \frac{\rho_1}{2} |u_1| u_1 + \frac{1}{S} \psi_i |u_v| u_v + \dot{u}_v \frac{m}{2} \quad (46)$$

Assuming that for a film of thickness small compared with the hydraulic diameter it holds

$$1-\alpha \approx \frac{U}{A} S \quad (47)$$

and assuming $\sqrt{\alpha} \approx 1$, equation (44) can be rewritten,

$$\frac{\partial}{\partial t} S + \frac{\partial}{\partial z} (u_1 S) = - \frac{m}{\rho_1} \quad (48)$$

Combining continuity and energy equations one derives:

$$S \rho_1 \frac{\partial H_1}{\partial t} + S \rho_1 u_1 \frac{\partial H_1}{\partial z} = q_w - m h_{fg} \quad (49)$$

from which the mass flux m exchanged between the liquid and vapour phases can be derived. Introducing m into the continuity equation (48) one has

$$\frac{\partial S}{\partial t} + \frac{\partial}{\partial z} (u_1 S) = - \frac{q_w}{\rho_1 h_{fg}} + \frac{S}{h_{fg}} \cdot \frac{\partial H_1}{\partial t} + \frac{S u_1}{h_{fg}} \frac{\partial H_1}{\partial z} \quad (50)$$

which is the basic equation describing the time and space variation of liquid film thickness at both clad and structure material surfaces.

In case the model of static film is applied, the above equation reduces to (imposing $u_1 = 0$)

$$\frac{\partial S}{\partial t} = - \frac{q_w}{\rho_1 h_{fg}} + \frac{S}{h_{fg}} \frac{\partial H_1}{\partial t} \quad (51)$$

With reference to the film at the clad surface the heat flux clad to vapour is given by

$$q_w = \alpha_{HK} (T_{Ha} - T_v) \quad (52)$$

The heat transfer coefficient clad-vapour α_{HK} has been calculated taking into account the diffusivity for turbulent heat exchange as explained in section 2.3.6.

For bubbles stretching into the upper liquid plenum the heat flux is calculated by

$$q_w = \alpha_{HK} (T_{PL} - T_v) \quad (53)$$

The plenum temperature T_{PL} is not constant (as in the BLOW-3 code version) but is calculated by means of an input value and taking into account the enthalpy exchange between condensing vapour and liquid in a given control volume (see section 3.2).

As explained in reference /1/ the time variation of the liquid film thickness is corrected for the end mesh zones of a vapour bubble by means of

$$\frac{dS}{dt}^* = \frac{dS}{dt} + |u_{PG}| \frac{S_o - S}{\Delta \Delta z} \quad (54)$$

where Δz is the bubble length in the lower or upper axial mesh zone, and u_{PG} is the velocity of the interface between vapour bubble and liquid slug. Equation (50) is discretized with forward differences with respect to time and with upwind differences for the space derivatives. Letting the index n refer to time, j refer to the central node of an Eulerian axial mesh, $j \pm 1/2$ to the upper and lower mesh boundaries one has:

$$\frac{S_j^{n+1} - S_j^n}{\Delta t_n} + 2 \frac{u_{lj}^n S_j^n - u_{lj-1}^n S_{j-1}^n}{\Delta z_j + \Delta z_{j-1}} = - \frac{q_{wj}^{n+1} + q_{wj}^n}{2h_{fg} \rho_{ij}^n} +$$

$$+ \frac{S_j^n}{h_{fg}} \left(\frac{\partial H_l}{\partial T_v} \right)_j^n \frac{T_{vj}^{n+1} - T_{vj}^n}{\Delta t_n} + \frac{S_j^n u_{lj}^n}{h_{fg}} c_{pl,j}^n \frac{T_{vj}^n - T_{vj-1}^n}{\Delta z_j + \Delta z_{j-1}} \quad \text{if } u_{lj} \geq 0 \quad (55)$$

$$\frac{S_j^{n+1} - S_j^n}{\Delta t_n} + 2 \frac{u_{lj+1}^n S_{j+1}^n - u_{ij}^n S_j^n}{\Delta z_{j+1} + \Delta z_j} = \frac{q_{wj}^{n+1} + q_{wj}^n}{2h_{fg} \rho_{ij}^n} +$$

$$+ \frac{S_j^n}{h_{fg}} \left(\frac{\partial H_l}{\partial T_v} \right)_j^n \frac{T_{vj}^{n+1} - T_{vj}^n}{\Delta t_n} + \frac{S_j^n u_{lj}^n}{h_{fg}} c_{pl,j}^n \frac{T_{vj+1}^n - T_{vj}^n}{\Delta z_{j+1} + \Delta z_j} \quad \text{if } u_{lj} < 0 \quad (56)$$

under the assumption of thermodynamic equilibrium of liquid film and vapour over the cross section.

Dropping the last term at both sides of these equations leads to the application of the static film model (discretization of above equation (51)).

b) Comparison with previous model of static film

Comparison of results obtained with the application of the models of static and moving film shows that

- i) transport of liquid film mass in axial direction due to vapour drag may exceed by a large factor the mass exchanged between the two phases due to vaporization or condensation.
- ii) dryout spots may occur shortly after boiling inception but they are rapidly rewetted (when using the moving film model). These two results confirm the conclusions reported in references /16/, /17/

iii) when using the static film model rewetting may only occur due to bubbles axial displacement and passage of a liquid slug over dried-out zones. When the moving film model is applied rewetting is continuously occurring (at least in the first boiling phase, before total voiding of the channel) owing to liquid mass transport in axial direction.

iv) when using the static film model a minimum film thickness is normally set to a value which corresponds to about 0.95 void fraction in the channel. If in some axial mesh zone the calculated liquid film thickness drops below the specified value dryout is assumed. This feature, which was originally introduced by Schlechtendhal in the BLOW-2 programme /18/, was maintained in the BLOW-3 code to compensate for the fact that the static film is not drained by the vapour. It implies the disadvantage that the total coolant mass balance is not rigorously respected.

In the moving liquid film model the minimum liquid film thickness is set to zero and the continuity equations of both phases are satisfied rigorously.

v) in both static and moving film models the overall energy balance in the channel is preserved. Clad and fuel temperatures may be anyway overestimated and burn-out predicted too soon in the static film model due to insufficient rewetting of dried-out zones.

vi) in case the problem to be simulated is characterized by a rapid overpower transient or severe loss of flow conditions (or combination of these two simulated accidents) and voiding of the coolant channel is rapidly obtained, the difference between results gained with the application of the two methods is not very relevant. On the contrary, in case the problem to be modelled is characterized by mild transients and quasi stationary boiling conditions are maintained over a long time interval the moving liquid film model leads to results which are appreciably different from those supplied by the static film model and closer to the reality as the analysis of SCARABEE single pin in-pile experiments has shown /19/.

vii) the additional numerical effort necessary to solve equation (50) instead of equation (51) is negligible.

2.3.5 Calculation of liquid film velocity and of interfacial shear stress between liquid and vapour.

a) Statement of the problem

In Appendix C of reference /1/ is discussed the opportunity of calculating the interfacial friction factor between liquid film and flowing vapour by means of the Wallis correlation /20/

$$\psi_i = \psi_v \left(1 + 300 \frac{S}{D_h} \right) \quad (57)$$

where

ψ_v = friction coefficient for the vapour flowing alone in the channel

S = liquid film thickness

D_h = hydraulic diameter

This correlation is assumed to hold for "rough annular flow" conditions. In a one-dimensional two-phase annular flow the film is smooth as long as the vapour velocity does not exceed a critical value. Above it the friction factor rises rapidly because of the formation of waves and the annular flow becomes "rough". At higher vapour velocities liquid droplets are entrained and the flow regime tends to become homogeneous (mist) flow, characterized by large friction factors.

The theoretical interpretation of the SCARABEE in-pile boiling experiments /3, 19/ has shown that the above Wallis formula is acceptable for well developed two-phase flow regime, but is not satisfactory (giving too large pressure drops) for the first boiling phase immediately after boiling inception, when the void fraction is about 0.8 (as it corresponds to the initialized liquid film thickness) nor in the condensation region where the void fraction becomes , in the BLOW model, as low as about 0.6.

Preserving the possibility of using optionally the above formula (57), the problem of calculating the pressure drops in the two-phase flow region has been re-examined and a new module has been introduced in the BLOW-3A code. This alternative calculation method provides results which are in good agreement with the Wallis formula for large void fractions, but yields lower pressure in case of low void fractions. The new approach consists in applying

the concept of two-phase multipliers, normally used in calculation methods based on homogeneous flow theories, to the heterogeneous multiple bubble slug ejection model upon which the BLOW-3 code is based.

Owing to the original structure of the BLOW-3 code, the calculation of two-phase pressure drops is performed with reference to the vapour phase, by numerically solving the momentum equation (2), which describes the space and time distribution of the vapour mass flux G_v in the bubbles.

The coupling between liquid and vapour phases is represented by the second term at the right hand side of this equation, where the interfacial factor Ψ_i is computed either with the Wallis formula (57) or alternatively with the method explained hereafter.

b) Theoretical formulation and assumptions

The method used for calculating the liquid film velocity and the interfacial friction factor is based upon the following assumptions:

- i) the two-phase flow can be represented by the "separate cylinders model"
- ii) The pressure drop in the separate cylinders equals the actual pressure drop, which implies no pressure drop in radial direction.
- iii) the pressure drop is due only to friction, i.e. acceleration forces are negligible.
- iv) the pressure drop can be calculated for either phase from the single-phase flow theory.

Let the two phase multiplier, referred to the vapour phase, be defined by:

$$\phi_v^2 = \frac{dp/dz}{(dp/dz)_v} \quad (58)$$

where dp/dz represents the actual pressure drop and $(dp/dz)_v$ the pressure drop which would occur if the vapour phase were flowing alone in the channel.

Calculating the actual pressure drop dp/dz by means of the interfacial friction factor Ψ_i and $(dp/dz)_v$ by means of the friction factor for the vapour phase Ψ_v and introducing into (53) one has /20/:

$$\Psi_i = \Psi_v \phi_v^2 \alpha^{5/2} \quad (59)$$

where α is the void fraction and Ψ_v is a known function of the vapour Reynolds number

$$\Psi_v = f(\text{Re}_v) \quad (60)$$

Let

$$X_{LM} = \left(\frac{1-x}{x} \right)^{0.9} \left(\frac{\rho_v}{\rho_l} \right)^{0.5} \left(\frac{\mu_l}{\mu_v} \right)^{0.1} \quad (61)$$

be the Lockhart-Martinelli parameter.

The usual application consists in considering the two-phase flow as homogeneous, deriving by thermal balance the (average) quality x for a given channel axial section, hence the Lockhart-Martinelli parameter X_{LM} . Empirical correlations allow then to derive the two-phase multiplier Φ_v in dependence on the flow regimes (laminar/turbulent) in either phase. Equation (58) yields the actual pressure drop dp/dz , as $(dp/dz)_v$ can easily be calculated for the vapour phase flow. This usual approach cannot be followed in case of a multiple bubble model. The quality of the two phase flow cannot be derived by thermal balance as average value for a given axial section because this would assume a model of homogeneous flow which does not hold for the BLOW-3 code. The alternative approach is to define, for a given axial section, a "local" quality as ratio of the vapour mass flux to the mass flux of both phases:

$$x = \frac{G_v}{G_v + G_l} = \frac{\alpha \rho_v u_v}{\alpha \rho_v u_v + (1-\alpha) \rho_l u_l} \quad (62)$$

and to calculate, beside the vapour velocity u_v , the liquid phase velocity u_l .

Both velocities could be derived by solving simultaneously the momentum equations (2) and (46) for the vapour and liquid phases respectively. Although possible, this method implies a considerable numerical effort. The theoretical formulation of the problem has therefore been simplified with the following approach:

- a) for a given axial mesh, the liquid film thickness, hence the void fraction α , is known;
- b) solution of equation (2) has afforded the axial distribution of vapour velocity along a bubble.

- c) axial distribution of liquid film velocity is not derived by solving the momentum equation for the liquid phase, but accepting the simplifying equations of the boundary layer theory. To this purpose two further assumptions are necessary:
- v) acceleration forces are negligible with respect to shear stresses (assumption compatible with iii) above)
- vi) The shear stress is constant across the liquid film and equal to the interfacial shear stress

$$\tau_i = \frac{\Psi_i}{2} \rho_v |u_v - u_i| (u_v - u_i) \quad (63)$$

where u_i represents the film velocity at the interface with the vapour phase.

For the calculation of the dimensionless quantities of the boundary layer theory, the shear stress has to be known. As it depends, like the quality x , on u_i it is evident that the solution of the problem illustrated above requires the calculation of the liquid film velocity. A numerical solution has been attained by means of an iterative computing scheme which is explained hereafter.

c) Iterative calculation scheme

For a cross section of a bubble where the vapour velocity u_v has been previously calculated, let

$$u_i = \beta u_v \quad (64)$$

($0 < \beta < 1$) be a trial film velocity. Assuming that space distributions of pressure and temperature, hence the vapour physical properties are known along a bubble (as previously calculated in the subroutine DPDA), equations (58) to (62) yield a trial figure for the quality, the Lockhart-Martinelli parameter X_{LM} , and the interfacial friction factor Ψ_i .

Let an experimental relation be known between the Lockhart-Martinelli parameter and the two phase multiplier referred to the liquid phase

$$\phi_1 = ((dp/dz)/(dp/dz)_1)^{1/2}$$

$$\phi_1 = f(X_{LM}) \quad (65)$$

According to the "separated cylinders model" the following theoretical relation exists between the two-phase multipliers referred to the vapour and liquid phase:

$$\left(\frac{1}{\phi_v^2}\right)^{1/n} + \left(\frac{1}{\phi_l^2}\right)^{1/n} = 1 \quad (66)$$

where $n=2$ for laminar flow, 2.375 to 2.5 for turbulent flows analyzed on a basis of friction factor, and 2.5 to 3.5 for turbulent flows calculated on mixing-length basis. Equation (66) supplies a family of curves relating ϕ_v to ϕ_l , which can be used to fit experimental data. Wallis /20/ suggests $n=3.5$ as a good choice for all flow regimes.

Equation (66) yields ϕ_v from the previously determined (trial) ϕ_l , hence (59) and (63) yield the interfacial friction factor Ψ_i and the shear stress τ_i . Following the notation of the boundary layer theory, let

$$u_1^* = \sqrt{\frac{\tau_i}{\rho_l}} \quad (67)$$

be the friction velocity, and

$$S^+ = \frac{S u_1^* \rho_l}{\mu_l} \quad (68)$$

$$u_1^+ = \frac{u_1}{u_1^*} \quad (69)$$

the dimensionless liquid film thickness and velocity.

The mass flow of the liquid phase is given by

$$W_1 = \int_{A_1} \rho_l u_1 dA = \int_0^S 2\pi r \rho_l u_1 dr = \rho_l \bar{u}_1 A_1 \quad [\text{kg/s}] \quad (70)$$

where $A_1 = (1-\alpha)A$ is the area of the cross section A occupied by the film and \bar{u}_1 represents the mean value of the film velocity over the area A_1 .

Defining the dimensionless mass flow as

$$W_1^+ = \frac{W_1}{2\pi r_w \mu_1} \quad (71)$$

where r_w is the radius of the outer wall of the flow channel one has:

$$W_1^+ = \int_0^{S^+} \left(1 - \frac{y}{r_w}\right) u_1^+ dS^+ \quad (72)$$

with $y = r_w - r$.

Assuming that the dimensionless velocity distribution over the film thickness is given by the "universal velocity profile" /21/

$$\begin{aligned} u_1^+ &= S^+ & S^+ < 5 \\ u_1^+ &= -3.05 + 5 \ln S^+ & 5 \leq S^+ < 30 \\ u_1^+ &= 5.5 + 2.5 \ln S^+ & 30 \leq S^+ \end{aligned} \quad (73)$$

and introducing into (72) one has for the dimensionless mass flow in the laminar layer ($S^+ < 5$), the transition zone ($5 \leq S^+ < 30$) and the turbulent layer ($30 \leq S^+$) respectively:

$$W_1^+ = \frac{S^{+2}}{2} - \frac{S^{+3}}{3Re^*}$$

$$W_1^+ = -8.05 S^+ + 5 S^+ \ln S^+ + 12.45 - \frac{1}{Re^*} (2.5 S^+ \ln S^+ - 2.77 S^{+2} + 10) \quad (74)$$

$$W_1^+ = 3 S^+ + 2.5 S^+ \ln S^+ - 63.75 - \frac{1}{Re^*} (2.125 S^{+2} + 1.25 S^{+2} \ln S^+ - 574.6)$$

with

$$Re^* = \frac{u_1^* r_w}{\nu_1} \quad (75)$$

From (65) and (66) one derives for the mean film velocity

$$\bar{u}_1 = \frac{W_1^+ \mu_1}{\rho_1 S} \quad (76)$$

This figure can be used to replace (64) as a new trial and the calculation repeated till a desired accuracy has been attained. This iterative scheme affords results independent from the initial trial and converges rapidly. A few iterations are sufficient to calculate the mean film velocity with a relative error smaller than 10^{-4} . After completing the iteration, equation (63) yields the interfacial friction coefficient to be inserted in equation (2) for calculating the pressure drop in the two-phase flow region.

The above explained iterative method is summarized in the scheme of Fig. 7. The method has been extensively checked in the framework of the theoretical interpretation of the SCARABEE single pin in-pile experiments /19/ and of sodium boiling experiments in out-of-pile seven pin bundles /5/, /26/.

d) Numerical Results

The results of the iterative scheme explained in the previous paragraph depend strongly on the choice of the correlation (65) between the parameter X_{LM} and the two-phase pressure drop multiplier. Results obtained by the original experimental work of Lockhart and Martinelli /7/ have been approximated by assuming different plots for the two phase multiplier according to the flow regime in either phase, namely

$$\begin{aligned} \phi_{tt} &= 4 X_{LM}^{-0.590 + 0.0855 \lg_{10} X_{LM}} && \text{for } X_{LM} \leq 1 \\ \phi_{tt} &= 4 X_{LM}^{-0.590 + 0.231 \lg_{10} X_{LM}} && 1 < X_{LM} \leq 10 \\ \phi_{tt} &= 1.75 && 10 < X_{LM} \end{aligned} \quad (77)$$

for turbulent regimes in both liquid film and vapour and

$$\begin{aligned} \phi_{11} &= 2.66 X_{LM}^{-0.516 + 0.142 \lg_{10} X_{LM}} && X_{LM} \leq 1 \\ &= 2.66 X_{LM}^{-0.516 + 0.276 \lg_{10} X_{LM}} && 1 < X_{LM} \leq 10 \\ &= 1.53 && 10 < X_{LM} \end{aligned} \quad (78)$$

for laminar flow regimes in both phases. In case only one phase is laminar it has been assumed

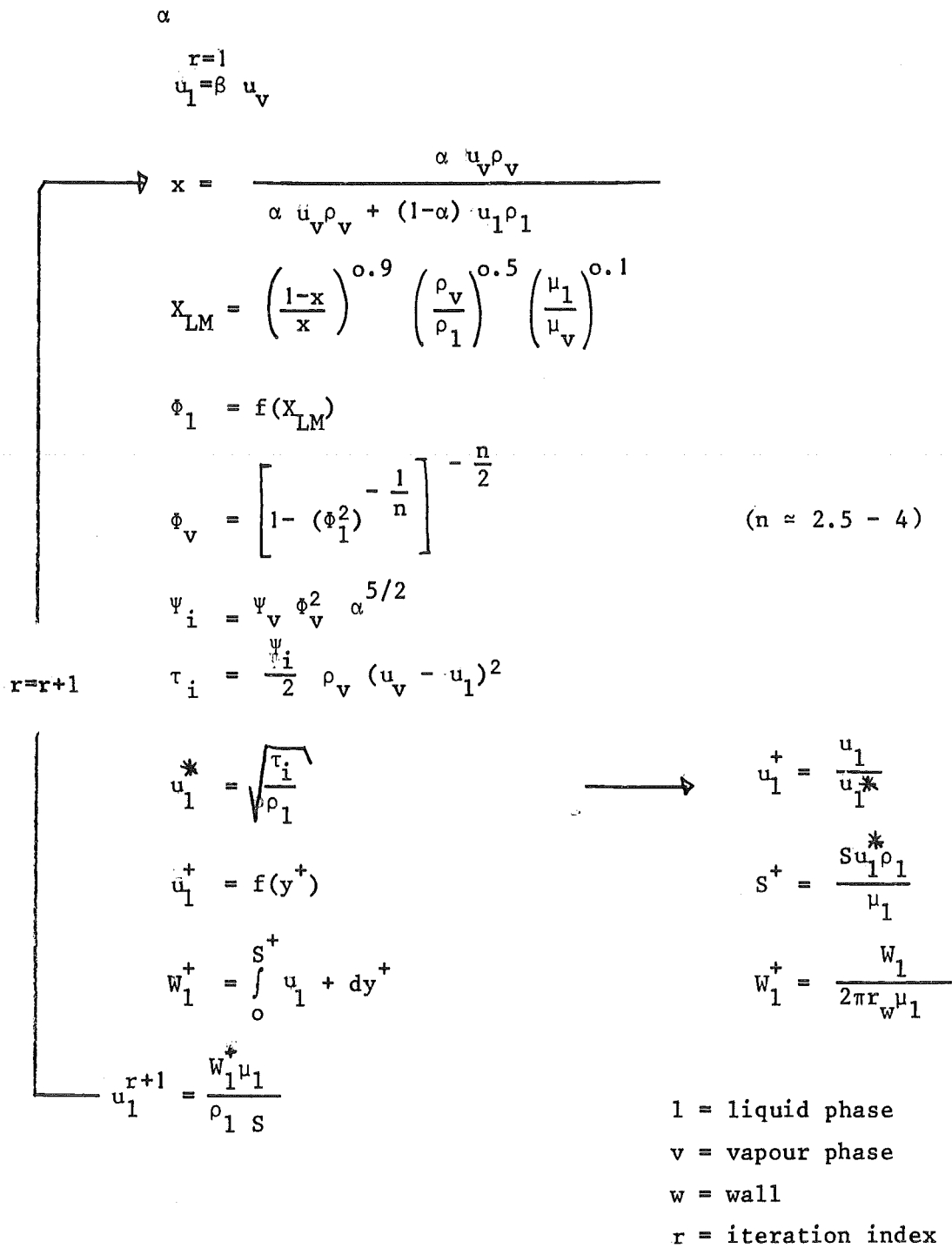


Fig. 7 Iteration scheme for calculation of liquid film velocity

$$\phi_{1t} = \phi_{t1} = \frac{\phi_{tt} + \phi_{11}}{2} \quad (79)$$

For most practical purposes a simplification may be introduced by assuming for $X_{LM} < 1$ and for every flow regime in both phases

$$\phi_1 = 3.6 X_{LM}^{-0.764} \quad (80)$$

A parametric analysis has been performed to assess the validity of the numerical approach explained previously. Results obtained with the application of the correlation (80) are shown in Fig /8/ which plots the interfacial friction coefficient against the film thickness assuming the vapour mass flux as parameter. The film thickness ranges from 0 to 150 μm which corresponds, in case of the SCARABEE geometry /3/ for which the results were obtained, to a void fraction in the range 1 - 0.6.

The temperature, upon which the physical properties of both phases depend, does not play a relevant role and has been fixed to 1000 $^{\circ}\text{C}$. In this figure the friction coefficient derived with the iterative method is compared with the values supplied by the Wallis formula (57). One can remark the good agreement in the range 0 - 70 μm film thickness, while in the range 70 - 150 μm the values given by the Wallis formula are considerably larger.

Figs 9 and 10 show results obtained with application of the correlations (7.7), (7.8) and (7.9), i.e. taking into account the flow regimes in both phases, for vapour mass fluxes 10 and 50 $\text{kg}/\text{m}^2 \text{ sec}$ respectively. These figures show the transition between different flow regimes as the critical Reynolds number ($\text{Re}_c = 2000$) in either phase has been reached.

The ratio vapour to liquid film mean velocity is shown in Fig. 11 against the liquid film thickness for several values of the vapour mass flux.

The numerical investigations have been completed by applying, as alternative to the above correlations by Lockhart-Martinelli, the results obtained by Pepller with sodium boiling tests performed at KfK /22/. Evaluation of these tests has led to the following correlations for the two phase pressure drop multipliers referred to the liquid and vapour phases respectively

$$\phi_1 = 8.2 X_{LM}^{-0.55} \quad (81)$$

$$\phi_v = 8.2 X_{LM}^{0.405} \quad (82)$$

These correlations do not satisfy equation (66) with n in the range 2.5-4. For X_{LM} between 0.1 and 1 equation (66) is approximately satisfied taking $n = 6$. Application of the above correlations in the iterative calculation of the interfacial friction factor leads to results which lay for above those supplied by either the Wallis formula or the Lockhart-Martinelli correlation. A comparison of some worths is shown in Table II. The ratio vapour velocity to liquid film mean velocity as derived with application of the Peppler correlation is shown in Fig. 12.

Interfacial friction factor Ψ_i				
VAPOUR MASS FLUX (kg/m ² sec)	Film thickness / μm /	Peppler Equation (81)	Lockhart-Martinelli Equations (77), (78)	Wallis Equation (57)
$G_v = 10$	30	4.08	0.29	0.93
	60	7.83	0.75	1.70
	100	9.98	0.72	2.74
	140	9.72	1.24	3.77
$G_v = 50$	30	1.02	0.08	0.30
	60	1.92	0.085	0.55
	100	2.46	0.094	0.89
	140	2.42	0.19	1.22

Table II Comparison of interfacial friction factors obtained with application of the Peppler, Lockhart-Martinelli and Wallis correlations.

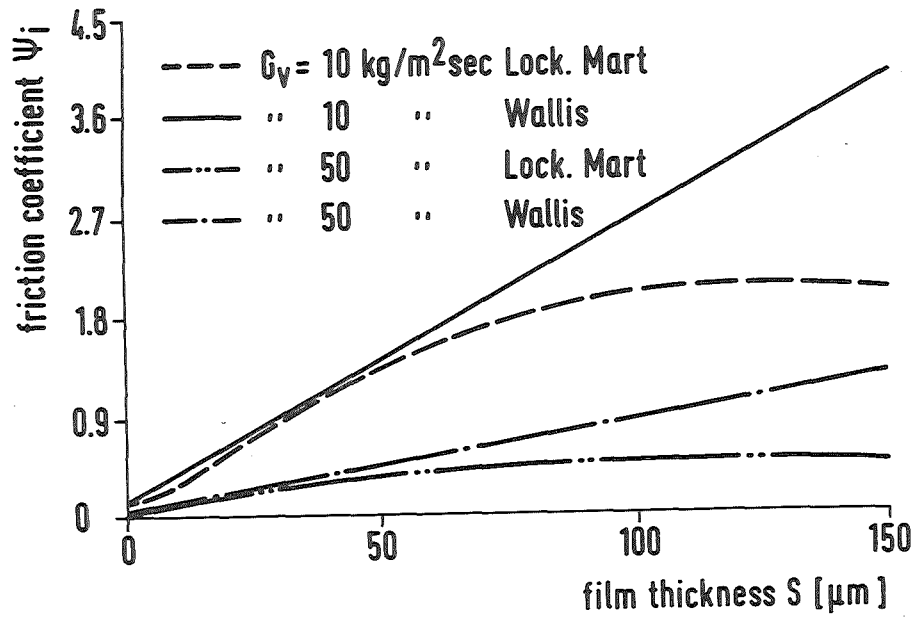


Fig. 8

Fig. 8 - Comparison between interfacial friction coefficients calculated with the Wallis formula and with the Lockhart-Martinelli correlation versus liquid film thickness. (Geometry of SCARABEE experiments /3/).

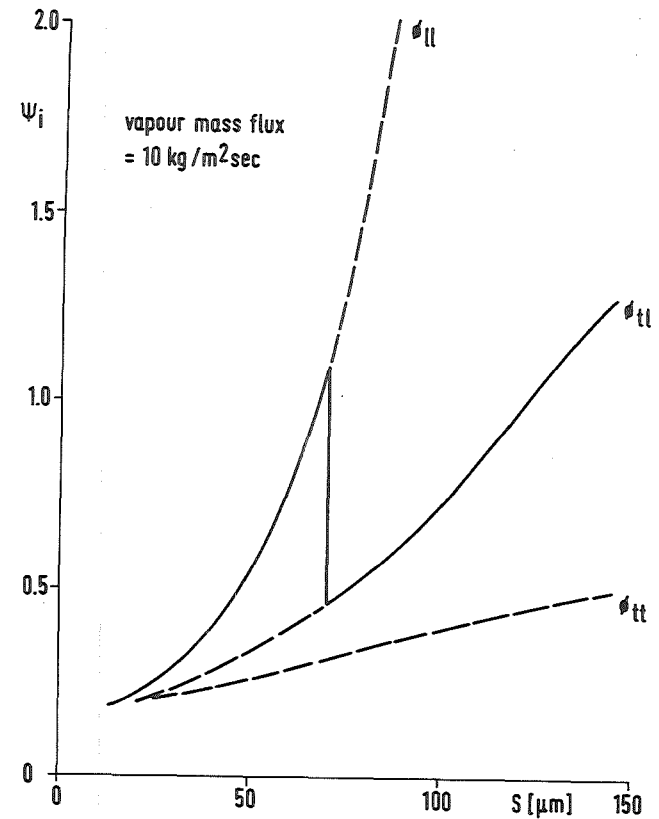


Fig. 9

Fig. 9 - Interfacial friction coefficients between liquid film and vapour versus liquid film thickness (for vapour mass flux $G_v = 10 \text{ kg/m}^2\text{sec}$)

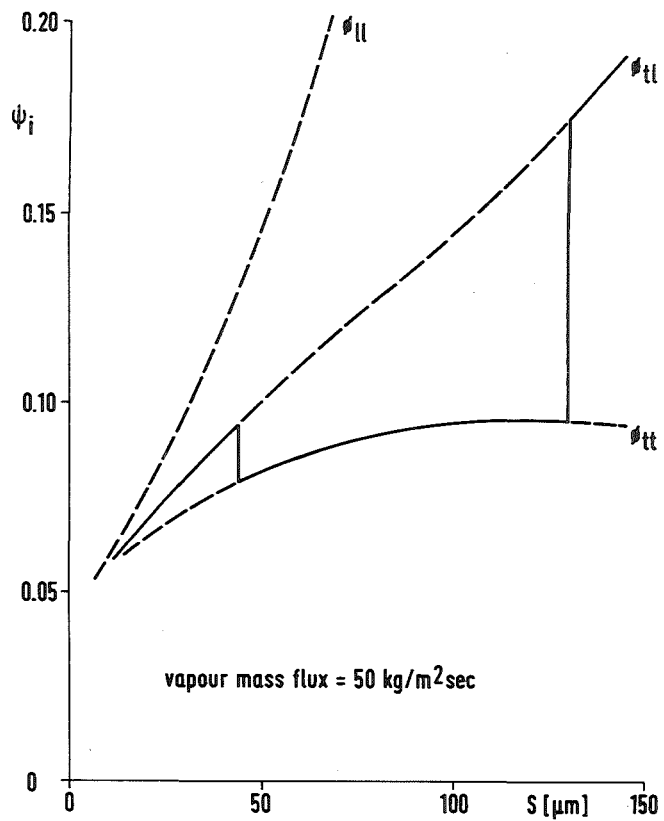


Fig. 10

Fig. 10 - As above with $G_v = 50 \text{ kg/m}^2\text{sec}$

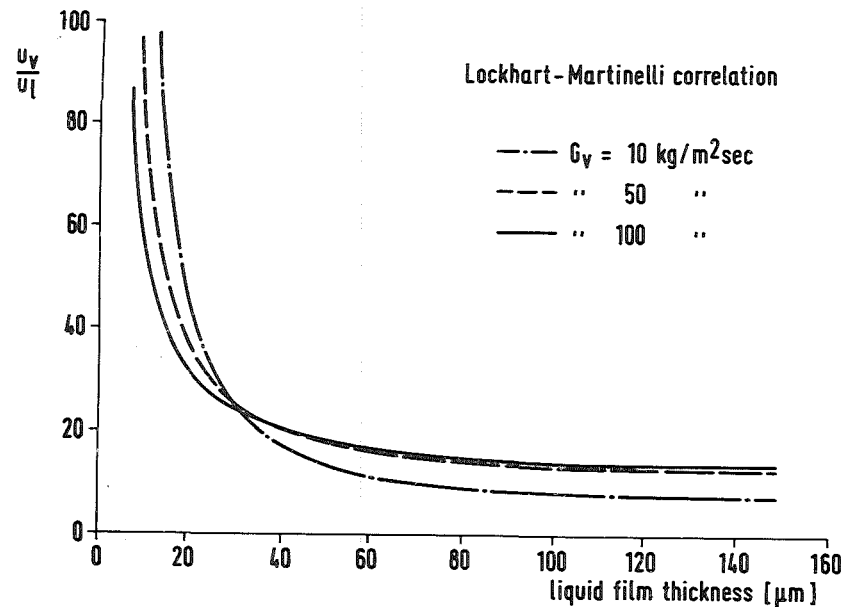


Fig. 11

Fig. 11 - Ratio vapour to liquid film mean velocity versus liquid film thickness (Results obtained with the Lockhart-Martinelli correlation)

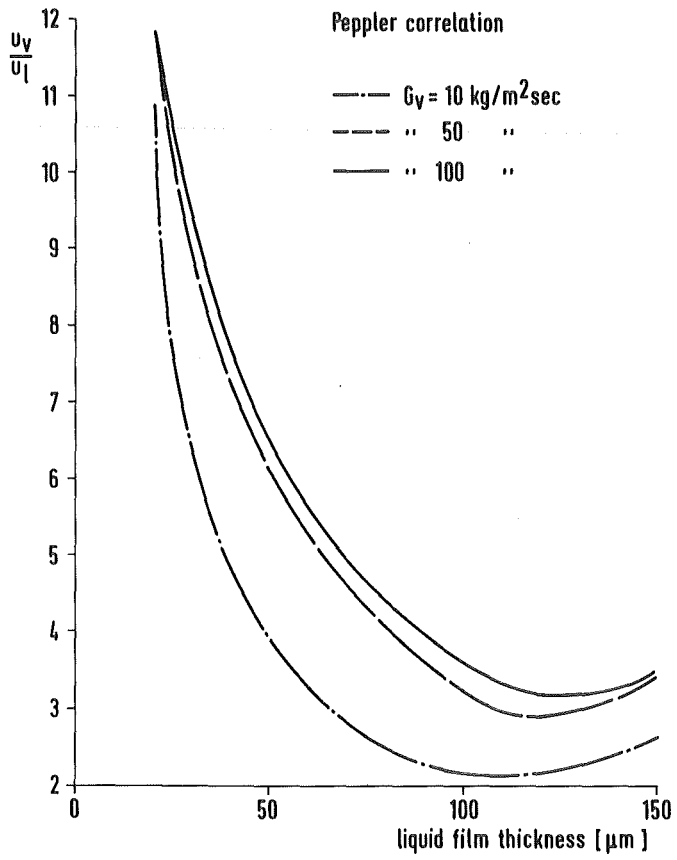


Fig. 12

Fig. 12 - As above (Results obtained with the Pepler correlation)

2.3.6 Some considerations about turbulent heat transfer through liquid film

According to the model discussed in reference /23/, the liquid film can be separated into a laminar sublayer flowing at the wall (called base-film) and a turbulent layer moving over the base film. The transition between laminar and turbulent subregions has been assumed to correspond to the critical dimensionless distance from the wall $y_{cr}^+ = yu^*/\nu = 20$. For a film of dimensionless thickness $S^+ = Su^*/\nu$ smaller than y_{cr}^+ the heat transfer coefficient is determined by conduction through the laminar sublayer:

$$h_1 = \frac{\lambda}{S} \quad (83)$$

For a fully developed liquid film, consisting of both laminar and turbulent subregions, the equations for momentum and heat transfer can be written as:

$$\tau = \rho_1 (\nu + \nu_\epsilon^*) \frac{du}{dy} \quad (84)$$

$$q = \rho_1 c_{p1} (\alpha^2 + \alpha_\epsilon^2) \frac{dT}{dy} \quad (85)$$

where ν_ϵ^* and α_ϵ^2 are the eddy diffusivities for momentum and heat transfer respectively.

Letting T_H and T_V be the clad (or structure) surface temperature and the vapour temperature, integration of (85) over the film thickness S yields:

$$q \int_0^S \frac{1}{\alpha^2 + \alpha_\epsilon^2} dy = \int_{T_H}^{T_V} \rho_1 c_{p1} dT \approx \rho_1 c_{p1} (T_V - T_H) \quad (86)$$

when the physical properties of the liquid film are considered constant over its thickness.

Defining an overall heat transfer coefficient h through the liquid film by

$$q = h(T_H - T_V) \quad (87)$$

and comparing with (86) one has

$$h = \frac{\rho_1 c_{p1}}{\int_0^S \frac{dy}{\alpha^2 + \alpha_\epsilon^2}} = \frac{\nu \rho_1 c_{p1}}{\int_0^S \frac{1}{\frac{1}{Pr} + \frac{\nu_\epsilon/\nu}{Pr_t}} dy} \quad (88)$$

where $Pr = \nu/\alpha^2$ and $Pr_t = \nu_\epsilon/\alpha_\epsilon^2$ are the molecular Prandtl number and the turbulent Prandtl number respectively.

In terms of dimensionless quantities the above equation becomes:

$$h = \frac{\rho_1 c_{p1} u^*}{\int_0^{S^+} \frac{1}{1/Pr + (\nu_\epsilon/\nu)/Pr_t} dy^+} \quad (89)$$

Equation (88) reduces to (83) for a thin film consisting only of the laminar sublayer as in this case α_ϵ^2 is negligible compared to α^2 . The heat transfer coefficient h can therefore be split into two terms, the laminar one h_1 , and a "turbulent" term h_t defined by

$$h_t = \frac{\nu \rho_1 c_{p1}}{\int_{y_{cr}}^S \frac{dy}{\frac{1}{Pr} + \frac{\nu_\epsilon/\nu}{Pr_t}}} \quad (90)$$

where the integral is computed over the thickness of the turbulent layer of the film. It holds then

$$\frac{1}{h} = \frac{1}{h_1} + \frac{1}{h_t} \quad (91)$$

which is equivalent to the direct application of equation (89). Equation (89) has been applied in test cases under the assumption that the ratio of the eddy diffusivity for momentum transfer ν_ϵ to that for heat α_ϵ^2 (the turbulent Prandtl number) is constant. A parametrical analysis has been performed varying the turbulent Prandtl number in the range 0.8 - 1.5 and comparing the resulting overall heat transfer coefficient with the value which

would be derived by applying eq. (83) to the full film thickness. It has been shown that the resulting heat transfer coefficient is very sensitive to relatively small changes of Pr_t , increasing rapidly as Pr_t decreases. The value $Pr_t = 1.5$ has been eventually chosen as it is applicable for fluids with low molecular Prandtl numbers. Results of test calculations performed with $Pr_t = 1.5$ are shown in the following Table III for some values of the vapour mass flux and of the liquid film thickness.

These results show that the heat transfer coefficient through a turbulent liquid film with Reynolds number between 10^3 and 2×10^3 , calculated taking into account the contribution of the laminar and turbulent sublayers may exceed by roughly 10 to 50 per cent the figures obtained by applying the simple conduction law ($h = \lambda/S$) to the full film thickness.

In the liquid film model discussed in the above mentioned reference /23/ which anyway refers to fluids with molecular Prandtl number >1 , a wavy film shape is also taken into account. This leads to the conclusion that "the turbulent contribution to the overall heat transfer coefficient ranges from about 45 - 90 percent of the total". The influence of the wavy film shape has not been investigated at KfK as its modelling would not be applicable (without large programme modifications) to the BLOW-3A code.

The above results must be interpreted only as a qualitative indication of the influence of turbulence of the liquid film on the overall heat transfer coefficient. It must be remarked once again that results are very sensitive to some parameters like the turbulent Prandtl number and the eddy diffusivity.

	α	u_v (m/sec)	u_1 (m/sec)	$Re_v = \frac{\rho_v u_v D_{hv}}{\mu_v}$	$Re_1 = \frac{4Sp_1 u_1}{\mu_1}$	$\bar{h} = W/m^2 \text{ } ^\circ C$	$h_1 = \frac{\lambda}{S} x$ $x = 10^{-5}$	h from (89) $x = 10^{-5}$
<hr/>								
$G_v = 50 \text{ kg/m}^2 \text{ sec}$								
S = 100	0.73	75.5	3.41	6375	6869	5.64	5.93	
S = 150	0.60	75.5	3.65	5885	11021	3.77	4.34	
<hr/>								
$G_v = 100 \text{ kg/m}^2 \text{ sec}$								
S = 100	0.73	150.9	6.34	12752	12777	5.64	6.81	
S = 150	0.60	150.9	6.56	11769	19824	3.77	5.57	
<hr/>								

Table III Comparison between heat transfer coefficient across liquid film based on the conduction approximation ($h_1 = \lambda/S$) and based on the separate contributions of laminar and turbulent sublayers.

2.4 Calculation of temperature distributions in fuel and clad during melting or solidification

The temperature distributions in the fuel and clad during melting or solidification are calculated in the subroutines KOPHI and KOPHIH respectively using essentially the same model, as explained hereafter.

Let the fuel or clad material of an axial mesh be concentrated in N discrete nodes and

$$m_i = \rho_i V_i \quad (i = 1, \dots, N) \quad (1)$$

be the mass corresponding to one node. Let F_h denote the fusion heat necessary to melt the unit mass of material. The total amount of energy necessary to melt the material associated to node i will then be

$$E_i = F_h m_i = F_h \rho_i V_i \quad (2)$$

Let T_f denote the fusion temperature and $T_{i,n}$ the temperature of node i resulting from normal computation of the temperature distribution at time step t_n . If $T_{i,n}$ is greater than the melting temperature T_f a correction is applied as long as the energy production in that node integrated since start of melting is smaller than the fusion heat. In this case it is assumed that $T_{i,n}$ remains at the melting temperature T_f . The computed temperature increment

$$\Delta T_{i,n} = T_{i,n} - T_f \quad (3)$$

(positive while melting, negative during solidification) corresponds to an amount of energy

$$\Delta Q_{i,n} = \rho_i c_{pi} \cdot \Delta T_{i,n} \quad (4)$$

per unit volume which is not spent by rising the clad temperature, but absorbed as latent heat during the melting process. The energy $\Delta Q_{i,n}$ computed for time step t_n is normally far below the total energy E_i necessary to melt the mass of material associated to node i; it is therefore stored from the very first time step, say n_0 , at which $\Delta T_{i,n}$ was found to be positive and the resulting sum for the volume V_i .

$$S_i = \sum_{n_0}^n Q_{i,n} V_i \quad (5)$$

is compared to E_i . When S_i becomes greater than E_i the mass m_i is completely molten; the clad temperature $T_{i,n}$ so far corrected down to T_f , from this time on rises again, and the energy amount $S_i - E_i$ accounts for a temperature increment

$$\frac{S_i - E_i}{\rho_i c_{pi}} \quad (6)$$

above T_f .

The percentage of the material associated to the node i , which is molten at time t_n is

$$w_i = S_i/E_i \quad (7)$$

The mean value over the volumes V_i gives the percentage of molten material for all the nodes of a given radial mesh:

$$\Omega = \frac{\sum_1^N i w_i \cdot V_i}{\sum_1^N i V_i} \quad (8)$$

A comparison between this discrete calculation model and an analytical treatment for the temperature distribution in the clad during melting has been presented in reference /6/.

Symbols used in this section

- N number of radial nodes of the fuel or clad mesh
- m mass (kg)
- V volume (m^3)
- ρ density (kg/m^3)
- c_p specific heat (J/kg $^{\circ}C$)

- T Temperature ($^{\circ}\text{K}$)
- T_f Fusion temperature ($^{\circ}\text{K}$)
- t time (sec)
- F_h Latent fusion heat (J/kg)
- E Energy (J)
- S Energy absorbed by the clad material during melting (or liberated during solidification) (J)
- Q Energy absorbed or liberated per unit volume (J/m^3)
- w percentage of molten clad material associated to a node (dimensionless)
- Ω percentage of total molten clad material of a radial mesh (dimensionless)

Subcripts

- i ($i = 1, 2, \dots, N$) refers to a mesh node
- n refers to time step t_n .

3. Further programme details

In this chapter are explained some topics which regard in general the programme organisation, like the time step control, or its applicability to peculiar experimental conditions. The simulation of a typical experimental rig is shown in section 3.3 together with the calculation of the equivalent heat transfer coefficient from the structure outer surface to a surrounding medium. The way of simulating a (generally undesired) leakage of coolant through a path in parallel with the main flow is dealt with in section 3.4.

The calculation of geometrical data for an equivalent channel representing in the one-dimensional approximation a subchannel of a bundle is explained in section 3.5 on the basis of a practical case. This example of application is intended to serve as a guideline for the user in the preparation of input data regarding the geometrical configuration.

Further programme details are explained in Section III.2 together with the description of the Subroutine in which the calculation is performed. The most important among these are:

- Numerical treatment of the vapour energy equation for the determination of integral values of vapour pressure and temperature. See description of Subroutine ENBL.
- Correction of vapour pressure and temperature distributions along the bubble length to achieve consistency with integral values. See description of Subroutine ITSØL.
- Calculation of heat transfer coefficient coolant-structure assuming a linear temperature distribution across the structural layer. See description of Subroutine AKTST.
- An explanation of data printed-out onto the paper hard copy is given in the description of the Subroutines STATO (steady state data) and AUSGAB (transient data).

3.1 Time step control

For numerical integration of the transient equations two different time step levels have been introduced in the BLOW-3A programme: A macro and a micro time step level. The macro time step defines those time-points in which all variables are calculated which determine input and boundary conditions by time dependent functions e.g. power density, inlet/outlet pressure of the coolant channel, coolant inlet temperature, pressure drop coefficient of the inlet orifice, thermal conditions at an external by-pass. Along a macro time step a linear variation of the relevant variables between the calculated point values is assumed. The macro time step is determined by input. Three different values can be chosen dependent on the integration time. Two refer to the macro time step in single phase flow conditions. One is applied for times less than an input value t_{Rampe} and the other one if the actual time is larger than t_{Rampe} . The third macro time step refers to times during the integration if two phase flow conditions have been achieved. The macro time step is internally modified if single phase flow conditions approach boiling onset at the prespecified value of superheat at one axial mesh of the coolant channel. To reach this time as exactly as possible it is checked in a predictor step whether the prespecified superheat may be exceeded locally at any axial location in the coolant channel. For this predictor step it is assumed that the time derivative from the last integration step remains constant along the next macro time step. If the prespecified superheat is exceeded at any local position of the coolant channel, the macro time step is reduced in such way that at the end of the macro time step the conditions for boiling initialization are just met.

Each macro time step can be subdivided into several micro time steps which are applied for integration of the mass conservation, energy and momentum equations. In single phase flow conditions the micro time step has been fixed to be not larger than 0.05 sec. Though the numerical solution scheme of the single phase flow equations is unconditionally stable in case of constant properties it has been proven necessary to limit the integration time step. This is due to numerical reasons as propagation of round-off errors and due to non-linearities introduced by temperature dependent properties. In case of calculations for two-phase flow conditions an automatic procedure has been implemented adjusting an optimum micro time step for integration of the mass conservation, energy and momentum equations. Two types of criteria are applied:

1. Adjustment of the time step due to physical phenomena
2. Adjustment of the micro time step due to the convergence behaviour of the integration scheme.

To 1) Determination of an appropriate micro time step due to physical phenomena refers to four criteria:

- the maximum volume change of a bubble during one micro time step normally should not be larger than 10%
- a bubble interface should not move axially in one micro time step more than the length of the smallest axial Euleria mesh of the coolant channel
- if axial pressure gradients in the two phase flow zone are larger than $1.0E + 05 \text{ N/m}^2/\text{m}$ the micro time steps should not exceed 1 msec
- if the average pressure inside one bubble is expected to change by more than 5% during a micro time step, the micro time step is halved.

To 2) Determination of an appropriate micro time step for integration due to the convergence behaviour of the integration scheme:

- if more than five iterations of the energy and momentum equations have been necessary in the preceding micro time step the next micro time step is halved.
- if less than three iterations of the energy and momentum equations have been necessary in the preceding micro time step the micro time step is doubled.

Relevant checks for the micro time step control are made in the subroutines ITCB and LITCB respectively. The micro time step is calculated in the subroutine STEP in such a way that it exactly fits into the macro time step sequence.

3.2 Heat and mass exchange between upper liquid slug and coolant in upper plenum.

For determination of the temperature variation in the uppermost axial segment of the test section, it is necessary to calculate coolant temperatures in the plenum above it. In BLOW-3A the following procedure has been adopted:

1. Above the test section a control volume V_c is defined, characterizing the amount of liquid sodium in the upper plenum taking part in the heat and mass exchange process

$$V_c = RLA \cdot AR \text{ (NM}^2\text{)}$$

RLA: effective reduced length taking into account the inertia of the liquid sodium above the test section (input parameter)

AR(NM²): flow cross section of the uppermost axial segment of the test section.

As initial coolant temperature in the control volume is taken the stationary coolant outlet temperature.

2. It is assumed that enthalpy and mass exchange of the control volume with the moving upper slug takes place only via convective mass flow variations in axial direction. Mixing effects in radial direction inside the upper plenum are neglected.
3. Above the control volume a coolant plenum temperature is specified by input and is kept constant during the transient phase.
4. Along the control volume the coolant temperature variation is taken to be S shaped with upper and lower boundary values which depend on the mass flow direction (see following sketch).
5. If a bubble extends into the upper control volume its temperature is kept at the last calculated value. This means that the enthalpy change in the control volume due to vapour flow is neglected.

6. If liquid sodium enters the test section from the upper plenum the coolant temperature is set to the transiently calculated temperature in the control volume.

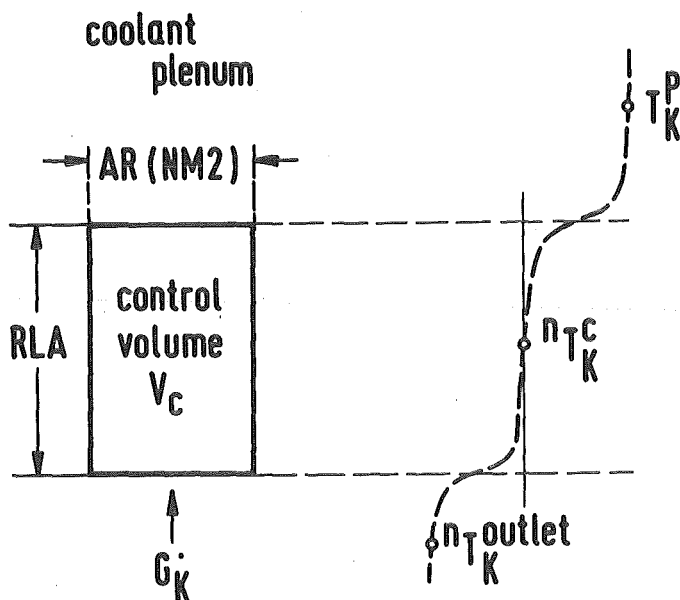


Fig. 13: Sketch showing the control volume V_c for heat and mass exchange in upper plenum.

With these assumptions the energy equation for the upper control volume is solved:

$$\rho_K^c \frac{\partial H_K^c}{\partial t} + G_K \frac{\partial H_K^c}{\partial z} = 0 \quad (1)$$

Integration over the control volume V_c and an implicit time discretization lead to the following expression:

$$\rho_K^c V_c \left({}^{n+1}H_K^c - {}^nH_K^c \right) / \Delta t_n + G_K^{n+1} F_c \left({}^{n+1}H_K^{c,U} - {}^{n+1}H_K^{c,L} \right) = 0 \quad (2)$$

with $F_c = V_c / \Delta t$. The indexes U, L refer to the upper and lower coolant volumes bounding the control volume V_c .

Taking all values of specific heat to be the same and constant over the time step this equation reduces to:

$$\rho_K^c V_c (T_K^{c,n+1} - T_K^c) / \Delta t_n = - G_K F_c (T_K^{c,U,n+1} - T_K^{c,L,n+1}) = 0 \quad (3)$$

hence:

$$T_K^{c,n+1} = T_K^c - \frac{G_K F_c \Delta t_n}{\rho_K^c V_c} (T_K^{c,U,n+1} - T_K^{c,L,n+1}) \quad (4)$$

As initial condition it holds:

$$T_K^c (t=0) = T_K^{\text{outlet}} (t=0) \quad (5)$$

The boundary conditions are:

$$T_K^{c,U,n+1} = \begin{cases} T_K^c & \text{if } G_K \geq 0 \\ T_K^P & \text{if } G_K < 0 \end{cases} \quad (6)$$

$$T_K^{c,L,n+1} = \begin{cases} T_K^{\text{outlet}} & \text{if } G_K \geq 0 \\ T_K^c & \text{if } G_K < 0 \end{cases} \quad (7)$$

where T_K^P is the coolant plenum temperature.

3.3 Simulation of a typical experimental test rig and calculation of the heat transfer coefficient from the structure outer wall to a by pass flow.

An important problem which has to be solved for the correct interpretation of in-pile or out-of-pile experiments is the simulation of the experimental test rig by calculating an equivalent heat transfer coefficient for the heat losses beyond the structure outer surface. As an example of this calculation, let a number $l = 1, 2, \dots, L$ of layers of known physical properties separate the pin (or bundle) from a by pass flow as represented in the sketch of Fig. 14, the layer $l = 1$ being the pin structure itself. Let one of this layers (for $l = \gamma$) be a vacuum gap!

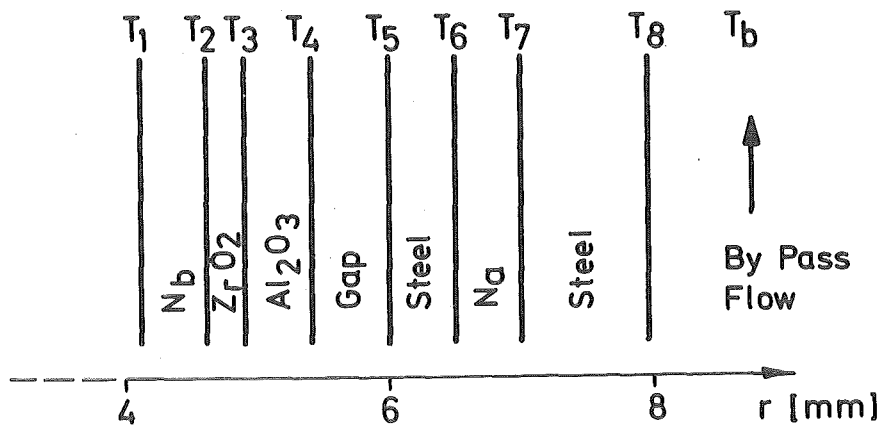


Fig. 14: Sketch showing a typical experimental test rig to be simulated for the calculation of the heat transfer coefficient from structure to a by-pass flow. This geometrical configuration is typical for the SCARABEE experiments /3/.

For a steady state situation with heat flux q flowing outside the structure outer surface the overall heat transfer coefficient can be calculated as follows: let r_i , T_i be the radius and temperature of the inner cylindrical surface of the i -th layer and λ_i its thermal conductivity; T_b the temperature of the by pass flow. Assuming that the vacuum gap surfaces behave like a gray body with integral emissivities ϵ_γ , $\epsilon_{\gamma+1}$, the overall thermal resistance per unit axial length is given by

$$R = \sum_1^{L+1} R_i \quad (8)$$

with

$$R_i = \frac{\ln(r_{i+1}/r_i)}{2\pi\lambda_i} = \frac{T_i - T_{i+1}}{q} \quad (i=1,2,\dots,L; i \neq \gamma) \quad (9)$$

and

$$R_\gamma = (T_\gamma - T_{\gamma+1})/q \quad (10)$$

The radiative heat flux is:

$$q_r = 2\pi r_\gamma F_\epsilon \sigma (T_\gamma^4 - T_{\gamma+1}^4) \quad (11)$$

when σ is the Stefan Boltzmann constant and

$$F_\epsilon = \left[\frac{1}{\epsilon_\gamma} + \frac{r_\gamma}{r_{\gamma+1}} \left(\frac{1}{\epsilon_{\gamma+1}} - 1 \right) \right]^{-1} \quad (12)$$

is the emissivity factor of the gap surfaces. In stationary conditions

$$q = q_r.$$

Assuming that the boundary temperatures T_1 and T_b are known, equation (11) together with

$$q \sum_1^{\gamma-1} R_i = T_1 - T_\gamma \quad (13a)$$

$$q \sum_{\gamma+1}^L R_i = T_{\gamma+1} - T_b \quad (13b)$$

forms a system of three equations for the unknowns q , T_γ , $T_{\gamma+1}$. Eliminating $T_{\gamma+1}$ and q one has:

$$\sum_0^\gamma c_j T_\gamma^j = 0 \quad (14)$$

where c_j depend only on the layers thermal resistances and on the boundary temperatures. Equation (14) can be solved numerically for T_γ assuming the bypass temperature constant and varying the structure inner temperature stepwise in the range expected to be covered during the transient calculation of a simulated accident (for instance, in the range 600 - 1200 °C). Results may be plotted as function of the variable $x = T_1 - T_b$ and approximated by means of a polynome in x . From the known T_γ equations (13) then yields the stationary heat flux q . An overall heat transfer coefficient can then be defined by

$$\alpha_S = \frac{q}{2\pi R_S (T_S - T_b)} \quad (15)$$

where $R_S = (R_1 + R_2)/2$ is the radius of the cylindrical surface through the structure mid point and $T_S \approx T_1$ is the bulk structure material temperature calculated in the code. Calculations for real cases are normally performed assuming $\epsilon_\gamma = \epsilon_{\gamma+1} \approx 0.8$ which applies to strongly oxidized gap surfaces.

In some cases the pin structure consists of several layers, for instance oxide shoop layers coating the structure material in order to reduce the thermal losses. As the code allows for only one structural material, the layers can be replaced by an equivalent one with the same thermal inertia and the physical properties of the main structural material. Letting R_i , R_{i+1} be the radii of the inner and outer surfaces of the i -th layer and ρ_i , c_{pi} its density and specific heat ($i=1$ referring to the main structural layer), the outer radius R_e of the equivalent structure is given by:

$$\rho_1 c_{p1} (R_e^2 - R_1^2) = \sum_{i=1}^N \rho_i c_{pi} (R_{i+1}^2 - R_i^2) \quad i=1, 2, \dots, N \quad (16)$$

where N represents the number of layers to be replaced by the equivalent one.

In case of a bundle structure similar considerations apply to the geometry of a properly defined equivalent channel (see section 3.5 for the definition of equivalent channels).

Due to the fact that the above calculation of the heat transfer coefficient refers to a steady state situation a correction must be applied for a transient calculation to take into account the thermal inertia of the structure material. To this purpose a modified time varying heat transfer coefficient is defined as follows: with reference to the symbols used in section II-6-2.1, the heat loss beyond the structure is given in the stationary case and per unit axial length by

$$Q_o = \frac{\alpha_{ww} F}{V_S} (T_{So} - T_w) \quad (17)$$

where T_{So} is the steady state structure temperature. In the transient state the heat loss is (assuming T_w constant):

$$Q(t) = \frac{\alpha_{ww} F}{V_S} [T_S(t) - T_w] \quad (18)$$

$Q(t)$ may be split into two terms, by introducing $\pm T_{So}$ into brackets:

$$Q(t) = \frac{\alpha_{ww} F}{V_S} [T_{So} - T_w] + \frac{\alpha_{ww} F}{V_S} [T_S(t) - T_{So}] = Q_o + Q_1(t) \quad (19)$$

where $Q_1(t)$ represents the increment of heat losses due to the temperature rise above the stationary value T_{So} . A correct computation of $T_S(t)$ implies a correct value of the heat transfer coefficient α_w and therefore a good estimation of $Q_1(t)$. Let introduce a time dependent parameter $\beta = 1 - e^{-\delta t}$, where δ is a constant to be estimated, and write the total heat losses as

$$Q(t) = Q_0 + \beta Q_1(t) = Q_0 + (1 - e^{-\delta t}) Q_1(t). \quad (20)$$

$\delta = 0$ implies $Q(t) = Q_0$ and therefore represent the limiting case of very large thermal inertia of the structure. Its temperature would not increase above T_{So} and the thermal losses would be kept to a minimum.

Large δ imply $\beta = 1$, hence the highest thermal losses, corresponding to a minimum of the structure thermal inertia.

Introducing β into (19) and re-arranging one derives:

$$Q(t) = \frac{F_w}{V_S} \left[T_S(t) - T_w \right] \alpha_w \cdot \left[1 - \frac{T_S(t) - T_{So}}{T_S - T_w} e^{-\delta t} \right] \quad (21)$$

Comparison with (18) shows that introducing the parameter β is equivalent to assume as heat transfer coefficient instead of α_w the corrected value:

$$\alpha_w^* = \alpha_w \left[1 - \frac{T_S(t) - T_{So}}{T_S - T_w} e^{-\delta t} \right]. \quad (22)$$

A good evaluation of the heat transfer coefficient has been reached in most cases with δ ranging from 0.01 to 2.

This time-dependence of the heat transfer coefficient has to be programmed in the subroutine WWST.

3.4 Leakage Flow representation

The presence of an unwanted leakage flow in parallel to the main coolant flow, which may characterize some experiments, can be taken into account in a separate submodule of the programme (called BYPASS, with some related sub-routines). It calculates the effects of the leakage flow by considering a variable pressure drop coefficient in the inlet valve under the assumption that friction pressure drops in the leakage path dominate the acceleration pressure drops.

Letting G_c , G_l , G_t be the channel, leakage and total mass flow rate respectively, it holds

$$G_t = G_c + G_l \quad (23)$$

Without representation of the leakage flow the inlet valve pressure drop would be calculated as

$$\Delta p_{Bl} = \zeta \frac{G_c |G_c|}{2\rho} \quad (24)$$

while the real pressure drop is

$$\Delta p_{Bl, real} = \zeta \frac{G_t |G_t|}{2\rho} = \zeta \frac{|G_c + G_l| (G_c + G_l)}{2\rho} \quad (25)$$

which can be written

$$\Delta p_{Bl, real} = \zeta_e \frac{G_c |G_c|}{2\rho} \quad (26)$$

with the definition of an "equivalent" inlet valve pressure drop coefficient

$$\zeta_e = \zeta \frac{(G_c + G_l) |G_c + G_l|}{G_c |G_c|} \quad (27)$$

The pressure drop across the inlet valve is therefore larger than it would be calculated if the leakage path were neglected.

3.5 Definition of one-dimensional channels equivalent to several sub-channels of a pin bundle.

This section illustrates with a practical example the application of the computer programme BLOW-3A to the calculation of a multi-pin bundle by means of a proper definition of one-dimensional channels equivalent to several subchannels of the bundle. Emphasis is given to the calculation of equivalent geometrical data. The following explanation is intended to serve as a guide-line for a user willing to use the programme for similar applications.

Data for the following example are taken from the out-of-pile 7-pin bundle experiments carried out in the NSK loop at KfK and documented in reference /24/. Results of the theoretical interpretation of these electrically heated experiments with the computer programme BLOW-3A have been presented in /5/. The experiments belong to a series of test runs performed in the framework of the SNR-300 development and simulating a failure of the electrical power supply to the pumps of a fast reactor. The way of defining equivalent channels is essentially the same also for in-pile experiments and for reactor subchannels.

Let refer, for convenience, to a particular experiment, 7-2/16, of the above series characterized, in the steady state, by the following data:

outlet pressure	1.52 bar
inlet pressure	4.18 bar
inlet flow velocity	3.0 m/sec
inlet temperature	562 °C
outlet temperature	735 °C
pin power	16.8 KW
heated section length	0.6 m
linear power	281 W/cm
heat flux	150.3 W/cm ²

Geometrical data:

pin diameter	6 mm
pitch	7.9 mm
thickness of hexagonal wrapper	1.5 mm
central subchannels cross section/hydraulic diameter D_h	12.88 mm ² /5.47 mm

peripheral subchannels cross section/ D_h	18.72 mm ² /4.32 mm
corner subchannels cross section/ D_h	5.05 mm ² /2.61 mm
Full bundle cross section/ D_h	219.90 mm ² /4.25 mm
unheated pin length above the heated section	455 mm

One wants to define two equivalent channels for the simulation with the computer programme, the first (referred to as KKN = 1) equivalent to the six central subchannels of the bundle, the second (referred to as KKN = 2) equivalent to the full bundle.

A) Calculation of input data for the equivalent channel KKN = 1

The six inner subchannels are powered by the central pin, plus six time one third of the peripheral pins thus making three times the power of a single pin. The area of the six inner subchannels is therefore divided by three to get the area of one equivalent channel (powered by one pin). The area of the peripheral subchannels (also divided by three) is considered as "structure" material and replaced for the calculation by an "equivalent steel" volume (V_S) with the same thermal inertia of the flowing sodium

$$V_S \rho_S c_{p_S} = V_{Na} \rho_{Na} c_{p_{Na}} \quad (28)$$

The electrical heaters are replaced for the calculation by an ideal fuel material with physical properties carefully determined by volume averaging the properties of the several material with which the heaters were built. Details of the calculation of the physical properties of the equivalent fuel material are not reported here as they are not essential for the definition of geometrical data of the equivalent channels.

In the following the superscript "t" refers to total number of real subchannels and the superscript "e" refers to the equivalent subchannel. The index K refers to the coolant and S to the structural material.

With reference to the input description (Card 17 of the Input Data, see Section III.4) the equivalent geometrical data are defined as follows.

i) Meshes between NMO and NM1 inclusive (NMO < M < NM1)

- RBR = 2.4×10^{-3} m (real value)
- DCAN = 0.6×10^{-3} m (real value)
- RKUE is calculated as follows:

The cross section of the inner six subchannels is

$$F_K^t = 6 \times 12.88 \times 10^{-6} = 77.28 \times 10^{-6} \text{ m}^2$$

The cross section of the equivalent channel is

$$F_K^e = \frac{F_K^t}{3} = 25.8 \times 10^{-6} \text{ m}^2 = AR$$

The outer radius of the equivalent ring channel is given by the equation

$$\pi(RKUE^2 - (RBR + DCAN)^2) = F_K^e = 25.8 \times 10^{-6} \text{ m}^2$$

which yields

$$RKUE = 4.15 \times 10^{-3} \text{ m}$$

- VSTRUK

The volume of steel equivalent to the sodium in the six peripheral subchannels is given per unit axial length by

$$V_S^t \rho_S c_{p_S} = V_{Na} \rho_{Na} c_{p_{Na}}$$

Inserting the values of ρ and c_p calculated at a proper reference temperature and

$$V_{Na} = 6 \times 18.72 \times 10^{-6} \frac{\text{m}^3}{\text{m}}$$

one has

$$V_S^t = 26.6 \times 10^{-6} \frac{\text{m}^3}{\text{m}}$$

hence

$$VSTRUK = V_S^e = \frac{V_S^t}{3} = 8.9 \times 10^{-6} \text{ m}^2$$

- VDUF

The energy exchange between the coolant in the six inner subchannels and the equivalent structural material occurs through the surface of separation between inner and peripheral subchannels which, per unit axial length, is

$$F_S^t = 6 \times 1.9 \times 10^{-3} \frac{\text{m}^2}{\text{m}}$$

hence

$$F_S^e = \frac{F_S^t}{3} = 3.8 \times 10^{-3} \text{ m}$$

and by definition

$$VDUF = \frac{V_S^e}{F_S^e} = \frac{8.9 \times 10^{-6}}{3.8 \times 10^{-3}} = 2.34 \times 10^{-3} \text{ m}$$

- DBOND = 1.0×10^{-6} m (assumed value)
- FWFS = 1.14 (as for channel KKN = 2 (see later) for which a geometrical definition is straightforward).

ii) Meshes with index M < NMO

Geometrical data are calculated as above, apart from VSTRUK and VDUF for which the volume of the central pin is also taken into account. Indicating within apices the modified values one has:

$$- \text{VSTRUK} = V_S^{e'} = V_S^e + \pi \cdot (RBR + DCAN)^2 = 37.2 \times 10^{-6} \text{ m}^2$$

$$- \text{VDUF} = \frac{V_S^{e'}}{F_S^e + 2\pi(RBR + DCAN)} = 1.64 \times 10^{-3}$$

iii) Meshes with index M > NM1

These meshes simulate the experimental rig above the top end of the unheated section of the pins. The area corresponding to three times the pin cross section becomes now available for the coolant flow, in addition to the area of the inner subchannel.

- RBR input as in case i) but not used for these meshes
- DCAN input as in case i) but not used for these meshes
- RKUE

One has

$$\begin{aligned} F_K^t &= 6 \times 12.88 \times 10^{-6} + 3 \times \pi(RBR + DCAN)^2 = \\ &= 162.1 \times 10^{-6} \end{aligned}$$

$$F_K^e = \frac{F_K^t}{3} = 54.05 \times 10^{-6} \text{ m}^2 = AR$$

and the equation

$$\pi(RKUE^2 - (RBR + DCAN)^2) = F_K^e$$

yields

$$RKUE = 5.12 \times 10^{-3} \text{ m}$$

- VSTRUK

To the area of the peripheral channels must now be added the area corresponding to four times the pin cross section. This resulting area has to be converted into equivalent steel surface (volume per unit length) by multiplying it by the ratio $\frac{\rho_{Na} c_{pNa}}{\rho_S c_{pS}} \approx 0.237$. Taking also into account the corner sub-channels one has

$$\begin{aligned} V_S^t &= \{6x (\text{Area of peripheral channel}) + 6x (\text{Area of corner channel}) \\ &\quad + 4x (\text{Pin cross section})\} \frac{\rho_{Na} c_{pNa}}{\rho_S c_{pS}} = \\ &= \{6 (18.72 + 5.05) \times 10^{-6} + 4 \cdot \pi \cdot 3^2 \times 10^{-6}\} 0.237 \\ &\approx 60.6 \times 10^{-6} \text{ m}^2 \end{aligned}$$

hence

$$VSTRUK = V_S^e = \frac{V_S^t}{3} = 20.2 \times 10^{-6} \text{ m}^2$$

- VDUF

Considering that the surface through which the heat exchange occurs is now (per unit axial length) six times the pitch one has:

$$\begin{aligned} F_S^t &= 6 \times 7.9 \times 10^{-3} \\ F_S^e &= \frac{F_S^t}{3} = 15.8 \times 10^{-3} \text{ m} \end{aligned}$$

hence

$$VDUF = \frac{V_S^e}{F_S^e} = \frac{20.2 \times 10^{-6}}{15.8 \times 10^{-3}} = 1.28 \times 10^{-3} \text{ m}$$

- DBØND input as in case i) but not used for these meshes.
- FWFS = 1.14 (see explanation for KKN = 2)

B) Calculation of input data for the equivalent channel KKN = 2

i) Meshes between NMO and NM1 inclusive (NMO ≤ M ≤ NM1)

- RBR = 2.4×10^{-3} m (real value)
- DCAN = 0.6×10^{-3} m (real value)
- RKUE

The full bundle cross section is

$$F_K^t = 219.9 \times 10^{-6} \text{ m}^2$$

which must now be divided by seven to get the cross section of one equivalent channel

$$F_K^e = \frac{F_K^t}{7} = 31.4 \times 10^{-6} \text{ m}^2 = AR$$

The equation

$$\pi(RKUE^2 - (RBR + DCAN)^2) = F_K^e = 31.4 \times 10^{-6}$$

yields

$$RKUE = 4.36 \times 10^{-3} \text{ m}$$

- VSTRUK

The real volume of the hexagonal wrapper (length $\approx 6 \times 12.7$ mm; thickness = 1.5 mm) is now taken into account:

$$V_S^t = 6 \times 12.7 \times 1.5 \times 10^{-3}$$

$$VSTRUK = V_S^e = \frac{V_S^t}{7} = 16.3 \times 10^{-6} \text{ m}^2$$

- VDUF

The structure inner surface is

$$F_{S_2}^t = 6 \times 12.7 \times 10^{-3} \text{ m}$$

hence

$$F_{S_2}^e = \frac{F_{S_2}^t}{7} = 10.9 \times 10^{-3} \text{ m}$$

$$VDUF = \frac{V_{S_2}^e}{F_{S_2}^e} = \frac{16.3 \times 10^{-6}}{10.9 \times 10^{-3}} = 1.49 \times 10^{-3} \text{ m}$$

- DBØND = 1.0×10^{-6} m (assumed value)

- FWFS

The outer and inner structure surfaces are distant 12.5 and 11.0 mm respectively from the central pin axis, hence

$$FWFS = \frac{12.5}{11} = 1.14$$

ii) Meshes with index M < NMO

Geometrical data are calculated as above, apart from VSTRUK and VDUF for which again the volume of the central pin is now taken into account. Indicating with apices the new values one has:

- VSTRUK = $V_S^{e'}$ = $V_S^e + \pi(RBR + DCAN)^2 = 44.6 \times 10^{-6} \text{ m}^2$

- VDUF = $\frac{V_S^{e'}}{F_S^e + 2\pi(RBR + DCAN)} = 1.50 \times 10^{-3}$

) Meshes with index M>NM1

The only input value which differs from the previous ones is RKUE which is calculated taking into account that the full cross section is now available for the coolant flow.

- RKUE

$$F_K^t = (\text{Bundle cross section}) + 7 \times (\text{pin cross section}) = 420 \times 10^{-6} \text{ m}^2$$

$$F_K^e = \frac{F_K^t}{7} = 60. \times 10^{-6} \text{ m}^2 = \text{AR}$$

and the equation

$$\pi(\text{RKUE}^2 - (\text{RBR} + \text{DCAN})^2) = F_K^e$$

yields

$$\text{RKUE} = 5.28 \times 10^{-3} \text{ m}$$

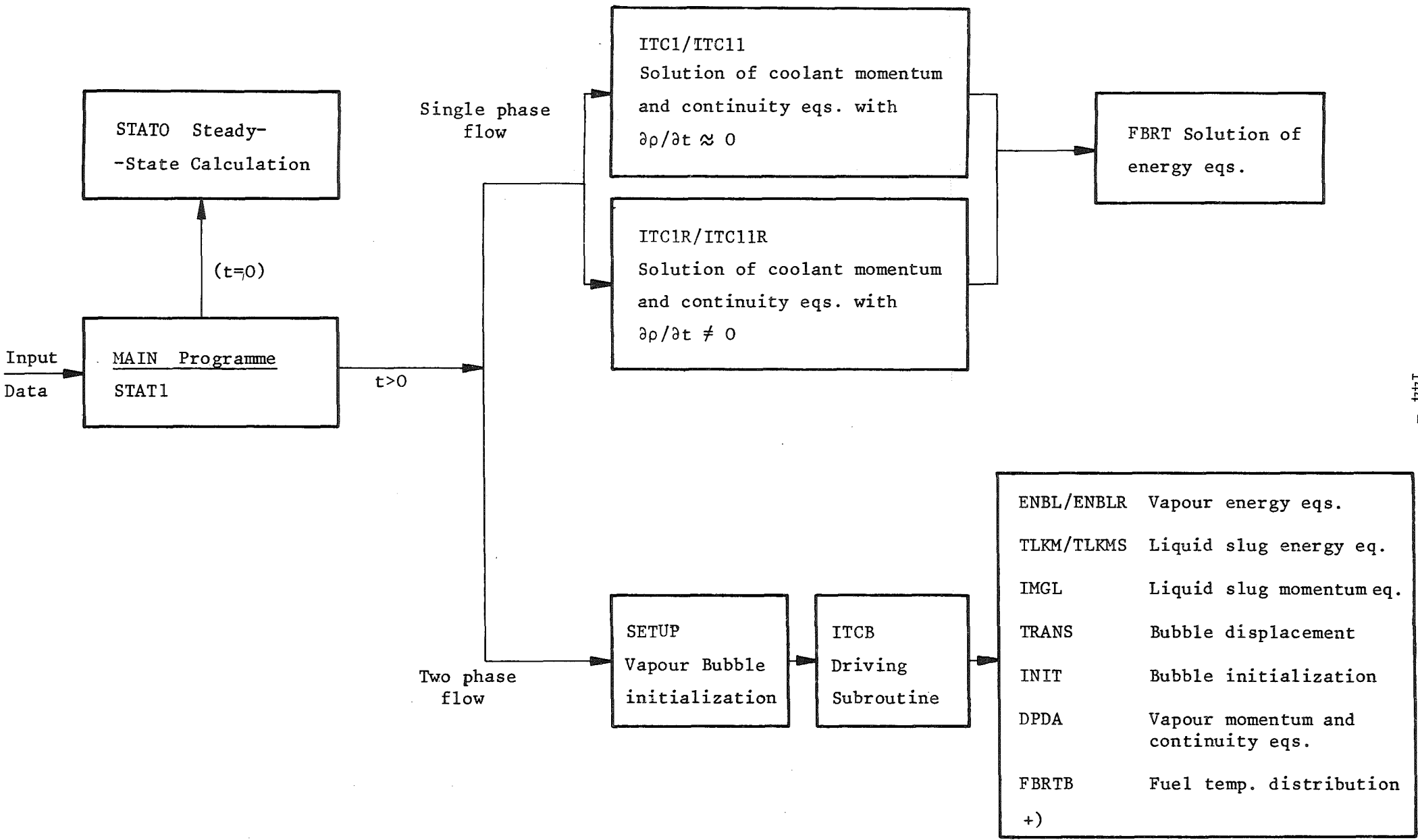


Fig. 15: General block diagram of BLOW-3A

(+) See Description of Subroutine ITCB for further details)

PART III - CODE STRUCTURE

1. General Structure of the Computer Programme

1.1 Main organization

The block diagram of Fig.15 shows the programme organization.

The main driving programme, called STAT1, transfers the control to other subprogrammes according to the stage of the calculation, drives the management of data for the different channels as well as the print-out of data, creation of files for plotting facilities and terminates the calculation when the allowed CPU time is running out.

The programme control is transferred to the Subroutine STATO for reading input data and performing the stationary calculation.

For the single phase flow calculation the programme control is transferred to the Subroutines ITC1R, ITC11R (or alternatively ITC1, ITC11 if a simplified solution of the continuity equation is sufficient) which are coupled to the Subroutine FBRT for the calculation of the fuel temperature distribution.

The very first bubble initialization, at boiling inception is performed in Subroutine SETUP.

The main driving subprogramme for the two-phase calculation is the Subroutine ITCB. At the end of the explanation of the tasks performed by Subroutine ITCB (section 2.1) is given a list which shows the sequence of subprogrammes called by it.

1.2 List of Subroutines and Functions

The subroutines of BLOW-3A are listed hereafter in two groups, in alphabetical order within each group.

GROUP 1 contains all the "basic" subroutines which do not need to be modified by the programme user for simulating his peculiar problem.

GROUP 2 contains the "problem oriented" subroutines which must be modified by the user for his problem, unless the optional version is applicable. This group is split into two subgroups:

- a) containing "general" problem oriented subroutines, most of them defining initial or boundary conditions;
- b) containing the subroutines which must be used for the simulation of leakage flow as explained in Section II.C.3.4.

GROUP 1 - Basic Subroutines

AKTCL	ENBLR	ITCB	PRELI	STØFF
AKTST	FBRT	ITC1	PRØBR	TIØ
ATØM	FBRTB	ITC11	PRØCA	TLKM
ATØM1	FBRT2	ITC1R	RESET	TLKMS
AUSGAB	FITHI	ITC11R	REZØN	TRANS
BLØPLS	IDENT	KØPHI	SETZ1R	XCFI
BØRN	INIT	KØPHIH	STATO	XFF1
DIED	IMGL	LHTCL	STAT1	
DPDA	IMPACT	LHTST	SETUP	
ENBL	ITSØL	MIDI	STEP	

GROUP 2 - Problem oriented Subroutines

a) General

BLØPLØ
FPKØUT
FPKO
FØKINN
FZETAD
TBPS
WQDT
WWST
XABRC

b) Leakage flow option

BYPASS (MAIN Programme)
FZETA1
FZETA2
LITCB
LITC1
LITC11
LITC1R
LTC11R
LZETAD

In GROUP 3 are listed the programme functions for the calculation of material properties. These are split into four subgroups headed by the underlined names of the Members in which they are organized: a) (Member UPUO) Functions for calculating fuel material properties; b) (Member CAN4981) Functions for calculating the properties of canning (Steel 4981); c) (Member NATRIUM) Functions for calculating the properties of sodium; d) Functions for calculating the properties of structural material, either Niobium (d1) Member STRUNIØB) or Steel (d2) Member STRU4981). Obviously, the user must link to the programme either the functions of subgroup d1) or those of subgroup d2).

GROUP 3 - Functions

a) <u>UPUØ</u>	b) <u>CAN4981</u>	c) <u>NATRIUM</u>
RØUPUØ	WLCAN	RØNAL EHNAL
WLUPUØ	RØCAN	RØNAVS EHNALS
CPUPUØ	FTCAN	CPNAL VPNA
FTUPUØ	CPCAN	CPNALS VTNA
FHUPUØ	RHCAN	WLNAL VHNH
RHUPUØ	FHCAN	PRNAL VØNAV
GAUPUØ	GACAN	ZDNAL X1X2X4
		ZDNAV
d1) <u>STRUNIØB</u>	d2) <u>STRU4981</u>	
RØSTRU	RØSTRU	
CPSTRU	CPSTRU	
WLSTRU	WLSTRU	
FTSTRU	FTSTRU	

In the same order in which Subroutines and Functions are listed here, they are explained in the following Sections 2.1 to 2.3. Emphasis has been given to the description of the most important insofar they allow the understanding of the general programme structure and of the numerical methods involved. In many of the Subroutines details of interest from the theoretical viewpoint are also given as far as the related topic was not covered in the theory part of this report. Conversely, some Subroutines have been treated in less detail when the relative explanation can be found in other sections.

As a rule, for all Subroutines of GROUP 2a (and a few others as well), the

arguments transferred between calling programme and Subroutine have been defined, thus enabling the user to adapt it to his problem.

1.3 Organisation in Members

The above listed Subroutines are organized in the following Members. Underlined is the Member's Name (generally the name of the first Subroutine in the Member) followed by the names of the other subroutines (if any) in the Member itself.

BYPASS, LZETAD, FZETA1, FZETA2, LITC1, LITC11, LITC1R, LTC11R, LITCB
DPDA
ENBL, ENBL1, SETZ1R
FBRT, FBRTB, FBRT2, KØPHI, KØPHIH, PRØBR, PRØCA
FITHI, MIDI, PRELI, REZØN
FTKINN, FPKØUT, FPKO, FZETAD, WQDT, TBPS, WWST
IMGL, TLKM, TLKMS, TRANS, IDENT, INIT
IMPACT, ATØM, ATØM1, RESET, BØRN, DIED
ITCB
ITC1, ITC11, ITC1R, ITC11R
SETUP
STATO
STAT1 (MAIN Programme)
STØFF, STEP, ITSØL, XFF1, XCFI
TIØ, BLØPLS, BLØBLØ, AUSGAB
XABRC, LHTCL, LHTST, AKTCL, AKTST

The organization of programme Functions in Members is shown in GROUP 3 above.

1.4 Overlay Structure

The following Overlay Structure can be used:

- Branch ALPHA-1
Subroutine STATO

- Branch ALPHA-2
Subroutines WQDT, FPKO, FPKØUT, FTKINN, FBRT2, KØPHI, KØPHIH, PRØCA,
PRØBR
- Branch BETA-1
Subroutines ITC1, ITC11, ITC1R, ITC11R, FBRT
- Branch BETA-2
Subroutines ENBL, ENBL1, SETZ1R
- Branch GAMMA-1
Subroutines TLKM, TLKMS, FBRTB, TRANS, IDENT, STEP, STØFF, XCFI, RESET,
INIT
- Branch GAMMA-2
Subroutines BØRN, ATØM, ATØM1, FITHI, MIDI, REZØN, PRELI, IMPACT

1.5 Remarks for the user

Subroutines of GROUP 1 above have not to be modified by the user.

Subroutines of GROUP 2a must be adapted to the particular problem considered, unless the standard version is already applicable.

Subroutines of GROUP 2b must be used in case leakage of coolant flow is simulated. In this case the three Members STAT1, ITC1, ITCB must be replaced by Member BYPASS.

The standard double precision programme version (without Overlay) requires about 700 K of core region. The full programme consists of about 15000 statements.

During the single-phase flow the code calculates roughly 2 seconds problem time in one minute CPU time on the computer IBM 3033. During the two-phase flow one can compute in one hour CPU time from 5 to 12 seconds problem time, according to the axial extension of the bubble region. The larger the zone with annular flow, the longer is the calculation time.

2. DESCRIPTION of Subroutines

2.1 Basic Subroutines

Subroutine AKTCL (HKCL, SCL, TKK, TCA)

This subroutine computes the clad-vapour heat transfer coefficient in the bubble region by means of the formula

$$\alpha = \frac{\lambda_{Na}}{SCL} \quad (1)$$

where λ_{Na} is the thermal conductivity of sodium.

List of parameters:

HKCL	heat transfer coefficient (output parameter)	(W/m ² °C)
SCL	liquid film thickness at the clad surface	(m)
TKK	vapour temperature	(°C)
TCA	clad superficial temperature	(°C)

Subroutine AKTST (STRUK, VDUF, HKTST, SST, TKK, TST)

This subroutine computes the structure material - vapour heat transfer coefficient in the bubble region by means of the formula:

$$\frac{1}{\alpha} = \frac{1}{\alpha_{SK}} + \frac{1}{\alpha_c} \quad (2)$$

where

$\alpha_{SK} = \frac{\lambda_{Na}}{SST}$ = heat transfer coefficient due to convection (λ_{Na} = thermal conductivity of sodium) (W/m² °C)

α_c = heat transfer coefficient which takes into account the conduction in the structure, under the assumption of a linear temperature distribution through its thickness. (W/m² °C)

The conductive term is calculated as follows. Let

- T_K be the bulk sodium temperature ($^{\circ}\text{C}$)
 T_S be the structure temperature (calculated in only one node at the centre of the structural layer) ($^{\circ}\text{C}$)
 S be the structure thickness (m)
 R_s the radius of the inner structure surface (m)
 $V_{\text{STRUK}} \simeq 2\pi R_s \cdot S$ the structure volume per unit axial length (m^2)
 $F = 2\pi R_s$ the structure inner surface per unit axial length (m)
 $V_{\text{DUF}} = V_{\text{STRUK}}/F \simeq S$ (m)
 q heat flux through the structure (W/m^2)
 λ_S structure thermal conductivity ($\text{W}/\text{m}^{\circ}\text{C}$)
 x a coordinate axis with origin at the structure inner surface and oriented outwards. (m)

In case a linear temperature distribution through the structure is assumed

$$T(x) = T_K - 2 \frac{(T_K - T_S)}{S} x \quad (3)$$

the heat flux q is given by

$$q' = - \lambda_S \text{grad } T \simeq \lambda_S \frac{(T_K - T_S)}{S/2} \quad (4)$$

which can be written

$$q = \alpha_c (T_K - T_S) \quad (5)$$

with

$$\alpha_c = \frac{\lambda_S}{S/2} \simeq \frac{\lambda_S}{V_{\text{DUF}}/2} \quad (6)$$

The overall heat transfer coefficient will therefore be given by

$$\frac{1}{\alpha} = \frac{1}{\alpha_{\text{SK}}} + \frac{1}{\lambda_S/(V_{\text{DUF}}/2)} \quad (7)$$

List of parameters:

STRUK	dummy
VDUF	see input description (m)
HKTST	heat transfer coefficient (output parameter) ($\text{W/m}^2 \text{ } ^\circ\text{C}$)
SST	liquid film thickness at the structure surface (m)
TKK	vapour temperature ($^\circ\text{C}$)
TST	structure material temperature ($^\circ\text{C}$)

Subroutine ATOM

This subroutine is used to define the physical situation which occurs when two vapour bubbles coalesce.

The logical decision to join two adjacent bubbles is taken by the programme when the slug between them has become shorter than 2 mm. When the upward vapour mass flux in the uppermost mesh zone of the lowermost bubble exceeds $1000 \text{ kg/m}^2 \text{ sec}$ coalescing may occur provided the pressure difference across the interlaying liquid slug does not exceed 0.75 bar and provided the bubble distance does not exceed a given figure which depends on this pressure difference.

Following the gathering of two bubbles in a given Eulerian zone, all physical quantities characterizing the newly formed bubble must be defined or calculated for that zone, mainly: vapour pressure, temperature, density, mass flow and liquid film thickness at clad and structure. The mass of the liquid slug between the bubbles is taken into account and equally distributed to clad and structure liquid films. This effect contributes largely to rewetting of dried-out zones in combination with the application of the model of moving liquid film. Furthermore, the integral pressure and temperature of the new bubble are calculated by calling the subroutine ATOM1.

The subroutine ATOM is split into four main branches according to the four possible combinations of the two indexes NDAM(K) and NDAM(KP1) of the bubbles K and KP1 (it is reminded that NDAM(K) = 0 means that the bubble length covers less than three zones, hence only integral values of pressure and temperature are calculated for it; NDAM(K) = 1 means that the bubble stretches over at least three zones, hence pressure and temperature distributions are computed for it). Coalescing of two bubbles with both indexes NDAM equal to zero may or may not produce a bubble with NDAM equal to one, while one index equal to one obviously assures that the resulting bubble has index one.

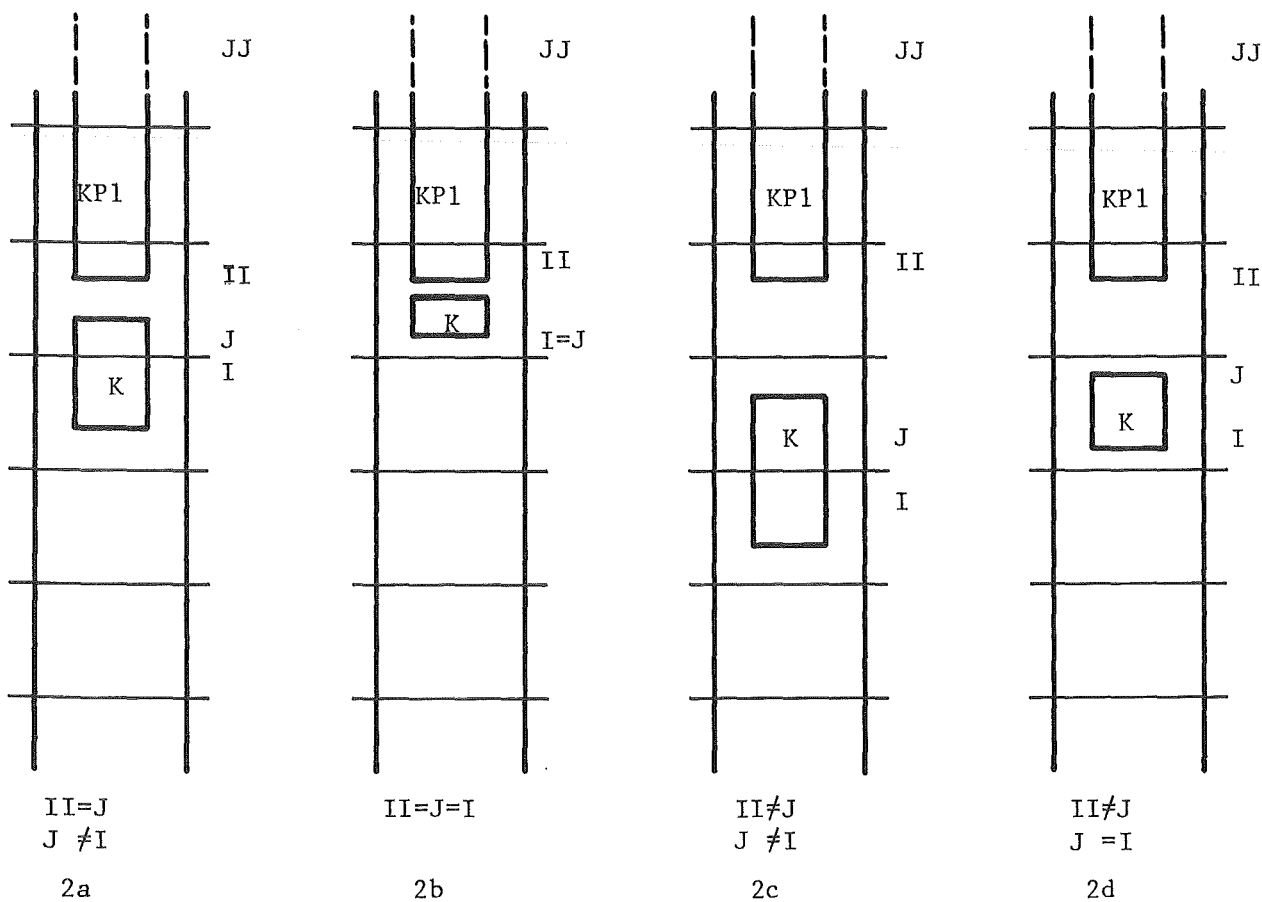
When two bubbles K, KP1 coalesce, the index KP1 of the uppermost one is preserved for the new bubble, while index K becomes free for a new bubble initialization. At the end of subroutine ATOM the index IDKR of the new bubble is defined (see subroutine IDENT for the meaning of the index IDKR) and the bubble configuration in the coolant channel is updated by calling subroutine DIED.

The sketches of Fig. 16 show the configuration of the coalescing bubbles K, KP1 according to the four possible combinations of the indexes NDAM(K), NDAM(KP1). In the sketch I, J are the indexes of the mesh zones with the lower and upper phase boundaries of the lowermost bubble; II, JJ are the zone indexes of the phase boundaries of the uppermost bubble. It holds obviously: $I \leq J \leq II \leq JJ$.

It must be remarked that coalescence of bubbles separated by one full Eulerian mesh zone, as shown in sketch 4.1a, is possible only when the vapour mass flux in the lowermost bubble exceeds the above mentioned threshold.

Subroutine ATØM1

This subroutine is called by subroutine ATØM to calculate the integral pressure and temperature of a bubble produced when two adjacent bubbles coalesce. The method used for this calculation is explained in the description of subroutine ITSØL.



2nd case

Fig. 16.2

Coalescing bubbles:	$NDAM(K) = 0$	$J - I \leq 1$
	$NDAM(KP1) = 1$	$JJ - II \geq 2$
Resulting bubble	$NDAM(KP1) = 1$	$JJ - I \geq 2$

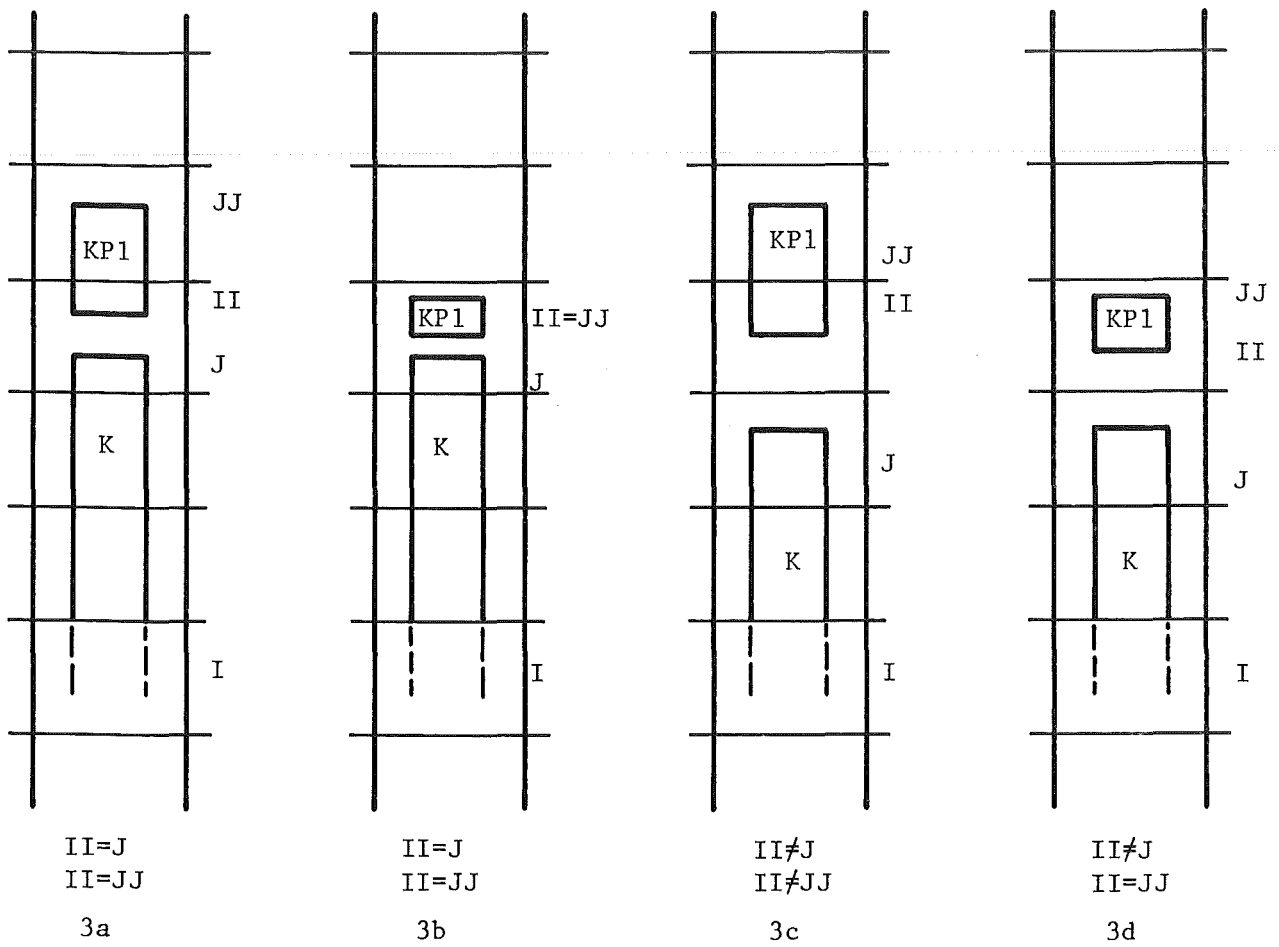
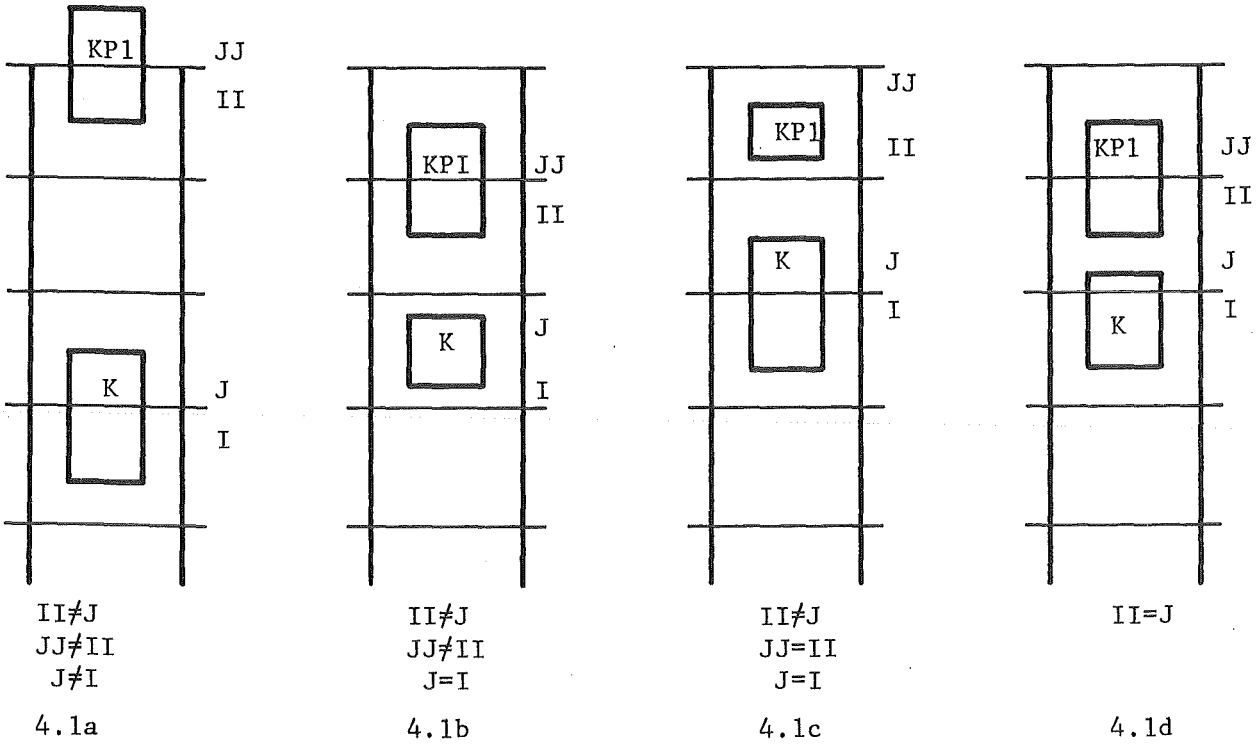


Fig. 16.3 3rd case

Coalescing bubbles:	NDAM(K) = 1	J-I ≥ 2
	NDAM(KP1)=0	JJ-II ≤ 1
Resulting bubble :	NDAM(KP1)=1	JJ-I ≥ 2

4.1 Resulting bubble: $NDAM(KP1)=1$ $JJ-I \geq 2$



4.2 Resulting bubble: $NDAM(KP1)=0$ $JJ-I \leq 1$

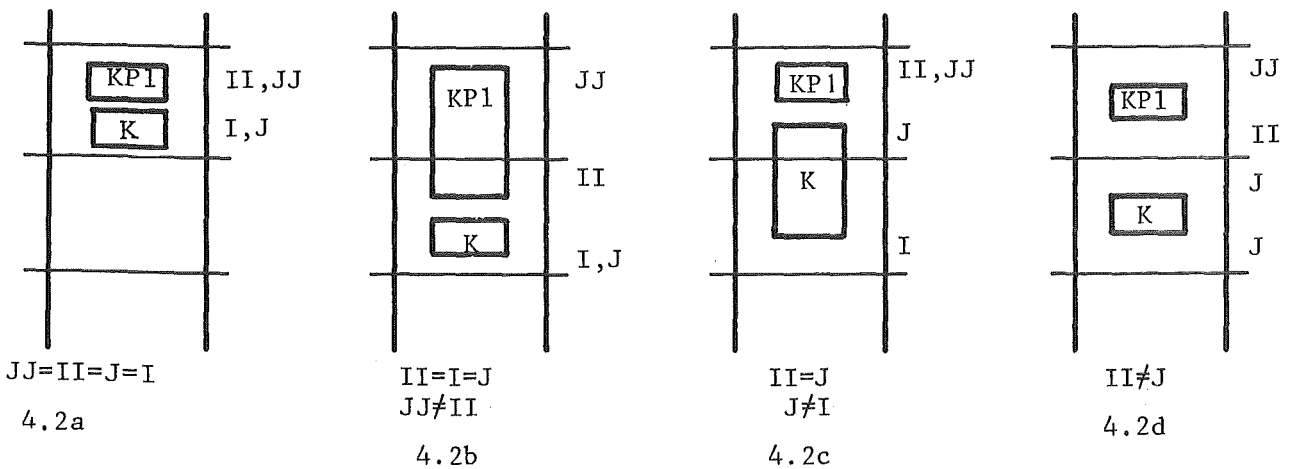


Fig. 16.4 4th case

Coalescing bubbles: $NDAM(K) = 0$ $J - I \leq 1$
 $NDAM(KP1) = 0$ $JJ - II \leq 1$

Subroutine AUSGAB

This subroutine is driven by the main program (subroutine STAT1) to print-out data on the paper hard-copy with the frequency determined by the input parameter LP1 for the single phase flow calculation and LP2 for the two-phase flow calculation (see Input Description, Section III.4). Every LP1 (LP2) time steps a full print-out is made available (for every channel KKN) with the following information:

i) During single phase flow calculation

A heading containing

- problem time (T) (sec)
- channel number (KKN)
- channel type (KONT) (see also Input Description)
- coolant temperature in upper plenum (TPLEN) ($^{\circ}\text{C}$)
- inlet coolant temperature (TKIN) ($^{\circ}\text{C}$)
- outlet coolant temperature (TKOUT) ($^{\circ}\text{C}$)
- inlet coolant pressure (N/m^2)
- outlet coolant pressure (N/m^2)
- mean value of mass flux (XXMAN1) ($\text{kg/m}^2\text{sec}$)

Data for every mesh node $M = 1, 2, \dots, \text{NM2}$ (at the mid-point of every mesh zone) consisting of:

- mesh index (M)
- axial coordinate (z) of bottom boundary of the M-th zone (m)
- coolant velocity (VKMN) (m/sec)
- coolant mass flux (XMAN) ($\text{kg/m}^2\text{sec}$)
- coolant pressure (PKMN) (N/m^2)
- coolant saturation temperature (TSAT) ($^{\circ}\text{C}$) corresponding to the pressure PKMN
- structure temperature (TSN) ($^{\circ}\text{C}$)
- coolant temperature (TKN) ($^{\circ}\text{C}$)
- clad temperatures in the outer (TCA), middle (TCM) and inner (TCI) nodes ($^{\circ}\text{C}$)
- specific power generation (QGEST) (W/m^3)

Fuel temperatures follow for the axial nodes NMO to NM1 inclusive:

- average fuel temperature (TBM) ($^{\circ}\text{C}$)
- central fuel temperature (TBO) ($^{\circ}\text{C}$)
- radial fuel temperatures in the NN radial nodes (TB(1) to TB(NN)) ($^{\circ}\text{C}$)

Calculated pressure drops

- in the channel, from inlet of mesh $M = 1$ to outlet of mesh $M = \text{NM2}$
(DPGNR) (N/m^2)
- in the inlet valve (DLPBL1) (N/m^2)

and coefficient (ZETAD) for the calculation of pressure drop in the inlet valve.

The thickness of fuel-clad gap (SPALT) and the heat transfer coefficient through this gap (HBRC) follow for every axial mesh.

Information about flow conditions (NBOIL(KKN) = 0 for single phase flow, NBOIL(KKN) = 1 for two phase flow) complete the print-out.

ii) During the two-phase flow calculation

The set of data is presented in quite the same arrangement as above, the difference consisting in the suppression of the column of the saturation temperatures (TSAT) and the insertion of two column for liquid film thickness at the clad (SCL) and at the structure surfaces (SST) in the bubbles region, and the information about time elapsed since boiling inception (TBOIL).

Between two consecutive full sets of data (appearing LP2 time steps apart) a concise set of information is given every time step, containing:

- channel number (KKN)
- problem time at the end of a macro-time-step (TT)
- problem time at the end of a micro-time-step (TTKU) (TTKU = TT at the instant of printing data)
- time elapsed since boiling inception (TBOIL)
- last micro-time-step (DTKUE)
- number of iterations performed in the Subroutine ITCB during last micro-time-step (ITER)

- bubble index (K)
- mean value of vapour pressure (inside bubble K) (PV) (N/m^2)
- mean value of vapour temperature (TV) ($^{\circ}C$)
- mass flux in the slug below (GL(K,1)) and above (GL(K,2)) bubble K
- velocity of liquid-vapour interfaces at the lower (VL(K,1)) and upper boundaries (VL(K,2)) of bubble K.
- Axial position of lower (ZL(k,1)) and upper (ZL(K,2)) boundaries of bubble K
- vapour pressure distribution inside bubble K (in case NDAM(K) = 1).

When the problem time lies in the interval $(N,9) \div (N+1)$ (where N is a positive integer) information about power losses beyond the structure outer surface is printed out with the same presentation as far the stationary case (see description of Subroutine STATO).

Subroutine BLØWPLS

It writes onto the file FT11001 (see Section III.5) data for the generation of the "Standard" Plots which include inlet mass flow, fuel, clad, coolant and structure temperatures against time, as well as time variation of liquid film thickness at clad and structure and spreading of two-phase flow region. The temperatures are plotted for the node with the stationary top power generation (referred to as NMP) and the node with the stationary largest coolant temperature (MPEAK). The percentage of clad and fuel molten materials in these nodes are also plotted against time.

Data for the plot generation are written first onto an array named VCPS which contains 80 alpha-numeric characters followed by the specific information for up to ten channels. The block of data written every IDELTT time steps has length NZS and is stored onto the above file from which it can be assessed with the plot programme PLOTCP /25/ to produce the diagrams via a plotting device.

Subroutine BØRN

Preliminary general remarks:

a bubble is characterized by an index K (ranging from 1 to NB = maximum number of bubbles in the channel) which is stored in the L-th word of the array IND, L being the ordered position occupied by the bubble in the channel counting from the channel inlet upwards. Therefore: $K = \text{IND}(L)$.

The bubble K is further characterized by a number stored in the K-th word of the array IDK, defined by $\text{NM2} \times J + I + 1$ where: NM2 = number of axial zones ($\text{NM2} \leq 30$); I = lowermost zone covered at least partially by the bubble; J = uppermost zone covered by the bubble.

Therefore:

$$\text{IDK}(K) = \text{NM2} \times J + I + 1$$

The integer number IDK(K) defines implicitly the indexes I, J hence the boundary zones of the bubble. They can be explicitly derived as:

$$J = (\text{IDK}(K) - 2) / \text{NM2}$$

$$I = 1 + \text{MOD}(\text{IDK}(K) - 2, \text{NM2})$$

The subroutine BØRN is called after every initialization of a new bubble.

It a) looks for the lowest free index K, and assigns it to the bubble; b) defines IDK(K) as function of the indexes I = J of the zone in which the bubble has been initialized; c) increases the number KB of existing bubbles by a unity; d) determines the new bubble configuration rearranging the array IND in which bubble indexes are ordered from the channel inlet upwards.

Subroutine DIED

(see general remarks in the explanation of subroutine BORN). This subroutine is called when a vapour bubble vanishes or disappears by coalescing with the bubble above it. The subroutine a) makes the bubble index K free; b) decreases the number KB of existing bubbles by a unity; c) rearranges the array IND in which bubbles indexes are ordered from the channel inlet upwards.

Subroutine DPDA

This subroutine solves the coupled energy, continuity and momentum equations for the vapour phase, dealing separately with every bubble present in the channel.

Details of this calculation are given in Appendix A1 of reference /1/. It can be summarized as follows:

1. for every bubble vapour velocities at the upper and lower phase interfaces are assumed as known boundary conditions. These velocities are derived by a previous solution (performed in subroutine IMGL) of the momentum equation for the adjacent liquid slugs.
2. The coupled energy and continuity equations are solved, with the above boundary conditions, to find the new vapour mass flow axial distribution. Vapour production due to film vaporization and vapour condensation in the colder bubble region represent the source term of the above equations. Vapour production does not depend only on the thermal heat flux to the vapour but may also be determined by vapour pressure oscillations ("flashing").
3. Solution of the momentum equation to find the vapour axial pressure distribution assuming as boundary conditions the pressure at the phase interfaces.

The mesh zone with the maximum vapour pressure is first determined, hence the pressure increments in the adjacent zones in the upward and downwards directions are calculated.

Shear stresses between vapour and liquid film phase are calculated by taking into account the liquid film velocity. An input flag (ICFI3) allows choosing between a calculation of the average shear stresses in a zone or a calculation of three values, in the middle of the zone and at its boundaries.

The shear stress calculation, driven by the subroutine DPDA, is performed in the subroutine XCFI.

4. The vapour axial temperature distribution is calculated by assuming saturation conditions.
5. A check of the physical consistency of the pressure and temperature axial distributions is performed by comparing the mass of vapour present in the bubble as deduced from the calculated distribution with the mass derived by

the average pressure. Should the discrepancy in the vapour mass exceed a given threshold, a correction of the pressure and temperature distribution would be performed. This consistency check is performed in the subroutine ITSOL.

Details of the calculations performed in DPDA are given in reference /1/ and in Section II.C.2.3.2.

Subroutine ENBL

Calculates the source terms $X\phi 1(K)$, $X\phi 2(K)$, $XM1(M)$, $XM2(M)$, $XU1(K)$, $XU2(K)$ for the bubble K as explained in Section II.C.2.3.2.b and solves the coupled energy and continuity equations for the vapour phase to derive the integral vapour pressure.

Values referred to time level t_{n-1} are used.

The mean value of vapour pressure at time t_n is calculated as

$$p_v^n = p_v^{n-1} + \left(\frac{dp_v}{dt} \right)^{n-1} \Delta t. \quad (8)$$

The time derivative of the pressure vapour is given by (see Reference /1/, section 4.2.2.1, formula (48))

$$\frac{dp_v}{dt} = \frac{1}{L} \frac{\int_0^L \frac{U}{A} q dz - h_{fg} \bar{\rho}_v \frac{dL}{dt}}{\frac{U}{A} S \bar{\rho}_l \frac{dH_1}{dp_v} + h_{fg} \frac{\partial \bar{\rho}_v}{\partial p_v}} \quad (9)$$

where

S = liquid film thickness (m)

A = cross flow area (m^2)

h_{fg} = vaporization enthalpy (J/kg)

H_1 = liquid enthalpy (J/kg)

L = bubble length (m)

\bar{p}_v = mean value of vapour pressure (N/m^2)

q = heat flux to vapour (W/m^2)

t = time (sec)

U = perimeter of clad outer surface (U_H) or structure inner surface (U_S)

$\bar{\rho}_v$ = mean value of vapour density (kg/m^3)

With reference to the list of symbols given in section III.3 the above terms are calculated as:

$$L = ZL(K,2) - ZL(K,1) \quad (10)$$

$$\frac{dL}{dt} = \frac{1}{\rho_1} (GL(K,2) - GL(K,1)) \quad (11)$$

$$\int_0^L \frac{U}{A} q \, dz = \sum_M \left\{ \frac{U_H}{A} \alpha_c (T_{ca} - T_v) + \frac{U_S}{A} \alpha_s (T_S - T_v) \right\} dz \quad (12)$$

$$\frac{U_S}{A} \frac{1}{\rho_1} \frac{dH_1}{dp_1} = \frac{1}{\rho_1} \cdot DHLDP \cdot \sum_M \left\{ \frac{U_H}{A} SCL + \frac{U_S}{A} SST \right\} dz \quad (13)$$

DHLDP (= dH_1/dp_1) and DRØDP (= $d\rho/dp$) are calculated in the subroutine STØFF. α_c, α_s are the heat transfer coefficients clad-vapour and structure-vapour through the liquid film.

Subroutine ENBLR

Performs the same calculation as the Subroutine ENBL, but using values referred to time level t_n .

Subroutine FBRT

This subroutine computes the transient temperature distributions in fuel, clad, coolant and structure material during the single phase flow. Heat losses from the structure material to the external medium are taken into account. The diffusion equations for the heat transfer can be solved with an implicit or explicit scheme, according to the choice of input parameter TETA (see input description). Solution is attained by means of the Gauss-Seidel iteration method. Letting $i-1$, i , $i+1$ indicate any three consecutive nodes in radial direction, the Gauss-Seidel iteration scheme is based on a formula of the type

$$A_i^r T_i^{r+1} = B_i^{r+1} T_{i-1}^{r+1} + C_i^r T_{i+1}^r + D_i^r + R_i \quad (14)$$

where r is an iteration index within the actual time step, A_i , B_{i-1} , C_{i+1} , D_i are coefficients depending on material properties and geometry, R_i is a known quantity depending on the temperature distribution at the end of the previous time step. Applying this equation from the fuel axial node outwards, consecutively for all radial nodes of an axial mesh zone, the already determined temperature of the adjacent node $i-1$ (T_{i-1}^{r+1}) is used for the estimation of the new temperature of node i (T_i^{r+1}) together with the previous temperature of the adjacent node $i+1$ (T_{i+1}^r). The calculation starts computing once and for all the known values (variables referred with index l - see list of symbols) and then iterates simultaneously the temperatures for all radial nodes as long as the maximum difference between two consecutive values $T_i^{r+1} - T_i^r$ exceeds a given threshold.

Details about the derivation of the above equation and the Gauss-Seidel iteration scheme are given in section II.C.2.1.

Owing to the fact that coolant temperatures are calculated in this subroutine within the same iteration scheme as clad and structure temperatures, heat fluxes from coolant to clad and structure are always recalculated (symbols QQ3 to QQ6 - see list of symbols).

After completing the iterative procedure, the average fuel temperature is calculated (subroutine FBRT2). In case the melting temperature has been attained in some nodes in either fuel or clad material the temperature distribution is calculated differently for these nodes, taking into account the latent transformation heat (subroutines KOPHI and KOPHIH for fuel and clad respectively).

Subroutine FBRTB

This subroutine computes the transient temperature distributions in fuel, clad and structure material during the two-phase flow calculation. The main difference with respect to the subroutine FBRT is that the coolant temperatures are not calculated in FBRTB but in other subroutines (TLKM, TLKMS for the liquid slugs, DPDA for the vapour temperatures in the bubbles) driven by the calling programme ITCB. The coolant temperature distribution is therefore assumed in FBRTB as boundary condition. Heat fluxes from coolant to clad and structure are constant in FBRTB, but recalculated within the calling programme ITCB accounting for bubble displacements, variation in vapour temperature and liquid film thickness.

The heat diffusion equations are solved for fuel, clad and structure material with the same Gauss-Seidel iteration method as explained for the subroutine FBRT (Details are given in section II.C.2.1).

Contrary to Subroutine FBRT, calculation of mean fuel temperature and of temperature distribution in fuel and clad in case of melting are not performed in FBRTB but in the calling subroutine ITCB.

Subroutine FBRT2

This subroutine calculates the average fuel temperature for every axial zone by taking into account the mass of fuel material associated to each radial node.

Subroutine FITHI

This subroutine calculates the axial distribution of liquid film thickness at clad and structure. An input flag (IFLAG2) allows choosing between the application of the model of static liquid film and the model of moving film.

The first model assumes the liquid film velocity as negligible with respect to the vapour velocity. The moving film model solves rigorously the continuity equation for the liquid phase using the axial liquid film velocity distribution calculated in the subroutine XCFI.

In case the static film model is applied, the liquid film is considered to vanish (dry-out) when its thickness decreases below a given threshold (input parameter SMIN) which is normally set to one half up to two-thirds of the initial film thickness (S0). This accounts implicitly for the fact that the film would be drained by the flowing vapour. In case the moving film model is applied the calculation proceeds up to dry-out (SMIN can be set as low as 1 μm).

From the programming viewpoint the subroutine is split into two main branches according to the fact that the film is in front of a "short" (NDAM(K) = 0) or of a "long" (NDAM(K) = 1) bubble.

Let I be the index for the lowermost zone of a bubble, M (ranging from I + 1 to J - 1) for all the inner bubble zones, J for the uppermost zone.

In case NDAM(K) = 0 are calculated either

a) SCL(M), SST(M) for a bubble contained in one Eulerian zone (I = J = M)

or

b) SCL1(K), SST1(K), SCL2(K), SST2(K) for a bubble K stretching over two zones (J = I + 1)

In case NDAM(K) = 1 are calculated:

SCL1(K), SST1(K) for the lowermost zone I

SCL(M), SST(M) for every inner zone M

SCL2(K), SST2(K) for the uppermost zone J.

Subroutine IDENT

This subroutine is called when a liquid-vapour phase boundary moves from a zone to an adjacent one. It defines for the bubble K the integer number IDK(K), thus implicitly giving the zones in which the lower and upper phase boundaries lie (see remark made in the description of subroutine BØRN).

In case a bubble is ejected into the upper coolant plenum and vapour condenses there, the subroutine calculates the momentum of the resulting upper slug from the momentum of the previous upper slugs and that of the upper reduced length.

Subroutine INIT

This subroutine is used to initialize the symbols defining the physical state of a bubble in an Eulerian mesh to which it has moved or to which it has stretched.

The subroutine is split into two main branches dealing respectively with "short" bubbles (NDAM(K) = 0) and with "long" bubbles (NDAM(K) = 1) i.e. bubbles stretching over at least three Eulerian meshes. Transitions from one case to the other are obviously foreseen in both directions.

The symbols which have to be initialized are those summarized in Table I following the description of subroutine SETUP and the symbols defining the energy vapour to clad and structure, namely: XØ1(K), XØ2(K), XM1(M), XM2(M), XU1(K), XU2(K).

Subroutine IMGL

Solves the momentum equation for the liquid slugs between vapour bubbles as explained in Section II.C.2.3.3.b, determining the time derivative of the coolant mass flow in the slugs $(\frac{dG_K}{dt})^n$. The updated value of the mass flow is

then calculated by

$$G_K^{n+1} = G_K^n + \left(\frac{dG_K}{dt}\right)^n \Delta t_n \quad (15)$$

The coolant momentum equation is also solved for the inlet and outlet liquid columns, taking into account the respective reduced lengths (RLE, RLA) which represent the coupling between the test section and the primary coolant loop.

Subroutine IMPACT

It is called by the driving subroutine ITCB when a bubble collapses and the two adjacent liquid slugs coalesce. It calculates the momentum of the new slug taking into account the contributions of the previously existing slugs, the resulting mass flux, its time derivative, and the new distributions of coolant pressure and temperature.

Subroutine ITCB

This subroutine is the main driving programme for the two-phase calculation. It accomplishes to the following functions:

- 1) Time step control (by calling subroutine STEP). The specified macro-time step (DELTT) may be divided in an even number of micro-time steps in case same convergence criterion requires it. Conversely, the micro-time step may be increased without exceeding the macro-time step.
- 2) Calculation of new power generation and boundary conditions, namely: inlet (upstream of the inlet valve) and outlet coolant pressures (subroutines FPKO and FPKOUT), coolant inlet temperature (subroutine FTKINN) and inlet valve pressure drop coefficient (subroutine FZETAD).
- 3) At the beginning of a new micro-time step, before the actual calculation starts, variables of the previous time step are fetched to be used for the following iteration scheme. Particularly, energy exchange between vapour and adjacent clad and structure are determined from the solution of the energy equation for the vapour phase (subroutine ENBL). Programme symbols referring to the previous time step are characterized by the index "1" (see list of variables).
- 4) Following the calculation of the energy exchanged by the vapour phase, new bubble dimensions are calculated hence new phase boundaries determined (subroutine TRANS). Every bubble, characterized by an index K, receives a new label IDKR(K) which implicitly identifies the zones over which it stretches (subroutine IDENT).
- 5) The most important characteristic of the two phase flow calculation is the solution of the momentum equation of the vapour phase which determines the axial distribution of pressure and temperature within every bubble. This calculation is made only (see subroutine DPDA) when a bubble stretches over at least three mesh zones, partially covered zones being also taken into account. As long as a bubble is "short" (covers less than three zones) only its average pressure and temperature are calculated. A flag (NDAM(K)) first initialized to 0, is turned to 1 when the bubble length has been reached which requires axial pressure and temperature distributions to be calculated.

When a long bubble shrinks and becomes shorter than three mesh zones the flag is turned back to zero and axial distributions replaced by integral pressure and temperature values (subroutine RESET).

- 6) When a bubble moves to a new zone, some variables (like film thickness, vapour mass flow, pressure and temperature) are initialized in that zone (subroutine INIT).
- 7) Temperature distribution in the liquid slugs between bubbles and in the lower and upper liquid columns are calculated in Lagrangian meshes in the subroutine TLKM. Heat fluxes coolant-clad and coolant-structure referring to the actual time step (variables QQ3 to QQ6) are also calculated in TLKM for the zones which are totally or partially filled by a liquid slug. For the zones which are partially covered by a liquid slug (and partially contain a vapour bubble) the contributions to the total heat fluxes arising from the vapour to clad and structure exchange are added before the subroutine FBRTB is called (see later).
- 8) The energy equation for the vapour phase is newly solved iteratively with reference to the actual bubble configuration (hence using variables with index "R") (subroutine ENBLR). A control of the convergence of the adopted method is made by comparing subsequent values of the integral bubble pressure.
- 9) In case the above iterative scheme does not converge, the programme automatically restores the situation valid at the very beginning of the ITCB calculation by performing a "back-initialization" (subroutine INIT) and halves the actual time step by going back to subroutine STEP (Point 1). Otherwise the calculation proceeds as follows.
- 10) The axial pressure and temperature distributions are calculated in every bubble stretching over at least three zones (partial zones included) by solving the momentum equation for the vapour phase in Eulerian meshes. Pressures at phase boundaries are assumed as boundary conditions (subroutine DPDA).
- 11) The momentum equation for the liquid slugs is solved to determine the slug velocities (subroutine IMGL).

- 12) Heat fluxes clad-coolant and coolant-structure (QQ3 to QQ6) are calculated as explained at point 7) by taking into account the contributions arising from the zones which are totally or partially filled with vapour. Radial temperature distributions in fuel, clad and structure material are then calculated for the axial zones which are in the two-phase flow region (subroutine FBRTB).

Steps 3) to 12) are organized in an iterative calculation which proceeds as long as it is necessary to achieve full consistence of the pressure profile in the bubbles with heat fluxes, hence temperature distributions in fuel, clad and structure. When this situation has been reached next step is performed, namely:

- 13) Calculation of temperature distributions in fuel, clad, structure for the full channel (subroutine FBRTB) particularly for the zones in the single phase flow domain for which the above explained iteration procedure does not apply. In the zones where fuel or clad fusion temperature has been reached, the temperature distribution is corrected by taking into account the latent transformation heat (subroutines KØPHI and KØPHIH for fuel and clad respectively) and the percentage of molten material is calculated (subroutine PRØBR, PRØCA). Eventually the average fuel temperature is calculated (subroutine FBRT2).
- 14) With reference to the newly achieved bubbles and liquid slugs configuration (hence using variables with index "R" in the programme) the temperature distribution in the liquid slugs and heat fluxes QQ1, QQ2 are calculated. These values are first used by next time step, thus making the heat fluxes iteration scheme half-implicit.
- 15) Disappearing of bubbles and/or slugs. When a bubble shrinks and its length becomes smaller than a given figure (0.4 mm) the bubble is considered as vanished. The adjacent liquid slugs are connected (subroutine IMPACT) and the number of existing bubbles is reduced by one unity (subroutine DIED). Conversely, when the length of a liquid slug between two bubbles becomes smaller than 0.5 mm the bubbles coalesce and their number is also reduced by one unity (subroutine ATØM, DIED). In both cases the momentum equation for the remaining liquid slug is solved again to find the boundary conditions (velocity at the liquid-vapour interfaces) for next time step (subroutine IMGL).

In case only one bubble exists, and it vanishes, the impulse of previous lower and upper liquid columns, weighted with the respective lengths, are averaged to find the resulting impulse of the restored single-phase flow. Programme control is transferred to the subroutine STAT1 and a single phase calculation follows.

- 16) Film thickness calculation. The axial distribution of film thickness at clad and structure is calculated for every bubble, regardless of its length (subroutine FITHI). An input flag allows choosing between the model of static liquid film (in which the liquid film velocity is considered negligible with respect to the vapour velocity) and the model of moving film which solves rigorously the continuity equation for the liquid phase.
- 17) New pressure distribution is calculated in the liquid slugs (subroutine PRELI).
- 18) Initialization of new bubbles. In case the saturation temperature has been attained in a zone of a liquid slug a new bubble is initialized at the zone lower boundary with length 0.5 mm (subroutine SETUP). The bubble number is updated (subroutine BØRN), new Lagrangian meshes are initialized and the momentum equation for the resulting liquid slugs configuration is solved again. (subroutine IMGL).
- 19) The average coolant density is calculated taking into account the vapour density in the voided region (subroutine MIDI). This step is of importance for coupling the programme to reactor kinetic calculations.
- 20) A transformation of coolant and pressure temperature distributions from the Lagrangian to Eulerian meshes (subroutine REZØN) ends the calculation for the micro-time step. In case the assigned macro-time step had been halved, the programme goes back to step 1 (time step control) and the calculation proceeds up to the end of the macro-time step.
- 21) Print-out of results occurs in a reduced extent at the end of every macro-time step and to a full extent every LP2 macro time steps (see Input Description and Subroutine AUSGAB).

The following scheme shows in a compact form the succession of subroutines called by ITCB and the main iteration loops.

STEP		Time Step control
FPKO, FPKØUT, FTKINN, FZETAD		Boundary conditions
ENBL		Bubbles energy equation at t_{n-1}
TRANS	Bubbles displacement	
IDENT) updating of bubbles indexes	
RESET		
INIT	Initialization of bubbles in new zones	calculation for the two-phase
TLKM	Liquid Slugs Temperature	flow domain at t_n
ENBLR	Bubbles energy equation	
INIT	Back-Initialization	
DPDA	Vapour pressure distribution	
IMGL	Liquid slugs moment equation	
FBRTB	Fuel, clad, structure temperature distributions	
FBRTB		Temperature distributions in
KØPHI, KØPHIH	Fuel/clad melting	fuel, clad, structure for
PRØBR, PRØCA	Percentage of fuel/clad molten material	the full channel
FBRT2		
TLKMS		Liquid slugs temperature
IMPACT		
DIED		
IMGL		Vanishing of slugs or bubble
FITHI	Film thickness calculation	
ATØM, (DIED)IMGL		
IMGL		
PRELI		Liquid slugs pressure distribution
SETZ1R		Transfer data to next time step
SETUP, (BØRN)) Initialization of new bubbles
IMGL		
REZØN		From Lagrangian to Eulerian meshes
MIDI		Mean coolant density
AUSGAB		Print-out of data

Scheme: Sequence and main functions of Subroutines called by ITCB

Subroutines ITC1/ITC11

These subroutines are described together as they are strictly coupled to solve numerically the momentum equation for the single phase flow by means of a Predictor-Corrector iteration scheme.

ITC1 is the driving subprogramme for the single phase flow calculation and accomplishes the following functions:

- 1) Time step control. In case the assigned macro-time step (DELTT) is greater than 0.05 sec it is divided into an even number of micro-time steps (DTKUE). Print out of results occurs only at the end of the assigned macro-time step.
- 2) Power generation is calculated for the actual time (TT) and boundary condition are newly imposed: inlet (upstream of the inlet valve) and outlet pressures (subroutines FPKO, FPKOUT), inlet temperature (subroutine FTKINN) and the new coefficient for pressure drop in the inlet valve (in case an inlet-valve-driven mass flow reduction has to be imposed - subroutine FZETAD).
- 3) The momentum equation is solved by means of a Predictor-Corrector method for deriving the coolant mass flow. The Predictor step is done by calculating the time derivative of the inlet mass flow at the previous time interval (variables with index "1" in the programme) and extrapolating over the length DTKUE of the actual micro-time step.

The Corrector step is performed in the subroutine ITC11 by iterating the discretized momentum equation within the actual micro-time step. The heat transfer coefficients clad-coolant and coolant-structure are calculated at temperatures derived by extrapolating the gradient at the previous time step.

Once the heat fluxes have been calculated, the temperature distribution in fuel, clad and structure is computed (see subroutine FBRT) and control is transferred back to the subroutine ITC1. The subroutine ITC11 also computes the variables QQ1 to QQ6 (above called simply "heat fluxes") which are either physical heat fluxes or heat transfer coefficients used to calculate heat fluxes. Two of them (QQ1 and QQ2) are quantities referred to the previous time step, while the other (QQ3 to QQ6) refer to

the actual time step and are updated in subroutine FBRT within the iteration scheme for calculating the temperature distribution. (During the two-phase flow calculation the terms QQ1 to QQ6 are computed in the subroutines SETUP (initialization of QQ1, QQ2), TLKM(QQ3 to QQ6), TLKMS (QQ1, QQ2) and ITCB (QQ3 to QQ6)).

- 4) The coolant pressure distribution is next calculated in subroutine ITC1.
- 5) Once the calculation is finished for the actual time step, variables with index "R" are loaded into the memory locations of variables with index "I" (for example: TKN1(M) = TKNR(M)) which are used for next time step.
- 6) In case the saturation temperature, plus a given superheat, is exceeded in the coolant a "boiling flag" (NBOIL(KKN)) is turned to 1.

At the end of a macro-time step the programme control is transferred to the calling subroutine STAT1 and variables (with index "I") are written onto the intermediate data set (subroutine TIØ) to be assessed for next macro-time step.

The solution of the continuity equation for the coolant is coupled to the solution of the momentum equation in step 3 above. It is simplified by assuming that the time variation of the coolant density is negligible. This approximation is acceptable when relatively slow mass flow variations have to be modelled. For these cases the use of the subroutines ITC1/ITC11 is therefore suitable. Otherwise, for fast coolant temperature transients, they are better replaced by the couple of subroutines ITC1R/ITC11R. An input flag (IFLAG1) allows choosing between them.

Subroutines ITC1R/ITC11R

These subroutines are formally identical to the above explained subroutines ITC1/ITC11 apart from the solution of the continuity equation for the coolant. It is solved numerically taking into account the time variation of the coolant density. These subroutines must therefore be used, in alternative to the above ones, in case fast coolant temperature transients have to be calculated.

For numerical details see Section II.C.2.2.3.

Subroutine ITSØL

Following the calculation of the vapour pressure distribution in the bubbles one has to guarantee that the mass of vapour corresponding to this pressure and temperature distributions is consistent with the mass of vapour corresponding to integral values (averaged over the bubble length) of pressure and temperature. In general a mass unbalance exists which must be got rid of by applying a small shift to the pressure (and temperature) distributions, taking the mass of vapour which corresponds to integral values as reference. This correction is performed in the subroutine ITSØL together with the calling subprogrammes which are

- Subroutine ITCB, after solving the vapour energy equation (call of Subroutine ENBLR) with values referring to time level t_n
- Subroutine DPDA, after calculating the new (time level t_n) vapour pressure and temperature distributions.
- Subroutine ATØM, after calculating the vapour pressure and temperature distributions following a bubble coalescence.

The correction of vapour pressure distribution to get rid of the mass unbalance is carried-out as follows.

Let

- m be an index running over the vapour bubble axial meshes
- p_{vm} be the vapour pressure in the mid point of mesh m
- T_{vm} the vapour temperature in the mesh m
- V_m the volume occupied by the vapour in the mesh m
- \bar{p}_v the integral value (averaged over the bubble length) of the vapour pressure
- \bar{T}_v the integral value of vapour temperature
- M the mass of vapour in the bubble considered.

$$XXV = \sum_m V_m \quad (16)$$

is the total volume occupied by the bubble, while

$$XXX = \sum_m \frac{P_{vm} V_m}{T_{vm}} = M \cdot R \quad (17)$$

represent, apart from the gas constant R, the mass of vapour in the bubble. If the vapour pressure and temperature distributions were consistent with the integral values \bar{p}_v , \bar{T}_v the ratio

$$\frac{XXX}{XXV} = \frac{\sum_m \frac{P_{vm} V_m}{T_{vm}}}{\sum_m V_m} \quad (18)$$

would be equal to

$$XK = \frac{\bar{p}_v}{\bar{T}_v} \quad (19)$$

In general there will be an integral "vapour mass unbalance" defined by

$$\delta = \frac{\sum_m \frac{P_{vm} V_m}{T_{vm}}}{\sum_m V_m} - \frac{\bar{p}_v}{\bar{T}_v} \quad (20)$$

for the full bubble and a local (mesh dependent) unbalance δ_m , defined by the relationship

$$\frac{\delta_m V_m}{\delta \sum_m V_m} = \frac{\frac{P_{mv} V_m}{T_{vm}}}{\sum_m \frac{P_{vm} V_m}{T_{vm}}} \quad (21)$$

This states that the ratio of the local unbalance to the integral unbalance (both multiplied by the respective volumes) is equal to the ratio of the vapour mass present in the mesh m to the total mass of vapour.

The local unbalance is hence given by

$$\delta_m = \delta \frac{\frac{P_{vm}}{T_{vm}} \sum_m V_m}{\sum_m \frac{P_{vm} V_m}{T_{vm}}} \quad (22)$$

In the subroutine ITSØL the local vapour pressure is slightly shifted with an iterative process which stops when the local unbalance has been compensated for.

Subroutine KØPHI

In case the fuel temperature calculated with the Gauss-Seidel iteration method in the Subroutine FBRT or FBRTB exceeds in a mesh node the fusion temperature, a correction is applied in the subroutine KØPHI. It consists in re-setting the calculated node temperature back to the fusion temperature and storing the energy which corresponds to the previously calculated temperature increment above the fusion temperature. This process goes on as long as the stored energy, integrated over the subsequent time steps, does not exceed the latent fusion heat necessary to melt the mass of fuel material associated to the node. Similar procedure applies in case the fuel temperature decreases below the fusion temperature, the latent fusion heat being in this case liberated during the solidifying process.

Details of the calculations performed in this subroutine are given in section II.C.2.4.

Subroutine KØPHIH

The same process used for the correction of fuel node temperature, in case it exceeds the fusion temperature (explained in the description of subroutine KØPHI), is applied in subroutine KØPHIH for the correction of a clad node temperature - see section II.C.2.4 for details.

Subroutine LHTCL (HCKUE, VKK, DH, TKK, TBULK, TWAND, PKK, CNN1, CNN2, CN1, CN2, CN3)

This subroutine computes the heat transfer coefficient clad-coolant for the single phase flow regime.

List of parameters:

HCKUE	heat transfer coefficient (output parameter) ($W/m^2 \text{ } ^\circ C$)
VKK	coolant velocity (m/sec)
DH	hydraulic diameter of the flow cross section (m)
TKK	coolant temperature ($^\circ C$)
TBULK	Reference bulk temperature ($^\circ C$)
TWAND	Reference wall temperature (in the actual code version set equal to the coolant temperature) ($^\circ C$)
PKK	coolant pressure (N/m^2)
CNN1	see input description (I.D.)
CNN2	I.D.
CN1	I.D.
CN2	I.D.
CN3	I.D.

The Nusselt number is calculated by:

$$Nu = \frac{\alpha D_h}{\lambda_{Na}} = CNN1 + CNN2 \cdot R_e^{CN1} \cdot P_r^{CN2} \left(\frac{TWAND}{TBULK} \right)^{CN3} \quad (23)$$

where $\alpha = HCKUE$, λ_{Na} is the thermal conductivity of sodium and with the default values

$$\begin{aligned} CNN1 &= 7. \\ CNN2 &= 0.025 \\ CN1 &= 0.8 \\ CN2 &= 0.8 \\ CN3 &= 0. \end{aligned} \quad (24)$$

Subroutine LHTST (STRUK, HCKUE, VKK, DH, VDUF, TKK, TBULK, TWAND, TST, PKK, CNN1, CNN2, CN1, CN2, CN3)

This subroutine calculates the heat transfer coefficient coolant-structure for the single phase flow regime. It takes into account the convective heat transfer at the structure inner surface and the heat transfer due to conduction through the structure material, under the assumption of a linear temperature distribution in the structure. The convective term is calculated as in the Subroutine LHTCL, while the contribution due to conduction is calculated as in Subroutine AKTST.

List of parameters:

STRUK	dummy
HCKUE	heat transfer coefficient (output parameter)($W/m^2 \text{ } ^\circ C$)
VKK	coolant velocity (m/sec)
DH	hydraulic diameter of the flow cross section(m)
VDUF	see input description (I.D.)
TKK	coolant temperature ($^\circ C$)
TBULK	{ reference bulk and wall temperatures (in the actual code version set equal to the coolant temperature)
TWAND	
TST	Structure temperature ($^\circ C$)
PKK	coolant pressure (N/m^2)
CNN1	I.D.
CNN2	I.D.
CN1	I.D.
CN2	I.D.
CN3	I.D.

Subroutine MIDI

It calculates the average coolant density separately in the liquid slugs and in the mesh zones partially or totally covered by the two phase flow region.

Subroutine PRELI

Calculates the pressure distribution in the liquid slugs by applying zone by zone the formula (32) of Section II.C.2.3.3.

Subroutine PRØBR

In case the temperature of at least one fuel node equals or exceeds the fusion temperature, this subroutine calculates the percentage of molten fuel material for the full axial zone. In a node where the melting (or solidifying) process is progressing the percentage of molten material is given by the ratio of the stored energy (see subroutine KØPHI) to the latent fusion heat necessary to melt the fuel material associated to the node.

Subroutine PRØCA

In case the temperature of at least one clad node equals or exceeds the fusion temperature, this subroutine calculates the percentage of molten clad material for the full axial zone. The percentage of the molten material in a single node is given by the ratio of the stored energy (during melting or solidification) to the latent fusion heat necessary to melt the material associated to the node.

Subroutine PRØVW

This subroutine calculates for every axial zone the percentage of power generated which is lost beyond the structure material to the adjacent medium (for instance by-pass flow). In a zone out of the fuelled region, which is only powered by irradiation, the heat losses may be a large fraction of the heat generated in the zone itself.

Furthermore, the subroutine calculates the percentage of heat losses for the full channel.

Subroutine RESET

It is called when a "long" vapour bubble (for which calculation of local pressure and vapour temperatures were performed) collapses to a "short" one (stretching over less than three meshes) and it calculates updated integral values of vapour pressure and temperature.

Subroutine REZØN

This subroutine is used at the end of a macro-time step to transfer, by making a linear interpolation, some physical quantities from the Lagrangian meshes in which they were calculated to the Eulerian meshes for which results are output. The physical quantities involved are: coolant pressure, temperature, mass flow rate and velocity in the liquid slugs. In the bubbles region the corresponding physical quantities (vapour pressure and temperature, flow rate and velocity) have been previously calculated (in Subroutine DPDA) in an Eulerian mesh and need only be formally transferred to the arrays containing values to be output. For the Eulerian meshes containing phase boundaries (between vapour bubbles and liquid slugs) values referring to either liquid or vapour are output according to the fact that either liquid or vapour occupies the mesh mid-point. The output values always refer to mid point of the Eulerian meshes. Vapour or liquid temperatures are next used in the Subroutine MIDI to calculate the coolant density, taking into account the volume occupied by the vapour.

The Subroutine REZØN may also be used in the calling subprogramme ITCB before the end of a macro-time step, in case only a vapour bubble is present in the channel and it vanishes, due to total vapour condensation. (In practice a bubble is considered to vanish when its axial length decreases below 0.5 mm). In this case REZØN defines in the coolant the initial conditions for the subsequent single phase flow calculation.

PROGRAMMING REMARKS

The following Fortran symbols must be defined for every Eulerian mesh M filled by the coolant: TKN1(M), PKMN1(M), XMAN1(M), VKMN1(M), by making a linear interpolation between suitably chosen values referring to Lagrangian meshes, stored in the arrays TL(K,ML), PL(K,ML), GL(K,2) for the liquid slug above the bubble K or TLE(K,ML), PLE(K,ML), GL(K,1) for the inlet liquid slug. ML in an

index, running from 1 to $MS_{\geq 1}$, which identifies in ascending order the Lagrangian meshes in the liquid slug above bubble K (or running from 1 to $LME_{\geq 1}$ to identify in descending order the Lagrangian meshes in the inlet liquid slug).

For a given Eulerian mesh M, the Subroutine first looks for the indexes of the Lagrangian meshes which overlap partially or totally the mesh M. Let ML_1 , ML_2 ($ML_2 > ML_1$) be the indexes of the first and last Lagrangian meshes overlapping the mesh M. If $ML_1 = ML_2$ (i.e. the Eulerian mesh is fully overlapped by only one Lagrangian mesh) the values of the physical variables of this Lagrangian mesh are transferred to mesh M.

If $ML_2 = ML_1 + 1$ a linear interpolation between these two Lagrangian meshes determines the values of the physical variables at the mid-point of mesh M.

If $ML_2 > ML_1 + 1$ (three or more Lagrangian meshes cover the Eulerian mesh M) the programme looks for the two Lagrangian meshes (with index ML_3 , ML_4) close to the mid-point of mesh M and interpolates linearly between them.

The above procedure applies also to the inlet slug, with the only difference that in this case the Lagrangian meshes are indexed from the top to the bottom (inlet).

Subroutine SETZ1R

This subroutine is called by subroutine ITCB after ending the calculation for the current time step Δt_n . It transfers the content of the storage locations referenced by programming symbols ending with the letter R (for instance $TCANR(M)$) to storage locations referenced by programming symbols ending with the integer 1 (for instance $TCAN1(M)$).

The content of the latter storage locations is transferred, via the subroutine $TI\emptyset$, to a sequential file to be assessed at next time step t_{n+1} , after ending the calculation for all channels at time step t_n .

Subroutine STATO

This subroutine performs the stationary calculation. Its main tasks can be subdivided as follows:

- 1) Reading input data. These can be split into a) data of general validity for the calculation (channel-independent data) and b) data referring to a single channel, mainly geometrical data, specific power and boundary

conditions. (Detailed information is given in the input-data description).

- 2) Calculation of further geometrical data and linear power generation. A full list of these geometrical data referring to clad and fuel discretization are given in section II-C-1.1.
- 3) Calculation of mass flow from the given temperature boundary conditions and channel power.
- 4) Calculation of axial temperature distribution taking into account heat losses beyond the structure material.
- 5) Calculation of coolant pressure drop in the channel. This pressure drop has to be smaller than the specified pressure drop between inlet (upstream of the inlet valve) and outlet, the difference being the pressure drop in the inlet valve.
- 6) Assuming the temperature distribution in the coolant as boundary condition, the heat diffusion equations are solved for fuel, clad and structure with the Gauss-Seidel iteration scheme. Three nodes are considered in the clad (associated to inner, middle and outer surfaces) and up to eleven nodes in the fuel (a central node and up to ten nodes in radial direction). One node is taken in the structural material.
- 7) Calculation of stationary fuel-clad gap width accounting for thermal strains.
- 8) Determination of the axial zones with peak coolant temperature and peak power generation (see input description for further details) to be used for "standard" and "bubble" plot initialization.
- 9) Initialization of variables for subsequent transient calculation. A number of variables have to be zeroed before the transient calculation starts.
- 10) Writing stationary results for the calculated channel onto an external file.

11) Stationary results are printed out in the following order:

- physical dimensions used
- channel number (KKN)
- channel type (KØNT) (see also input description)
- number of nodes in axial direction (NM2)
- last axial mesh of fuelled zone (NM1)
- number of axial nodes in fission gas region (NMO-1)
- number of radial nodes in fuel (NN) (beside the node on the fuel axis)
- length of fission gas region (HSPALT), length of core region (with-
out HSPALT: HKUEKA = HCØRE - HSPALT)
- grid distance (DABST)
- pressure drop coefficient PSI (see input description)

Geometrical data for the NM2 axial nodes are next printed out in the following order:

- axial node index M
- axial coordinate Z of the bottom boundary of the M-th zone
- length DELTZ of the M-th zone
- outer coolant channel radius (RKUE)
- fuel outer radius (RBR)
- clad thickness (DCAN)
- stationary gap width (DBØND)
- ratio structure volume to inner surface area (VDUF)
- structure volume (VSTRUK)
- hydraulic diameter of the coolant channel (DH)

For the axial zones from NMO to NM1 inclusive are then printed out:

- percentage of power generated in fuel, clad, coolant and structure
(ANTB, ANTC, ANTK, ANTS respectively)
- specific power (QGES) (in W/m^3)
- linear power (CHIST) (W/m)
- ratio real fuel density to theoretical density (DPO)
- percentage of Plutonium in fuel (CNPU)
- stoichiometric Oxygen to metal ratio of the fuel (STØE)
- ratio of pin circumference to area of flow section (XBRKT)

- ratio of structure inner circumference to area of flow section (XSTKT)
- area of flow section (AR)
- Reynolds number of the flow (RE)

The radial power distribution in the fuel pellet and the total pin power are printed next.

Temperature distributions are headed by following information:

- number of iterations (ITM) performed to calculate the coolant temperature distribution
- coolant mass flux (XXMAN1). Remark that in the calculation the mass flow (kg/ sec) is used, while the mass flux (kg/m²sec) is printed out.
- coolant inlet temperature (TKINNO) and pressure upstream of the inlet valve.
- coolant outlet temperature (TKOUT) and pressure.

These are followed by:

- axial node index (M)
- axial coordinate (Z) of bottom boundary of the M-th zone
- coolant velocity (VKMN)
- coolant pressure (PKMN)
- structure temperature (TST)
- coolant temperature (TKN)
- clad temperatures in the outer (TCA), middle(TCM) and inner radial nodes (TCI).

Fuel temperatures follow for the axial nodes from NMO to NM1 inclusive:

- average fuel temperature (TBM)
- central fuel temperature (TBO)
- radial fuel temperatures in the NN radial zones, TB(1) to TB(NN).

All above values refer to the mid-point of an axial zone.

Calculated pressure drops and heat losses follow in the order:

- channel pressure drop (DPGNR) (without accounting for inlet valve pressure drop)

- inlet valve pressure drop (DLPBL1)
- coefficient for pressure drop calculation in the inlet valve (ZETADO) (see description of subroutine FZETAD)
- thickness of fuel-clad gap (SPALT) and assumed heat transfer coefficient through the gap (HBRC)
- power loss in every axial mesh (W)
- percentage of power losses in every axial mesh
- linear power losses (W/m) in every axial mesh
- calculated structure temperature (TSTNR), assumed temperature of by-pass flow (if any) (TBYPSR) and their difference (TSTNR-TBYPSR), which determines the power losses to the by-pass flow.
- total power losses in the channel
- percentage of power lost in the full channel.

"Standard" and "Bubble" plots information follow:

- length in 4-Bytes words of vectors containing data to be plotted (NZS, NZB respectively). Apart from a few heading words these lengths depend on the number of channels NKKN.
- zone with peak power (MPEAK) and with coolant peak temperature (NMP)
- specific power (QGES) in the MPEAK zone.
- inlet pressure (PKOO), outlet pressure (PKONO) and pressure drop (DPS) (values transferred to the plotting subroutines).

Subroutine STAT1 (MAIN Programme)

This subroutine drives the stationary and transient calculations. Its main functions are performed in the following order:

- 1) Reading input data of interest for transient calculation (see input description)
- 2) In case the problem time is zero, the stationary calculation is performed by means of subroutine STATO (see description of subroutine STATO) and subsequently files are initialized for data to be plotted. This step 2 is skipped in case the problem time is greater than zero (restart).
- 3) Data from the previous (stationary or transient) calculation are read

from the apposite data set (see input description and data sets management).

- 4) Time dependent power generation and by-pass flow temperature are fetched by calling the subroutines WQDT, TBPS.
- 5) The logical decision of carrying on a single phase or a two-phase calculation is then taken on the basis of the results from the calculation of previous time step. In the first case the subroutine ITC1 or ITC1R is called, in the second case the subroutine ITCB. An input flag (IFLAG) allows choosing between the subroutines ITC1 and ITC1R for the single phase calculation. The continuity equation is solved in ITC1R accounting for the time derivative of coolant density, which is neglected in ITC1. ITC1R has therefore to be preferred for fast coolant temperature transients while ITC1 may be used for slow transients.
- 6) In case a single phase calculation has been performed and the saturation temperature has been reached in the coolant, the two phase flow calculation is initialized by calling the subroutine SETUP.
- 7) At the end of a time step results for the computed channel are written on an external data set.

Steps 3) to 7) are repeated for all the channels, afterwards time is incremented by a time step. The calculation stops when either the maximum problem time has been exceeded or the CPU time left available is less than three times the duration of the calculation for last time step. In both cases a restart file is written.

Subroutine SETUP

This subroutine initializes the symbols characterizing a vapour bubble in a coolant zone where the saturation temperature has been exceeded by the given amount of superheat. The subroutine is called for the first time by the subroutine STAT1 for the initialization of the first bubble at the transition from single phase flow to two phase flow. Subsequently it is called by subroutine ITCB, the driving subprogramme for the two phase flow calculation. As the treatment of the Lagrangian meshes in the coolant is different in the two

cases (depending on whether separated liquid slugs previously existed or not) the subroutine is correspondingly split into two main branches: the first initializes the very first bubble, the second every subsequent one. In any case the bubble is initialized at the lower boundary of a coolant zone with a length of 0.5 mm. Following sketch (1) shows the meaning of some symbols characterizing its position. Basically initialization of a bubble implies:

- a) definition of its position with respect to the Eulerian meshes.
- b) determination of average vapour temperature and pressure
- c) definition of initial film thickness
- d) (only for the very first initialization of the bubble (call from STAT1)) definition of heat fluxes from vapour to clad and coolant (symbols QQ1, QQ2). This heat fluxes initialization is not required for subsequent bubbles, as it occurs in subroutine ITCB.
- e) solution of momentum equation for the upper and lower liquid slugs determining the liquid slug velocities and the time derivative of the coolant mass flow for the slugs.
- f) definition of Lagrangian meshes in the liquid slugs and calculation of temperature and pressure distributions
- g) calling the subroutine BØRN which I) determines the new bubble configuration ordered from inlet to outlet of the channel and assigns to the new bubble an index K stored in the array IND; II) assigns to the bubble of index K a number stored in the array IDK which implicitly determines the lower and upper phase boundaries (see subroutine IDENT)
- h) set the index NBOIL (KKN) to a value greater than zero (thus indicating boiling inception), and initialize the time since boiling TBOIL (KKN).

The symbols to be defined when a bubble with index K is initialized in the zone MB are listed hereafter: (see also list of symbols for the physical meaning)

ZL(K,1), ZL(K,2)
DZK(K,1), DZK(K,2)
DDELTZ(K,1), DDELTZ(K,2)
PV(K)
TV(K)
SCL(MB), SST(MB)
SCL1(K), SCL2(K)

SST1 (K), SST2(K)
GL(K,1), GL(K,2)
FF(K,1), FF(K,2)

For the liquid slug above the bubble:

TL(K,I)
PL(K,I) I ranging from 1 to LM(K) (= number of
DZK(K,I) Lagrangian meshes in the slug above the bubble K)
VDZK(K,I)

For the liquid slug below the bubble (assuming it is the lowermost slug):

TLE(I)
PLE(I) for I ranging from 1 to LME (number of Lagrangian
DZKE(I) meshes in the lowermost slug)
VDZKE(I)

Following sketch I shows the meaning of some symbols characterizing a bubble just after initialization. Sketch II shows the same symbols for a bubble stretching over three Eulerian meshes. Sketch II is complemented by the list of symbols given in Table IV, which summarizes the words which have to be defined in a bubble with reference to vapour mass flow, pressure, temperature, density and liquid film thickness).

(Remark: symbols shown in sketches I, II refer to time t_{n-1} , while symbols of Table IV, ending with the letter R refer to time t_n).

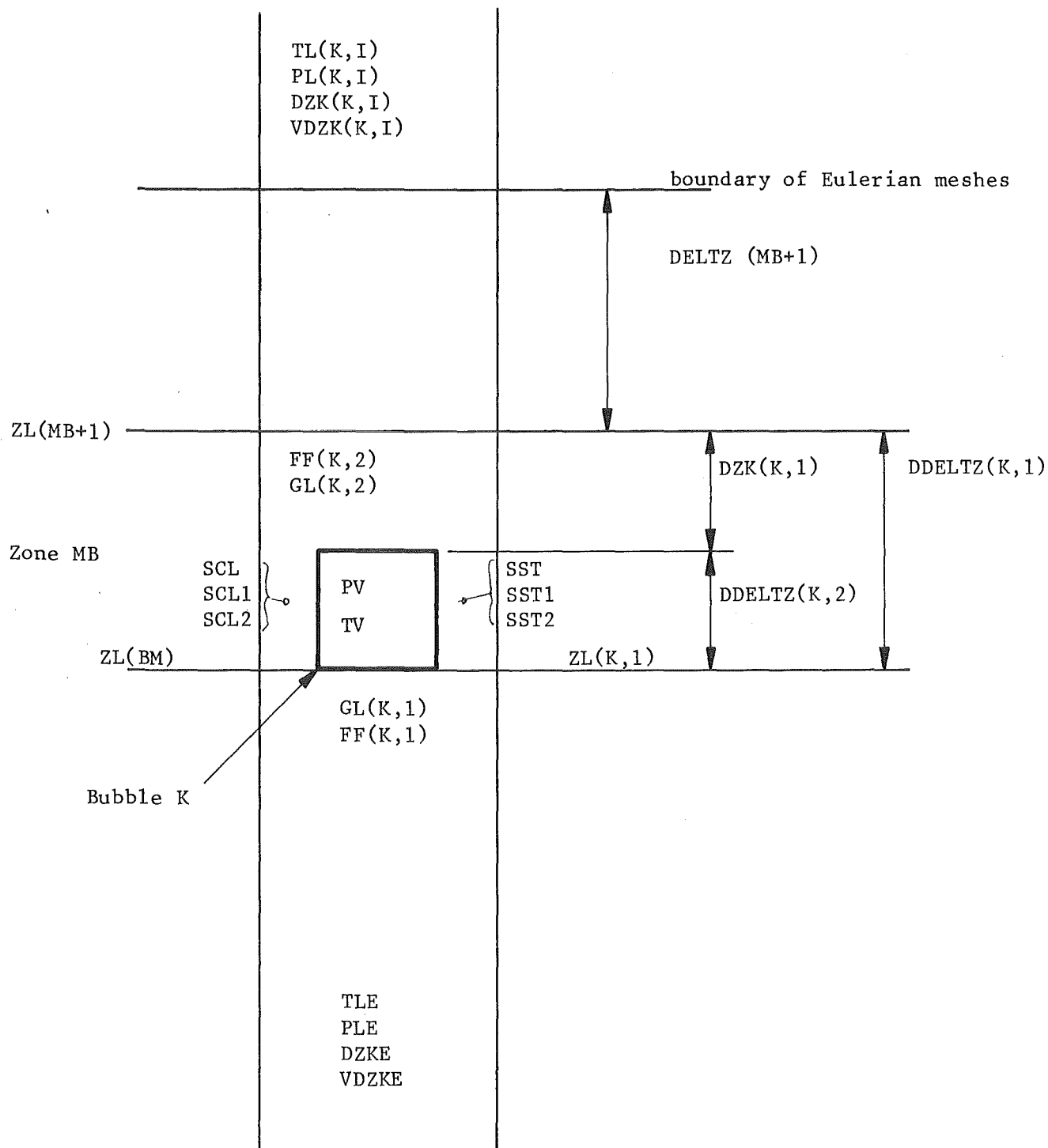


Fig. 17: Sketch I - Symbols characterizing a bubble initialized in Subroutine SETUP

Fig. 18: Sketch II - Symbols characterizing the configuration of a bubble stretching over at least three Eulerian meshes-
(See also Table IV)

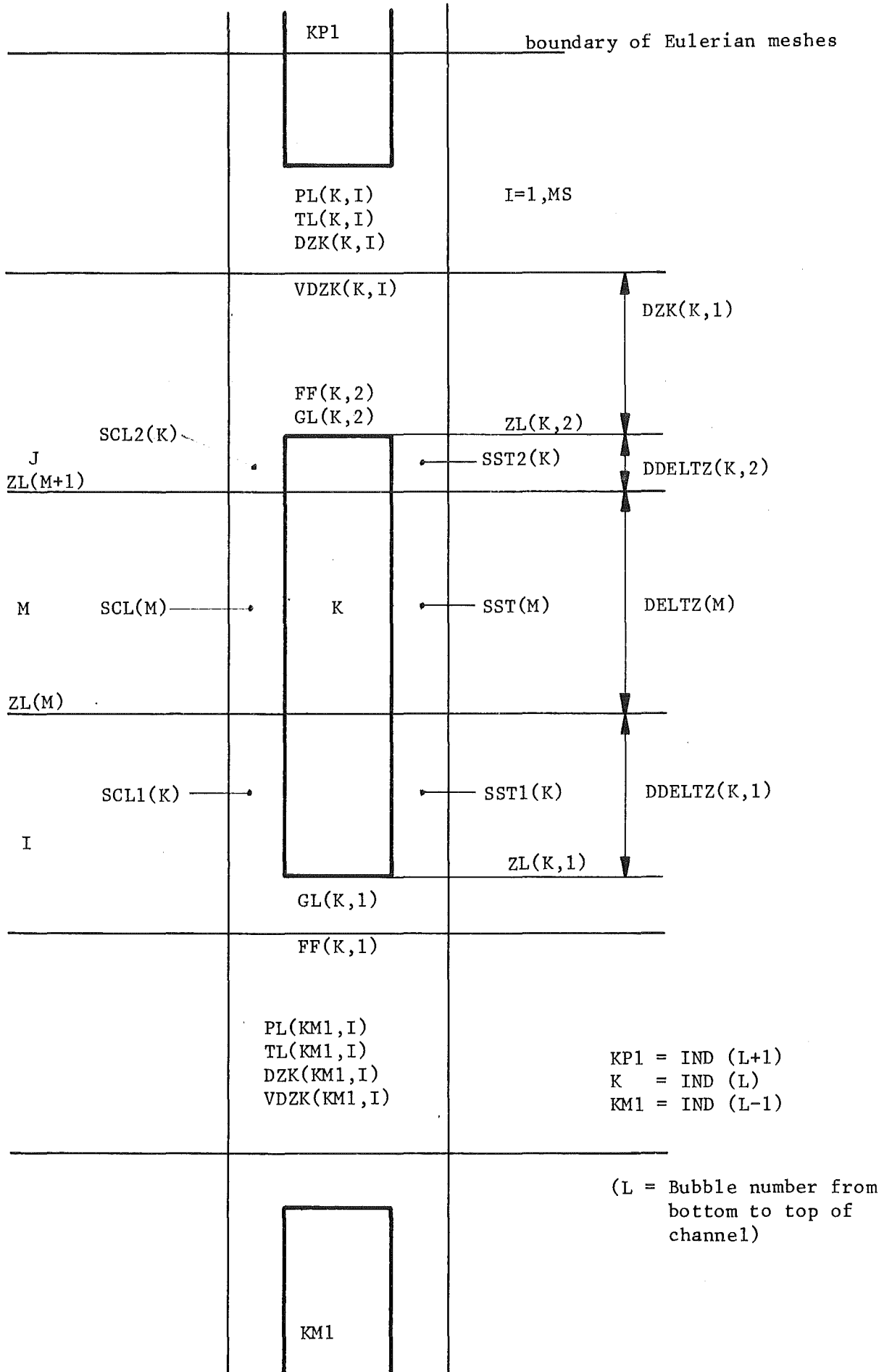


TABLE IV - Symbols which define the physical state of a bubble K stretching over at least three Eulerian meshes with reference to vapour mass flow (G), pressure (P), temperature (T), density (R), liquid film thickness at clad and structure (S). (Symbols refer to time t_n).

	G	P	T	R	S
In the bubble uppermost Eulerian mesh	GVFR(K,2)	PVFR(K,2)	TVFR(K,2)	RØVRK(K,2)	SCL2(K)
	GV2R(K)	PV2R(K)	TV2R(K)	RØV2R(K)	SST2(K)
In all bubble inner meshes	GVØR(M)				
	GVMR(M)	PVMR(M)	TVMR(M)	RØVMR(M)	SCL(M)
	GVIR(M)				SST(M)
In the bubble lowermost Eulerian mesh	GV1R(K)	PV1R(K)	TV1R(K)	RØV1R(K)	SCL1(K)
	GVFR(K,1)	PVFR(K,1)	TVFR(K,1)	RØVFR(K,1)	SST1(K)
Integral values		PVR(K)	TVR(K)		

(Symbols without the end letter R, for instance GVF(K,2), refer to the previous time step t_{n-1}).

Subroutine STEP

Performs the time step control during the two-phase flow calculation. Determines the micro-time step as a fraction of the given macro-time step, taking into account convergence criteria and time derivatives of some parameters characterizing the bubbles pressure and volume. See section II.C.3.1 for details.

Subroutine STØFF

It calculates the following derivatives

- dT_v/dp_v (DTDP) derivative of vapour temperature with respect to pressure at saturation
- $d\rho_v/dp_v$ (DRØDP) derivative of vapour density with respect to pressure at saturation
- dH_l/dp_l (DHLDP) derivative of liquid specific enthalpy with respect to pressure.

Subroutine TIØ

At the end of a macro-time step it writes channel dependent data onto a contemporary disk and reads then back at the beginning of next macro-time steps (see also section III.5).

Subroutine TLKM

Solves the energy equation for liquid slugs with reference to Lagrangian meshes as explained in Section II.C.2.3.3.c and using values referred to the actual time level t_n .

Subroutine TLKMS

As for Subroutine TLKM, but using values referred to the time level t_{n-1} .

Subroutine TRANS

It calculates the updated axial position of the liquid-vapour interfaces ZL (lower and upper bubble boundaries) by

$$ZL^{n+1} = ZL^n + \left(\frac{dz}{dt}\right)^n \Delta t_n \quad (25)$$

where the time derivative of the interface displacement is given by

$$\left(\frac{dz}{dt}\right)^n = \left(\frac{G_K}{\rho_K}\right)^n \quad (26)$$

The mass flux in the liquid slugs G_K is provided by the calculation performed in the Subroutine IMGL.

Subroutine XCFI (CFI, TK, GG, DH, SCL, SST, CH21, CH22, IFLAG1, IFLAG2, VKMR, ALPHA, M, PSI, DABST, SSS, NGRID, NM1)

This subroutine computes the friction coefficient at the interface liquid-vapour in the two-phase flow region. The flag IFLAG2 allows choosing between the application of the Wallis formula (57) or of the two-phase multiplier concept with the Lockhart-Martinelli (57) correlation (77). (See Section II.C.2.3.5). In the first case the liquid film velocity may be optionally calculated (and applied to solve the continuity equation for the liquid film phase in subroutine FITHI); in the second case the liquid film velocity is always calculated.

List of parameters

CFI	Interfacial friction coefficient (output parameter)
TK	Vapour temperature ($^{\circ}\text{C}$)
GG	Vapour mass flux ($\text{kg}/\text{m}^2 \cdot ^{\circ}\text{C}$)
DH	Hydraulic diameter of flow cross section (m)
SCL	Thickness of liquid film at the clad surface (m)
SST	Film thickness at the structure surface (m)

CH21	see input description (I.D.)
CH22	I.D.
IFLAG1	I.D.
IFLAG2	I.D.
VKMR	Liquid film velocity (m/sec)
ALPHA	Void fraction
M	axial mesh index
PSI	I.D.
DABST	I.D.
SSS	Equivalent liquid film thickness (resulting from the contributions of both SCL and SST) used for calculating the interfacial friction coefficient.
NGRID	I.D.
NM1	I.D.

Subroutine XFF1 (NGRID, KUEL, XFF1, DH, TKNN, VKK, PKNN, CH21, CH22, PSI, DABST, NM1, M)

This subroutine computes the friction coefficient for the single phase flow as function of the flow Reynolds number. Additional pressure drops due to the spacers are taken into account.

List of parameters

NGRID	see input description (I.D.)
KUEL	I.D.
XFF1	friction coefficient for single phase flow pressure drops (output parameter)
DH	hydraulic diameter of flow cross section (m)
TKNN	coolant temperature ($^{\circ}$ C)
VKK	coolant velocity (m/sec)

PKNN	coolant pressure (N/m ²)
CH21	I.D.
CH22	I.D.
PSI	I.D.
DABST	I.D.
NM1	I.D.
M	axial zone index

2.2 Problem oriented Subroutines

a) Subroutines of GROUP 2a (General)

Subroutine BLØPLØ (VCPØ)

It allows the user to write every IDELTT time steps onto file FT13F001 (see Section III.5) an array of data for option plot generation. The array VCPØ of length 273 words has to be filled partially or totally by the user with any data transferred to this Subroutine by means of the COMMON Blocks.

Subroutine FPKØUT (NKKN, KKN, TTKU, PKØNO, PKØN1, PKØN)

This subroutine allows programming the time variation of coolant outlet pressure.

List of parameters:

NKKN	number of equivalent channels
KKN	channel index
TTKU	actual problem time (sec)
PKØNO	stationary outlet coolant temperature (N/m^2)
PKØN1	coolant pressure in the zone $M=NM2$ at time t_{n-1} (N/m^2)
PKØN	coolant pressure in the zone $M=NM2$ at time t_n (time TTKU) (N/m^2)

Subroutine FPKO (NKKN, KKN, TTKU, PKOO, PKON1, PKON, PKØNO, PKON1, PKØN, PDEC1, PDEC2, PDEC3)

This subroutine allows programming the time variation of coolant inlet pressure, upstream of the inlet valve.

List of parameters:

NKKN	number of equivalent channels
KKN	channel index
TTKU	actual problem time (sec)
PKOO	stationary inlet coolant pressure (N/m^2)

PKON1	coolant pressure in the zone M=1 at time t_{n-1}	(N/m ²)
PKON	coolant pressure in the zone M=1 at time t_n (time TTKU)	(N/m ²)
PKØNO	stationary outlet coolant pressure	(N/m ²)
PKØN1	coolant pressure in the zone M=NM2 at time t_{n-1}	(N/m ²)
PKØN	coolant pressure in the zone M=NM2 at time t_n (time TTKU)	(N/m ²)
PDEC1	} coefficients for programming a pump coast down (see input description)	
PDEC2		
PDEC3		

Subroutine FTKINN (NKKN, KKN, TTKU, TKINNO, TKIN1, TKINR)

This subroutine allows to programme the time variation of the coolant inlet temperature.

List of parameters:

NKKN	number of equivalent channels (see input description)
KKN	channel index
TTKU	actual problem time (sec)
TKINNO	stationary coolant inlet temperature (°C)
TKIN1	coolant temperature in the zone M=1 at time t_{n-1} (°C)
TKINR	coolant inlet temperature in the zone M=1 at time t_n (time TTKU) (°C)

Subroutine FZETAD (NKKN, KKN, TTKU, ZETADO, ZETAD)

This subroutine allows to simulate a coolant mass flow reduction by programming the time variation of the inlet valve pressure drop coefficient.

List of parameters:

NKKN	number of equivalent channels
KKN	channel index
TTKU	actual problem time (sec)
ZETADO	stationary inlet valve pressure drop coefficient (this value is calculated by the subroutine STATO and must not be modified)
ZETAD	inlet valve pressure drop coefficient at time TTKU.

The pressure drop in the inlet valve is calculated by

$$\Delta p_{B1} = ZETAD \cdot \frac{G^2}{2\rho} \quad (27)$$

where G is the coolant mass flow and ρ the coolant density at inlet.

Subroutine TBPS (NM2, TT, DELTT, TKINNO)

This subroutine is used to programme the time variation of the by-pass flow temperature.

List of symbols:

NM2	number of axial zones
TT	problem time at the end of the macro-time step (sec)
DELTT	macro-time step (sec)
TKINNO	stationary coolant inlet temperature ($^{\circ}$ C)

The by-pass temperature TBPSR(M) and TBPPS1(M), referred to time level t_n

and t_{n-1} respectively, are transferred through a COMMON block. Unless otherwise programmed by the user the by-pass temperature is taken constant and equal to the stationary inlet temperature of the coolant (TKINNO).

Subroutine WQDT (NKKN, NM2, KKN, QGESO, QGES, QGEST, T, DELTT, TEND)

This subroutine is used to programme the time variation of the specific power generation.

List of parameters:

NKKN	number of equivalent channels
NM2	number of axial zones
KKN	channel index
QGESO	stationary specific power generation (W/m^3)
QGES	specific power generation at the beginning of the macro-time step (W/m^3)
QGEST	specific power generation at the end of the macro-time step (time T) (W/m^3)
T	problem time at the end of the macro-time step (sec)
DELTT	macro-time step (sec)
TEND	problem end-time (sec).

Subroutine WWST (M, NMO, NM1, T1, TS1, XKS, INDEX)

This subroutine computes the heat transfer coefficient from the structure material to an external medium (for instance to a by-pass flow) for calculating the power losses. In case the heat transfer coefficient is set to zero the channel structure is considered to be adiabatic.

List of parameters:

M	axial zone index
NMO	first fuelled axial zone
NM1	last fuelled axial zone (see input description)

T1 by-pass flow temperature ($^{\circ}\text{C}$)
TS1 structure material temperature ($^{\circ}\text{C}$)
XKS heat transfer coefficient (output parameter) ($\text{W}/\text{m}^2 \text{ }^{\circ}\text{C}$)
INDEX index allowing to choose between a formula valid for the stationary case (INDEX = 0) and a (time dependent) formula for the transient case (INDEX = 1).

Subroutine XABRC (HBRC, HGAP, TCINN, TCCM, DBØND, RBR, BØND, M)

This subroutine computes the fuel-clad heat transfer coefficient.

List of parameters:

HBRC fuel-clad heat transfer coefficient (output parameter)
HGAP see input description (I.D.) ($\text{W}/\text{m}^2 \text{ }^{\circ}\text{C}$)
TCINN superficial fuel temperature ($^{\circ}\text{C}$)
TCMM inner clad superficial temperature ($^{\circ}\text{C}$)
DBØND fuel-clad gap (See input description) (m)
RBR outer fuel radius (m)
BØND dummy
M axial zone index.

b) Subroutines of GROUP 2b (Leakage flow option)

With the exception of LZETAD, the Subroutines of this group replace corresponding standard subroutines, the difference just concerning programme details which are too laborious to be reported.

BYPASS is the Member name and contains the MAIN programme (thus replacing STAT1)

Subroutines FZETA1 and FZETA2 are used together with LZETAD (see later) to calculate a very smooth time variation of the pressure drop coefficient in the inlet valve. They are basically equivalent to Subroutine FZETAD).

Subroutine LITCB replaces ITCB

Subroutine LITC1 replaces ITC1

Subroutine LITC11 replaces ITC11

Subroutine LITC1R replaces ITC1R

Subroutine LTC11R replaces ITC11R

Subroutine LZETAD (NKKK, KKN, TTKU, ZETADO, ZETAD)

For the list of parameters see Subroutine FZETAD.

This subroutine is used in case a leakage flow in parallel to the main coolant flow must be simulated. It allows to impose a mass flow reduction by programming the time variation of the inlet valve pressure drop coefficient.

With reference to the formulas (23) to (27) of section II.C.3.4 the calculation performed in this subroutine goes through the following steps.

- i) ζ is calculated first by means of a time function supplied by the user, of the type $\zeta = \zeta_0 \exp(at)$ where ζ_0 is the stationary value of the pressure drop coefficient for the inlet valve (automatically computed in subroutine STATO), 'a' is a suitable constant and t is time.
- ii) The pressure drop across the channel Δp_c is calculated by using the channel mass flow rate G_c from the previous time step.
- iii) An analytical or empirical relationship between the channel pressure drop and the leakage flow has to be supplied by the user on the basis of the characteristics of the experimental facilities. From this relationship the leakage flow rate is derived.
- iv) Equation (25) of section II.C.3.4 supplies the equivalent pressure drop coefficient ζ_e .
- v) Equation (24) is then applied by introducing ζ_e instead of ζ :

$$\Delta p_{B1} = \zeta_e \frac{|G_c| G_c}{2\rho} \quad (28)$$

2.3. Functions

The Functions of the following list are essentially the same as in the MAPLIP (See reference /9/), the only difference consisting in that they are organized in separate Members and are directly accessed by the programme. The Functions are listed in the same sequence as they are included in the respective Members (see Group 3 in Section 1.1).

a) Member UPUØ

It contains functions used for calculating physical properties of fuel.

Function RØUPUØ (TK, PØRVØL, CNPU)

It calculates the fuel density (kg/m^3) as function of:

TK fuel temperature ($^{\circ}\text{K}$)
PØRVØL fraction of fuel volume occupied by pores
CNPU concentration of Plutonium oxide in the fuel.

Function WLUPUØ (TK, XPØR, CNPU, S)

It calculates the thermal conductivity ($\text{W/m } ^{\circ}\text{K}$) of the fuel as function of:

TK fuel temperature ($^{\circ}\text{K}$)
XPØR fraction of fuel volume occupied by pores
CNPU concentration of plutonium oxide in the fuel
S stoichiometry (oxygen to metal O/Me ratio).

Function CPUPUØ (TK)

It calculates the specific heat at constant pressure ($\text{J/Kg } ^{\circ}\text{K}$) of fuel as function of its temperature TK ($^{\circ}\text{K}$).

Function FTUPUØ (CNPU)

It calculates the fuel fusion temperature ($^{\circ}\text{K}$) depending on the concentration of plutonium oxide (CNPU).

Function FHUPUØ (DUMMY)

It calculates the latent heat of fuel (J/Kg).

Function RHUPUØ (DUMMY)

It calculates the latent heat released by the fuel material during solidification (J/kg).

Function GAUPUØ (TK)

It calculates the thermal linear expansion coefficient for fuel material ($^{\circ}\text{K}^{-1}$) as function of its temperature TK ($^{\circ}\text{K}$).

b) Member CAN4981

It contains Functions for calculating physical properties of cladding (Steel 4981)

Function WLCAN (TK)

It calculates the thermal conductivity of the clad material ($\text{W}/\text{m}^2\text{K}$) as function of its temperature TK ($^{\circ}\text{K}$).

Function RØCAN (TK)

It calculates the clad density (kg/m^3) as function of its temperature TK ($^{\circ}\text{K}$).

Function FTCAN (DUMMY)

It calculates the clad fusion temperature ($^{\circ}\text{K}$).

Function CPCAN (TK)

It calculates the specific heat of clad material ($\text{J}/\text{kg } ^{\circ}\text{K}$) at constant pressure, as function of its temperature TK ($^{\circ}\text{K}$).

Function RHCAN (DUMMY)

It calculates the latent heat released by the clad material during solidification (J/kg).

Function FHCAN (DUMMY)

It calculates the clad latent fusion heat (J/kg).

Function GACAN (TK)

It calculates the thermal linear expansion coefficient for clad material ($^{\circ}\text{K}^{-1}$) as function of its temperature TK ($^{\circ}\text{K}$).

c) Member NATRIUM

It contains Functions for calculating physical properties of sodium.

Function RØNAL (TK)

It calculates the sodium density (Kg/m^3) at saturation temperature TK ($^{\circ}\text{K}$).

Function RØNAVS (TK)

It calculates the density (kg/m^3) of sodium vapour at saturation temperature TK ($^{\circ}\text{K}$).

Function CPNAL (TK, PNM2)

It calculates the specific heat ($\text{J}/\text{kg } ^{\circ}\text{K}$) of sodium at constant pressure PNM2 (N/m^2) as function of its temperature TK ($^{\circ}\text{K}$).

Function CPNALS (TK)

It calculates the specific heat ($\text{J}/\text{kg } ^{\circ}\text{K}$) of sodium vapour at saturation temperature TK ($^{\circ}\text{K}$).

Function WLNAL (TK)

It calculates the thermal conductivity ($\text{W}/\text{m } ^{\circ}\text{K}$) of liquid sodium as function of its temperature TK ($^{\circ}\text{K}$).

Function PRNAL (TK, PNM2)

It calculates the Prandtl number of sodium as function of its temperature TK ($^{\circ}\text{K}$) and pressure PNM2 (N/m^2).

Function ZDNAL (TK)

It calculates the dynamic viscosity of sodium ($\text{N sec}/\text{m}^2$) as function of its temperature TK ($^{\circ}\text{K}$).

Function ZDNAV (TK)

It calculates the dynamic viscosity of sodium vapour (N sec/m^2) as function of its temperature TK ($^{\circ}\text{K}$).

Function EHNAL (TK, PNM2)

It calculates the specific enthalpy (J/kg) of liquid sodium as function of its temperature TK ($^{\circ}\text{K}$) and pressure PNM2 (N/m^2).

Function EHNALS (TK)

It calculates the specific enthalpy (J/kg) of sodium vapour at temperature TK ($^{\circ}\text{K}$).

Function FPNA (TK)

It calculates the pressure (N/m^2) of sodium vapour at saturation temperature TK ($^{\circ}\text{K}$).

Function VTNA (PNM2)

It calculates the saturation temperature ($^{\circ}\text{K}$) of sodium vapour corresponding to the pressure PNM2 (N/m^2).

Function VHNA (TK)

It calculates the vaporization enthalpy (J/kg) of sodium at temperature TK ($^{\circ}\text{K}$).

Function VØNAV (TK, PNM2)

It calculates the specific volume (m^3/kg) of sodium vapour at temperature TK ($^{\circ}\text{K}$) and pressure PNM2 (N/m^2).

Subroutine X1X2X4

Auxiliary subroutine, called by Function VHNA, to calculate the molecular weight of sodium.

d1) Member STRUNIØB

It contains Functions for calculating physical properties of Niobium as structural material.

Function RØSTRU (TK)

It calculates the structural material density (kg/m^3) as function of its temperature TK ($^{\circ}\text{K}$).

Function CPSTRU (TK)

It calculates the specific heat at constant pressure ($\text{J/kg } ^{\circ}\text{K}$) of structural material as function of its temperature TK ($^{\circ}\text{K}$).

Function WLSTRU (TK)

It calculates the thermal conductivity ($\text{W/m } ^{\circ}\text{K}$) of structural material as function of its temperature TK ($^{\circ}\text{K}$).

Function FTSTRU (DUMMY)

It calculates the fusion heat (J/kg) of structural material.

d2) Member STRU4981

This Member contains Functions with the same name as those of the previous Member, but calculating physical properties of Steel 4981 as structural material.

3. List of FORTRAN Symbols

Symbol and dimensions	Common Block	Definition and Units
A	AZDM	Parameter used to programme the time variation of the inlet valve pressure drop coefficient according to the formula $ZETAD = ZETADO \exp(A \cdot TTKU)$ (to be supplied by the user in the Subroutine LZETAD and (not in common) in the subroutine FZETAD (sec^{-1}))
ANTB(30)	DTIT7	Percentage of channel power density produced in the fuel (dimensionless) (see input description)
ANTC(30)	DTIT7	Percentage of channel power density produced in the clad material (dimensionless) (see input description)
ANTK(30)	DTIT7	Percentage of channel power density produced in the coolant (dimensionless) (see input description)
ANTS(30)	DTIT7	Percentage of channel power density produced in the structure material (dimensionless) (see input description)
AQG	-	Flow rate through inlet valve (m^3/h)
AR(30)	DTIT5	Area of flow cross section in axial mesh zone M (m^2)
AR1	A1FA2F	Area of flow cross section in the first (inlet) axial mesh zone (=AR(1)) (m^2)
AV	DTIT5	Ratio of flow cross section area in axial mesh zone NM1 to cross section area in axial mesh zone NM2

Symbol and dimensions	Common Block	Definition and Units
A1F	-	<p>Coefficient which relates the pressure drop Δp_{Dyn} across the leakage flow path to the leakage mass flow rate M_f by means of the formula</p> $\Delta p_{\text{Dyn}} = a_{1f} \cdot M_f + a_{2f} \cdot M_f \cdot M_f$ <p>(to be supplied by the user in case leakage path has to be simulated) ($\text{m}^{-1} \text{sec}^{-1}$)</p>
A2F	A1FA2F	<p>Coefficient which relates the pressure drop across the leakage flow path to the leakage flow rate by means of the above formula (to be supplied by the user in case leakage path has to be simulated) ($\text{m}^{-1} \text{kg}^{-1}$)</p>
BETA2 (M)	DITCB2	<p>Auxiliary coefficient (ratio of velocity of phase boundary to length of bubble partial end mesh zone) to calculate the film thickness in the end meshes of a bubble (see equation (61) of /1/ (sec^{-1})) (See also equation 54 of section II.C.2.3.4)</p>
BOND	DTIT8	Name of bonding (see input description)
CAN	DTIT8	Name of clad material (see input description)
CHIST(30)	DTIT7	Channel linear power in axial mesh M (W/m)
CH21	DTIT8	Coefficient used to calculate the friction factor for single phase flow (see input description) (dimensionless)
CH22	DTIT8	Coefficient used to calculate the friction factor for single phase flow (see input description) (dimensionless)
CNN1	DTIT8	Coefficient used to calculate the clad-coolant heat transfer coefficient (see input description) (dimensionless)
CNN2	DTIT8	Coefficient used to calculate the clad-coolant heat transfer coefficient (see input description) (dimensionless)

Symbol and dimensions	Common Block	Definition and Units
CN1	DTIT8	Coefficient used to calculate the clad-coolant heat transfer coefficient (see input description) (dimensionless)
CN2	DTIT8	Coefficient used to calculate the clad-coolant heat transfer coefficient (see input description) (dimensionless)
CN3	DTIT8	Coefficient used to calculate the clad-coolant heat transfer coefficient (see input description) (dimensionless)
CNPU(30)	DTIT8	Percentage of PuO in the fuel (see input description)
CPK (30)	DTIT10	(In this Common block only in Subroutine STATO) Coolant specific heat (J/kg °C)
DABST	DTIT5	Distance between grid spacers (see input description) (m)
DBØND(30)	DTIT5	Width of gap between fuel and clad (m)
DCAN(30)	DTIT5	Clad thickness (m)
DDELTZ(10,2)	DTIT4	Distance between lower/upper (I=1/2) phase boundary of bubble with index K and Eulerian mesh boundary above/below (I=1/2) it (m)
DELHA(30)	DTIT10	Parameter which characterizes the phase state of clad material associated to the outer surface node in the axial mesh zone M (DELHA(M)=1 if the material is completely molten; DELHA(M)=0 if the material is either solid or not completely molten (dimensionless)
DELHI(30)	DTIT10	Parameter characterizing the phase state of clad material associated to the inner surface node in the axial mesh zone M (dimensionless)
DELHM(30)	DTIT10	Parameter characterizing the phase state of clad material associated to the middle surface node in the axial mesh zone M (dimensionless)

Symbol and dimensions	Common Block	Definition and Units
DELMBN(30,10)	DTIT8	Parameter which characterizes the phase state of fuel material in the axial mesh zone M, radial node N (DELMBN(M,N)=1 if the material is completely molten; DELMBN(M,N)=0 if the material is either solid or not completely molten) (dimensionless)
DELMBO(30)	DTIT8	Parameter characterizing the phase state of central node fuel material in the axial zone M (dimensionless)
DELTN(10)	DFBRT	difference of radial fuel temperatures between consecutive iterations (if the maximum value exceeds 0.5 °C a new iteration is started)
DELTT	DTVAR2	Macro-time step (sec)
DELTZ(30)	DTIT5	Length of axial mesh zones M (m)
DH(30)	DTIT5	Hydraulic diameter of axial mesh zones M (m)
DHLDP(10)	DITCB1	ratio of liquid enthalpy increment over the micro-time step to the increment of vapour pressure of bubble K (m^3/kg)
DLPBL1	DTIT1	Coolant pressure drop in the inlet valve at time t_n (N/m^2)
DPDT(10)	DTIT4	Increment of the mean value of the vapour pressure of bubble K in the micro-time step at time t_{n-1} ($\text{N}/\text{m}^2 \text{sec}$)
DPDTR(10)	DITCB1	Increment of the mean value of the vapour pressure of bubble K in the micro-time step at time t_n ($\text{N}/\text{m}^2 \text{sec}$)
DPDTRI(10)	DITCB1	Increment of the mean value of the vapour pressure inside the bubble K in the micro-time step. Worth used for iteration within the micro-time step ($\text{N}/\text{m}^2 \text{sec}$)
DPGN	DTIT1	Coolant pressure drop in the channel at time t_n (N/m^2)

Symbol and dimensions	Common Block	Definition and Units
DPGN1	DTIT1	Coolant pressure drop in the channel at time t_{n-1} (N/m^2)
DPS	DTVAR3	Stationary coolant pressure drop between channel inlet (upstream of the throttle valve) and outlet (N/m^2)
DPO(30)	DTIT8	ratio of fuel density to theoretical density (see input description)
DBRB	DTIT6	Thickness of the radial mesh zones in fuel column (m)
DRBR2	DTIT6	= DRBR * * 2 (m^2)
DRC	DTIT6	Half clad thickness (m)
DRC2	DTIT6	= DRC * * 2 (m^2)
DRØDP(10)	DITCB1	ratio of increment (over the micro-time step) of vapour density to increment of vapour pressure of bubble K (sec^2/m^2)
DTBN(30,10)	DTIT1	Increment of fuel temperature in the axial mesh M, radial node N (M,N) in the micro-time step ($^{\circ}C/sec$)
DTBO(30)	DTIT1	Increment of the fuel axial temperature in the axial mesh M in the micro-time step ($^{\circ}C/sec$)
DTCA(30)	DTIT1	Increment of clad temperature at the outer surface of axial mesh M in the micro-time step ($^{\circ}C/sec$)
DTCI(30)	DTIT1	Increment of clad temperature at the inner surface of axial mesh M in the micro-time step ($^{\circ}C/sec$)
DTCM(30)	DTIT1	Increment of clad temperature at the middle surface of axial mesh M in the micro-time step ($^{\circ}C/sec$)
DTDP(10)	DITCB1	ratio of rest liquid film temperature increment over the micro-time step to increment of the integral vapour pressure of bubble K ($^{\circ}C m^3/J$)

Symbol and dimensions	Common Block	Definition and Units
DTK(30)	DTIT2	Increment of coolant temperature in the axial mesh M in the micro-time step ($^{\circ}\text{C}/\text{sec}$)
DTKUE	DTVAR2	Micro-time step (sec)
DTSH(10)	DTVAR1	Superheat assumed for boiling initialization in the coolant channel KKN at time t_n ($^{\circ}\text{C}$)
DTSHA(10)	-	Superheat assumed for initialization of the very first bubble in channel KKN (see input description) ($^{\circ}\text{C}$)
DTSHB(10)	-	Superheat assumed for initialization of subsequent bubbles in channel KKN (see input description) ($^{\circ}\text{C}$)
DTST(30)	DTIT1	Increment of structure temperature in the axial mesh M in the micro-time step ($^{\circ}\text{C}/\text{sec}$)
DXIG(10)	-	Coolant enthalpy difference between outlet and inlet of channel KKN (J/kg)
DZ(10,2)	DITCB2	Displacement of lower/upper (I=1,2) phase boundary of bubble K (K,I) during the micro-time step (m)
DZK(10,30)	DTIT4	Length of Lagrangian meshes in the liquid slug above bubble K at time t_{n-1} (m)
DZKE(50)	DTIT4	Length of Lagrangian meshes in the inlet liquid slug at time t_{n-1} (m)
DZKER(50)	DITCB2	Length of Lagrangian meshes in the inlet liquid slug at time t_n (m)
DZKR(10,30)	DITCB2	Length of Lagrangian meshes in the liquid slug above bubble K at time t_n (m)
FACR(11)	DTIT7	Radial power distribution in the fuel pellet (central node and NN radial nodes) in relative units (see input description) (dimensionless)
FAX(30)	-	Axial channel power distribution (see input description for meaning and units)
FF(10,2)	DTIT4	Time derivative of coolant mass flux at the lower (I=1) or upper (I=2) phase interface of bubble K (K,I) at time t_{n-1} ($\text{kg}/\text{m}^2 \text{sec}^2$)

Symbol and dimensions	Common Block	Definitions and Units
FFNR	DTIT3	Time derivative of integral coolant mass flux at time t_n ($\text{kg/m}^2 \text{sec}^2$)
FFN1	DTIT3	Time derivative of integral coolant mass flux at time t_{n-1} ($\text{kg/m}^2 \text{sec}^2$)
FFR(10,2)	DITCB2	Time derivative of coolant mass flux at the lower (I=1) or upper (I=2) phase interface of bubble K (K,I) at time t_n ($\text{kg/m}^2 \text{sec}^2$)
FFR1(10,2)	DITCB2	Time derivative of coolant mass flux at the lower/upper (I=1/2) phase boundary of bubble K (K,I). Worth stored for iteration within the micro-time step ($\text{kg/m}^2 \text{sec}^2$)
GL(10,2)	DTIT4	Coolant mass flux in the slug below/above (I=1/2) bubble K at time t_{n-1} ($\text{kg/m}^2 \text{sec}$)
GLR(10,2)	DITCB2	Coolant mass flux in the slug below (I=1) or above (I=2) the bubble K (K,I), at time t_n ($\text{kg/m}^2 \text{sec}$)
GVF(10,2)	DTIT9	Vapour mass flux at the lower (I=1) or upper (I=2) phase interface for bubble K (K,I), at time t_{n-1} ($\text{kg/m}^2 \text{sec}$)
GFR(10,2)	DITCB2	Vapour mass flux at the lower or upper phase interface for bubble K, at time t_n ($\text{kg/m}^2 \text{sec}$)
GVI(31)	DTIT9	Vapour mass flux at inlet of the axial Eulerian mesh M at time t_{n-1} ($\text{kg/m}^2 \text{sec}$)
GVIR(31)	DITCB2	Vapour mass flux at inlet of the axial Eulerian mesh M at time t_n ($\text{kg/m}^2 \text{sec}$)
GVM(30)	DTIT9	Vapour mass flux in the middle of axial Eulerian mesh M at time t_{n-1} ($\text{kg/m}^2 \text{sec}$)
GVMR(30)	DITCB2	Vapour mass flux in the middle of axial Eulerian mesh M at time t_n ($\text{kg/m}^2 \text{sec}$)
GVMR1(30)	DITCB2	Vapour mass flux in the middle of axial Eulerian mesh M. Worth stored for iteration within the micro-time step ($\text{kg/m}^2 \text{sec}$)

Symbol and dimensions	Common Block	Definition and Units
GVØ(30)	DTIT9	Vapour mass flux at outlet of the axial Eulerian mesh M at time t_{n-1} ($\text{kg}/\text{m}^2 \text{sec}$)
GVØR(30)	DITCB2	Vapour mass flux at outlet of the axial Eulerian mesh M at time t_n ($\text{kg}/\text{m}^2 \text{sec}$)
GV1(10)	DTIT9	Vapour mass flux in the lowermost (partial) mesh of bubble K at time t_{n-1} ($\text{kg}/\text{m}^2 \text{sec}$)
GV1R(10)	DITCB2	Vapour mass flux in the lowermost (partial) mesh of bubble K at time t_n ($\text{kg}/\text{m}^2 \text{sec}$)
GV1R1(10)	DITCB2	Vapour mass flux in the lowermost (partial) mesh of bubble K. Worth stored for iteration within the micro-time step ($\text{kg}/\text{m}^2 \text{sec}$)
GV2(10)	DTIT9	Vapour mass flux in the uppermost (partial) mesh of bubble K at time t_{n-1} ($\text{kg}/\text{m}^2 \text{sec}$)
GV2R(10)	DITCB2	Vapour mass flux in the uppermost (partial) mesh of bubble K at time t_n ($\text{kg}/\text{m}^2 \text{sec}$)
GV2R1(10)	DITCB2	Vapour mass flux in the uppermost (partial) mesh of bubble K. Worth stored for iteration during the micro-time step ($\text{kg}/\text{m}^2 \text{sec}$)
HBRC(30)	DTIT10	Fuel-clad heat transfer coefficient ($\text{W}/\text{m}^2 \text{ } ^\circ\text{C}$)
HBRCN(30)	DFBRT	Heat transfer coefficient through the fuel-clad gap in axial mesh zone M at time t_n ($\text{W}/\text{m}^2 \text{ } ^\circ\text{C}$)
HBRCN1(30)	DFBRT	Heat transfer coefficient through the fuel-clad gap in axial mesh zone M at time t_{n-1} ($\text{W}/\text{m}^2 \text{ } ^\circ\text{C}$)
HCF(10)	DITCB1	Auxiliary parameter (clad and structure film thickness weighted over the respective circumferential length and multiplied by the bubble length) used to solve the energy and continuity equations for the vapour phase at time t_{n-1} (m)
HCFR(10)	DITCB1	Auxiliary parameter used to solve the energy and continuity equations for the vapour phase at time t_n (m)

Symbol and dimensions	Common Block	Definition and Units
HCKUE	-	Clad-Coolant heat transfer coefficient ($W/m^2 \text{ } ^\circ C$)
HCØRE	DTIT5	Length of the test section from inlet to mesh zone NM1 inclusive (HCØRE=HSPALT+HKUEKA) (m)
HFG(10)	DITCB1	Vaporization enthalpy for bubble K (J/kg)
HGAP	DTIT8	Stationary fuel-clad heat transfer coefficient (see input description) ($W/m^2 \text{ } ^\circ C$)
HGAPM(30)	WIDTH	Transient fuel-clad heat transfer coefficient ($W/m^2 \text{ } ^\circ C$)
HKCL(30)	DITC11	Heat transfer coefficient clad-coolant in the axial mesh zone M, at time t_n ($W/m^2 \text{ } ^\circ C$)
HKCL1(30)	DITC11	Heat transfer coefficient clad-coolant in the axial mesh zone M, at time t_{n-1} ($W/m^2 \text{ } ^\circ C$)
HKST(30)	DITC11	Heat transfer coefficient coolant-structure in the axial mesh zone M, at time t_n ($W/m^2 \text{ } ^\circ C$)
HKST1(30)	DITC11	Heat transfer coefficient coolant-structure in the axial mesh zone M, at time t_{n-1} ($W/m^2 \text{ } ^\circ C$)
HKUEKA	DTIT5	Length of the axial breeder zone above the core (section between axial mesh zones NMO and NM1 inclusive) (m)
HSPALT	DTIT5	Length of the fission gas section (m)
HTØP	DTIT5	Length of the coolant mixing section (m) (test section above mesh zone NM1 to NM2 inclusive)
I	-	Index normally used to identify the Eulerian axial mesh zone of the lower phase boundary of bubble K.

Symbol and dimensions	Common Block	Definition and Units
IBV(10)	-	Array used to store the indexes I (identifying the lower phase boundaries) of bubbles upon which some calculation has to be performed later in the programme.
IDELTT	-	Flag determining the frequency with which, at the end of the macro-time steps, data for plots generation are written onto intermediate data files (see input description)
IDK(10)	DTVAR1	Index which implicitly determines the axial meshes of the two phase boundaries for bubble K at time t_{n-1} . (Lower phase boundary is in mesh zone $I=1+MØD(IDK(K)-2), NM2$). Upper phase boundary is in mesh zone $J=(IDK(K)-2)/NM2$. (See also description of Subroutine BØRN).
IDKR(10)	DITCB2	Index which implicitly determines the axial meshes of the phase boundaries for bubble K at time t_n (see description of Subroutine BØRN)
IERRØR	DTVAR1	Identifier for additional output selection during the two phase flow calculation (see input description)
II	-	Index normally used to identify the first Eulerian axial mesh zone above the zone containing the lower phase boundary of bubble K ($II = I + 1$)
IND(10)	DTVAR1	Array containing the bubble indexes K ordered from the bottom to the top of the channel (see also description of Subroutine IDENT)
IPLØT(10)	-	Flag for channel KKN, used for writing with frequency IDELLT data for plots generation.
IPVR	-	Index used in ITCB (LITCB) to iterate the solution of the vapour energy equation performed with the Subroutine ENBLR.
J	-	Index normally used to identify the Eulerian axial mesh zone of the upper phase boundary of bubble K.

Symbol and
dimensions

Common Block

Definition and Units

JBV(10)	-	Array used to store the indexes J (identifying the upper phase boundaries) of bubbles upon which some calculation has to be performed later in the programme.
JJ	-	Index normally used to identify the first Eulerian axial mesh zone below the zone containing the upper phase boundary of bubble K (JJ=J-1).
K	-	Index normally used to identify a bubble.
KB	DTVAR1	Actual number of bubbles in channel KKN
KBV(10)	-	Array used to store the indexes K of bubbles upon which some calculation has to be performed later in the programme.
KKN	DTVAR1	Index of channel which is actually being calculated.
KK11KK(10)	-	Index used to select the frequency of printing results of the single phase flow calculation at the end of the macro-time step
KK22KK(10)	-	Index used to select the frequency of printing results of the two phase flow calculation at the end of the macro-time step
KMU(26)	DTVAR3	Index defined in subroutine STATO to count the elements of the half dynamic arrays VCPS and VCPØ, used for data plotting in the subroutines BLØPLS and BLØPLØ.
KØNT	DTVAR1	Type of coolant channel (see input description)
KUEL	DTIT8	Name of coolant (see input description)
LM(10)	DTVAR1	Number of Lagrangian meshes in the liquid slug above bubble with index K.
LME	DTVAR1	Number of Lagrangian meshes in the inlet liquid slug.
M	DTVAR1	Index normally used to identify the Eulerian axial meshes from channel inlet to outlet

Symbol and dimensions	Common Block	Definition and Units
MPEAK	DTVAR3	Index of axial mesh zone with the stationary peak power generation (used for plot generation)
MS	-	Index normally set equal to LM(K) (see LM)
NB	DTVAR1	Maximal number (=10) of bubbles allowed in a coolant channel
NBDTR	-	Unit number of disk storage from which channel dependent data are read sequentially (see input description)
NBDTW	-	Unit number of disk storage to which channel dependent data are written sequentially (see input description)
NBLASE(10)	BLASET	Flag used to re-initialize single phase flow conditions after vanishing of all bubbles in coolant channel KKN.
NBØIL(10)	DTVAR1	Flag characterizing the phase flow in channel KKN (NBØIL(KKN)=0 for single phase flow, NBØIL(KKN)=2 for two phase flow).
NDAM(10)	DTVAR1	Flag for bubble K which either drives the calculation of vapour axial pressure distribution inside the bubble (NDAM(K)≠0) or the calculation of mean value of vapour pressure (NDAM(K)=0).
NDAMO(10)	-	Array storing the bubble flags of array NDAM at the beginning of the macro-time step. These flags have to be accessed in case time step halving is required.
NDR	DTVAR1	Number of printouts since boiling inception
NKKN	DTVAR1	Number of coolant channels (see input description)
NGRID	DTVAR1	Identifier for spacers (see input description)

Symbol and dimensions	Common Block	Definition and Units
NMP	DTVAR3	Index of axial mesh with the peak stationary coolant temperature (used for plot generation)
NMTØP	WIDTH	Index of axial mesh inside the zone (NMO, NM1) beyond which only very little heat production is assumed (see input description)
NMO	DTVAR1	First axial mesh of fuel column (see input description)
NM1	DTVAR1	Last axial mesh of fuel column (see input description)
NM2	DTVAR1	Number of axial zones in the coolant channel (see input description)
NN	DTVAR1	Number of radial mesh nodes inside the fuel pellets (see input description)
NNMIN	DTVAR1	= NN - 1
NPLØTB	DTVAR3	Flag for "bubble plot" option (see input description)
NPLØTØ	DTVAR3	Flag used for driving the optional plot facility (see input description)
NPLØTS	DTVAR3	Flag for standard plot option (see input description)
NSAUL	DTVAR1	Identifier of the solution of the heat transfer equation in the pin (see input description)
NTFB(30)	DITCB2	Flag used to drive the solution of the heat transfer equations in Subroutine FBRTB for the axial mesh zone M. For NTFB(M)=1 "old" and "new" terms (referring to time points t_{n-1} and t_n respectively) of the discretized equations are calculated. Subsequently, for NTFB(M) > 1, only "new" terms are calculated within the Gauss-Seidel iteration scheme.
NTKU	-	Number of micro-time steps which, at time point TTKU, have already been calculated within the macro-time step DELTT

Symbol and dimensions	Common Block	Definitions and Units
NTKUE	-	Number of micro-time step which, at time point TTKU, have still to be calculated, within macro-time step DELTT.
NTMAT	DTVAR1	Iteration index for the solution of the momentum equation. If the difference of the mass flow (XXMANR-XXMAN1/XXMANR) or its time derivative ((FFNR1-FFNR/FFNR) between two iterations is less than a given threshold the iteration stops. If the iteration index becomes greater than 30 or the ratio valve pressure losses to test channel pressure losses (DLPBL1/DPGN) is greater than 15 an approximate solution of the momentum equation is obtained (used only for single phase flow calculation).
NZEIT	DTVAR1	Number of macro-time steps calculated since boiling inception.
NZB	DTVAR3	Length of data array to be written every IDELLT time steps onto file FT12FOO1 for "bubble plot" generation.
NZØ	DTVAR3	Length of data array to be written every IDELLT time steps onto file FT12FOO1 for option plot generation.
NZS	DTVAR3	Length of data array to be written every IDELLT time steps onto file FT11FOO1 for standard plot generation.
PDEC1	DTVAR1	Coefficient to describe time variation of coolant inlet pressure (see input description) (sec ⁻¹)
PDEC2	DTVAR1	Coefficient to describe time variation of coolant inlet pressure (see input description) (sec ⁻²)
PDEC3	DTVAR1	Coefficient to describe time variation of coolant inlet pressure (see input description) (sec ⁻³)

Symbol and dimensions	Common Block	Definition and Units
PELLET	DTIT8	Name of fuel (see input description)
PERB(30)	DTVAR4	Percentage of molten fuel material in the axial mesh zone M (dimensionless)
PERCA(30)	DTVAR4	Percentage of molten clad material in the axial mesh zone M (dimensionless)
PKIN(30)	DTIT1	Coolant pressure at inlet of Eulerian axial mesh M at time t_n (N/m^2)
PKIN1(30)	DTIT1	Coolant pressure at inlet of Eulerian axial mesh M at time t_{n-1} (M/m^2)
PKMN(30)	DTIT1	Coolant pressure in the middle of Eulerian axial mesh M at time t_n (N/m^2)
PKMN1(30)	DTIT1	Coolant pressure in the middle of Eulerian axial mesh M at time t_{n-1} (M/m^2)
PKØN(30)	DTIT1	Coolant pressure at outlet of Eulerian axial mesh M at time t_n (N/m^2)
PKØNO	DTIT1	Stationary channel outlet pressure (N/m^2)
PKØN1(30)	DTIT1	Coolant pressure at outlet of Eulerian axial mesh M at time t_{n-1} (N/m^2)
PKON	DTIT1	Channel inlet pressure at time t_n (N/m^2)
PKON1	DTIT1	Channel inlet pressure at time t_{n-1} (N/m^2)
PKOO	DTIT1	Stationary channel inlet pressure (N/m^2)
PL(10,30)	DTIT4	Coolant pressure of Lagrangian mesh MS in the liquid slug above the bubble with index K (K,MS) at time t_n (N/m^2)
PLE(50)	DTIT4	Coolant pressure in the Lagrangian meshes of the inlet slug at time t_n (N/m^2)
PSI	DTIT5	Coefficient used for the simulation of spacers (see input description)
PV(10)	DTIT4	Average vapour pressure inside the bubble with index K at time t_{n-1} (N/m^2)
PVF(10,2)	DTIT9	Vapour pressure at the lower (I=1) or upper (I=2) phase interface for bubble with index K (K,I) at time t_{n-1} (N/m^2)

Symbol and dimensions	Common Block	Definition and Units
PVFR(10,2)	DITCB1	Vapour pressure at the lower/upper (I=1/2) phase interface of bubble K(K,I) at time t_n (N/m^2)
PVFR1(10,2)	DITCB1	Vapour pressure at the lower/upper (I=1/2) phase interface of bubble K. Worth stored for iteration within the micro-time step (N/m^2)
PVM(30)	DTIT9	Vapour pressure in the axial Eulerian mesh zone M at time t_{n-1} (N/m^2)
PVMR(30)	DITCB1	Vapour pressure in the axial Eulerian mesh zone M at time t_n (N/m^2)
PVR(10)	DITCB1	Mean value of vapour pressure inside the bubble K at time t_n (N/m^2)
PVRO(10)	DITCB1	Mean value of vapour pressure inside the bubble K at the beginning of a micro-time step (N/m^2)
PVR1(10)	DITCB1	Mean value of vapour pressure inside the bubble K at time t_{n-1} (N/m^2)
PV1(10)	DTIT9	Vapour pressure in the lowermost (partial) mesh of bubble K at time t_{n-1} (N/m^2)
PV1R(10)	DITCB1	Vapour pressure in the lowermost (partial) mesh of bubble K at time t_n (N/m^2)
PV2(10)	DTIT9	Vapour pressure in the uppermost (partial) mesh of bubble K at time t_{n-1} (N/m^2)
PV2R(10)	DITCB1	Vapour pressure in the uppermost (partial) mesh of bubble K at time t_n (N/m^2)
P2	A1FA2F	Coefficient used to find the mass flow rate in the leakage path in dependence on the pressure drop across the test section.
QGEMN(30)	DTIT7	Specific pin power in the axial mesh M at the end of a micro-time step (W/m^3)
QGEMN1(30)	DTIT7	Specific pin power in the axial mesh M at the beginning of a micro-time step (W/m^3)
QGES(30)	DTIT7	Specific pin power in the axial mesh M at time t_{n-1} (W/m^3)
QGEST(30)	DTIT7	Specific pin power in the axial mesh M at time t_n (W/m^3)

Symbol and dimensions	Common Block	Definition and Units
QGESD(30)	DTIT7	Stationary specific pin power axial distribution (W/m^3)
QGESOM	DTVAR3	Peak stationary power density (in axial mesh zone MPEAK) (W/m^3)
QQ1(30)	DTIT7	Power transferred per unit area between coolant (both vapour and liquid phases) and clad surface in the axial mesh M at time t_{n-1} (W/m^2)
QQ2(30)	DTIT7	Power transferred per unit area between coolant (both vapour and liquid phases) and structure surface in the axial mesh M at time t_{n-1} (W/m^2)
QQ3(30)	DTIT7	Coefficient used to calculate the power transferred per unit area between clad surface and coolant (both vapour and liquid phases) in the axial mesh M at time t_n (W/m^2)
QQ4(30)	DTIT7	Coefficient used to calculate the power transferred per unit area between structure inner surface and coolant (both vapour and liquid phases) in the axial mesh M at time t_n (W/m^2)
QQ5(30)	DTIT7	Heat transfer coefficient between coolant and structure, calculated for the axial mesh M taking into account the bubbles configuration at time t_n ($\text{W/m}^2 \text{ } ^\circ\text{C}$)
QQ6(30)	DTIT7	Heat transfer coefficient between clad and coolant, calculated for the axial mesh M taking into account the bubbles configuration at time t_n ($\text{W/m}^2 \text{ } ^\circ\text{C}$)
QRCA	DTIT6	Defined by $\text{QRCA} = (\text{RCA} - \text{DRC}/4.) / \text{RCA}$ where: RCA = clad outer radius; DRC = half clad thickness (see Subroutine STATO)
QRCH	DTIT6	Defined by $\text{QRCH} = (\text{RCA} - \text{DRC}/2.) / \text{RCA}$ with the above meaning of the symbols (see Subroutine STATO)
QRCMI	DTIT6	Defined by $\text{QRCMI} = (\text{RCM} - \text{DRC}/2.) / \text{RCM}$ where: RCM = radial coordinate of the clad middle node; DRC = half clad thickness (see Subroutine STATO)

Symbol and dimensions	Common Block	Definition and Units
QRCPL	DTIT6	Defined by $QRCPL=(RCM+DRC/2.)/RCM$ with the above meaning of the symbols (see Subroutine STATO)
QRMIN(10)	DTIT6	Defined for the radial mesh zone N by $QRMIN(N)=(R(N)-DRBR/2.)/R(N)$ (see Subroutine STATO)
QRMIV	DTIT6	Defined by $QRMIV=(RBR(1)-DRBR/4.)/RBR(1)$ (see Subroutine STATO)
QRPL(10)	DTIT6	Defined for the radial mesh zone N by $QRPL(N)=(R(N)+DRBR/2.)/R(N)$ (see Subroutine STATO)
QRPLH	DTIT6	Defined by $QRPLH=(RCI+DRC/2.)/RCI$ where RCI = clad inner radius, DRC = clad half thickness (see Subroutine STATO)
QRPLV	DTIT6	Defined by $QRPLV=(RCI+DRC/4.)/RCI$ with the above meaning of the symbols (see Subroutine STATO)
QXMAN1	-	Volumetric flow rate through the channel (m^3/h)
QXMB(10)	DITCB1	Integral heat flux from clad and structure to vapour for bubble K at time t_{n-1} (W/m^2)
QXMBR(10)	DITCB1	Integral heat flux from clad and structure to vapour for bubble K at time t_n (W/m^2)
R(10)	DTIT6	Radius of the outer cylindrical surface of the radial mesh zones in the fuel column (m)
RBR(30)	DTIT5	Fuel pellet outer radius, assumed to be equal to the clad inner radius (see input description) (m)
RCA(4)	-	Radius of the four cylindrical surfaces bounding the three clad nodes (only used in Subroutine PRØCA) (m)
RKUE(30)	DTIT5	Equivalent coolant channel radius (see input description) (m)
RLA	DTIT5	Reduced inertial length at channel outlet (see input description) (m)
RLE	DTIT5	Reduced inertial length at channel inlet (see input description) (m)

Symbol and dimensions	Common Block	Definition and Units
RMIN(10)	DTIT6	Radius of the middle cylindrical surface of the radial mesh zones in the fuel column (m)
RØL(10)	DITCB1	Liquid film density at the temperature which corresponds to the mean value of vapour pressure in bubble K (kg/m^3)
RØV(10)	DITCB1	Mean value of vapour density inside bubble K at time t_n (kg/m^3)
RØVF(10,2)	DTIT9	Vapour density at the lower (I=1) or upper (I=2) phase interface for bubble K (K,I) at time t_{n-1} (kg/m^3)
RØVFR(10,2)	DITCB1	Vapour density at the lower (I=1) or upper (I=2) phase interface for bubble K (K,I) at time t_n (kg/m^3)
RØVM(30)	DTIT9	Vapour density in the axial Eulerian mesh M at time t_{n-1} (kg/m^3)
RØVMR(30)	DITCB1	Vapour density in the Eulerian axial mesh M at time t_n (kg/m^3)
RØV1(10)	DTIT9	Vapour density in the lowermost (partial) mesh of bubble K at time t_{n-1} (kg/m^3)
RØV1R(10)	DITCB1	Vapour density in the lowermost (partial) mesh of bubble K at time t_n (kg/m^3)
RØV2(10)	DTIT9	Vapour density in the uppermost (partial) mesh of bubble K at time t_{n-1} (kg/m^3)
RØV2R(10)	DITCB1	Vapour density in the uppermost (partial) mesh of bubble K at time t_n (kg/m^3)
SCLR(30)	DTIT4	Clad film thickness in the axial mesh zone M at time t_n (m)
SCL1R(10)	DTIT4	Clad film thickness in the lowermost (partial) mesh of bubble K at time t_n (m)
SCL2R(10)	DTIT4	Clad film thickness in the uppermost (partial) mesh of bubble K at time t_n (m)
SMAX	-	Maximum film thickness at both clad and structure material (see input description) (m)
SMIN	DTIT4	Minimum film thickness at both clad and structure material (see input description) (m)

Symbol and dimensions	Common Block	Definition and Units
SPALTO(30)	WIDTH	Stationary fuel-gap width calculated on the basis of linear thermal expansion without accounting for the initial gap width (m)
SPALT1(30)	WIDTH	Stationary fuel-gap width calculated taking into account the initial gap width in cold state. For the transient calculation it represents the gap width at time t_{n-1} (m)
SPALT2(30)	WIDTH	Transient fuel-gap width at time t_n (m)
SSTR(30)	DTIT4	Structure film thickness in the axial mesh zone M at time t_n (m)
SST1R(10)	DTIT4	Structure film thickness in the lowermost (partial) mesh of bubble K at time t_n (m)
SST2R(10)	DTIT4	Structure film thickness in the uppermost (partial) mesh of bubble K at time t_n (m)
STDP	AlFA2F	Stationary pressure drop including the pressure losses in the inlet valve and in the inlet and outlet reduced lengths (N/m^2)
STØE(30)	STØECH	Fuel stoichiometry of O/Me ratio in axial zone M (see input description)
STRUK	DTIT8	Name of structural material (see input description)
SO	DTIT4	Film thickness for bubbles initialization (see input description)
TBMNR(30)	DTIT2	Average fuel temperature at time t_n ($^{\circ}C$)
TBMN1(30)	DTIT2	Average fuel temperature at time t_{n-1} ($^{\circ}C$)
TBNR(30,10)	DTIT2	Fuel temperature at time t_n in the node (M,N). (M=1, 30 index for axial mesh zones, N=1, 10 index for radial nodes) ($^{\circ}C$)
TBN1(30,10)	DTIT2	Fuel temperature at time t_{n-1} ($^{\circ}C$)
TBØIL(10)	DTVAR2	Time since start of boiling in channel KKN. It is set to zero in case single phase flow reestablishes (sec)

Symbol and dimensions	Common Block	Definition and Units
TBR2(30,10)	DFBRT	Fuel temperature in the node (M,N) (M=1,30 index for axial mesh zones, N=1,10 index for radial nodes). Used for iteration with the Gauss-Seidel method within the micro-time step ($^{\circ}\text{C}$)
TBYPSR(30)	FWFST	Temperature of by-pass flow at time t_n ($^{\circ}\text{C}$)
TBYPS1(30)	FWFST	Temperature of by-pass flow at time t_{n-1} ($^{\circ}\text{C}$)
TBONR(30)	DTIT2	Axial fuel temperature at time t_n ($^{\circ}\text{C}$)
TBON1(30)	DTIT2	Axial fuel temperature at time t_{n-1} ($^{\circ}\text{C}$)
TBOR2(30)	DFBRT	Axial fuel temperature used for iteration with the Gauss-Seidel method within the micro-time step ($^{\circ}\text{C}$)
TBOT(30)	DTIT10	Axial fuel temperature used in the Gauss-Seidel iteration scheme referring to the previous iteration step (r-1) ($^{\circ}\text{C}$)
TCANR(30)	DTIT2	Outer clad surface temperature at time t_n ($^{\circ}\text{C}$)
TCAN1(30)	DTIT2	Outer clad surface temperature at time t_{n-1} ($^{\circ}\text{C}$)
TCAR2(30)	DFBRT	Outer clad surface temperature in axial mesh zone M. Used for iteration with the Gauss-Seidel method within the micro-time step ($^{\circ}\text{C}$)
TCINR(30)	DTIT2	Inner clad surface temperature at time t_n ($^{\circ}\text{C}$)
TCIN1(30)	DTIT2	Inner clad surface temperature at time t_{n-1} ($^{\circ}\text{C}$)
TCIR2(30)	DRBRT	Inner clad surface temperature in axial mesh zone M. Used for iteration with the Gauss-Seidel method within the micro-time step ($^{\circ}\text{C}$)
TCMN1(30)	DTIT2	Temperature of clad middle surface at time t_{n-1} ($^{\circ}\text{C}$)

Symbol and dimensions	Common Block	Definition and Units
TCMNR(30)	DTIT2	Temperature of clad middle surface at time t_n ($^{\circ}\text{C}$)
TCMR2(30)	DFBRT	Temperature of clad middle surface in axial mesh zone M. Used for iteration with the Gauss-Seidel method within the micro-time step ($^{\circ}\text{C}$)
TETTA(10)	DTVAR1	Identifier for the solution of the heat transfer equations in channel KKN. (see input description)
TEXT(20)	-	Text identifying the problem to be calculated also used for headings of plot data sets (see input description)
TKINNO	DTIT2	Stationary coolant inlet temperature ($^{\circ}\text{C}$)
TKINR(30)	DTIT2	Coolant temperature at inlet of an axial Eulerian mesh zone at time t_n ($^{\circ}\text{C}$)
TKIN1(30)	DTIT2	Coolant temperature at inlet of an axial Eulerian mesh zone at time t_{n-1} ($^{\circ}\text{C}$)
TKNR(30)	DTIT2	Coolant temperature in the middle of an axial Eulerian zone at time t_n ($^{\circ}\text{C}$)
TKN1(30)	DTIT2	Coolant temperature in the middle of an axial Eulerian zone at time t_{n-1} ($^{\circ}\text{C}$)
TKØNR(30)	DTIT2	Coolant temperature at outlet of an axial Eulerian zone at time t_n ($^{\circ}\text{C}$)
TKØN1(30)	DTIT2	Coolant temperature at outlet of an axial Eulerian zone at time t_{n-1} ($^{\circ}\text{C}$)
TL(10,30)	DTIT4	Coolant temperature of the Lagrangian mesh MS in the liquid slug above the bubble K (K,MS) at time t_{n-1} ($^{\circ}\text{C}$)
TLE(50)	DTIT4	Coolant temperature in the Lagrangian meshes of the inlet liquid slug at time t_{n-1} ($^{\circ}\text{C}$)
TLER(50)	DITCB1	Coolant temperature in the Lagrangian meshes of the inlet liquid slug at time t_n ($^{\circ}\text{C}$)
TLR(10,30)	DITCB1	Coolant temperature of the Lagrangian mesh MS in the liquid slug above the bubble K (K,MS) at time t_n ($^{\circ}\text{C}$)

Symbol and dimensions	Common Block	Definition and Units
TPLE(10)	-	Temperature in coolant upper plenum above channel KKN at time t_n ($^{\circ}\text{C}$)
TPLEN	DTVAR1	Stationary temperature in coolant upper plenum (see input description) ($^{\circ}\text{C}$)
TRAMPE	-	Time instant after which the time step for single phase flow calculation may be changed (see input description)
TSAT(30)	-	Coolant saturation temperature. Only used in Subroutines ITCL, ITC1R ($^{\circ}\text{C}$)
TSBR	DTIT2	Fuel fusion temperature ($^{\circ}\text{C}$)
TSCA	DTIT2	Clad fusion temperature ($^{\circ}\text{C}$)
TSST	DTIT2	Structure material fusion temperature ($^{\circ}\text{C}$)
TSTNR(30)	DTIT2	Temperature of structure material at time t_n ($^{\circ}\text{C}$)
TSTNO(30)	DTIT2	Stationary temperature of structure material ($^{\circ}\text{C}$)
TSTN1(30)	DTIT2	Temperature of structure material at time t_{n-1} ($^{\circ}\text{C}$)
TSTR2(30)	DFBRT	Temperature of structural material. Used for iteration with the Gauss-Seidel method within the micro-time step ($^{\circ}\text{C}$)
TT	DTVAR2	Problem time at the end of the actual time step (sec)
TTKU	-	Actual problem time referring to the end of a micro-time step (sec)
TTKUH	AZDM	Time point at which the coefficient ZETAD for the pressure drop in the inlet valve, programmed as function of time, exceeds ZDM/2. For times greater than TTKUH a smooth curve for the time variation of the inlet valve pressure drop coefficient is used (only used for leakage flow).
TV(10)	DTIT4	Average vapour temperature inside the bubble K at time t_{n-1} ($^{\circ}\text{C}$)

Symbol and dimensions	Common Block	Definition and Units
TVF(10,2)	DTIT9	Vapour temperature at the lower (I=1) or upper (I=2) phase interface for bubble K (K,I) at time t_{n-1} ($^{\circ}\text{C}$)
TVFR(10,2)	DITCB1	Vapour temperature in the lower or upper phase interface for bubble K (K,I), at time t_n ($^{\circ}\text{C}$)
TVM(30)	DTIT9	Vapour temperature in the axial Eulerian mesh zone M at time t_{n-1} ($^{\circ}\text{C}$)
TVMR(30)	DITCB1	Vapour temperature in the axial Eulerian mesh zone M at time t_n ($^{\circ}\text{C}$)
TVMR1(30)	DITCB1	Vapour temperature in the axial Eulerian mesh zone M. Worth stored for iteration within the micro-time step ($^{\circ}\text{C}$)
TVR(10)	DITCB1	Average vapour temperature inside the bubble K at time t_n ($^{\circ}\text{C}$)
TV1(10)	DTIT9	Vapour temperature in the lowermost (partial) mesh of the bubble K at time t_{n-1} ($^{\circ}\text{C}$)
TV1R(10)	DITCB1	Vapour temperature in the lowermost (partial) mesh of bubble K at time t_n ($^{\circ}\text{C}$)
TV1R1(10)	DITCB1	Vapour temperature in the lowermost (partial) mesh of bubble K. Worth stored for iteration within the micro-time step ($^{\circ}\text{C}$)
TV2(10)	DTIT9	Vapour temperature in the uppermost (partial) mesh of bubble K at time t_{n-1} ($^{\circ}\text{C}$)
TV2R(10)	DITCB1	Vapour temperature in the uppermost (partial) mesh of bubble K at time t_n ($^{\circ}\text{C}$)
TV2R1(10)	DITCB1	Vapour temperature in the uppermost (partial) mesh of bubble K. Worth stored for iteration within the micro-time step ($^{\circ}\text{C}$)
ULCIR(30)	UFILM	Velocity of clad liquid film at the lower boundary of Eulerian axial mesh zone M at time t_n (m/sec)
ULCMR(30)	UFILM	Velocity of clad liquid film in the middle of Eulerian axial mesh zone M at time t_n (m/sec)

Symbol and dimensions	Common Block	Definition and Units
ULCØR(30)	UFILM	Velocity of clad liquid film at the upper boundary of Eulerian axial mesh zone M at time t_n (m/sec)
ULC1R(10)	UFILM	Velocity of clad liquid film in the middle of the lowermost (partial) mesh zone of bubble K at time t_n (m/sec)
ULC2R(10)	UFILM	Velocity of clad liquid film in the middle of the uppermost (partial) mesh zone of bubble K at time t_n (m/sec)
ULCFR(10,2)	UFILM	Velocity of clad liquid film at the lower/upper (I=1/2) phase interface of bubble K (K,I) at time t_n (m/sec)
ULSIR(30)	-	Velocity of structure liquid film at the lower boundary of Eulerian axial mesh zone M at time t_n (m/sec)
ULSMR(30)	-	Velocity of structure liquid film in the middle of Eulerian axial mesh zone M at time t_n (m/sec)
ULSØR(30)	-	Velocity of structure liquid film at the upper boundary of Eulerian axial mesh zone M at time t_n (m/sec)
ULS1R(10)	-	Velocity of structure liquid film in the middle of the lowermost (partial) mesh zone of bubble K at time t_n (m/sec)
ULS2R(10)	-	Velocity of structure liquid film in the middle of the uppermost (partial) mesh zone of bubble K at time t_n (m/sec)
ULSFR(10,2)	-	Velocity of structure liquid film at the lower/upper (I=1/2) phase interface of bubble K (K,I) at time t_n (m/sec)

Symbol and dimensions	Common Block	Definition and Units
UNBN(30,10)	DTIT8	Specific fusion heat stored in the fuel material of axial mesh zone M, radial node N, during melting or solidification at time t_n (J/m^3)
UNBO(30)	DTIT8	Specific fusion heat stored in the fuel central node of axial mesh zone M during melting or solidification at time t_n (J/m^3)
UNHA(30)	DTIT10	Specific fusion heat stored in the clad material of the outer surface node in axial mesh zone M during melting or solidification at time t_n (J/m^3)
UNHI(30)	DTIT10	Specific fusion heat stored in the clad material of the inner surface node in axial mesh zone M during melting or solidification at time t_n (J/m^3)
UNHM(30)	DTIT10	Specific fusion heat stored in the clad material of the middle surface node in axial mesh zone M during melting or solidification at time t_n (J/m^3)
UOBN(30,10)	DTIT8	Specific fusion heat stored in the fuel material of axial mesh zone M, radial node N, during melting or solidification at time t_{n-1} (J/m^3)
UOBO(30)	DTIT8	Specific fusion heat stored in the fuel central node of axial mesh zone M during melting or solidification at time t_{n-1} (J/m^3)
VCBL(201)	-	Array used to store data to be written onto file FT12F001 for "bubble Plot" generation
VCPØ	-	Array used to store data to be written onto file FT13F001 for option plot generation
VCPS(273)	-	Array used to store data to be written onto file FT11F001 for standard plot generation
VERH	-	ratio of the mass flow through the leakage path to the mass flow through the test channel
VKMN(30)	DTIT3	Coolant velocity in the axial mesh M at time t_n (m/sec)
VKMN1(30)	DTIT3	Coolant velocity in the axial mesh M at time t_{n-1} (m/sec)

Symbol and dimensions	Common Block	Definition and Units
VDUF(30)	DTIT5	Ratio of volume to inner surface area of structure per unit length (see input description) (m)
VDZK(10,30)	DTIT4	Volume of coolant in the Lagrangian meshes of the liquid slug above the bubble with index K at time t_{n-1} (m^3)
VDZKE(50)	DTIT4	Volume of coolant in the Lagrangian meshes of inlet liquid slug at time t_{n-1} (m^3)
VDZKER(50)	DITCB2	Volume of coolant in the Lagrangian meshes of inlet liquid slug at time t_n (m^3)
VDZKER(10,30)	DITCB2	Volume of coolant in the Lagrangian meshes of the liquid slug above the bubble with index K at time t_n (m^3)
VSTRUK(30)	DTIT5	Volume of structural material per unit length (see input description) (m^2)
VØLNN(30)	DTIT6	Volume of fuel material associated to the peripheral node (node NN) in axial mesh zone M (m^3)
VØLN1(30,10)	DTIT6	Volume of fuel material associated to the nodes N (N=1.....NN) in axial mesh zone M (m^3)
VO(30)	DTIT6	Volume of fuel material associated to the pin axial nodes (m^3)
WWSTR(30)	FWFS	Heat transfer coefficient from structure outer surface to the adjacent medium at time t_n ($W/m^2 \text{ } ^\circ C$)
WWST1(30)	FWFS	Heat transfer coefficient from structure outer surface to the adjacent medium at time t_{n-1} ($W/m^2 \text{ } ^\circ C$)
XBRKT(30)	DTIT5	Ratio of pin circumference to area of flow section for axial mesh zone M (m^{-1})
XKK(30)	-	Ratio of the linear power generated in the channel axial mesh zone M to π times the volumetric specific power (m^2)
XLBN1(30,10)	DFBRT	Thermal conductivity of fuel at mesh node (M,N) (M=1,30 index for axial zones, N=1,10 index of radial nodes) at time $(t_{n-1} + t_n)/2$. ($W/m^2 \text{ } ^\circ C$)

Symbol and dimensions	Common Block	Definition and Units
XLCAN1(30)	DFBRT	Thermal conductivity of clad material of the outer surface of axial mesh zone M at time $(t_{n-1} + t_n)/2$. (W/m ⁰ C)
XLCIN1(30)	DFBRT	Thermal conductivity of clad material at the inner surface of axial mesh zone M at time $(t_{n-1} + t_n)/2$. (W/m ⁰ C)
XLCMI(30)	DTIT10	(In this Common block only in Subroutine STATO). Thermal conductivity of clad material in the mid point between inner and middle clad nodes. (W/m ⁰ C)
XLCPL(30)	DTIT10	(In this Common block only in Subroutine STATO). Thermal conductivity of clad material in the mid point between middle and outer clad nodes. (W/m ⁰ C)
XMANR(30)	DTIT3	Coolant mass flux in the axial mesh M at time t_n (kg/m ² sec)
XMAN1(30)	DTIT3	Coolant mass flux in the axial mesh M at time t_{n-1} (kg/m ² sec)
XMAST(10)	-	Stationary mass flow in channel KKN (kg/sec)
XM1(30)	DITCB1	Heat flux from clad and structure to vapour in axial mesh node M at time t_{n-1} (used for calculating the source term in the solution of the continuity and energy equations of the vapour phase) (W/m ²)
XM1R(30)	DITCB1	Heat flux from clad and structure to vapour in axial mesh node M at time t_n . (Used for calculating the source term in the solution of the continuity and energy equations of the vapour phase) (W/m ²)
XM2(30)	DITCB1	Auxiliary parameter to calculate the source term for axial zone M at time t_{n-1} in the solution of the continuity and energy equations for the vapour phase (kg/m ²ⁿ⁻¹)
XM2R(30)	DITCB1	Auxiliary parameter to calculate the source term for axial zone M at time t_n in the solution of the continuity and energy equations for the vapour phase (kg/m ²ⁿ)

Symbol and dimensions	Common Block	Definition and Units
XØ1(10)	DITCB1	Heat flux from clad and structure to vapour in the uppermost (partial) zone of bubble with index K at time t_{n-1} (used for calculating the source term in the solution of the energy and continuity equations of the vapour phase) (W/m^2)
XØ1R(10)	DITCB1	Heat flux from clad and structure to vapour in the uppermost (partial) zone of bubble with index K at time t_n (W/m^2)
XØ2(10)	DITCB1	Auxiliary parameter to calculate the source term for the solution of energy and continuity equations of the vapour phase in the uppermost (partial) zone of bubble with index K at time t_{n-1} (kg/m^2)
XØ2R(10)	DITCB1	Auxiliary parameter to calculate the source term for the solution of energy and continuity equations of the vapour phase in the uppermost (partial) zone of bubble with index K at time t_n (kg/m^2)
XSTKT(30)	DTIT	Ratio of structure inner circumference to area of flow section for axial mesh zone M (m^{-1})
XU1(10)	DITCB1	Heat flux from clad and structure to vapour in the lowermost (partial) zone of bubble with index K at time t_{n-1} (used for calculating the source term in the solution of the energy and continuity equations of the vapour phase) (W/m^2)
XU1R(10)	DITCB1	Heat flux from clad and structure to vapour in the lowermost (partial) zone of bubble with index K at time t_n (W/m^2)
XU2(10)	DITCB1	Auxiliary parameter to calculate the source term for the solution of energy and continuity equations of vapour phase in the lowermost (partial) zone of bubble with index K at time t_{n-1} (kg/m^2)
XU2R(10)	DITCB1	Auxiliary parameter to calculate the source term for the solution of energy and continuity equations of the vapour phase in the lowermost (partial) zone of bubble with index K at time t_n (kg/m^2)

Symbol and dimensions	Common Block	Definition and Units
XX	WIDTH	Correction factor of mean fuel temperatures used for radial fuel expansion calculation (see input description)
XXMANR	DTIT3	Mean value of the coolant mass flux through the channel at time t_n ($\text{kg}/\text{m}^2\text{sec}$)
XXMAN1	DTIT3	Mean value of the coolant mass flux through the channel at time t_{n-1} ($\text{kg}/\text{m}^2\text{sec}$)
Z(31)	DTIT5	Axial coordinate of the upper boundary of Eulerian meshes, including an additional mesh in outlet plenum (m)
ZDM	AZDM	Maximum value of the inlet valve pressure drop coefficient used to simulate a mass flow run down (to be supplied by the user in Subroutine ZETAD) (dimensionless)
ZETAC	DTIT5	Coefficient for calculation of coolant pressure drop at flow section enlargement (dimensionless)
ZETAD	DTIT5	Coefficient for calculation of coolant pressure drop across the channel inlet valve at time t_n (dimensionless)
ZETADO	DTIT5	Coefficient for calculation of stationary coolant pressure drop across the channel inlet valve (dimensionless)
ZL(10,2)	DTIT4	Axial coordinate of the lower/upper ($I=1/2$) phase boundary of bubble K (m)
ZSLUG	DTVAR1	Length of generated Lagrangian meshes at channel inlet or outlet by reentry (see input description) (m). In some cases, depending on the length of the Eulerian meshes, Lagrangian meshes may be generated with a length equal to a fraction of ZSLUG.

4. Input and output descriptions

A) Input Description

By the card number is indicated in brackets the format for reading input data. Options which are suggested (as corresponding to the most advanced code version) are underlined.

Card 1 (18A4)

TEXT identification text of the case considered. This text is used as well for identification of the PLOT-data sets

Card 2 (6I4)

NPLØTS identification for the standard plot option.

If NPLOTS = 0 no standard plot prepared

If NPLOTS > 0 relevant data for the standard plot are written on file number FT11FO01

NPLØTB identification for the bubble plot option.

If NPLØTB = 0 no bubble plot prepared

If NPLØTB > 0 relevant data for the bubble plot are written on file number FT12FO01

NPLØTØ identification for the optional plot to be specified by the user.

If NPLØTØ = 0 no optional plot prepared

If NPLØTØ > 0 specified plot data are written on file number FT13FO01

IDELTT frequency for plotting data (IDELTT > 0). Every IDELTT time steps plot data are written on the respective files.

LP1 for the single phase coolant conditions every LP1th time step output is written (LP1 > 0)

LP2 for the two phase flow situation every LP2th time step output is written (LP > 0)

Card 3 (2I4)

NBDTR unit number of disk storage from which channel dependent data are read sequentially (NBDTR = 1)

NBDTW unit number of disk storage to which channel dependent data are written sequentially (NBDTW = 3)

Card 4 (9I4)

NKKN number of coolant channels ($1 \leq NKKN \leq 10$)

NM2 number of axial zones in the coolant channel ($NM2 \leq 30$)

NSAUL identifier for the solution of the Fourier-equation in the pin

NSAUL = 1 Sauljev method

NSAUL = 0 implicit solution

IFLAG identifier for single phase coolant solution of the momentum equation

IFLAG \leq 0 axially constant mass flow distribution (ITC1, ITC11)

IFLAG > 0 axially dependent mass flow distribution (ITC1R, ITC11R)

ICFI identifier for two phase flow pressure drop correlation

ICFI1 \leq 0 Wallis correlation

ICFI1 > 0 Lockhart-Martinelli correlation

IFILM identifier for the liquid film simulation

IFILM \leq 0 quiescent film

IFILM > 0 moving film

ICFI3 identifier for two phase flow pressure drop calculation in a mesh

ICFI3 \leq 0 mean value per mesh

ICFI3 > 0 Simpson formula along mesh size used

IERRØR identifier for special output selection in two-phase flow region

IERROR = 0 normal output selection as determined with LP2

IERROR = 1 every time step a short print out of relevant two phase flow data is given additionally

IERROR = 2 overrides the LP2 output identifier, every time step a full print out of data is given

IERROR = 3..7 special identifiers for output selection in case of errors during the two phase flow computation for debugging

moving film the value is 10μ

SMAX maximum film thickness /m/.
If calculated values are larger than this number
the film thickness is kept constant at SMAX. Recommended
values are those, which correspond to about 60%
void fraction in the channel.

RLA reduced inertial length at the outlet /m/. RLA takes
into account the mixing plenum above coolant channel.

RLE reduced inertial length at the inlet /m/

TPLEN coolant temperature in the outlet above the
mixing plenum
(TPLEN \approx 600-750°C)

ZSLUG mesh size of generated liquid Lagrangian
meshes, /m/
(ZSLUG \approx (0.6 - 1.0) ΔZ_{\min})

Card 7 (4G10.4)

PDEC1 coefficient to describe inlet pressure variation

PDEC2 coefficient to describe inlet pressure variation

PDEC3 coefficient to describe inlet pressure variation

As example: $(\Delta p_t)/(\Delta p_o) = \exp(PDEC1 * t + PDEC2 * t^2 + PDEC3 * t^3)$

(see subroutine FPKO)

TETA identifier for the solution of the Fourier equation
TETA = 0 explicit scheme (stability criterion
for time step

TETA = 0.5 Crank-Nicolson scheme

TETA = 1 implicit scheme

Card 8 (7G10.4)

(DTSHA(KKN),
KKN=1, NKKN) initial superheat for voiding initialization in
channel KKN /°C/

(0.5 < DTSHA < several $\times 10^0$ °C)

Card 9 (7G10.4)

(DTSHB(KKN), subsequent superheat for bubble initialization in channel KKN /°C/
KKN=1, NKKN) normally $0.5 < DTSHB < \text{several } ^\circ\text{C}$
(DTSHB(KKN) < DTSHA(KKN))

The following data are to be provided for SUBROUTINE STATO (steady state calculation).

Card 10 (I4)

NBD3 unit to which the steady state data are written (NBD3 = 1)
normally NBD3 = NBDTR

Card 11 (4I4)

LART identifier for channels with different materials as coolant, fuel, clad, structure or bonding ($1 \leq LART \leq 3$)

NMO first axial mesh of the fuel column. $M=(1, (NMO-1))$ is regarded as fission gas plenum. For the region $M=1$ up to $M=(NMO-1)$ only structure temperatures are calculated.

NM1 last axial mesh of the fuel column. $M=((NM1+1), NM2)$ is regarded as fuel element outlet. For this region no fuel temperatures are calculated. From $M=1$ up to $NM1$ the coolant flow area is constant. For $(NM1+1)$ up to $NM2$ a different coolant flow area can be defined.

NMTOP axial mesh inside the area (NMO, NM1) beyond that only very little heat production is assumed (normally $NMTOP = NM1$)

Card 12 (3G10.4)

TKINNO inlet coolant temperature /°C/
PKOO inlet plenum pressure / N/m^2 /
PKONO outlet plenum pressure / N/m^2 /

Card 13 (3G10.4)

CH21 coefficient f of the Re-dependent single
CH22 phase friction factor (calculated in Subroutine XFF1, XCFI).
 $f = CH21 * Re^{CH22}$

Card 14 (5G10.4)

CNN1 coefficients to determine the clad-coolant
CNN2 heat transfer coefficient
CN1
CN2 $Nu = CNN1 + CNN2 (RE)^{CN1} (Pr)^{CN2} (T_w/T_{bulk})^{CN3}$
CN3

Card 15 (5A4)

KUEL(L) name of coolant (NAL)
STRUK(L) name of structure material (4981, NB)
CAN(L) name of clad material (4981)
PELLET(L) name of fuel (UPUO)
BOND(L) name of bonding (SP(SPGA, NAL))
L=1, LART names are consistent with those used in the MAPLIB
(this card has to be provide LART-times)

All following cards have to be provided NKKK times. They are channel dependent input data.

Card 16 (3I4)

KØNT type of the coolant channel (L=1, LART)
KØNT = 1 (fuel pin)
KØNT = 2 (breeder pin)
KØNT = 3 (trimm pin)
NN number of radial meshes inside the fuel pellet
NGRID identifier for spacers
NGRID > 0 grids multiplier to friction losses in the region (NM1+1, NM2) compared to tube flow conditions
NGRID < 0 wires or rips
NGRID = number of rips or wires

Card 17 (7G10.4)

This card has to be provided NM2-times (M=1, NM2)

- RBR(M) fuel pellet outer radius assumed to be equivalent to the inner radius of the clad /m/
- DCAN(M) clad thickness /m/
- RKUE (M) equivalent coolant channel outer radius /m/
- VDUF(M) ratio of volume to surface area of structural material per unit length /m/
- VSTRUK(M) volume of structural material per unit length /m²/
- DBØND(M) gap width between fuel and clad /m/
- FWFS(M) ratio of equivalent outer to inner surface area of structural material. This ratio is used to calculate the surface area of the structural material to determine radial heat losses. It has to be chosen consistently with the surface area of structural material, for which the heat transfer coefficient between coolant flow area and bypass flow (TBPS) has been defined.

Card 18 (4G10.4)

This card has to be provided NM2-times (M=1, NM2)

- ANTB(M) percentage of power produced inside the fuel
- ANTC(M) percentage of power produced in the clad material
- ANTK(M) percentage of power produced in the coolant
- ANTS(M) percentage of power produced in the structure material

Card 19 (3G10.4)

This card has to be provided (NM1-NM0+1) times (M=NMO, NM1)

- DPO(M) ratio of fuel density to theoretical density
- CNPU(M) percentage of (PuO₂) in the fuel
- STOE(M) stoichiometry of O/Me-ratio

Card 20 (7G10.4)

DELTZ(M) axial mesh size /m/
(M=1,NM2) $(\Delta z_{\max})/(\Delta z_{\min})$ should not exceed values of
2-3 at maximum. For region (NM0, NM1) equal
spacing is preferred.

Card 21 (5G10.4)

DABST geometry description of spacers
if NGRID > 0 DABST equals the pitch between
adjacent pins /m/
if NGRID < 0 axial distance between grid
spacers /m/ (DABST > 0)

PSI description of spacers
if NGRID > 0 ratio of width to height of rips or
wires relevant for the equivalent
coolant channel
if NGRID < 0 multiplier to the hydrostatic pres-
sure at grids

HGAP heat transfer coefficient between fuel and clad
/ W/m²C /

SPALTE reference gap width for the simplified calculation
of a transiently varying gap /m/

XX correction factor of mean fuel temperatures used
for radial fuel expansion calculation (normally
XX=1)

Card 22 (G10.4)

TKOUT steady state coolant outlet temperature /°C/

Card 23 (2I4)

ML identifier for power normalization
ML = 1 total power generation in the channel
is used for normalization
ML = 2 peak power density is used for normali-
zation

MAX identifier for type of axial power distribution FAX(M)
MAX = -1 node power distribution
MAX = 1 nodewise power density distribution

Card 24 (G10.4)

QQSO power
if ML = 1 total power generation in the channel /W/
if ML = 2: peak power density in the channel / W/m³ /

Card 25 (7G10.4)

FAX(M), if MAX = 1: axial specific power distribution / W/m³ /
M=1, NM2 if MAX =-1: axial node power distribution / W /

Card 26 (7G10.4)

FACR(N), radial power distribution inside the fuel pellet
N=1, NM + 1 in relative units.

B) Output description

See description of subroutines STATO (steady state data) and AUSGAB
(transient data)

5. Auxiliary data sets and plotting facilities

The following external storage devices are used in BLOW-3A:

NDD3 = 1 unit for steady state data.
 FT01F001 to be specified on a contemporary
 disk

NBDTR = 1 read transient data from a file to be speci-
 fied as FT01F001 on a contemporary disk

NBDTW = 3 write transient data on a file to be specified
 as FT03F001 on a contemporary disk

FT04F001 Restart file from which transient data are read.
 This file has been specified from previous
 run as FT08F001 on a permanent disk

FT05F001 file for card input

FT06F001 file for paper output

FT08F001 restart file to be specified on a permanent disk. This file
 is written every 50th time step and at the end of a run.

FT11F001 file for standard plot data to be specified
 on a permanent disk

FT12F001 file for bubble plot data to be specified on
 a permanent disk

FT13F001 file for an optional plot data set to be spe-
 cified on a permanent disk.

Part IV Status of the experimental validation of the BLOW-3A programme
and code application for LMFBR safety analysis

Since the very beginning of the programme development theoretical work on the two-phase flow model used in BLOW-3A was accompanied by interpretation of experiments and application of the code in the LMFBR safety analysis. A review of theoretical interpretation work performed for in-pile and out-of-pile experiments can be found in /26/ and /30/. This work concentrated on single pin and 7-pin experiments in which various failure conditions were simulated as mass flow reduction, slow power increase, inlet blockage etc. The experiments were performed in 7-pin clusters of different design as wire wrapped bundles and bundles with grid spacers. Some examples of this work are documented in subsequent sections. In section 1 examples of interpretation work of the SCARABEE first phase in-pile experiments are given. In section 2 results of theoretical interpretation work of 7-pin out-of-pile experiments are documented demonstrating how the application of the BLOW-3A programme can contribute to a better understanding of experiments.

Besides application of the programme for theoretical interpretation of experiments BLOW-3A was extensively used in the framework of LMFBR safety analysis. On the one side these concerned analysis of the unprotected loss-of-flow accident in SNR-300 and SNR-2000 /29/, /30/ but covered as well consequence analysis of inlet blockages in the KNK-reactor /33/. Application for reactor analysis mostly was done with the CAPRI-code /29/ in which BLOW-3A is implemented as a module for description of boiling phenomena. Besides that BLOW-3A has been made available for incorporation in the EAC-code /34/ which is developed at the JRC Ispra to serve as a type of reference code for whole core accident analysis in the european community. In section 3 of this paragraph typical examples of results are given resulting from a simulation of a loss-of-flow accident in a large fast breeder reactor.

1. Theoretical interpretation of single-pin in-pile SCARABEE experiments

1.1 General

The experimental programme SCARABEE was performed by the Commissariat à l'Energie Atomique (CEA) in the CABRI-reactor, within the frame of general research on coolant accidents in LMFBR's /2/. Experiments were done to obtaine knowledge about consequences of local and global blockages, as well as pump failure simulations. The programme aimed also at analyzing the fuel element failure effects including failure propagation, behaviour of molten fuel and consequences of contact with liquid sodium. At the same time experimental data had to supply a basis for developing and validating theoretical models to describe the phenomena involved, at least up to loss of the pin or bundle integrity.

Theoretical analysis of experimental results has been done at KfK in the years 1974 to 1977 and has been documented in references /3/, /19/, /26/ as well as in a number of internal reports, issued at KfK. A short selection of these results is shown in this section. Work at KfK concentrated mainly on the interpretation of single-pin experiments with global mass flow reduction. It aimed at evaluating the thermalhydraulic aspects of two phase flow and its interaction with fuel pin deformation resulting from different loading conditions. As theoretical tools the computer programmes BLOW-3A and BREDA-2 /27/ were used.

The thermalhydraulics work at KfK developed in different steps. Firstly the recorded experimental data were transfered to KfK and a procedure was established to use efficiently the plotting facilities available at KfK. In a second step the boundary conditions of the SCARABEE test rig were analyzed to identify peculiarities of the loop arrangement which may have influenced the experimental sequence of events. A summary of the peculiarities identified during the course of the interpretation work is given in the following. The final status of the comparison between experiments and theoretical results is summarized in section 1.3. In section 1.4 conclusions are drawn from the interpretation work. Special attention is given to the status of our understanding of dominant physical mechanisms occuring during the SCARABEE experiments and to the question of prototypicality of the experimental series compared to reactor conditions.

1.2 Main characteristics of the SCARABEE experiments

During the interpretation work several peculiarities of the SCARABEE experimental rig and of the experiments performed have been identified. The main items concerned are explained hereafter.

i) Coupling factors and heat source distribution

Power production during SCARABEE experiments and its axial and radial distributions are determined by several features of test rig design and of the driver core which are known only with some uncertainties:

- neutronic coupling of the driver core to the test pin assembly;
- γ -heating in the structures and its axial and radial distributions;
- radial power profile in the test pin due to the thermal spectrum of the driver core;
- axially dependent pellet structure (full and hollow pellets) and pellet enrichment variations for some of the experiments.

These uncertainties influence the overall coupling coefficient between reactor and test pin power to a large extent. We have not worked in detail in this field but have used the information available at CEA. Coupling factors for every experiment were derived on the basis of three types of data:

- neutron transport and diffusion calculations as well as calculation of γ -heating. These were performed for the actual positioning of each test rig in the driver core;
- evaluation of thermocouple and mass flow measurements via calculation of thermal balances taking into account radial heat losses;
- investigation of fuel pellet restructuring taking the porosity distribution and the extension of differently restructured fuel as a measure of temperature distribution in the fuel pellets.

We have taken into account the calculated axial and radial power distributions but the uncertainty with regard to coupling coefficients could not be removed completely. The uncertainty of power production in the test pins thus remained

in the range of about 10%. For calculation purposes coupling coefficients therefore were taken first as a parameter to be varied in the above mentioned range. Because most of the single pin voiding experiments were performed for boundary conditions close to flow instabilities originating from two phase flow phenomena the uncertainty for the power production influenced the accuracy of the theoretical results. Eventually the value 1.88 kW (pin)/MW (reactor) was taken for the coupling factor.

ii) Leakage Flow

For most experiments the pressure drop characteristics of a leakage flow path influenced the stability of the two phase flow behaviour during the transient. The analysis aimed at investigating whether the measured levels of mass flow could be explained on the basis of calculated steady state pressure drop characteristics. Although some quasi stationary levels of mass flow could be justified, the application of the Lockhart-Martinelli correlation for the calculation of two-phase pressure drops did not confirm all measured mass flow levels. For the transient calculation it was found necessary to simulate both the test section and the leakage flow path in parallel. Especially for reduced mass flow rates with large pressure drops along the test section inlet and in the two phase flow regime, transient interaction between the two flow paths influenced the measured net mass flow variations strongly. In the final part of the transient, calculated mass flow rates through the test section and the leakage path have nearly the same magnitude. For the theoretically determined pressure drop characteristic of the leakage flow path no experimental verification is available. Therefore the range of uncertainty simulating the leakage flow theoretically cannot be given. Based on parametric simulations of dry-out and rewetting sequences in the two phase flow regime the current explanation for the experimentally observed flow oscillations is as follows: the short term sharp flow oscillations are mainly dominated by local dry-out and rewetting phenomena in the heated test section but the transient variation of the mean value is determined by the pressure drop characteristics of the parallel flow paths through the test section and the leakage gap. The leakage flow has a destabilizing effect onto the coolant mass flow, thus forcing large amplitude flow oscillations which superimpose and eventually dominate the slug oscillations due to the boiling phenomena. The influence of the leakage flow onto the development of the boiling pattern has been investigated in the calculations performed at KfK by means of a special submodule of the BLOW-3A code which has been made available for this

purpose. Details about the leakage flow representation are given in section II.C.3.4. Basically the method followed consists in using a known relationship (supplied by CEA experimental investigations) between the pressure drop across the test channel and the leakage mass flow. This relationship which holds for steady state conditions is applied in the BLOW-3A code under the assumption that acceleration forces acting onto the leakage mass flow are negligible. From the calculated pressure drop across the channel the mass flow in the leakage path is derived and subtracted from the total mass flow upstream of the inlet valve to find the mass flow through the test section. The coefficient for calculating the pressure drop in the inlet valve which normally depends on the flow streaming through the channel is modified to derive an equivalent coefficient which takes into account the total mass flow streaming through the inlet valve.

Numerical results showed that the leakage mass flow normally rises to worths which oscillate in the range of 1-2 times the mean value of the mass flow through the test channel before pin breakdown. The leakage flow representation has therefore proved to be a valuable feature to describe correctly the very last phase of the boiling phenomena as it explains the large mass flow oscillations observed.

iii) Radial heat losses

One special feature of the SCARABEE experiments is the twofold thermal isolation of the test pin from the surrounding test rig structure and the bypass flow. This thermal isolation extends along the heated but only partly along the non-heated section of the test pin. There is practically no thermal isolation in the uppermost part of the test rig. The twofold barrier in the heated part consists of two layers of low thermal conductivity materials (Al_2O_3 and ZrO_2) directly sprayed onto the Niobium tube and of a surrounding vacuum gap. By these provisions an excellent thermal isolation against the surrounding structure has been achieved. Steady state radial heat losses in this region amount to a few percents for normal flow and power conditions. In the uppermost part of the test section no thermal isolation has been provided for. Therefore radial heat losses in this section increase strongly and reach values of 15-30% along the whole test section dependent on the mass flow to power ratio of every single experiment. Thus steady state temperature distributions along the coolant channel are strongly influenced by the axially dependent radial heat loss variations.

For transients the situation becomes more complicated. Especially for fast mass flow reductions radial heat losses increase particularly in the non heated part of the test section. The increase is mainly determined by the temperature increase rate of the Niobium tube and its oxide layers. Therefore it was found necessary to simulate the thermal inertia of these materials properly. Once the two phase flow regime extends up to test rig sections with no thermal isolation recondensation phenomena on cold structures and associated transient radial heat losses in these areas dominate the two phase flow dynamics. Therefore approximations have been developed to simulate theoretically the time dependence of axially variable radial heat losses. Thermal conduction in the layered structure material and radiation effects across the vacuum gap have been taken into account. There are no specific experimental data available to check the accuracy of the approximations chosen for the theoretical analysis. Nevertheless, comparison of theoretical and experimental results have shown qualitatively that the simulation covers the main effects correctly. The influence of radial heat losses on two phases flow dynamics is strong if the two phase flow regime extends up to the axial regions where no thermal isolation is provided for.

The radial heat losses have been simulated by calculating the steady state heat transfer coefficient from the channel structure to the by-pass flow taking into account the thermal resistance of the vacuum gap separating the structure from the outer layers. (See Fig. 19 showing the cross section of the test rig). The inertia of the test rig structure has been anyway taken into account by means of a formula which introduces a time variation of the calculated heat transfer coefficient. A parametric analysis of the heat transfer coefficient, varying the gap conductivity (in case a non-perfect vacuum is assumed) and the integral emissivity of the gap surfaces, has been performed with a computing programme independent of BLOW-3A. It has led to the conclusion that the most reliable heat transfer coefficient is obtained making the assumption of a perfect vacuum gap with gray body integral emissivity of about 0.85, which corresponds to strongly oxidized gap surfaces. The method adopted to calculate the heat transfer coefficient to the by-pass flow takes into account the radiative thermal resistance of the vacuum gap and the resistance to conduction of all layers. It consists in deriving a quasi-stationary heat flux q in dependence on the temperature difference between structure outer surface and by-pass flow. The overall heat transfer coefficient is then defined as $K=q/(2\pi R_e (T_S - T_b))$ where R_e is the radius of the equivalent Niobium structure and T_S , T_b are the temperatures of the

structure outer surface and of the by-pass flow respectively. The calculation takes into account the dependence of material properties on the temperature. Details of this calculations have been given in section II.C.3.3.

1.3 Analysis of SCARABEE IV experiments

The SCARABEE single pin experiments, which were completed in summer 1974, comprised 18 test series whose main characteristics are summarized in table V. They can be classified in two groups characterized by rapid flow reduction at constant reactor power (experiments II to XI) and by slow overpower transients without flow reduction (experiments XII to XVIII). Within the first class of experiments the first five were run with a helium fill gas pressure of 1 bar; in those of the second group pressure was increased to 10, 20 and 30 bar (at 20 °C) and a different fill gas composition was chosen to simulate fission gas release during pin irradiation.

The experiments were run in subsequent phases: first a pre-irradiation aimed at reaching a prototypical fuel pellet microstructure due to material redistribution. A second phase was intended to test the thermal behaviour of the test section for different coolant flows and reactor power levels and to assess the thermohydraulic behaviour of coolant up to flow reversal and dry-out with subsequent fuel and clad melting. "Post mortem" analysis was performed to investigate the formation of central voids, extension of molten fuel regions and fuel dislocations.

Referring to /3/, /19/ and /26/ for the complete analysis of the thermal-hydraulic aspects of the SCARABEE experiments, we discuss here the most important results of the theoretical interpretation of the experiment SCARABEE IV. This test pin is shown schematically in Fig. 20. Half of the fuel pellets, 34 in total, were provided with a central hole in which the thermocouple TC8 was inserted for measuring the central temperature. Other thermocouples were applied to measure the temperature in the fuel-clad gap (TC10), at the clad surface (TC9 and TC11), and at coolant outlet (TC12). The fuel consisted of nearly stoichiometric UO_2 enriched to about 20% U-235. The clad material was AISI 316L. The most important data of SCARABEE IV are presented in table VI.

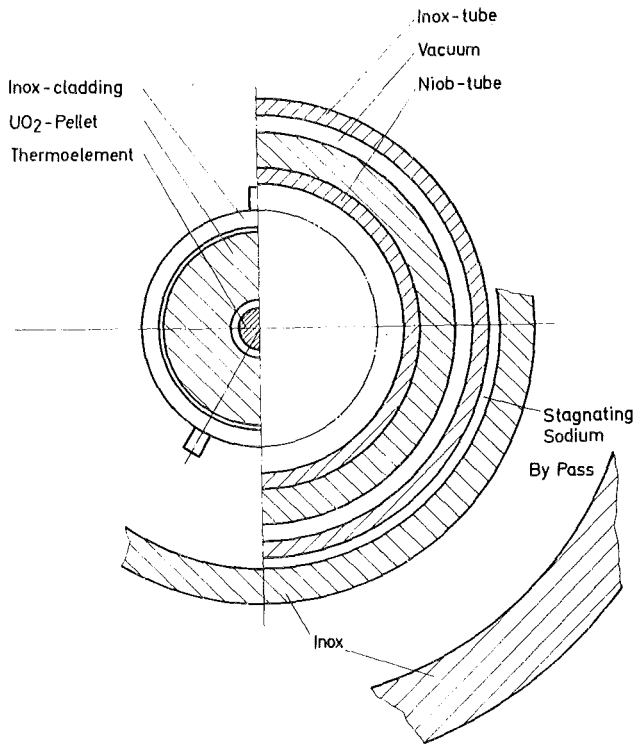
Table V.: SCARABEE single pin experiments

Experiment Nr.	Type	Inner pressure (at 20°C in bar)	Tests
II	g D	1	LZ,LLT,SDT
III	g D	1	LZ,LLT,SDT
IV	g D	1	LZ,LLT,SDT
V	3/6-blockage, 2 cm high at middle axial position	1	LZ,SDT
VI	g D	10	LZ,LLT,SDT
VII	g D	1	LZ,LLT,SDT
VIII	5/6-blockage, 2 cm high at upper axial position	1	LZ,DTP
IX	g D	20	LZ,LLT,SDT
X	g D	30	LZ,LLT,SDT
XI	g D	30	LZ,LLT
XII	Flow-coast-down tests	1	LZ,LLT
XIII	S L T	1	S L T
XIV	S L T	1	S L T
XV	g D	1	LZ,LLT,SDT
XVII	pump breakdown at over power	30	D T P

Symbols: g D - global flow reduction, S L T - fast power transient, L L T - slow power transient,
S D T - fast flow reduction (by valve), D T P - flow reduction (by pump), L Z - power cycles.

Table VI: Data of the SCARABEE IV test pin

Fuel:	material	UO ₂ with 20.05% U-235
	theoretical density	10.95 g/cm ³
	pellet density	10.13 g/cm ³
	porosity	7.5%
	O/Me	2.0017
	solid pellet	
	diameter	5.575 mm
	hollow pellet	
	inner diameter	1.650 mm
	outer diameter	5.567 mm
Cladding:	material	AISI 316 L
	inner diameter	5.80 mm
	outer diameter	6.70 mm
Fuel pin:	length of fuel column	340 mm
	configuration	17 solid pellets in the lower part, above them 17 hollow pellets
	radial gap width (cold state)	solid pellet 112.5 μm hollow pellet 116.5 μm
	filling gas	helium (assumed contamination 10% argon equivalent)
	gas pressure	1 bar at 20°C



SCARABEE - Cross - Section

Fig. 19:

Cross section of the test rig for single-pin SCARABEE experiments

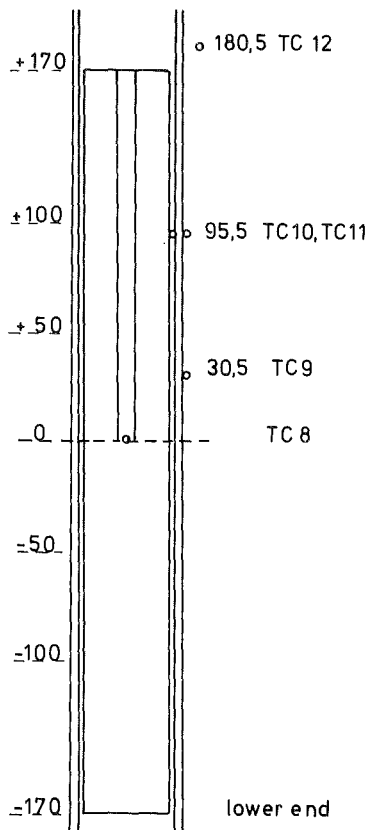


Fig. 20:

Scheme of fuel pin used in the SCARABEE experiments with position of some thermocouples for SCARABEE IV.

The preirradiation of the test pins was characterized by the following history: the first operation period aimed at reaching a defined restructuring of the fuel and deriving heat balances to determine the coupling factor between reactor core and test rig powers. This period was followed by a more or less large number of power cycles of variable length. Individual thermohydraulic tests were carried out in these cycles. For the analysis of the fuel behaviour during the first operation period and the following power cycles the computer code system SATURN-1 has been used /28/. With this code system the irradiation history has been simulated realistically so that details about thermal behaviour and restructuring of fuel have been made available at any time of the irradiation. Some characteristic results of the calculations are presented hereafter.

The irradiation history of SCARABEE IV was governed by a large number, 28 in total, of relatively short power cycles (240 till 9320 seconds). Results of theoretical interpretation are shown for two of the most representative experiments of the series SCARABEE IV (3064-2 and 3068-2). Mass flow reduction to about 30% of the stationary value at constant power is in these experiments the common feature which leads in a few seconds to boiling inception. The subsequent boiling evolution is different for the two experiments. In the first (3064-2) the reactor was scrammed immediately after boiling inception. In the second (3068-2) the reactor power was kept on up to clad melting and pin breakdown.

1.3.1 Experiment 3064-2

This experiment is characterized by a relatively slow reduction of coolant flow down to about 28% of the steady state value in about 9 sec at constant reactor power of 6.1 MW followed by a fast power transient down to about 1 MW (See Fig. 21). Some experimental and computed data referring to steady state and boiling inception are shown in Table VII. At about 9.8 sec after beginning of the flow transient boiling was detected (See Fig. 22). Boiling kept on for about three seconds during which the energy stored in the pin was released to the coolant. The theoretical calculations reproduce satisfactorily the experimental data through the boiling phase up to the definite reentry into single phase flow regime. Fig. 23 to 25 show a comparison of calculated and experimental temperatures at three axial levels, the third (TC12 in Fig. 25) being just above the top end of the heated section and thus representing the overall heat balance. Before reactor scram the dis-

	Experiment		Experiment		
	SCARABEE IV 3064-2	Calculation	SCARABEE IV 3068-2	Calculation	
Coolant inlet temperature °C	440	440	440	440	* A coupling coefficient c = 1.88 kW/MW between pin power and reactor power has been assumed
Coolant temperature (t=0) at level z=95.5 mm (TC12, see Fig 20)(°C)	608	616	595	606	
outlet temperature at t=0 (°C)	575	575	577	581	
Mass flow at t=0 (m ³ /h)	0.225	0.227	0.231	0.230	
Mass flow at boiling inception (m ³ /h)	0.060	0.057	0.070	0.069	
Boiling inception (sec)	9.80	9.77	5.25	5.35	
Reactor power * (MW)	6.1	6.1	6.1	6.1	

Table VII: Comparison between experimental and calculated data for SCARABEE IV 3064-2 and 3068-2 referring to steady state and boiling inception.

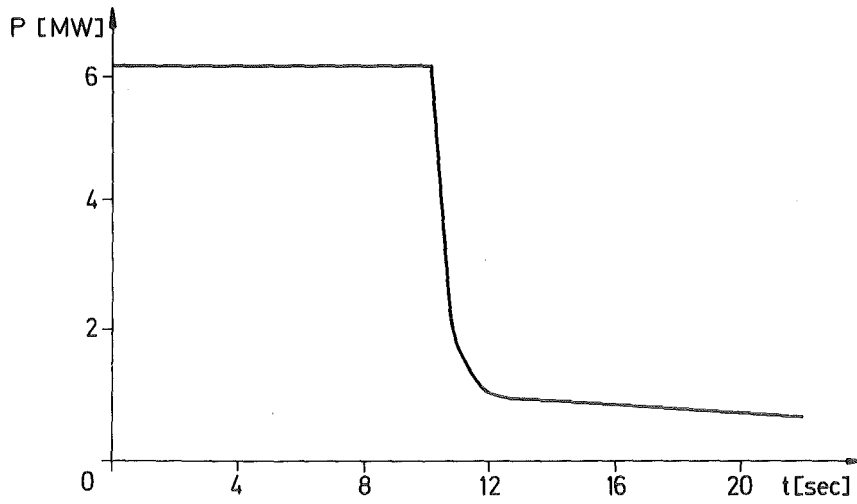


Fig. 21: Time variation of reactor power during the experiment. SCARABEE IV 3064-2.

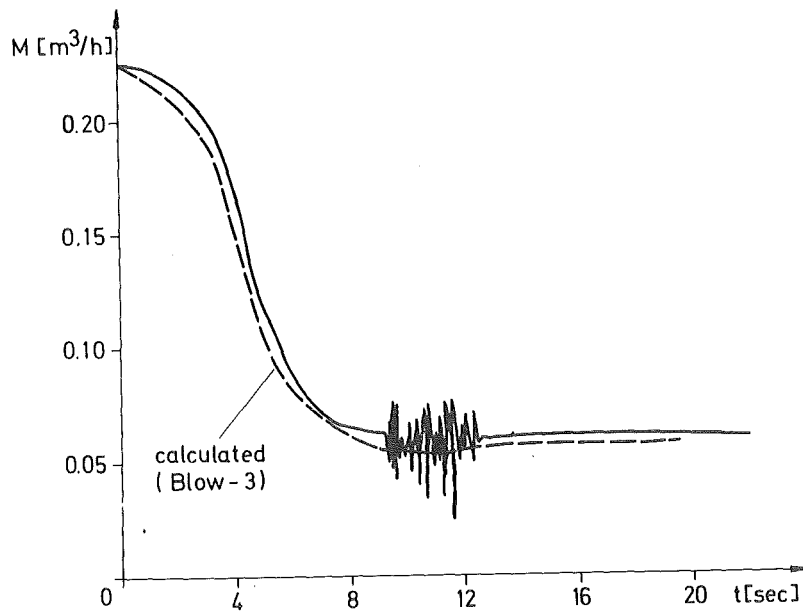


Fig. 22: Experiment SCARABEE IV 3064-2. Experimental and calculated flow rate versus time.

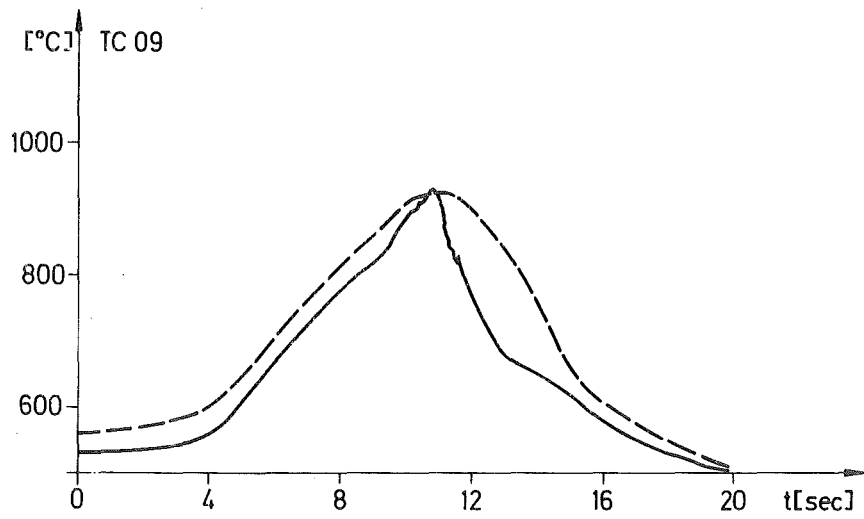


Fig. 23: Experiment SCARABEE IV 3064-2. Calculated and experimental coolant temperatures (thermocouple TC09 at axial level 30.5 mm)

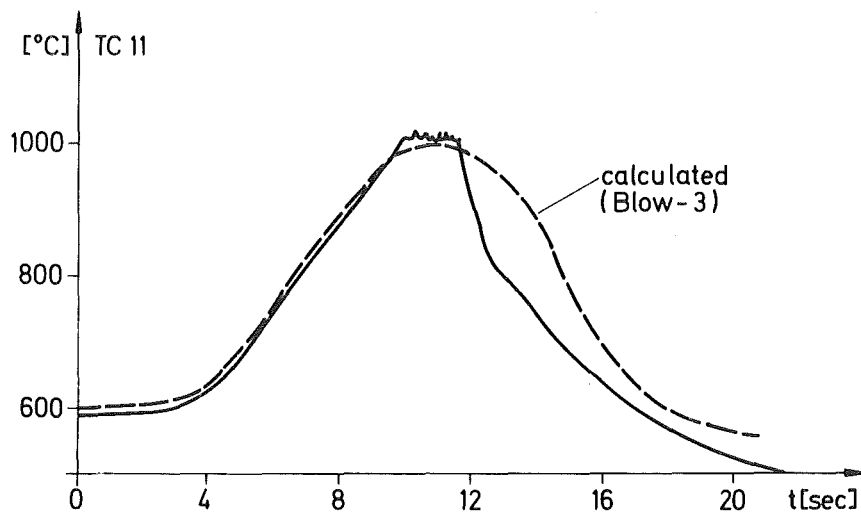


Fig. 24: Experiment SCARABEE IV 3064-2. Calculated and experimental coolant temperatures (thermocouple TC11, at axial level 95.5 mm; see Fig. 20).

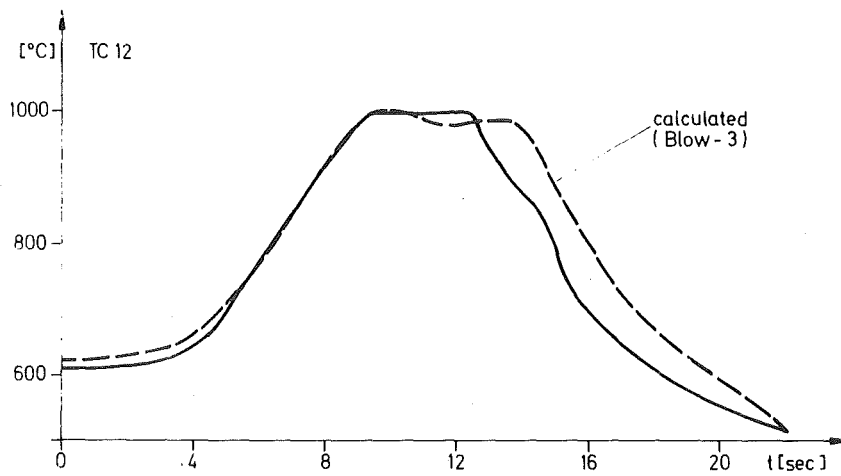


Fig. 25: Experiment SCARABEE IV 3064-2. Calculated and experimental coolant temperatures (thermocouple TC12, situated at axial level 180.5 mm, above the top end of the heated section; see Fig. 20)

crepancy between measured and calculated temperatures never exceeds about 8%. After the reactor scram the calculated coolant temperature decrease is delayed by about 1 sec with respect to the measurements. This is probably due to the difficult simulation of the heat losses in the experimental rig. However, in case of the uppermost thermocouple TC12, the slope of the experimental plot is well reproduced.

1.3.2 Experiment 3068-2

Experiment 3068-2 is characterized by a fast mass flow transient to about 30% of the steady state value by constant reactor power (6.1 MW). Aim of experimental and theoretical evaluations was the analysis of single and two phase flow up to clad melting and pin breakdown.

The computation of steady state temperatures and mass flow has afforded results in agreement with experimental data to within 5% and 2% respectively. Temperature drop in the upper channel section has been simulated allowing quite large heat losses in the region above the heated zone. Heat transfer coefficient to by-pass flow in this upper region refers to the assumption of strongly oxidized structure gap walls. Relevant data referring to the stationary computation are summarized in Table VII and compared with experimental ones.

Mass flow reduction occurs from the steady state value of $0.231 \text{ m}^3/\text{h}$ to $0.070 \text{ m}^3/\text{h}$ in 0.4 sec. By appropriate time variation of the pressure drop coefficient of the input valve, the final mass flow has been computed quite accurately ($0.069 \text{ m}^3/\text{h}$). Coolant temperature distributions during the subsequent 5 sec up to boiling inception have been computed with an accuracy within a few percents.

Assuming a small coolant superheat in the range 0.5 to 2°C , boiling starts between 5 and 5.4 sec after transient initiation, which corresponds quite accurately to the observed 5.25 sec. Boiling is stable during the first 0.8 sec after boiling inception. Small bubbles form in the hottest region above the heated zone and are rapidly drawn upwards into a cooler region where they recondensate. Between subsequent bubbles production single phase flow is reestablished.

After roughly 0.8 sec, since start of transient, bubbles become larger and do not vanish any more in the upper channel section. They expand gradually downwards into the heated zone. Due to increased drag force in the channel, pressure drop rises, thus leading to higher pressure axial distribution and higher temperatures in both vapour and liquid phases. Temperature raising rate agrees fairly well with experimental data. The difference which can be observed comparing computed and experimental plots arises from a somewhat too short computed transition phase between boiling inception and formation of larger bubbles. As mentioned above, this phase lasts some 0.8 sec, predicted by the code, against 1.5-2 sec experimentally observed. As a consequence of relatively quick downwards bubbles expansion, temperatures in the middle of heated zone increase too rapidly, thus leading to a more pronounced discrepancy between measured temperatures and corresponding computed values.

Results of the theoretical analysis performed for the experiment 3068-2 are shown in Figs. 26 to 35.

The experimentally measured flow rate in the test section, corrected by taking into account the leakage flow, is plotted in fig. 26 against time together with the mean value of the calculated mass flow. Comparison shows a good agreement all through the two phase flow regime up to pin breakdown which was experimentally recorded at about 14 sec after beginning of the flow transient. During the single phase calculation the leakage flow remains a few percents of the channel flow rate. The rise of pressure drop in the test section after boiling inception determines an increase of leakage flow as shown in Fig. 27. The ratio leakage to channel flow rate stabilizes at about 1.4 roughly 5 sec after boiling inception. Pressure drop calculation in the bubble region was performed with the method explained in section II.C.2.3.5. The assumed correlation between Lockhart-Martinelli parameter and two phase multiplier was based on the experimental work performed at KfK on single pin boiling experiments in a sodium loop /22/. Fig. 28 shows the normalized leakage flow versus the flow rate through the inlet valve. The plot consists of two branches:

The first (AB) is the locus of the working points from the steady state (point A) up to the end of mass flow reduction (point B). The working point remains in the neighbourhood of B all through the single phase flow calculation and part of the two-phase flow, up to about 7 sec, when the test mass flow starts decreasing. From this point on branch BC is described. The working point stabilizes eventually around C.

The time evolution of the voided region is shown in Fig. 29. Due to the small assumed superheat (0.5°C) bubbles vanish for roughly half a second after boiling inception and single phase flow reestablishes. Later on bubbles extend rapidly upwards and to a less extent downwards into the heated part of the test section. The voided region stabilizes about 7 sec after boiling inception stretching over roughly 60 cm. of the test section. Vapour production in the fuelled region and condensation in the upper zone produce large oscillations of the phase boundaries and are responsible for sodium ejection at channel outlet. In the annular flow model an initial clad and structure film thickness of $75\ \mu\text{m}$ was assumed which corresponds for the SCARABEE geometry to a void fraction 0.80. Liquid film velocity was derived from the calculation of two phase multipliers as explained in section II.C.2.3.5. The calculation predicts onset of dry-out at clad upper fuelled section after 9 sec and clad melting inception 3.5 sec later at roughly two third height of the fuelled region. Melting progresses rapidly downwards into the region of maximum power generation. Full clad melting takes roughly 2 sec, which agrees with the experimentally observed pin breakdown at 14 sec.

A comparison between calculated and measured coolant temperatures is shown in Figs. 30 to 33 which refer to several axial levels above the mid plane of the 340 mm fuelled length. Although some discrepancies are evident, and sometimes contradictory to each other, the general thermal balance which is represented by the reading of thermocouple TC12 (Fig. 32), situated above the top end of the fuelled zone, agrees fairly well with the calculated values up to 10 sec after transient initiation. In general, the saturation pressure, hence the coolant temperature, seems to be slightly underestimated. Although no experimental information is available, we present the calculated axial pressure distributions in the channel for several time points in Fig. 34. The plot for $t = 5.4$ sec corresponds to boiling inception. The figure shows the large increase with time of the pressure drop in the two-phase flow region.

Of major importance for the fuel thermal load and thermal flux to the coolant is the calculation of the transient fuel-clad gap width performed in parallel calculations with the module BREDA-2 of the CAPRI-2 programme system /29/. The gap heat transfer coefficient calculated with the programme SATURN-1 /28/ for the filling gas helium ranges from 4000 to $13000\ \text{W/m}^2\ ^{\circ}\text{C}$ corresponding to a gap width in the range 100-10 μm .

SCARABEE 4 3068-2 WITH LEAKAGE FLOW COUPLING-FACTOR=1.88

```

1 0 0 10 30 50
1 3
1 30 0 1 1 1 1 0 0
1. 0.1 0.1 0.002 20. 0.
0.000075 0.000010 0.000150 0.30 0.72 750. 0.015
-8. 0. 0. 0.5
1. 1.
1
1 5 25 16
440 4.30E05 2.48E05
0.396 -0.25
7. 0.025 0.8 0.8 0.
NAL 49814981UPUØSPGA
1 10 -1
2.90E-03 0.45E-03 4.10E-03 1.69E-03 7.91E-05 0.115E-03 1.317 (4. times)
2.90E-03 0.45E-03 4.10E-03 1.50E-03 3.86E-05 0.115E-03 1.317 (21)
2.90E-03 0.45E-03 4.10E-03 1.69E-03 7.91E-05 0.115E-03 1.317 (5)
0. 0. 0. 1. (4)
1.0101 0.0022 0.0004 0.0007 (6)
0.9638 0.0022 0.0004 0.0007 (6)
0. 0. 0. 1. (14)
0.925 0. 2.0017 (21)
0.04 0.03 0.03 0.03 0.03 0.03 0.03
0.03 0.025 0.025 0.035 0.038 0.032 0.022
0.022 0.021 0.02 0.02 0.02 0.032 0.032
0.032 0.032 0.032 0.032 0.032 0.032 0.037
0.037 0.040
0.3 0.2 5.E03 0.63E-041.
577.
2 1
1.482E09
1.30E06 1.30E06 1.30E06 1.30E06 1.451E09 1.477E09 1.482E09
1.469E09 1.431E09 1.378E09 1.307E09 1.213E09 1.112E09 1.013E09
0.919E09 0.827E09 1.20E06 1.20E06 1.20E06 1.20E06 1.20E06
1.20E06 1.20E06 1.20E06 1.20E06 1.20E06 1.20E06 1.20E06
1.20E06 1.20E06
1. 1. 1. 1. 1. 1. 1.
1. 1. 1. 1.

```

Table VIII: Input data for experiment SCARABEE IV 3068-2.

(Numbers in parenthesis at the right side indicate how many times the card must be input.)

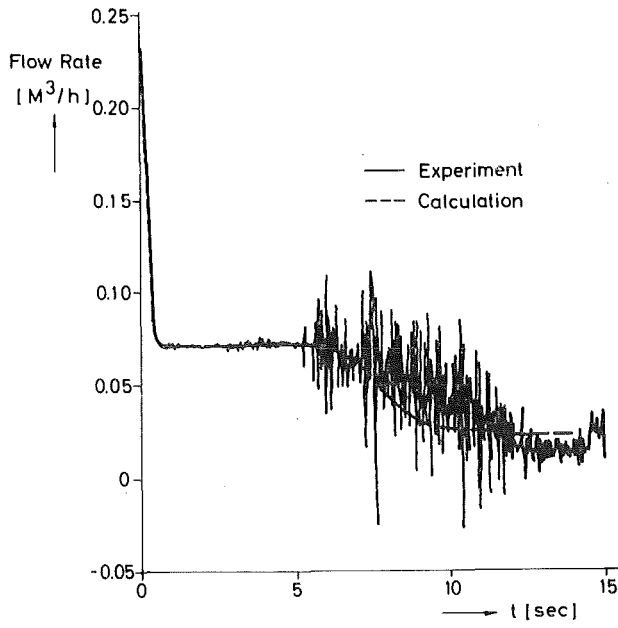


Fig. 26: Experiment SCARABEE IV 3068-2. Experimental and calculated flow rate versus time.

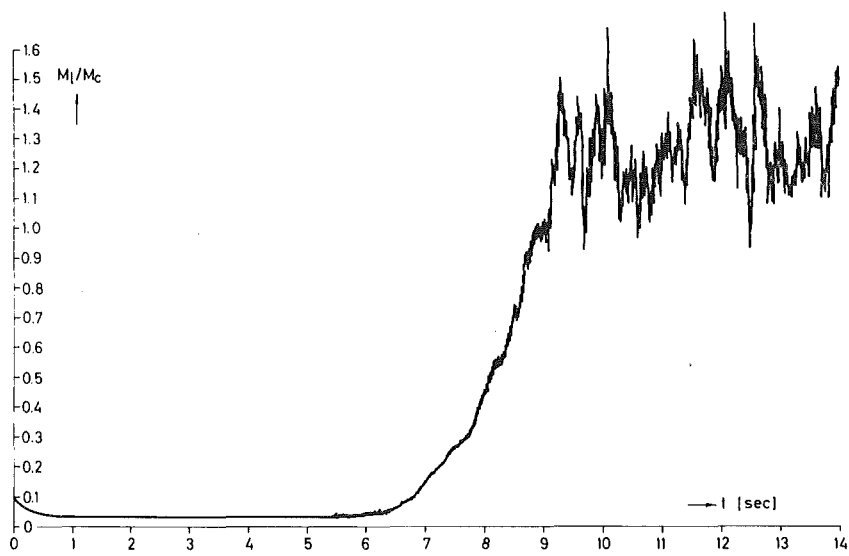


Fig. 27: Experiment SCARABEE IV 3068-2. Leakage to channel flow rate versus time.

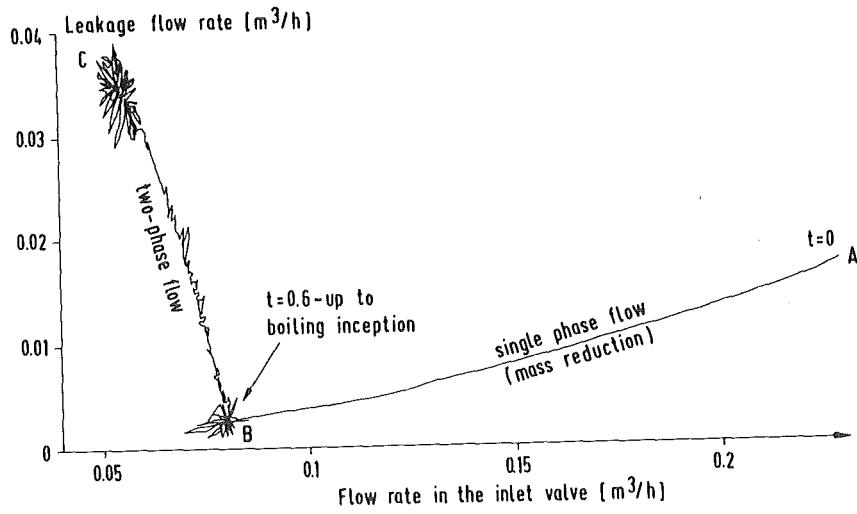


Fig. 28: Experiment SCARABEE IV 3068-2. Normalized leakage flow versus the flow rate through the inlet valve.

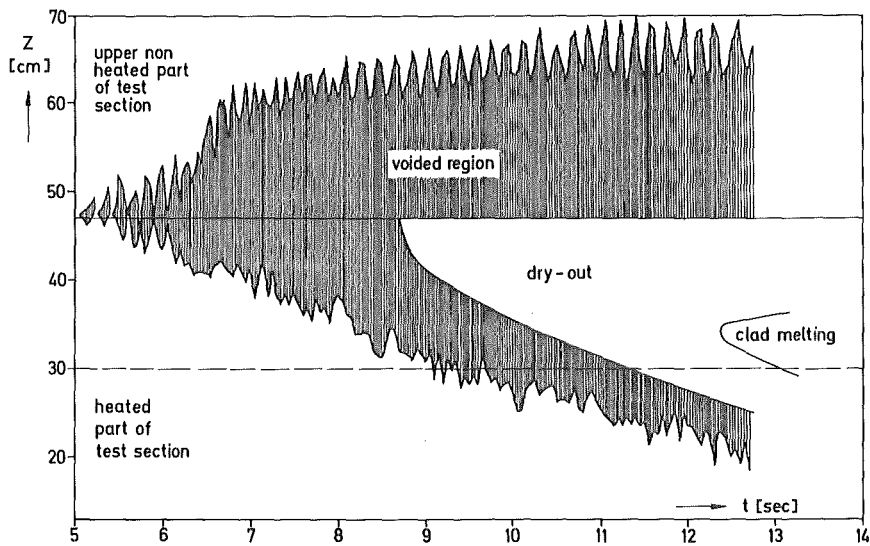


Fig. 29: Experiment SCARABEE IV 3068-2. Development of voided region, dry-out and clad melting versus time.

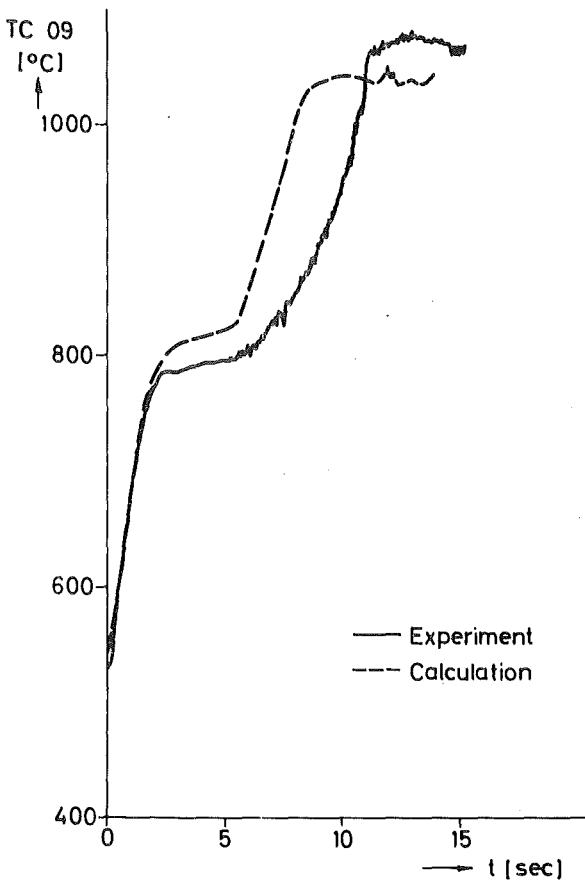


Fig. 30:

Experiment SCARABEE IV 3068-2.
Calculated and experimental
coolant temperatures (thermo-
couple TC09 at axial level
30.5 mm; see Fig. 20)

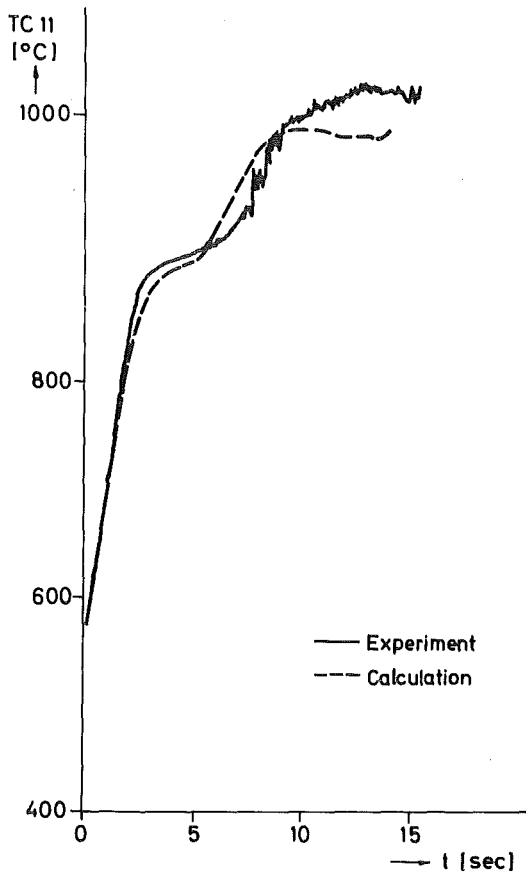


Fig. 31:

Experiment SCARABEE IV 3068-2.
Calculated and experimental
coolant temperatures (thermo-
couple TC11 at axial level
95.5 mm; see Fig. 20)

Fig. 32:

Experiment SCARABEE IV 3068-2.
Calculated and experimental
coolant temperatures (thermo-
couple TC12 at axial level
180.5 mm; see Fig. 20)

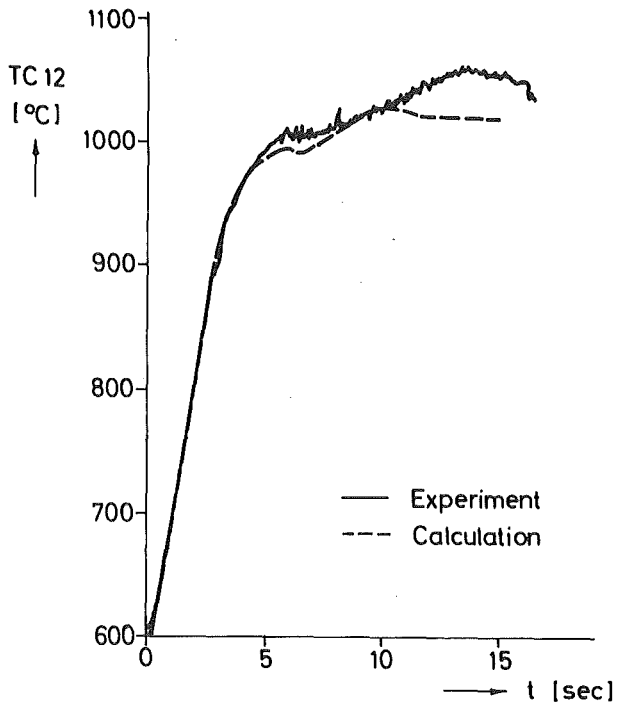
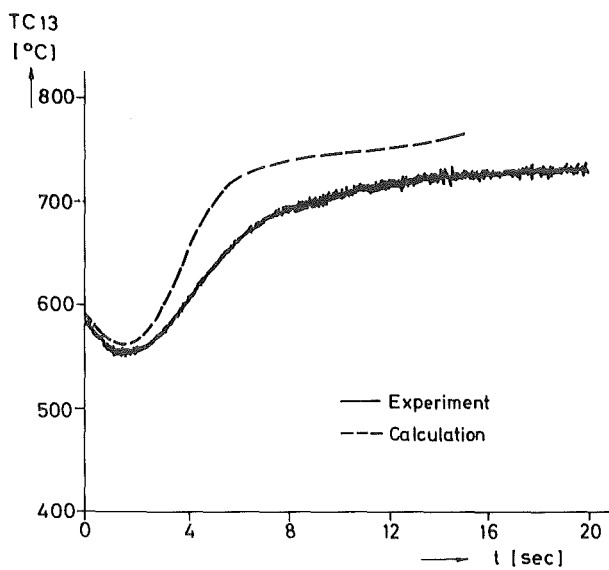


Fig. 33:

Experiment SCARABEE IV 3068-2.
Calculated and measured coolant
temperatures at axial level
497.5 mm above fuel mid-plane.



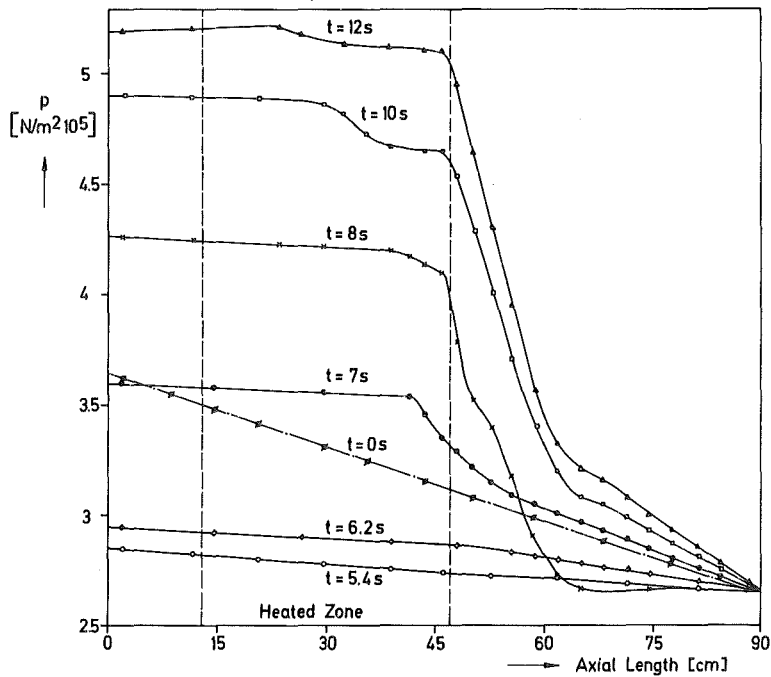


Fig. 34: Experiment SCARABEE IV 3068-2. Axial distribution of coolant pressure with time as parameter. The distribution at $t = 5.4$ sec corresponds to boiling inception.

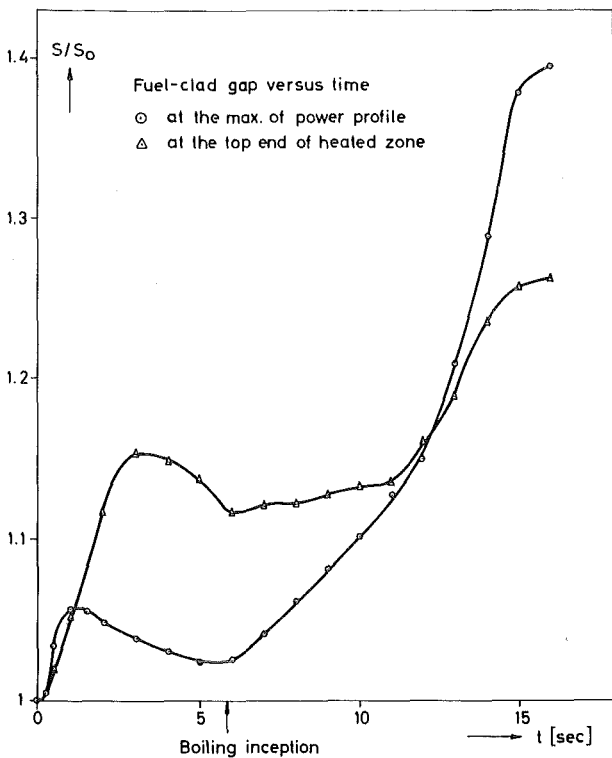


Fig. 35:

Experiment SCARABEE IV 3068-2. Normalized fuel-clad gap versus time.

Fig. 35 shows the time variation of the normalized gap width for two axial nodes. Pin radial expansion is more pronounced in the lower part of the heated section which corresponds to the maximum of the axial power distribution. The most severe transient starts at about 10 sec with onset of dry-out and leads eventually to pin disintegration.

1.4 Conclusion

The theoretical interpretation of the SCARABEE IV experiments discussed above was partially infirmed by difficulties inherent to the analysis of the experimental data, due to appearance of inconsistencies in various instrument readings. The most sever handicap for a successful analysis of the experiments was represented by the uncertainty of the coupling factor between reactor and pin power. Estimations made with different methods (thermal balances based on coolant temperature measurements as well as neutronic flux calculations) gave results scattered in a broad range. Eventually we have chosen the value 1.88 KW (pin)/MW (reactor) for the coupling factor.

Moreover, the SCARABEE test rig is not representative for typical reactor conditions. The main reasons for this are the large thermal inertia of the structural materials, the reduced length of the thermal shielding which does not prevent from large power losses in the upper part of the test section, the leakage flow which affects the transient behaviour mostly during the two phase flow. The leakage flow from the channel affects the oscillating behaviour of the liquid slugs during the two phase flow and has to be taken into account for a correct simulation of the amplitude of the inlet mass flow oscillations. However, its importance is limited when only a qualitative description of the various experimental phases (boiling initiation, dry-out onset, first flow reversal, inception of clad melting and pin failure) is desired. Quantitative results differ to some extent from the experimental ones because the leakage flow becomes dominant with respect to the channel flow in the last phase of the experiment before pin failure.

The implementation of the BLOW-3A programme aimed first at making possible the simulation of the above mentioned characteristics of the SCARABEE experiments. In spite of the uncertainties related to the experimental data, to the coupling factor, and to the simulation of the peculiar experimental features, the thermal-hydraulic analysis performed at KfK gave results which

are qualitatively in good agreement with the available experimental information and also quantitatively acceptable.

The theoretical analysis has proved the validity of the code improvements which enabled the analysis of boiling in experiments where no superheat was observed. Further typical features of the experiments like destabilizing effects produced by the leakage flow or thermal losses behind the complicated rig structure have been successfully described. Comparison of theoretical results with experimental data has shown a satisfactory agreement all through the two-phase flow regime up to pin breakdown and has allowed a better interpretation of experimentally observed boiling phenomena.

Apart from the code verification for the peculiar SCARABEE conditions, the analysis has yet enabled to individualize, in the sequence of events typical for sodium boiling under loss of coolant accidents, the aspects of the involved phenomena which strongly depend on the characteristics of the SCARABEE experiments and which cannot be straightly extrapolated to reactor conditions.

2. Theoretical interpretation of 7-pin bundle out of pile sodium experiments of the NSK series

2.1 General

In the framework of LMFBR safety analysis a number of sodium boiling experiments has been performed at KfK in the NSK (Natrium-Sieden-Kreislauf) test loop, with a bundle of seven electrically heated pins within hexagonal wrappers simulating a fast reactor subassembly.

The experiments of the series were intended to investigate the boiling behaviour following a simulated failure of the power supply to the pumps coupled with the coincident failure of the reactor to trip.

The main purpose of the experimental investigation was to assess the boiling initiation in the different subchannels of the bundle, to analyse location and rate of growth of the voided region, development of various flow regimes, onset of dryout in different subchannels and its incidence on pin temperature and flow reversal. Influence of initial superheat on boiling propagation to adjacent channels, and on dynamic behaviour of the coolant had also to be analysed.

Detailed results of these experiments on sodium boiling under flow rundown conditions and of the interpretation of the experimentally recorded data are given in reference /24/. Information about geometry of test section and pin bundle and its instrumentation, essential for the understanding of the present report, is given shortly in section 2.2.

The computational analysis of these experiments made with the BLOW-3A programme aimed at providing a further validation by assessing its suitability to interpret a pin bundle behaviour by means of equivalent single-pin channels. Results of these calculations are presented and discussed in the next sections.

2.2 Test Section and Instrumentation of the 7-pin bundles

The test section is illustrated in Fig. 36. The seven pins of 6 mm outer diameter lie on a 7.9 mm pitch, surrounded by a hexagonal wrapper. As the experimental work was carried out in the frame of SNR development the pin pitch and diameter, hence the hydraulic diameter of the subchannels, correspond to those of the SNR-300 fuel element. The pin surface heat fluxes

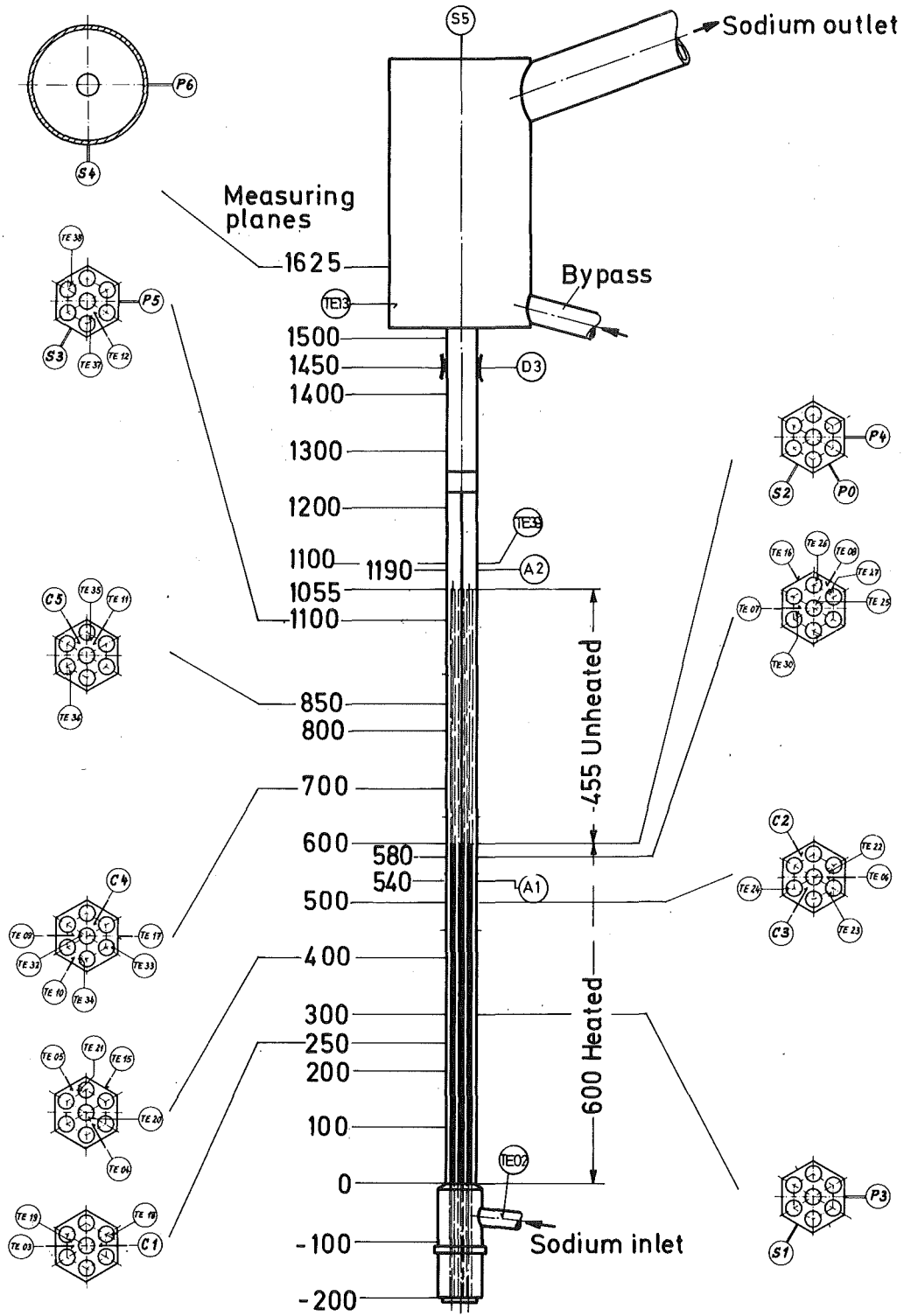


Fig. 36: Test section and measuring planes of the 7-pin bundle Nr. 2

also lay within the same range. However the length of the electrically heated section was 600 mm, compared with a fuelled length of 950 mm of the SNR core. The power distribution was linear along the axial height compared to the cosine power distribution valid for reactor conditions. To compensate for these differences some test parameters like coolant inlet temperature and pressure were selected so that the axial temperature and pressure profiles at onset of boiling became close to those calculated for a typical SNR subassembly.

At its upper end, pin geometry is preserved into the unheated region, which simulated the upper axial blanket and extends a distance of 455 mm. Above it the hexagonal wrapper is retained for a further 170 mm beyond which the test section becomes circular. The upper mixing chamber is positioned 925 mm from the upper end of the heated section.

Fig. 36 also illustrates the location of test section instrumentation. Details about data recording and correlation of signals are given in /31/. Basically the instrumentation consisted of

- a) Five Chen type bubble detectors (represented by the letter C in Fig. 36).
- b) Four piezo-electric pressure transducers (P3 to P6 in Fig. 36) to monitor rapid pressure fluctuations.
- c) Four inductive KAMAN transducers (S1-S4) also to monitor dynamic pressures.
- d) Two pressure transducers (P0-P2) measuring absolute pressures at the end of the heated section, and at channel inlet upstream of a throttle valve, respectively.
- e) A total of forty thermocouples (identified in Fig. 36 as TE)
- f) Six Jodel type void detectors (J1-J6).
- g) Two piezo-electric acoustic sensors (A1 and A2) and a piezo-electric microphone(S5).
- h) Permanent magnet flow meters monitoring inlet and outlet test section flows and bypass flow.

Of primary importance for the analysis of the transient voiding behaviour were, besides thermocouple measurements, the Chen detector signals which indicate unequivocally the presence of vapour. By the flow meter signals onset of boiling and first flow reversal were precisely determined. Further integration of their signals allowed to calculate "equivalent void" region, i.e. the length which would be occupied by the vapour. Evaluation of these recorded experimental data is documented in /24/.

For theoretical interpretation of the 7-pin experiments with BLOW-3A it is necessary to simulate the complicated structure of the electrical heaters as one single equivalent material with a uniform volumetric heat source and to represent the coolant flow area of the bundle geometry by only one representative single-pin coolant channel with structural material.

Details about the simulation of the electrical heaters and about the definition of the equivalent coolant channels are given in the next section.

2.3 Simulation of the electrical heaters and definition of equivalent channels

i) The electrical heaters

The geometrical configuration of the electrical heaters made it necessary to define six zones in axial direction with different equivalent materials. The physical properties of these "equivalent materials" have been determined by suitable averaging along the radial direction. Dominant for the calculations are average specific mass, thermal capacity and conductivity. The thermal conductivity of the material adjacent to the clad has been taken to simulate radial temperature gradients at the surface of the gap between heater and clad in the transient phase. The resulting zone structure is given in Table IX.

Table IX: Axial zone structure of the electrical heaters (Z=0 corresponds to the bottom of the heated zone)

Zone	axial position (mm)	material composition
I	$-230 \leq Z \leq -200$	inner Ni kernel, outer BN-layer
II	$-200 \leq Z \leq 0$	inner Cu kernel, outer BN-layer
III	$0 \leq Z \leq 600$	heated section: MgO, NiCr, outer BN-layer
IV	$600 \leq Z \leq 761$	inner Ni kernel, outer BN-layer
V	$761 \leq Z \leq 908$	Ni cylinder
VI	$908 \leq Z \leq 1055$	steel cylinder

The following physical properties of the equivalent materials have been used as homogeneous "fuel":

Zone I (from Z = -230 mm to Z = -200 mm; length = 30 mm) made of Copper (Cu) and Boron-Nitrite (BN)

Equivalent physical properties:

Density:

$$\rho \text{ (gr/cm}^3\text{)} = 5.713 - T \times 10^{-3} (0.229 + 0.532 \times 10^{-4} T) \quad (0 \leq T \leq 1083 \text{ }^\circ\text{C})$$

Specific heat:

$$c_p \left(\frac{\text{J}}{\text{gr } ^\circ\text{C}} \right) = 0.568 + 0.159 \times 10^{-3} T + 0.098 \left(\frac{T-1083}{1000} \right)^3 \quad (0 \leq T \leq 1083 \text{ }^\circ\text{C})$$

where T is the temperature ($^\circ\text{C}$).

An average thermal conductivity has not been calculated. It seems advisable to use the thermal conductivity of the BN external layer in order to properly calculate the thermal gradient at the outer heated surface, hence the heat flux through the clad. The thermal conductivity of Boron-Nitrite is strongly dependent on both temperature and considered direction through the BN layers, normally ranging between $\lambda = 0.12 \text{ W/cm } ^\circ\text{C}$ and $\lambda = 0.34 \text{ W/cm } ^\circ\text{C}$.

We used for our calculations the figure $\lambda = 0.18 \text{ W/cm } ^\circ\text{C}$.

Zone II (from $Z = -200 \text{ mm}$ to $Z = 0 \text{ mm}$; length = 200 mm) made of Boron-Nitrite (BN) (outer layer) and Nickel (inner layer).

Equivalent physical properties:

Density:

$$\rho \text{ (gr/cm}^3\text{)} = 5.676 - 0.2115 \times 10^{-3} T - 0.009 \left(\frac{T}{1000}\right)^3 \quad (0 \leq T \leq 1452 \text{ } ^\circ\text{C})$$

Specific heat:

$$c_p \left(\frac{\text{J}}{\text{gr } ^\circ\text{C}}\right) = 0.48 + 0.732 \times 10^{-3} T - 0.175 \left(\frac{T}{1000}\right)^2 + 0.98 \times \left(\frac{T}{1000}\right)^3 \quad (0 \leq T \leq 360 \text{ } ^\circ\text{C})$$

$$c_p = 0.665 + 0.21 \times 10^{-3} (T - 360) + \frac{1.2}{T-350} \quad (360 \leq T \leq 1452 \text{ } ^\circ\text{C}).$$

Zone III (heated zone, from $Z = 0$ to $Z = 600 \text{ mm}$) made of MgO, NiCr, BN (outer layer).

Equivalent properties:

Density:

$$\rho \text{ (gr/cm}^3\text{)} = 3.3414 - 0.1111 \times 10^{-3} T \quad (0 \leq T \leq 1600 \text{ } ^\circ\text{C})$$

Specific heat:

$$c_p \left(\frac{\text{J}}{\text{gr } ^\circ\text{C}}\right) = 0.96 + 0.2905 \times 10^{-3} T + 0.0382 \left(\frac{T-1500}{1000}\right)^5 \quad (0 \leq T \leq 1600 \text{ } ^\circ\text{C})$$

Zone IV ($Z = 600 - 761 \text{ mm}$, length = 161 mm) made of Boron-Nitrite (BN) (outer layer) and Nickel (inner).

Same physical properties as for Zone II.

Zone V ($Z = 761 - 908 \text{ mm}$, length = 147 mm) made of Nickel. We used the physical properties of MAPLIB (See Reference /9/).

Zone VI ($Z = 908 - 1055 \text{ mm}$, length = 147 mm) made of Steel 4981. Physical properties of MAPLIB /9/ have been used.

ii) Definition of equivalent channels

The hydraulic diameters of the three types of subchannels in the bundle (center, wall, edge) differ considerably from each other and are rather different from the mean value of the whole bundle. Therefore theoretical simulation of the transient bundle behaviour has been performed for two types of equivalent coolant channels:

- A. An equivalent central channel, which simulates the six inner central subchannels of the bundle. This representation is referred to as KKN=1.
- B. An equivalent mean channel simulating all 18 subchannels of the bundle (6 central, edge and wall-subchannels). This channel is referred to as KKN=2.

The equivalent central channel is powered from the central pin and one third of the six peripheral ones. Thus it simulates the hot part of the bundle. Mass and momentum exchange to the peripheral subchannels are not simulated explicitly. Only heat conduction to the surrounding sodium is taken into account. By the choice of the equivalent central channel it is intended to simulate properly the single phase conditions during the pump run down and to meet best the initialization conditions for voiding.

The equivalent mean channel simulates the whole bundle. The hexcan wrapper is taken into account as equivalent structural material. Thermal losses to the isolation of the test rig are evaluated. They correspond to one percent power loss at steady state conditions. By the choice of the equivalent mean channel it is intended to simulate properly voiding conditions in the bundle once the void front has expanded from the central to the wall and edge subchannels.

Characteristic data for the test rig and the two types of equivalent coolant channels are given in Table X.

Table X: Dimensions of the coolant channel representation

		Test rig	hot channel KKN = 1	mean channel KKN = 2
lower non-heated part	mm	80		80
heated length	mm	600		600
upper non-heated part	mm	455		455
outlet region hexcan structure	mm	170		40
outlet region circular structure	mm	300		430
pin diameter	mm	6		6
hydraulic diameters of heated subchannels				
edge	mm	2.61		
wall	mm	4.32		
central	mm	5.47		
mean	mm	4.25	4.56	4.23

All details regarding the definition of the geometrical data for the equivalent channels are given in section II.C.3.5.

2.4 Calculations and comparison with experimental data

2.4.1 The computed experiments

The seven pin bundle out-of-pile experiments of the NSK series investigated the boiling behaviour as a consequence of a pump run down accident in the SNR-300. Out of this series, three of the most relevant experiments have been chosen for the theoretical interpretation. They are representative of quite different conditions:

the first (Exp. 7-2/16) with heat flux 150.3 W/cm^2 , corresponding to 282 W/cm pin linear power, presented no superheat; the second (Exp. 7-2/24) with smaller heat flux (99.3 W/cm^2 , corresponding to 186 W/cm linear power) is characterized by a large superheat (about 68 degrees); in the third (Exp. 7-2/28) a total inlet valve blockage reduced the mass flow to zero in less than one second. The steady state conditions of these three experiments are listed in Table XI together with the procedure used to initiate the transient leading to boiling.

Table XI: Characterization of the computed NSK 7-2 experiments

Experiment	7-2/16	NSK 7-2/24	7-2/28
average steady state coolant conditions:			
peak heat flux density $[\text{W/cm}^2]$	150.3	99.3	152.6
inlet/outlet pressure $[\text{bar}]$	4.18/1.52	2.03/1.05	2.19/1.05
inlet/outlet temperature $[\text{°C}]$	562/735	553/715	559/730
coolant velocity $[\text{m/sec}]$	3.0	2.15	3.0
radial heat losses nom. to total power production $[\%]$	<1	<1	<1
Experimental conditions at voiding initiation:			
type	rapid flow reduction	rapid flow reduction	inlet valve blockage
peak coolant temperature rise rate $[\text{°C/sec}]$	42.	58.	118.
coolant velocity $[\text{m/sec}]$	1.13	0.33	0.
superheat $[\text{°C}]$	0.	68.	27.

EXPERIMENT 7-2/16

```

1 0 0 10 30 50
1 3
2 30 0 1 1 1 1 0 0
1. 0.1 0.1 0.002 16. 0.
0.000150 0.000010 0.000300 0.04 0.08 750. 0.015
-8. 0. 0. 0.5
0.5 0.5
0.5 0.5
1
1 3 26 26
562. 4.18E05 1.52E05
0.183 -0.2
7. 0.025 0.8 0.8 0.
NAL 49814981UPUØSPGA
1 9 -1
2.40E-03 0.60E-03 4.15E-03 1.64E-03 3.72E-05 0.10E-05 0.114E+01 (2 times)
2.40E-03 0.60E-03 4.15E-03 2.34E-03 0.89E-05 0.10E-05 0.114E+01 (24)
2.40E-03 0.60E-03 5.12E-03 1.28E-03 2.02E-05 0.10E-05 0.114E+01 (4)
0. 0. 0. 1. (2)
1. 0. 0. 0. (15)
0. 0. 0. 1. (13)
0.999 0. 2. (24)
0.06 0.06 0.04 0.04 0.04 0.04 0.04
0.04 0.04 0.04 0.04 0.04 0.04 0.04
0.04 0.04 0.04 0.055 0.05 0.05 0.05
0.05 0.05 0.05 0.05 0.05 0.02 0.02

0.02 0.02
0.1 1.14 1.E-04 0.1E-051.
735.
2 1
1.550E09
1. 1. 1.550E09 1.550E09 1.550E09 1.550E09 1.550E09
1.550E09 1.550E09 1.550E09 1.551E09 1.550E09 1.550E09 1.550E09
1.550E09 1.550E09 1.550E09 1. 1. 1. 1.
1. 1. 1. 1. 1. 1. 1.
1. 1.
0.01 0.01 0.01 0.01 0.01 1. 1.
0.01 0.01 0.01
1 9 -1
2.40E-03 0.60E-03 4.36E-03 1.50E-03 4.461E-05 0.10E-05 0.114E+01 (2)
2.40E-03 0.60E-03 4.36E-03 1.49E-03 1.631E-05 0.10E-05 0.114E+01 (24)
2.40E-03 0.60E-03 5.28E-03 1.49E-03 1.631E-05 0.10E-05 0.114E+01 (4)
0. 0. 0. 1. (2)
1. 0. 0. 0. (15)
0. 0. 0. 1. (13)
0.999 0. 2. (24)
0.06 0.06 0.04 0.04 0.04 0.04 0.04
0.04 0.04 0.04 0.04 0.04 0.04 0.04
0.04 0.04 0.04 0.055 0.05 0.05 0.05
0.05 0.05 0.05 0.05 0.05 0.02 0.02

0.02 0.02
0.1 1.14 1.E-04 0.1E-051.
735.
2 1
1.550E09
1. 1. 1.550E09 1.550E09 1.550E09 1.550E09 1.550E09
1.550E09 1.550E09 1.550E09 1.551E09 1.550E09 1.550E09 1.550E09
1.550E09 1.550E09 1.550E09 1. 1. 1. 1.
1. 1. 1. 1. 1. 1. 1.
1. 1.
0.01 0.01 0.01 0.01 0.01 1. 1.
0.01 0.01 0.01

```

Table XII: Input data for experiment 7-2/16. (Numbers in parenthesis at the right side indicate how many times the card must be input).

EXPERIMENT 7-2/24

```

1 0. 0 10 30 50
1 3
2 30 0 1 1 1 1 0 0
1. 0.1 0.1 0.002 16. 0.
0.000150 0.000010 0.000300 0.04 0.08 750. 0.015
-8. 0. 0. 0.5
68. 12.
2. 2.
1
1 3 26 26
553. 2.0E05 1.10E05
0.183 -0.2
7. 0.025 0.8 0.8 0.
NAL 49814981UPU0SPGA
1 9 -1
2.40E-03 0.60E-03 4.15E-03 1.64E-03 3.72E-05 0.10E-05 0.114E+01 (2 times)
2.40E-03 0.60E-03 4.15E-03 2.34E-03 0.89E-05 0.10E-05 0.114E+01 (24)
2.40E-03 0.60E-03 5.12E-03 1.28E-03 2.02E-05 0.10E-05 0.114E+01 (4)
0. 0. 0. 1. ~ (2)
1. 0. 0. 0. (15)
0. 0. 0. 1. (13)
0.999 0. 2. (24)
0.06 0.06 0.04 0.04 0.04 0.04 0.04
0.04 0.04 0.04 0.04 0.04 0.04 0.04
0.04 0.04 0.04 0.055 0.05 0.05 0.05
0.05 0.05 0.05 0.05 0.05 0.02 0.02

0.02 0.02
0.1 1.14 1.E-04 0.1E-051.
715.
2 1
1.034E09
1. 1. 1.034E09 1.034E09 1.034E09 1.034E09 1.034E09
1.034E09 1.034E09 1.034E09 1.035E09 1.034E09 1.034E09 1.034E09
1.034E09 1.034E09 1.034E09 1. 1. 1. 1.
1. 1. 1. 1. 1. 1. 1.
1. 1.
0.01 0.01 0.01 0.01 0.01 1. 1.
0.01 0.01 0.01
1 9 -1
2.40E-03 0.60E-03 4.36E-03 1.50E-03 4.461E-05 0.10E-05 0.114E+01 (2)
2.40E-03 0.60E-03 4.36E-03 1.49E-03 1.631E-05 0.10E-05 0.114E+01 (24)
2.40E-03 0.60E-03 5.28E-03 1.49E-03 1.631E-05 0.10E-05 0.114E+01 (4)
0. 0. 0. 1. ~ (2)
1. 0. 0. 0. (15)
0. 0. 0. 1. (13)
0.999 0. 2. (24)
0.06 0.06 0.04 0.04 0.04 0.04 0.04
0.04 0.04 0.04 0.04 0.04 0.04 0.04
0.04 0.04 0.04 0.055 0.05 0.05 0.05
0.05 0.05 0.05 0.05 0.05 0.02 0.02

0.02 0.02
0.1 1.14 1.E-04 0.1E-051.
715.
2 1
1.034E09
1. 1. 1.034E09 1.034E09 1.034E09 1.034E09 1.034E09
1.034E09 1.034E09 1.034E09 1.035E09 1.034E09 1.034E09 1.034E09
1.034E09 1.034E09 1.034E09 1. 1. 1. 1.
1. 1. 1. 1. 1. 1. 1.
1. 1.
0.01 0.01 0.01 0.01 0.01 1. 1.
0.01 0.01 0.01

```

Table XIII: Input data for experiment 7-2/24. (Numbers in parenthesis at the right side indicate how many times card must be input).

EXPERIMENT 7-2/28

```

1 0 0 10 30 50
1 3
2 30 0 1 1 1 1 0 0
0.2 0.01 0.025 0.002 32. 0:
0.000150 0.000010 0.000300 0.04 0.08 750. 0.015
-8. 0. 0. 0.5
27. 7.
0.5 0.5
1
1 3 26 26
559. 2.25E05 1.10E05
0.183 -0.2
7. 0.025 0.8 0.8 0.
NAL 49814981UFU0SPGA
1 9 -1
2.40E-03 0.60E-03 4.15E-03 1.64E-03 3.72E-05 0.10E-05 0.114E+01 (2 times)
2.40E-03 0.60E-03 4.15E-03 2.34E-03 0.89E-05 0.10E-05 0.114E+01 (24)
2.40E-03 0.60E-03 5.12E-03 1.28E-03 2.02E-05 0.10E-05 0.114E+01 (4)
0. 0. 0. 1. (2)
1. 0. 0. 0. (15)
0. 0. 0. 1. (13)
0.999 0. 2. (24)
0.06 0.06 0.04 0.04 0.04 0.04 0.04
0.04 0.04 0.04 0.04 0.04 0.04 0.04
0.04 0.04 0.04 0.055 0.05 0.05 0.05
0.05 0.05 0.05 0.05 0.05 0.02 0.02

0.02 0.02
0.1 1.14 1.E-04 0.1E-051.
730.
2 1
1.590E09
1. 1. 1.590E09 1.590E09 1.590E09 1.590E09 1.590E09
1.590E09 1.590E09 1.590E09 1.591E09 1.590E09 1.590E09 1.590E09
1.590E09 1.590E09 1.590E09 1. 1. 1. 1.
1. 1. 1. 1. 1. 1. 1.
1. 1.
0.01 0.01 0.01 0.01 0.01 1. 1.
0.01 0.01 0.01
1 9 -1
2.40E-03 0.60E-03 4.36E-03 1.50E-03 4.461E-05 0.10E-05 0.114E+01 (2)
2.40E-03 0.60E-03 4.36E-03 1.49E-03 1.631E-05 0.10E-05 0.114E+01 (24)
2.40E-03 0.60E-03 5.28E-03 1.49E-03 1.631E-05 0.10E-05 0.114E+01 (4)
0. 0. 0. 1. (2)
1. 0. 0. 0. (15)
0. 0. 0. 1. (13)
0.999 0. 2. (24)
0.06 0.06 0.04 0.04 0.04 0.04 0.04
0.04 0.04 0.04 0.04 0.04 0.04 0.04
0.04 0.04 0.04 0.055 0.05 0.05 0.05
0.05 0.05 0.05 0.05 0.05 0.02 0.02

0.02 0.02
0.1 1.14 1.E-04 0.1E-051.
730.
2 1
1.590E09
1. 1. 1.590E09 1.590E09 1.590E09 1.590E09 1.590E09
1.590E09 1.590E09 1.590E09 1.591E09 1.590E09 1.590E09 1.590E09
1.590E09 1.590E09 1.590E09 1. 1. 1. 1.
1. 1. 1. 1. 1. 1. 1.
1. 1.
0.01 0.01 0.01 0.01 0.01 1. 1.
0.01 0.01 0.01

```

Table XIV: Input data for experiment 7-2/28. (Numbers in parenthesis, at the right side indicate how many times card must input).

Radial expansion of voiding regions to peripheral subchannels and the rapidity with which coolant temperatures become uniform over the bundle cross section are strongly influenced by the presence of superheat. In experiment 7-2/16 peak coolant temperatures in the central and in the peripheral subchannels attain the same level only 0.85 sec after boiling inception. Contrary to this observation in experiment 7-2/24 at nucleation coolant exceeds the saturation temperature in the central subchannels over a length of about 180 mm. Boiling inception is followed by a pressure pulse of 0.8 bar amplitude originating a strong expulsion and being responsible for permanent oscillating behaviour of the coolant. The pressure pulse explains the fast propagation of boiling to the peripheral subchannels where temperatures equaled the central subchannels temperatures 0.1 sec after onset of boiling. Thus these two experiments represent extremes out of the whole series of pump run down simulation. The third experiment 7-2/28 with 27 °C superheat lies between the two others as far as the rapidity of boiling propagation in radial direction is concerned, but it is characterized by an extreme rapid rise rate of the peak coolant temperature (See Table XI) because of the total inlet flow blockage.

The input data used for the three computed experiments are given in Tables XII, XIII and XIV.

Before discussing in detail the results of the calculations separately for the three experiments, we present in Table XV a summary of relevant computed and experimental data.

Table XV: Comparison of experimental data obtained in the NSK loop with calculational results for the different equivalent channels.

Experiment	7-2/16		7-2/24		7-2/28	
	Exp.	KKN=1/2	Exp.	KKN=1/2	Exp.	KKN=1/2
Boiling inception (sec)	9.15	9.4/10.2	6.4	6.7/6.7	0.95	1.2/1.4
Power off after boiling inception (sec)	2.06		1.34		2.27	
flow reversal (sec)	10.85	10.8/11.12	6.38	6.69/6.74	-	-
onset of dry-out (sec)	11.0	10.4/11.03	6.94	6.75/7.08	2.91	1.31/1.84
duration of two phase flow cond. (sec)	4.12	5.74/3.62	5.75	6.25/4.60	19.7	20.3/19.6

As shown in this table, a good agreement between experiment and calculation has been achieved with regard to time intervals characterizing the boiling history. Calculated times of boiling initiation are slightly delayed compared to the experiments, because calculations were based on transient variations of pressure boundary conditions which led to saturation temperatures of the coolant at voiding initiation being slightly higher than those observed experimentally. The time period over which the two-phase flow conditions are maintained in the test section are underestimated by the average channel simulations and overestimated by the central subchannel representation. This results from the limitations of the one-dimensional theoretical approximation to describe the pin surface conditions of the seven pins with only one representative pin.

2.4.1.1 Experiment 7-2/16

The experimentally observed boiling inception at 9.15 sec since beginning of pump run down for experiment 7-2/16 is confirmed by the calculation with slight delay (9.4 sec). Owing to the slow exchange of enthalpy between central and peripheral subchannels, vapour was observed in the latter 0.55 sec after boiling inception. The calculation for the mixed channel simulating the full bundle predicts first boiling about 0.80 sec after onset of boiling in the hot channel.

Fig. 37 shows a comparison of the measured coolant inlet velocity after boiling inception with the theoretical results. The measured pressure upstream the inlet throttle valve is also compared with the pressure boundary condition as assumed for the calculation. The rapid mass flow reduction which follows boiling initiation is reproduced fairly by the calculation for the mixed channel which predicts satisfactorily the time point of first flow reversal (11.12 sec against the measured 10.85 sec). The subsequent mass flow oscillations are reproduced well by the calculation up to about 12 sec. The calculation for the central channel does not account for energy transfer to peripheral subchannels and therefore overestimates the coolant temperatures, especially after boiling inception. This leads to rapid mass flow reduction and early prediction of first flow reversal. Subsequent oscillations of mass flow as predicted by the hot channel have not been reproduced for clarity in Fig. 37.

Fig. 38 shows the calculated peak coolant temperatures for both channels against the experimentally recorded temperature in the central subchannel (TE 7). The above discussed characteristics of the simulation reflect in the good agreement of the temperatures calculated for the mixed channel while the hot channel manifestly overestimates them. The high temperature peaks in the calculation for $KKN=1$ are due to dryout periods followed by rewetting.

Fig. 39 shows the time variation of the predicted voided region for the simulated channels against the experimental plot. For better comparing with the experimental results the calculated boiling points have been shifted for both channels by 0.25 sec thus leading the boiling initiation for $KKN=1$ in agreement with the experiment. Time is given since boiling inception. The key problem of the theoretical calculation is the prediction of the moving phase boundary, especially into the heated section, and the overall energy balance which determines the duration of boiling beyond the time point of power switch off. Both points are covered with sufficient accuracy by the calculation for $KKN=2$, provided the time shift of 0.95 sec is taken into account. Dryout is predicted first at 11.1 sec (about 2 sec after experimental onset of boiling) and precedes shortly the first flow reversal. The calculation for the hot channel reflects the above mentioned overestimation of temperatures, vapour production and length of the voided region.

The time variation of the calculated liquid film thickness is shown for the axial Mesh $M = 11$ (See Input Data in Table XII) for the cladding and for the structural material in Figs. 40 and 41 respectively. Both plots refer to the equivalent channel $KKN=1$. The axial level of mesh $M = 11$ corresponds to $Z = 380$ in Fig. 39. The downward moving boiling front reaches this level at about $t = 1.3$ sec since boiling inception; rewetting of this mesh zone occurs after power shut off at about $t = 3.8$ sec, when the two-phase flow region is shrinking. In the intermediate time interval (1.5 to 3.6 sec) an annular flow regime develops and the liquid film thickness, initialized with the input value of $150 \mu\text{m}$, corresponding to $\alpha = 0.8$ void fraction, drops rapidly to zero at the cladding. Dryout intervals are interrupted by rewetting due to the passage of moving liquid slugs. The overall length of the dryout period agrees well with the experimental information. On the contrary, at the surface of the simulated structural material the liquid film thickness never drops to zero, as shown in Fig. 41.

Fig. 37:

Experiment 7-2/16. Inlet pressure boundary condition and comparison between experimental and calculated inlet velocities versus time.

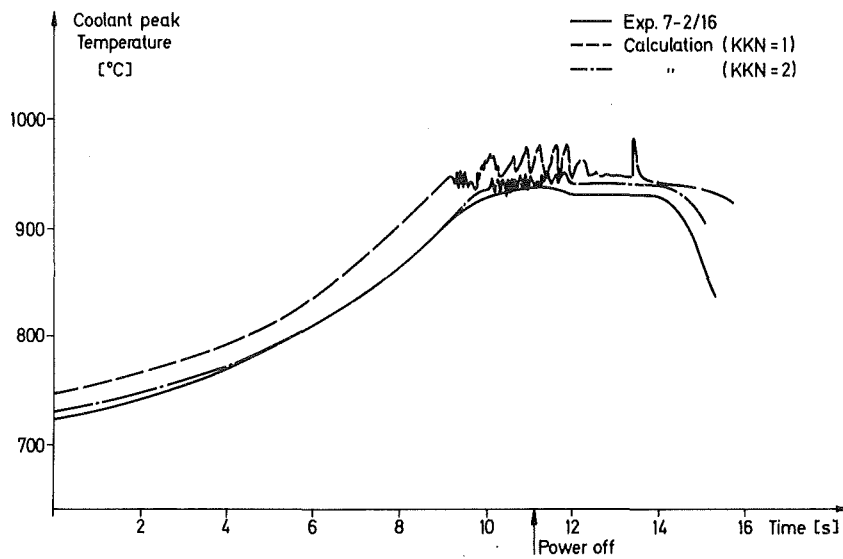
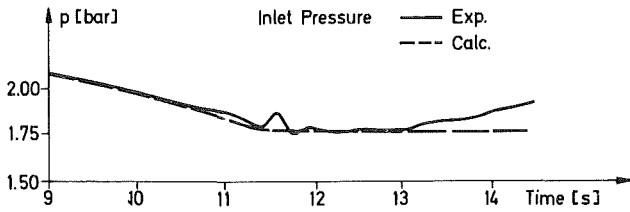
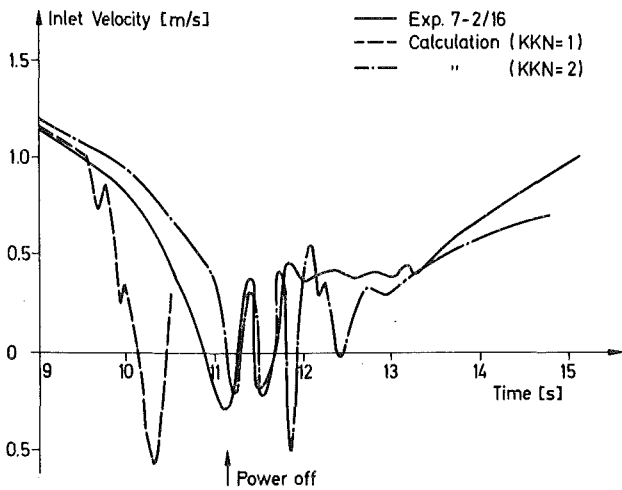


Fig. 38: Experiment 7-2/16. Experimental and calculated peak coolant temperatures versus time.

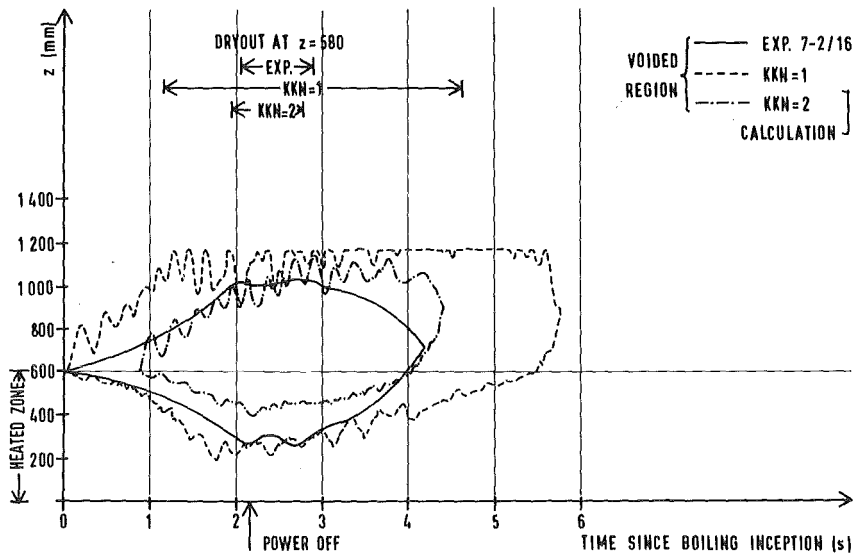


Fig. 39: Experiment 7-2/16. Experimental and calculated voided regions versus time.

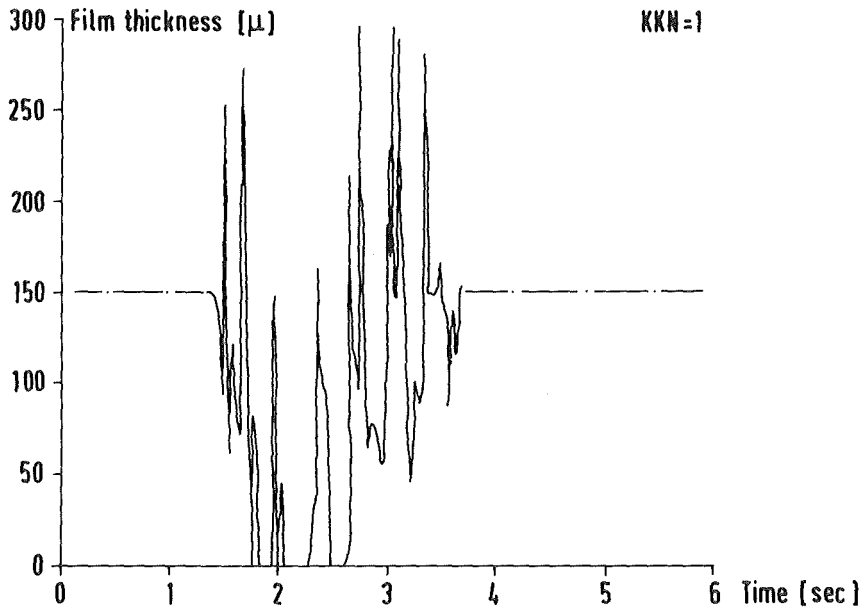


Fig. 40: Experiment 7-2/16. Calculated liquid film thickness at cladding in the axial mesh zone $M=11$ versus time, for equivalent channel $KKN=1$.

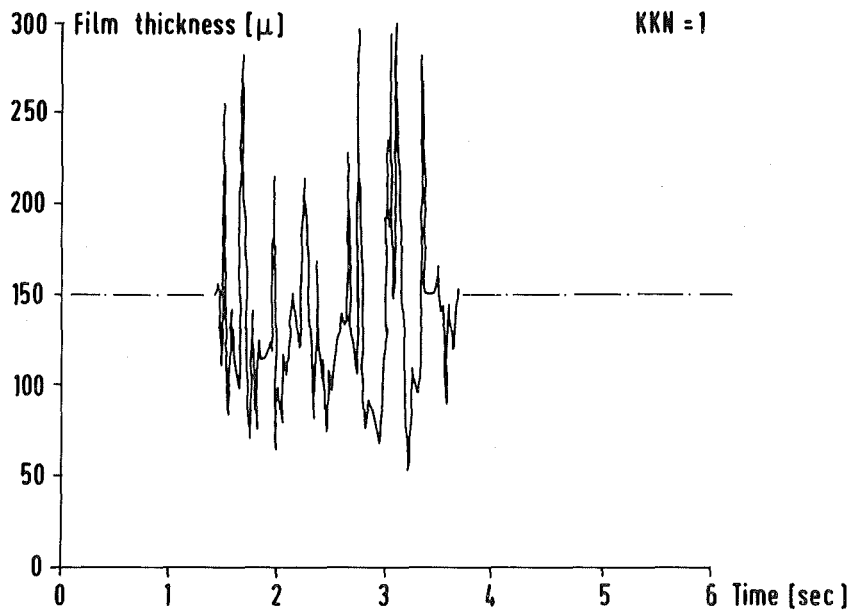


Fig. 41: Experiment 7-2/16. Calculated liquid film thickness at the structural material in the axial mesh zone M=11 versus time, for equivalent channel KKN=1.

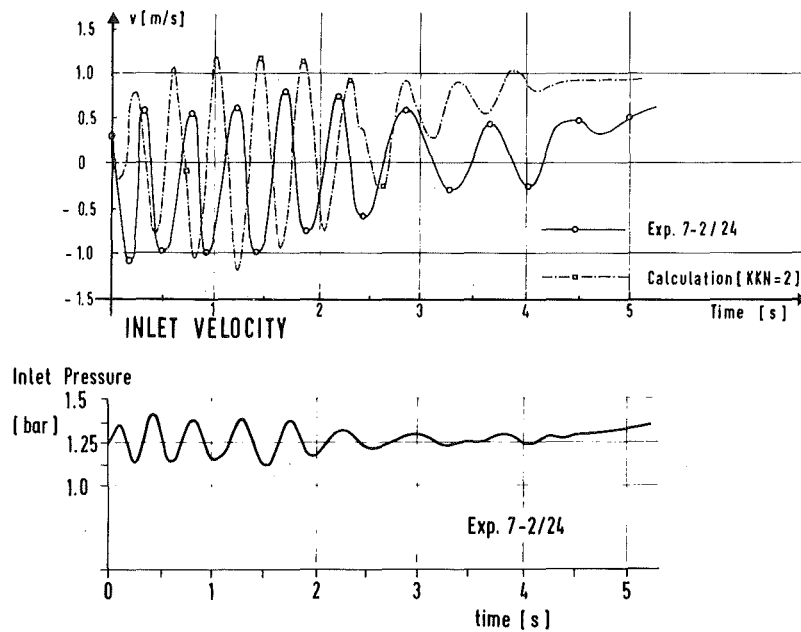


Fig. 42: Experiment 7-2/24. Inlet pressure boundary condition and comparison between experimental and calculated inlet velocities versus time.

2.4.1.2 Experiment 7-2/24

Fig. 42 represents the calculated inlet velocity against the experimental plot, together with coolant pressure upstream of the inlet valve which represents the inlet boundary condition for the calculation. The average period of the calculated mass flow oscillations (up to 2.5 sec after boiling inception) is about 400 msec while the experimentally recorded oscillations have a mean period of 460 msec. The calculated frequency is therefore in satisfactory agreement with the experimental one. The liquid column oscillates with velocities ranging between + 1 m/sec and - 1 m/sec, the amplitude of the positive half waves being larger than experimentally recorded.

Fig. 43 shows a comparison of recorded coolant peak temperature with the calculated values for $KKN=1$. The values for $KKN=2$ have been plotted only partially because they would overlap those for $KKN=1$. These plots make the coupling between central and peripheral subchannels of the bundle manifest. The pressure pulse due to the large superheat transfers mass and momentum to the edge subchannels, triggers boiling and makes temperatures to become quickly uniform over the full bundle cross section. From this point on, the mixed equivalent channel represents the bundle behaviour more accurately than the hot channel, as it has been observed also for the previous experiment. The temperature peaks in the calculation for $KKN=1$ are due to short dryout periods. They are terminated by subsequent rewetting due to passage of a liquid slug in front of a dried clad section. The flow regime is alternatively annular flow and slug flow, the latter dominating in the last boiling phase, after power switch off.

Fig. 44 shows the calculated voided region for the equivalent channels against the experimental results. The calculation for $KKN=2$ underestimates the space and time extent of the two-phase flow region, while the hot channel manifestly overestimates vapour rate production and spread of the voided region. The results from the calculation for $KKN=2$ are good up to 2 sec after boiling inception, while the subsequent phase of bubbles collapsing is not described accurately. The predicted dryout period is also too short compared with the experimental results. It must anyway be reminded that the duration of the experimentally observed dryout was not continuous but resulted from overlapping of several intervals as indicated by different thermocouples.

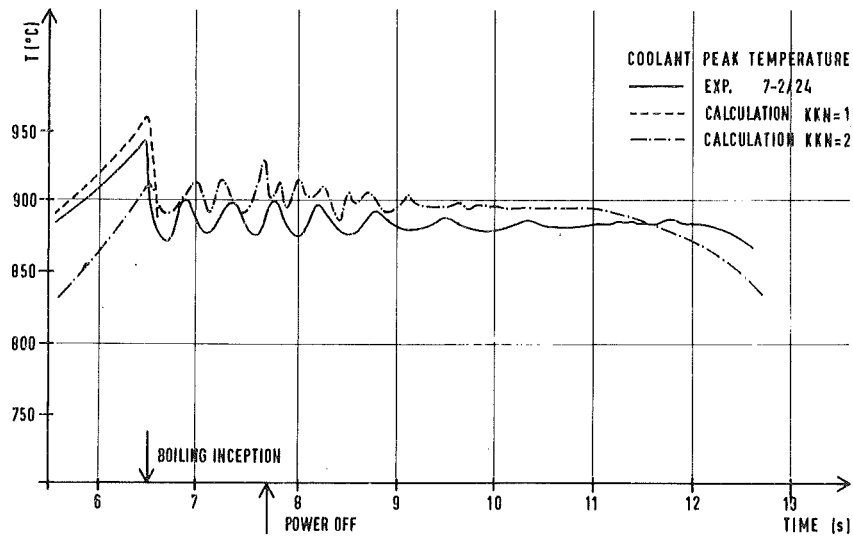


Fig. 43: Experiment 7-2/24. Experimental and calculated peak coolant temperatures versus time.

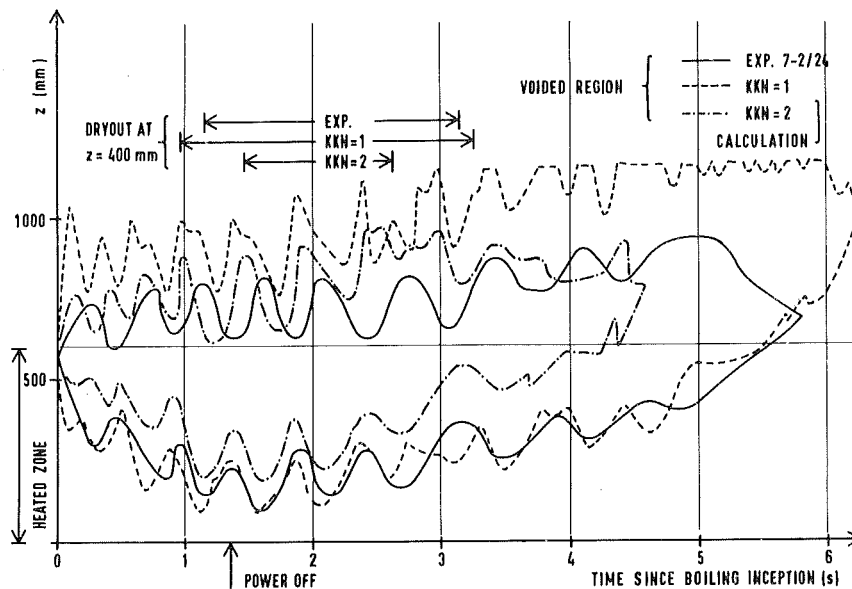


Fig. 44: Experiment 7-2/24. Experimental and calculated voided regions versus time.

In Figs. 45 and 46 calculated heater temperatures are compared with thermocouples reading for two different axial levels $Z = 400$ mm and $Z = 580$ mm, respectively. The shape of the plots shows clearly the temperature rise following onset of dryout and its fall when rewetting occurs. Keeping in mind the inaccuracy introduced by simulating the heaters as a clad uniform material with volumetric heat source distribution, the comparison shows a satisfactory agreement of the absolute value of the temperatures and of rate of energy release after power switch off. However the limitations inherent in the single pin approximation for several subchannels of a bundle are shown clearly in Fig. 46, where the experimental plot lies between those computed for $KKN=1$ and $KKN=2$. The energy stored in the heater of the first equivalent channel is overestimated during the transient and particularly during the dryout period while the contrary holds for the equivalent channel representing the full bundle. A more accurate calculation can be only obtained with a more-dimensional programme describing the transient behaviour of coolant and pins in control volumes having dimensions comparable with those of the subchannels of the bundle.

The time variation of the calculated liquid film thickness is shown for the axial mesh zone $M = 11$ (See Input data in Table XIII) for the cladding and the structural material in Figs. 47 and 48 respectively. Both plots refer to the equivalent channel $KKN=1$. The axial level of mesh $M = 11$ corresponds to $Z = 380$ in Fig. 44. These plots show that the initial boiling sequence is characterized by a very rapid reduction of the film thickness with first dryout within a few tenths of sec after boiling inception. This is due to the large superheat observed in this experiment, which leads at boiling inception to an extensive production of vapour with large velocities in the range of 50 to 120 m/sec in both directions. The vapour flow drains the liquid film causing dryout not only at the cladding surface, but also, for a short time interval, at the wall of the simulated structural material.

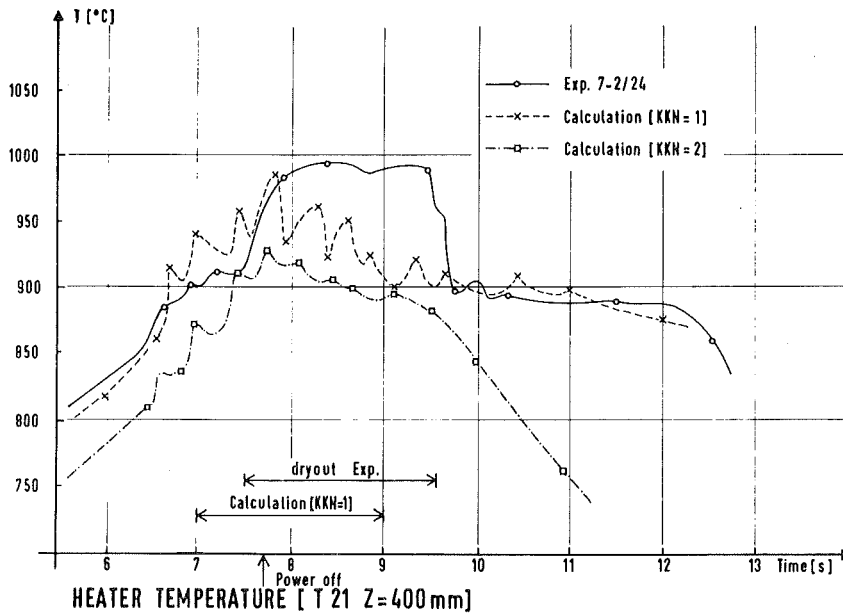


Fig. 45: Experiment 7-2/24. Experimental and calculated heater temperatures versus time at axial level $z = 400$ mm. ($z=0$ at the bottom of heated section).

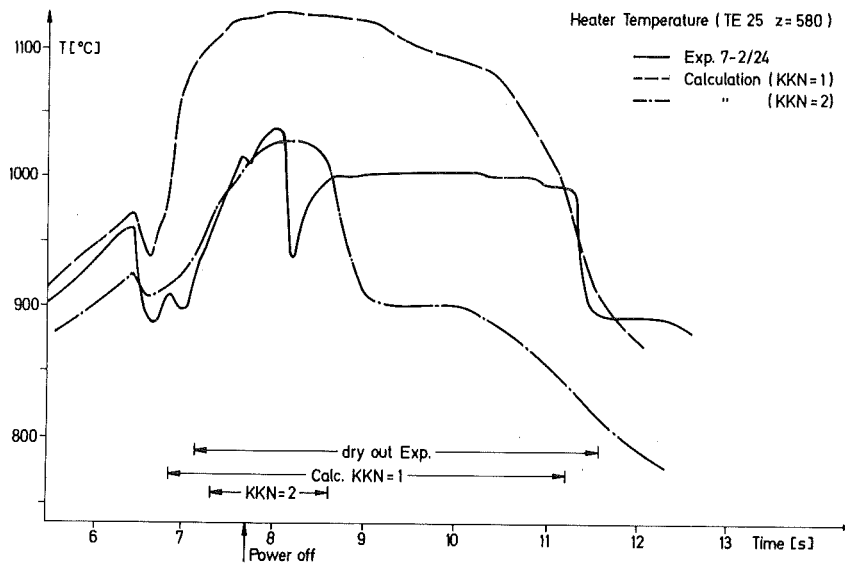


Fig. 46: Experiment 7-2/24. Experimental and calculated heater temperatures versus time at axial level $z = 580$ mm ($z=0$ at the bottom of heated section).

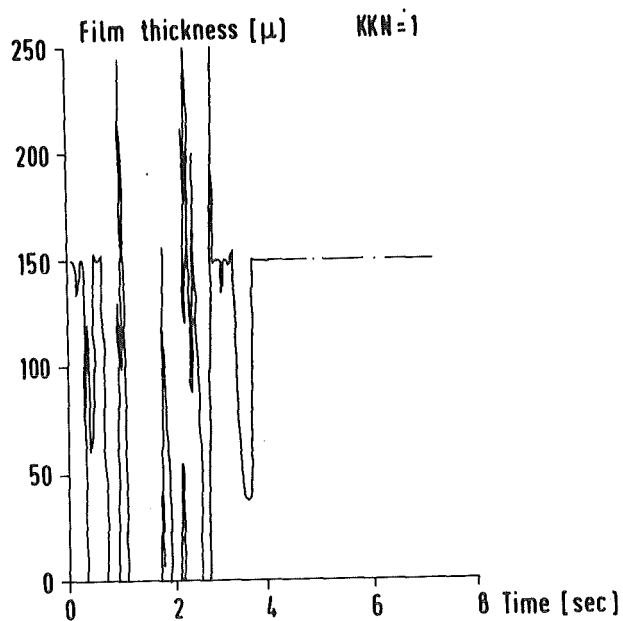


Fig. 47: Experiment 7-2/24. Calculated liquid film thickness at cladding in the axial mesh zone M=11 versus time, for equivalent channel KKN=1.

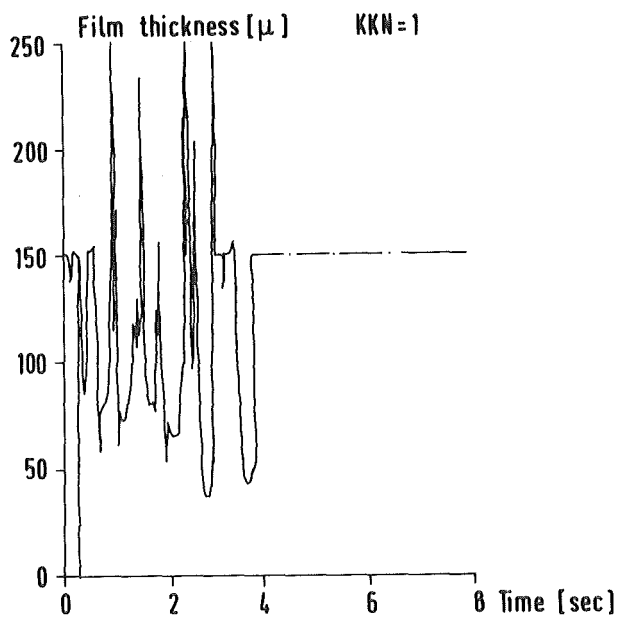


Fig. 48: Experiment 7-2/24. Calculated liquid film thickness at the structural material in the axial mesh zone M=11 versus time, for equivalent channel KKN=1.

2.4.1.3 Experiment 7-2/28

The total inlet blockage characteristic of this experiment has been simulated by increasing with time the pressure drop coefficient of the inlet valve. The resulting calculated inlet flow velocity is compared with the experimental plot in Fig. 49. Owing to the difficulty of simulating exactly the time variation of the mass flow, boiling inception is predicted by the calculation with about 0.2 sec delay with respect to the experiment. A coolant superheat of 27 °C, which is however somewhat uncertain, has been assumed. The temperature raising rate at boiling inception is in this experiment very large (about 120 °C/sec) and is reproduced with good accuracy by the calculation, as shown in Fig. 50. This figure gives a comparison between the experimental plot of the peak coolant temperature (thermocouple TC7) and the calculated values. The typical trend is recognizable, the experimental plot lying between those calculated for equivalent hot channel (KKN=1) and for the equivalent mean channel (KKN=2). The maximum discrepancy between experiment and calculation rises up to about 25 °C towards the end of the calculation, when the two-phase flow region shrinks, which corresponds to about 8% of the coolant temperature rise. The large calculated temperature peaks are due to dry-out sequences of short duration.

Results of measured and calculated axial void front propagation are plotted in Fig. 51 for the equivalent hot channel. The overall agreement, and in particular the duration of the two-phase flow regime, is considered to be very good and shows that the global balance of the enthalpy stored in the channel during the transient is correct. Some discrepancies however are evident as shown by the comparison between calculated and experimental heater wall temperatures in Fig. 52 (thermocouple TC21, situated at axial level $Z = 400$ mm). During dryout, in the time interval between about 2.5 and 10 seconds, the calculated temperatures are overestimated because BLOW-3A assumes a very poor residual heat transfer and neglects additional cooling effects due for instance to deposition of coolant droplets on the surface of the cladding. However the fuel temperature reached after rewetting agrees well with the experimental plot.

Due to the total blockage of the inlet valve, dryout is reached in the channel very rapidly not only at the cladding surface but also at the structural material as shown in Figs. 53 and 54 for the axial mesh zone $M = 11$ corresponding to the axial level $Z = 380$ mm in Fig. 51. The calculated length of

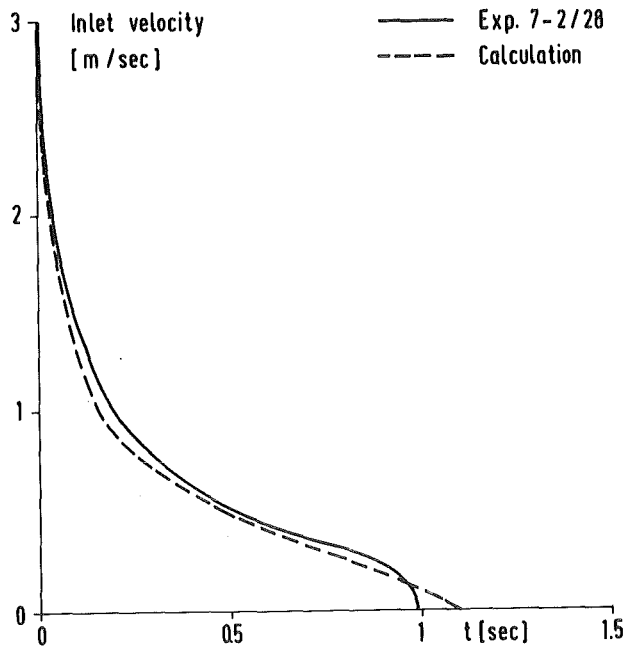


Fig. 49: Experiment 7-2/28. Comparison between experimental and calculated inlet velocities versus time.

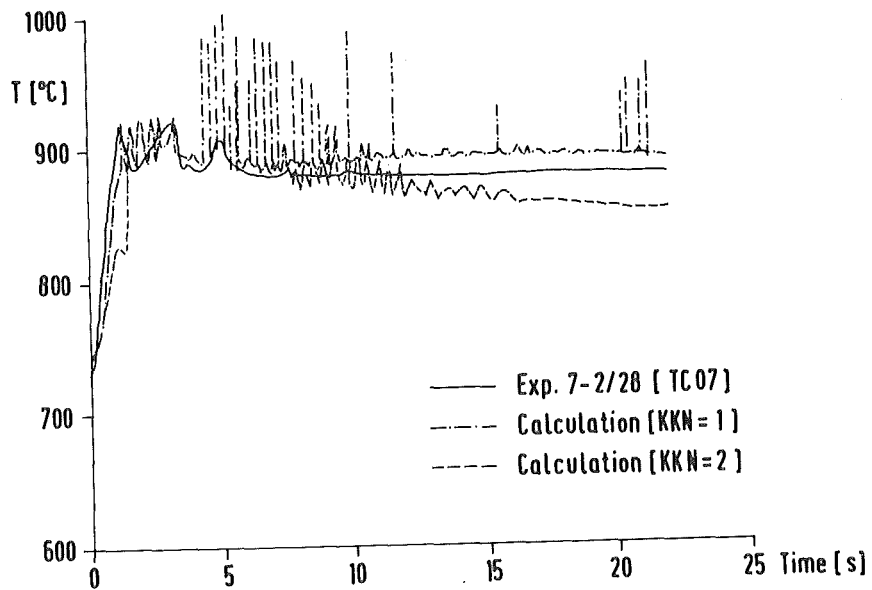


Fig. 50: Experiment 7-2/28. Experimental and calculated peak coolant temperatures versus time.

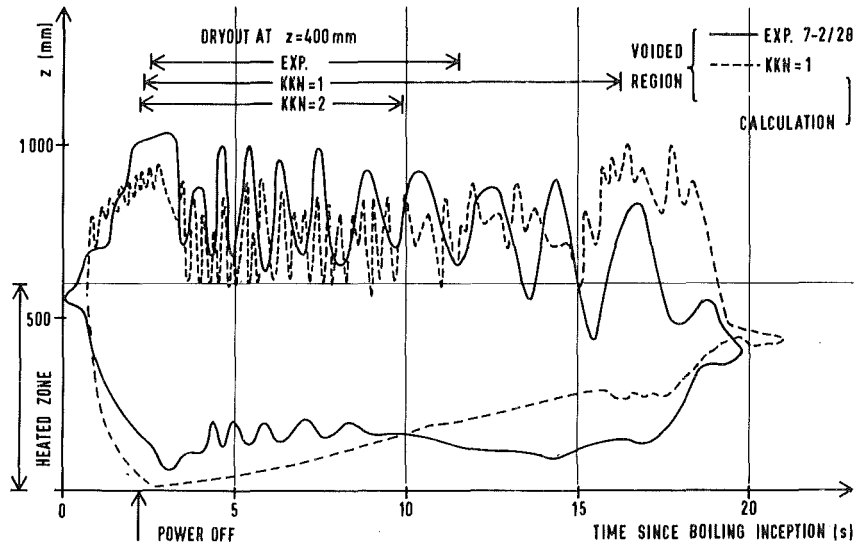


Fig. 51: Experiment 7-2/28. Experimental and calculated voided regions versus time.

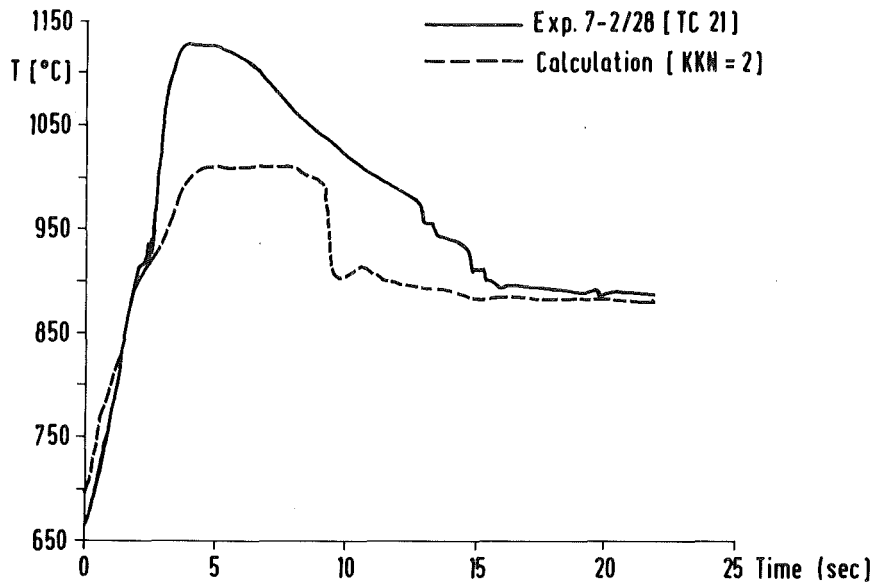


Fig. 52: Experiment 7-2/28. Experimental and calculated peak cladding temperature (outer surface) versus time.

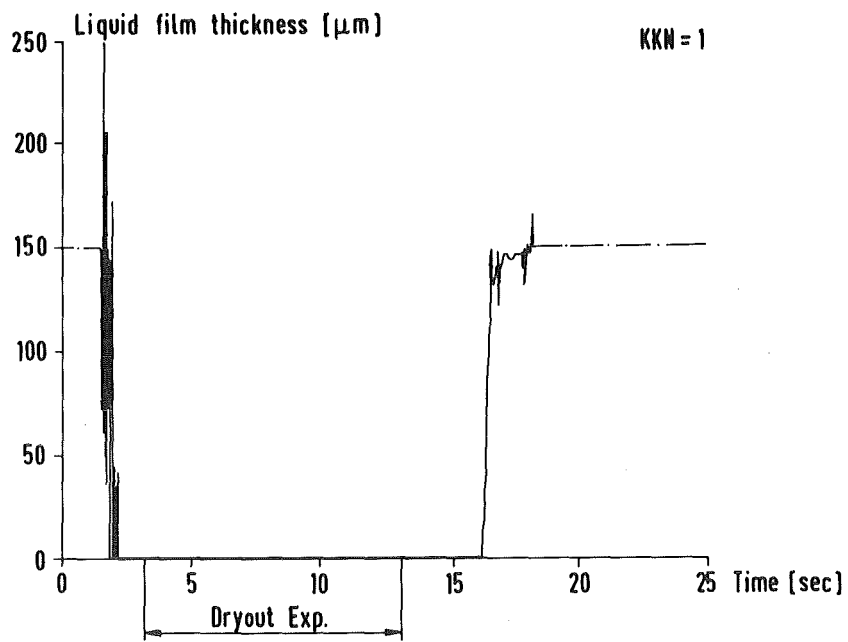


Fig. 53: Experiment 7-2/28. Calculated liquid film thickness at cladding in the axial mesh zone $M=11$ versus time, for equivalent channel $\text{KKN}=1$.

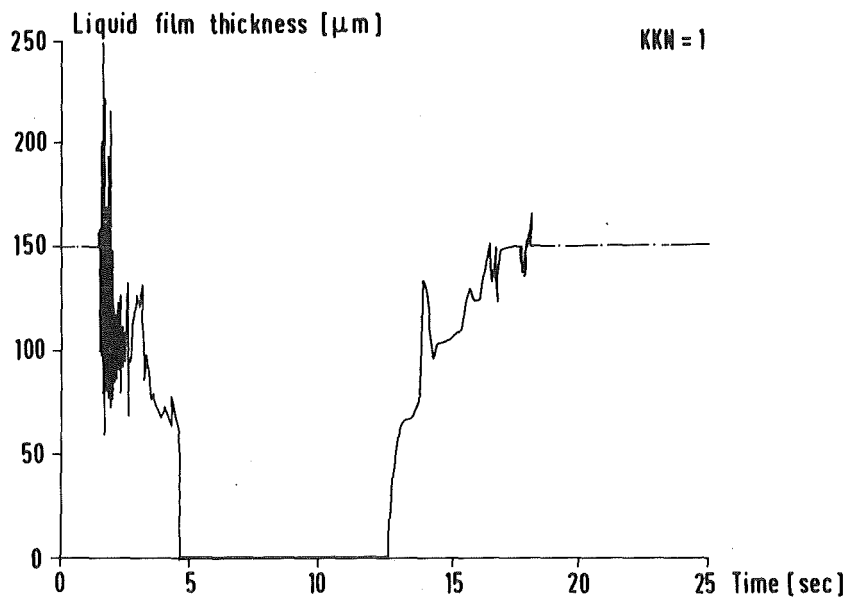


Fig. 54: Experiment 7-2/28. Calculated liquid film thickness at the structural material in the axial mesh zone $M=11$ versus time, for equivalent channel $\text{KKN}=1$.

the dryout interval is compared in Fig. 53 with the experimental information for axial level $Z = 400$ mm and shows an overestimation of about 2-3 seconds.

2.5 Conclusion

Theoretical interpretation of 7-pin bundle out-of-pile boiling experiments has been performed with the code BLOW-3A for three runs out of a series of experiments simulating pump run down conditions in a reactor. These experiments represented extreme conditions with regard to initialization at boiling onset one with high heat flux and no superheat, the second with lower heat flux and extreme superheat of about 70°C , the third characterized by a complete inlet flow blockage. Main purpose of the interpretation work has been to clarify whether a 7-pin bundle geometry can be simulated sufficiently well with a single channel representation and whether the newly introduced two phase pressure drop calculation based on the two-phase multipliers by Lockhart and Martinelli is reasonable in combination with a multiple bubble slug ejection model as BLOW-3A.

For the bundle simulation two different types of equivalent channels have been defined: one representing the hot central subchannels of the bundle geometry and one representing the whole bundle. For both channels properly averaged input data have been derived from experimental information at steady state conditions. Transient conditions of inlet and outlet pressure have been taken from the experiments thus representing feedback effects from the circuitry which is not directly simulated in BLOW-3A. Mass flow variations, development of voided regions, coolant and heater temperatures during the boiling phase have been compared with the computed results for the two equivalent channels. The following conclusions can be drawn from this analysis:

In the experiments rather strong feedbacks from the outer circuitry to the test section during the boiling sequence have been observed. Therefore an accurate simulation of the transient pressure boundary conditions at inlet and outlet is necessary.

Transient coolant temperatures in the two phase flow region are best approximated by the mean channel representation. The agreement with experimental data is sufficiently accurate. Those of the hot channel are slightly higher than the experimental ones.

Transient void zone extension in the test section compares quite well with experiments for the mean channel representation as long as the full power is maintained. Once the power is shut down considerable deviations are observed. This indicates that the phase of residual heat removal from the pins is to a large extent dominated by interaction phenomena between subchannels of the bundle.

Calculated inlet velocities and measured values show rather good agreement for the mean channel representation. First flow reversal is predicted too early for the case with high superheat. For the case with no superheat calculational results show a delayed first flow reversal compared to the experiment, while the calculated value for the hot channel representation is quite too low. Thus it can be deduced that the momentum exchange between subchannels, which cannot be simulated in a BLOW-3A-type analysis influences the time of first flow reversal in case of no superheat considerably.

Inlet mass flow oscillations, especially for the high superheat case, compare quite well with the experimentally observed frequency. This indicates that the use of a Lockhart-Martinelli type correlation for the determination of two phase flow pressure drop combined with a multiple bubble slug ejection model is reproducing the reality reasonably well.

The calculated heater temperatures indicate that the onset of dryout is predicted accurately in the equivalent mean channel, but somewhat too early in the hot channel representation, for which therefore the duration of the dryout sequences tends to be overestimated. In the experiments there is a rather strong interaction between inner and peripheral subchannels which cannot be simulated properly by BLOW-3A. As remarked previously, a detailed description would require a more-dimensional representation of the bundle.

In summary it can be stated that the theoretical interpretation of the 7-pin out-of-pile sodium experiments has shown it feasible to simulate the bundle geometry by means of properly chosen equivalent one-dimensional coolant channels. The BLOW-3A calculations give a realistic and consistent picture of all dominant phenomena, as axial extension of the two-phase flow region, flow reversal, onset of local dryout and restoring of single phase flow conditions after power shut-off. It could be proved that the single channel approximation is sufficiently accurate for conservative evaluation of the consequences of hypothetical accidents in LMFBRs. However, if radial incoherence of boiling onset must be described in more detail, as in the

case of voiding being initiated without or with negligible superheat, a more-dimensional representation of the bundle geometry is necessary.

3. Application of the BLOW-3A code for consequence evaluation of an unprotected loss-of-flow accident in the core of SNR-2000

The BLOW-3A programme is incorporated into the CAPRI-2 programme /29/ for theoretical simulation of hypothetical unprotected whole core accidents. In the subsequent section application of the boiling model within the scope of such accident simulations will be demonstrated. As an example investigations of some modifications of hydraulic design features of a reactor core designed for a reactor power of 2000 MW_e will be presented /32/. Analysis results for consequence evaluation of an unprotected loss-of-flow accident during the initiation phase will be discussed.

3.1 Characteristic data of the reactor core

To evaluate whether consequences resulting from unprotected whole core accident situations might have the potential to limit the magnitude of fast breeder reactors to be built, the behaviour of a reactor core designed for an electric power output of 2000 MW_e as consequence of an unprotected mild reactivity ramp rate insertion as well as an unprotected loss-of-flow accident was investigated /32/. Typical data of steady state conditions for the reactor core are listed in table XVI. The core zone as shown in fig. 55, consists of 613 positions, the radial breeder of 168. The core consists of two zones with different enrichment. The inner core zone contains 366 fuel elements, twelve control and shim-rod positions of the first safety system and 19 positions of the second shut down system. The outer core zone consists of 198 fuel element positions and 18 positions of the first control and shim rod system. With a core height of 120 cm and a length of 40 cm for the axial breeder the core has an outer diameter of about 5 m which leads to a H/D ratio of 0.25 which is already in the vicinity of a pan-cake core. Typical nuclear data of the core design are listed in table XVII including some safety related reactivity coefficients.

To simulate the steady state and transient behaviour of the core it is necessary to represent the thermohydraulic behaviour of groups of subassemblies by only one characteristic coolant channel. CAPRI-2 allows for simulating 30 different coolant channels to represent appropriately the whole core

Table XVI: Characteristic data of the SNR-2000 reactor core

Core geometry		
height	m	1.2
breeder thickness		
axial/radial	m	0.4/0.28
Number of fuel elements:		
Zone I/Zone II/rad. breeder	m	366/198/168
control rod positions		
first shut down system:		
Zone I/Zone II	-	12/18
second shut down system	-	19
core diameter:		
Zone I/Zone II/total	m	3.46/4.30/4.86
Fuel element design		
diameter of fuel pin	mm	7.6
P/D ratio	-	1.2
number of fuel pins/fuel element	-	271
width of fuel elements	mm	160.5
Thermohydraulic data		
total thermal power	MW	5000
peak nominal	W/cm	450
linear rating		
hot spot	W/cm	600
sodium inlet		380
temperature °C		
average outlet		545

Table XVII: Characteristic nuclear data of the SNR-2000 reactor core

enrichment zone I	%	14.5	
zone II	%	20.0	
peak nominal burn-up	MWd/t	80 000	
reactivity change per burn-up cycle	Δk	0.025	
fuel inventory			
core	t	52(U+Pu)	
total	t	122(U+Pu)	
fissile material			
core	t	6.2 Pu	
breeding ratio		1.18	
		BEC-A	EEC-B
<hr/>			
effective neutron life time	sec	$4.535 \cdot 10^{-7}$	$4.556 \cdot 10^{-7}$
effective β of delayed neutrons	-	$3.896 \cdot 10^{-3}$	$3.743 \cdot 10^{-3}$
maximum positive void reactivity	Δk	0.020	0.024
Doppler constant of core at nominal operational conditions			
wet	$T \frac{dk}{dT}$	$-7.8 \cdot 10^{-3}$	$-7.3 \cdot 10^{-3}$
dry		$-4.7 \cdot 10^{-3}$	$-4.4 \cdot 10^{-3}$

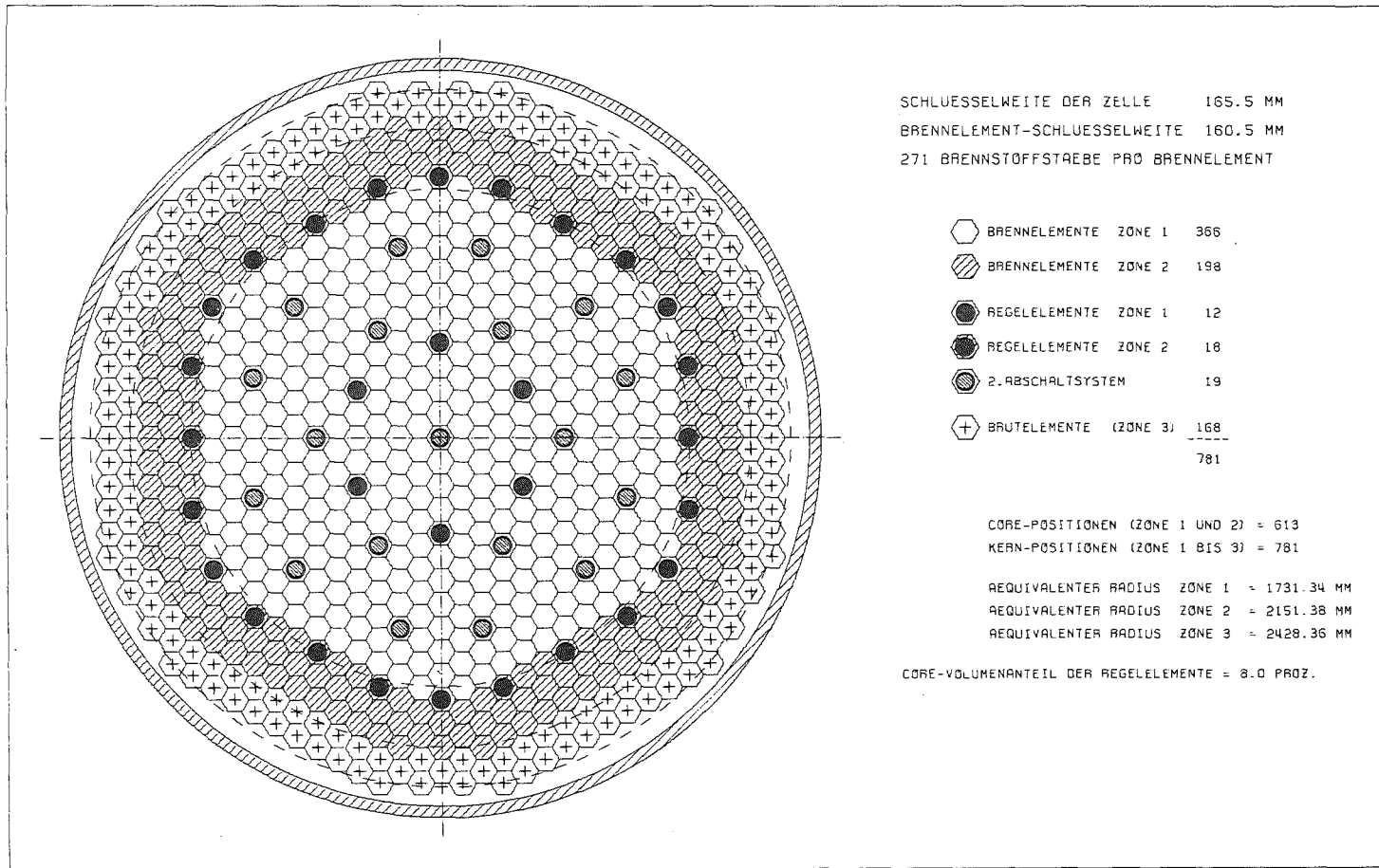


Fig. 55: Core cross section of the SNR-2000.

behaviour. Combination of fuel elements to one characteristic group follows some guidelines. These are:

1. Fuel elements of one group should all have the same burn-up level.
2. Power produced in the individual fuel elements should not deviate from the average value of the group by more than 5%.
3. For reasons of simplicity fuel elements grouped together should have radial positions in the core being close together.
4. Core zones with larger flux gradients and/or large gradients of reactivity worth curves have to be subdivided sufficiently fine.
5. Core zones with strong variations of the average coolant-heat-up along the fissile length have to be subdivided sufficiently fine.
6. The number of fuel elements grouped together are allowed to deviate strongly from numbers of neighbouring groups only if burn-up level, power production per fuel element, reactivity worth-curves and average coolant heat-up along the fissile length differ only little between groups.
7. Core zones, which are expected to influence only little the overall core behaviour, can be subdivided coarsely.
8. Fuel element grouping should allow for an easy calculation of reactivity worth curves.

If these guidelines are followed, the SNR-2000 core has to be represented by 30 coolant channels as shown in figures 56 and 57. More detailed information with regard to this aspect can be found in /32/.

The steady state thermohydraulic characteristics of the SNR-2000 reactor core have been evaluated on basis of detailed three-dimensional calculations. Two core configurations are of special interest for this two batch core: The begin of equilibrium cycle A (BEC-A) and the end of equilibrium cycle B (EEC-B). These two configurations are of special interest, because due to different control rod positions and burn-up level, thermohydraulic characteristics and reactivity worth curves show considerable differences. To demonstrate this, normalized axial power profiles for the BEC-A and EEC-B configurations are shown in fig. 58. The cross-hatched areas indicate varia-

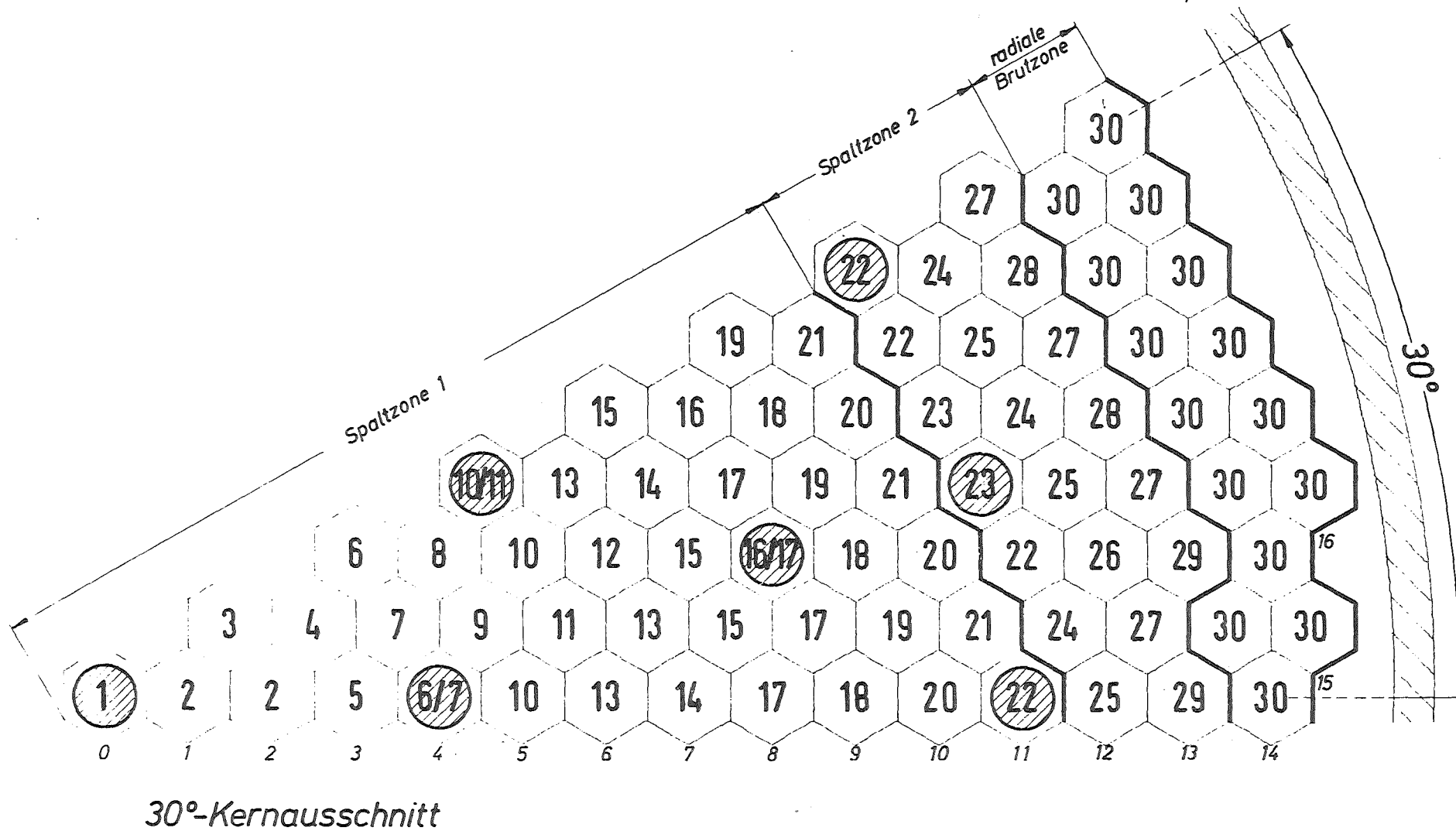


Fig. 56: Grouping scheme of core elements for characteristic coolant channels

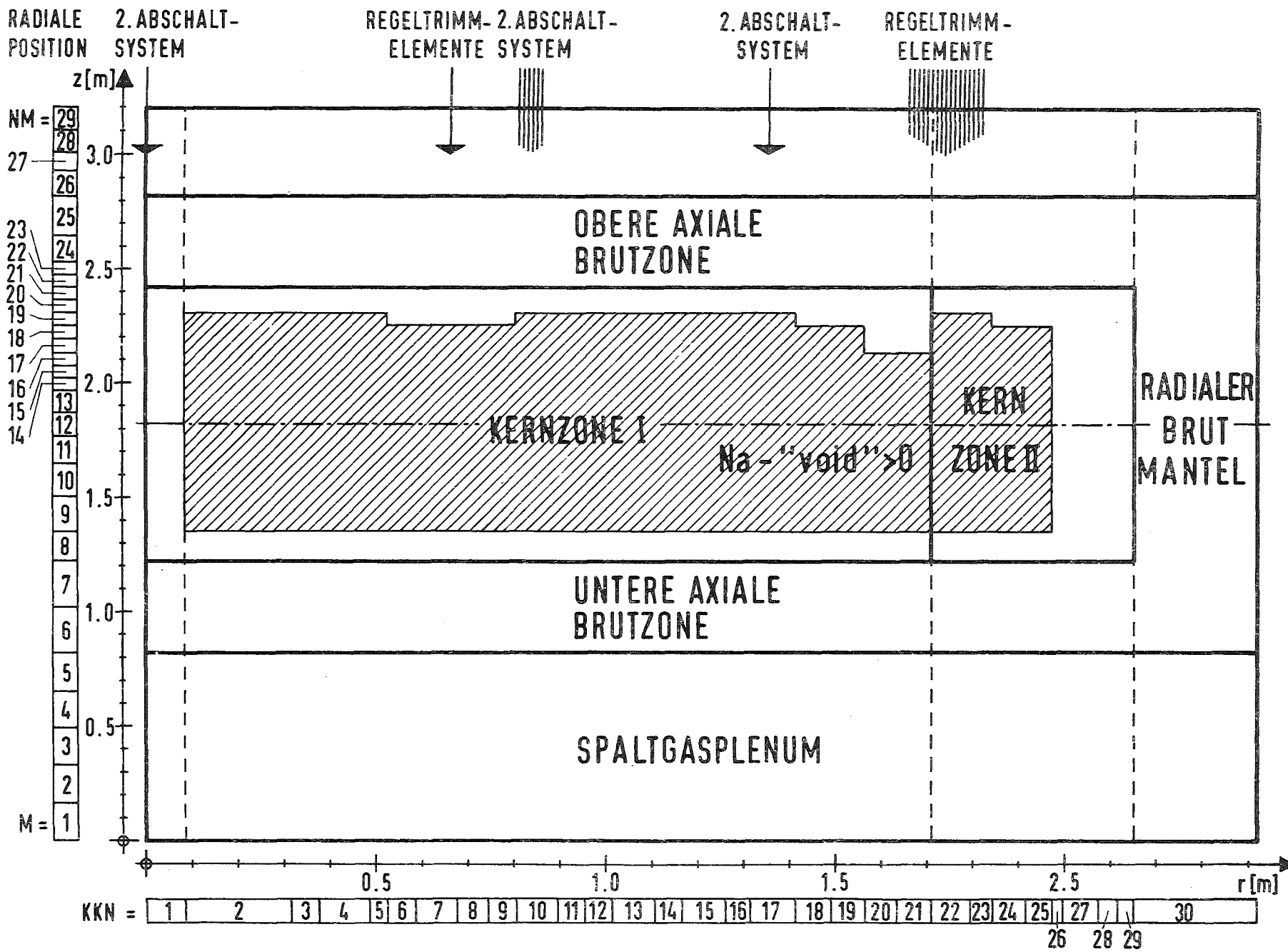


Fig. 57: Geometrical mesh of SNR-2000 with radial positions of control rods and the second safety systems

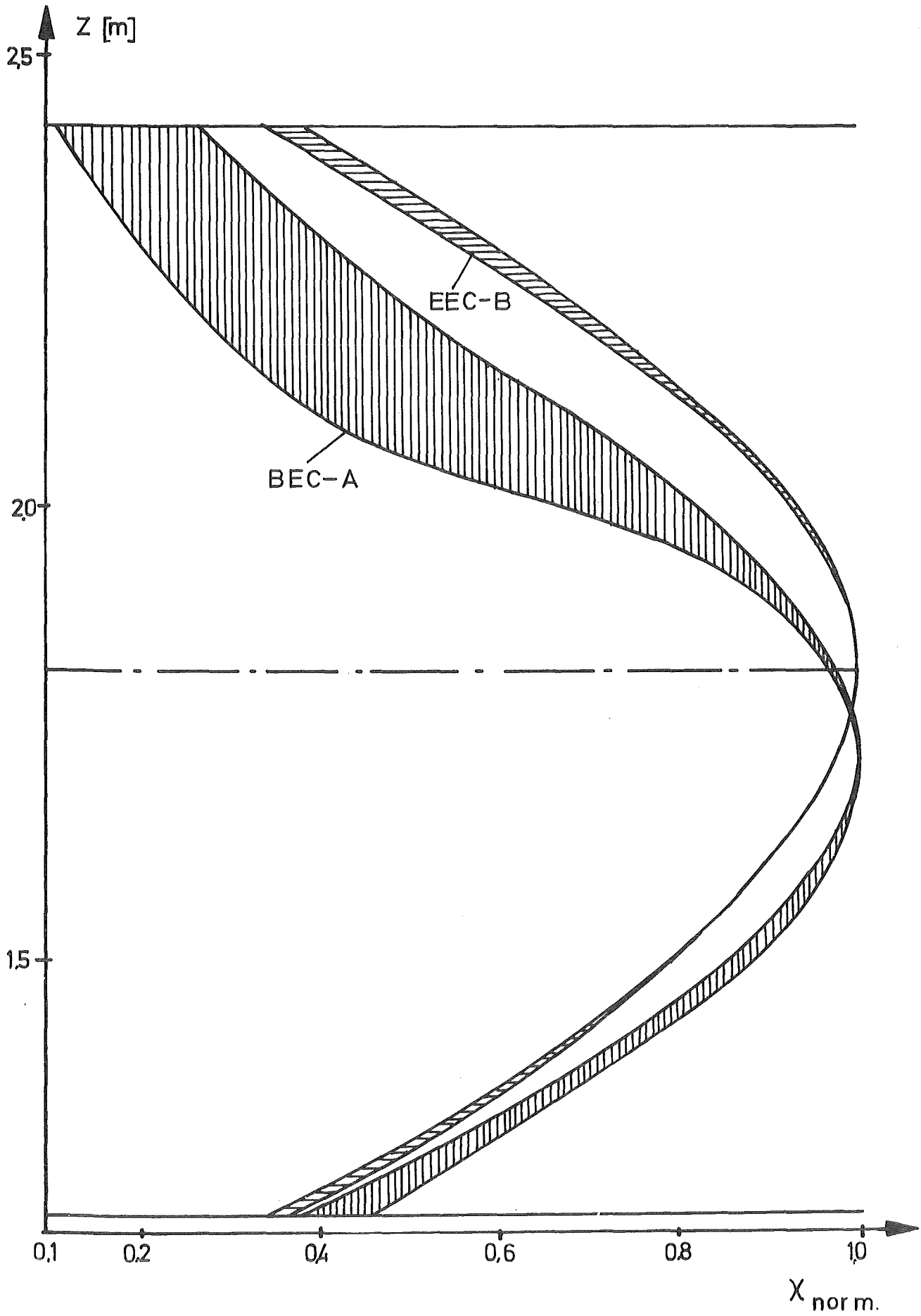


Fig. 58: Normalized axial profiles of linear rating for the BEC-A and EEC-B core configurations.

tions of these axial profiles dependent on the radial fuel element position. This variation is much stronger for the BEC-A configuration than for the EEC-B configuration. Besides that it can be seen that the peak power value for the BEC-A core is located slightly below core mid-plane and for the EEC-B just around core mid-plane. This can influence the event sequence considerably in the course of hypothetical unprotected core disruptive accidents.

3.2 Transient behaviour of the SNR-2000 reactor core

For the unprotected loss-of-flow accident in SNR-2000 the mass flow reduction in the core cooling is calculated from the following relation of the transient pressure variation in the inlet plenum:

$$p_E(t) = p_A^o + p_S^o + (p_E^o - p_A^o - p_S^o) F(t)$$

p_E^o - steady state coolant pressure in the inlet plenum [$\bar{\text{bar}}$]

p_A^o - steady state coolant pressure in the outlet plenum [$\bar{\text{bar}}$]

p_S^o - steady state pressure difference between the coolant inlet and outlet plenum [$\bar{\text{bar}}$]

$$F(t) = \exp(-2.77 \cdot 10^{-2} t + 2.9 \cdot 10^{-5} t^2 + 8.4 \cdot 10^{-8} t^3)$$

- normalized time function

t - time relative to mass flow reduction onset

As consequence of this pressure transient coolant mass flow reaches 50% of the steady state value within about 4 seconds. The subsequent boiling behaviour in the coolant channel with the largest steady state peak linear rating is plotted in fig. 59 relative to boiling onset. Conditions for the BEC-A and EEC-B core configurations are compared with each other. The transient evolution of the net reactivity and subsequent power variation for the respective core configurations are shown in fig. 60.

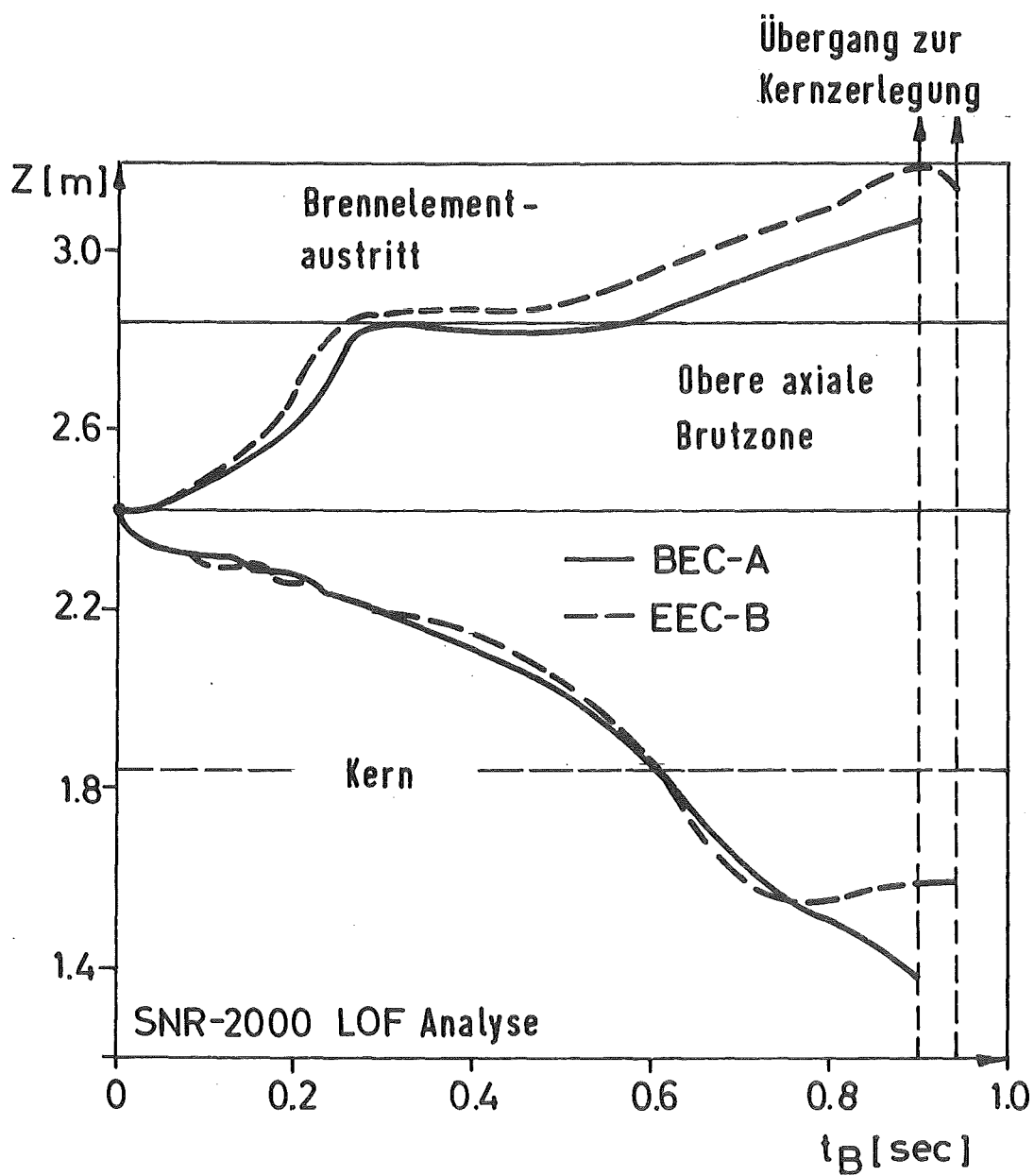


Fig. 59: Transient void front evolution in the coolant channel with the highest linear rating as consequence of a ULOF-accident

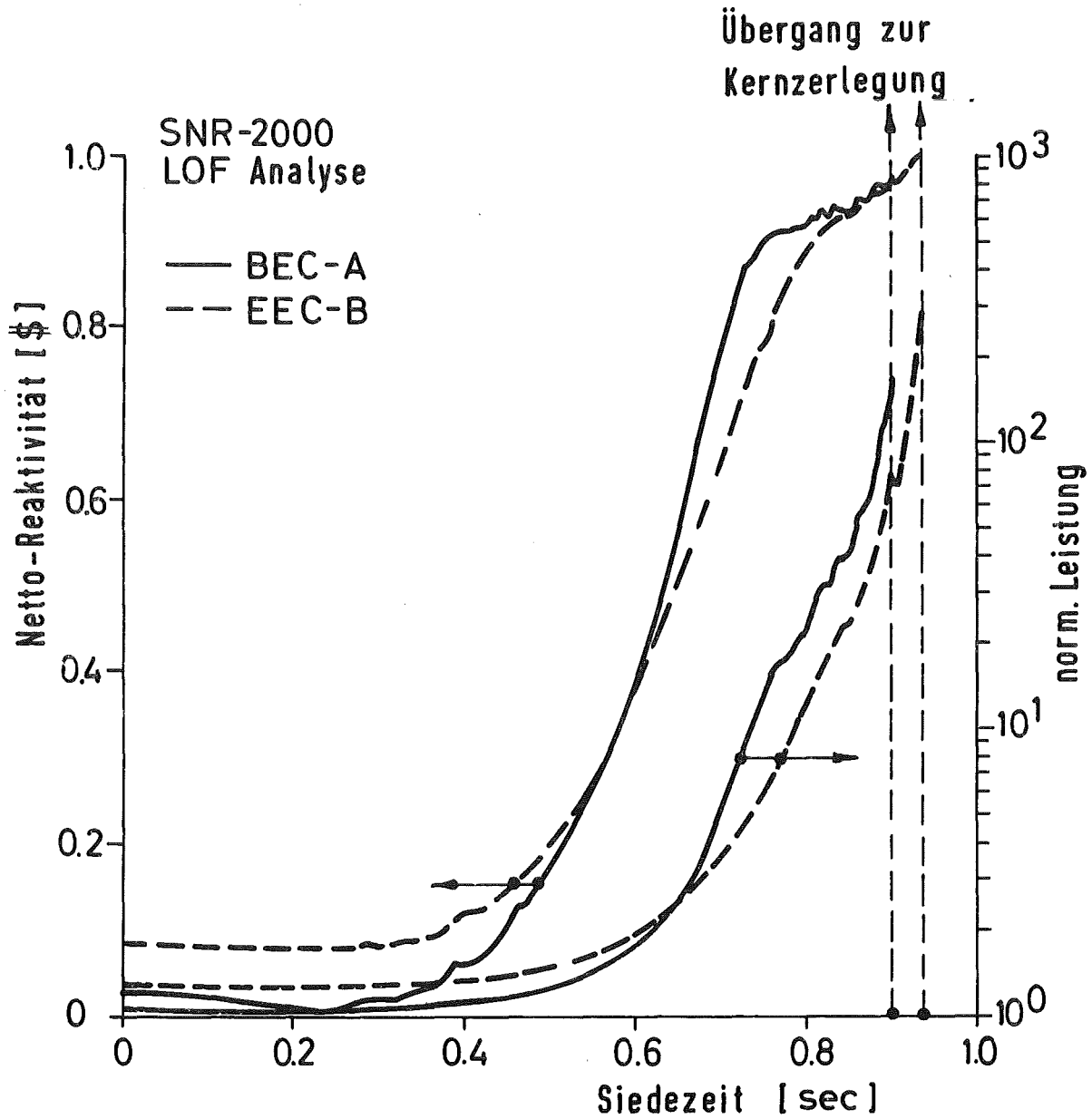


Fig. 60: Reactivity and power-evolution in the BEC-A and EEC-B core configurations as consequence of a ULOF-accident

As input for the BLOW-3A module following characteristic values have been chosen:

superheat of the coolant:	3 °K
liquid film model:	stagnant
initial film thickness on clad and structure:	170μ (80% void fraction)
minimal film thickness initiating local dry-out:	100μ (92% void fraction)
two-phase pressure drop correlation:	Wallis formula
Condensation coefficient for sodium vapour:	6.3 W/cm ² °K

As consequence of boiling onset in the different coolant channels the superimposed reactivity contributions initiate a power transient. If the radially averaged fuel temperature in a representative fuel pin exceeds a value of 3250 °C during the initiation phase simulation switch-over to a disassembly code like KADIS /38/ becomes necessary. Subsequent phenomena in whole core accident are dominated by fuel vapour pressure build-up and fission gas pressures which cannot be simulated with sufficient accuracy within the CAPRI-code system.

As can be seen in fig. 59 boiling is initiated at the upper end of the core zone. Due to the small superheat of the liquid sodium the void front progresses relatively slowly downwards in the beginning (0.2-0.3 sec). If the void front extends along axial areas with larger value of the linear rating rapid downwards boiling zone progression starts.

The transient dependencies of the net reactivity as well as core power resulting from the superimposed boiling sequences in different channels of the two core configurations analyzed are shown in fig. 60. About 0.5 sec after boiling onset rapid reactivity increase is calculated enhancing the net reactivity from 10 to 90 ¢ in about 0.2 sec. Due to the flat radial power profile in the EEC-B core configuration the associated power increase is steeper than that calculated for the BEC-A core configuration. For both core configurations the rapid reactivity increase is partly compensated by the Doppler-effect so that the condition for switch-over to a disassembly

Table XVIII: Characteristic data of the ULOF-accident in the SNR-2000

Core configuration		BEC-A	EEC-B
boiling onset	sec	6.90	6.55
norm. power	-	1.050	1.138
net reactivity	\$	0.024	0.066
clad melting onset	sec	7.712	7.482
norm. power	-	129	228
net reactivity	\$	0.969	0.985
axial position rel. to core height	%	65.	69.
Switch-over to disassembly	sec	7.717	7.486
norm. power	-	167	253
net reactivity	\$	0.976	0.980
percentage of fuel elements with two-phase flow conditions			
core zone I	%	61	47
core zone II	%	17	16
percentage of core in- ventory molten	%	32.8	33.2
reactivity ramp rates			
Doppler	\$/sec	-11	-17
axial expansion	\$/sec	-10	- 9
void	\$/sec	19	24
slumping	\$/sec	-	-

type calculation is reached prior to a situation in which superpromptcriticality in the core due to boiling is exceeded. Characteristic results of the accident evolution during the initiation phase are listed in table XVIII. It can be seen that boiling phenomena and Doppler-feedback dominate the accident evolution during the initiation phase in cores in which the maximum positive void worth is as large as in the SNR-2000. Clad motion and fuel movement become important only in situations in which disassembly type phenomena occur.

3.3 Influence of a slow mass flow reduction on the power evolution during the initiation phase

To evaluate possibilities of reducing the consequences of unprotected loss-of-flow accidents in large cores it was investigated whether a slower mass flow reduction might have considerable influences on the overall core behaviour. For this purpose the following normalized time variation for determination of the inlet pressure was applied for the SNR-2000 BEC-A core:

$$F(t) = \exp.(-5.84 \cdot 10^{-2} t + 1.8 \cdot 10^{-5} t^2 + 8.5 \cdot 10^{-7} t^3).$$

The resulting transient pressure boundary variation leads to a coolant mass flow reduction approximately 5 times slower than foreseen for the normal design of the SNR-2000. 50% of the steady state coolant mass flow is reached only after 20 sec.

As result of the slower mass flow reduction boiling in the characteristic coolant channel with the peak linear rating develops slightly differently. In fig. 61 both cases are compared with each other. In case of the slow mass flow variation boiling starts in the upper axial breeder and progresses downwards into the core only very slowly. About 0.5-0.7 sec after boiling onset flow reversal is achieved. This value compares to 0.2-0.3 sec for the normal mass flow reduction curve. Due to the dominance of liquid film evaporation from clad surfaces at axial locations of peak linear rating void front velocities are comparably large once core mid plane is achieved. This leads to the conclusion, that for cores with large maximum positive void reactivity worths as the one of the SNR-2000 modifications of the mass flow reduction curve alone do not have to much influence on the overall outcome of the accident, though boiling evolution is different in detail.

This becomes clearer if the power and net reactivity behaviour after boiling onset are compared as it is done in fig. 62 and table XIX. Though the time difference between boiling onset and switch-over to disassembly is nearly two times larger for the case with the slower mass flow reduction the overall state of the core at switch-over is not very different.

These two examples might be sufficient to demonstrate the role of the BLOW-3A model for the consequence analysis of unprotected hypothetical core disruptive accidents. Others can be found in /35, 36, 37/.

Table XIX: Characteristic data of the ULOF-accident in the SNR-2000 dependent on different mass flow reduction curves.

Core configuration mass flow reduction		BEC-A	
		rapid	slow
boiling onset	sec	6.90	34.0
norm. power	-	1.050	0.942
net reactivity	β	0.024	-0.025
clad melting onset	sec	7.712	35.423
norm. power	-	129	23.1
net reactivity	β	0.969	0.884
axial position rel. to core height	%	65	65
switch-over to disassembly	sec	7.717	35.476
norm. power	-	167	167
net reactivity	β	0.976	0.972
percentage of fuel elements with two-phase flow conditions			
core zone I	%	61.	64.
core zone II	%	17.	17.
percentage of core in- ventory molten	%	32.8	34.8
reactivity ramp rates			
Doppler	β/sec	-11	-12
axial expansion	β/sec	-10	- 8
void	β/sec	19	16
slumping	β/sec	-	2

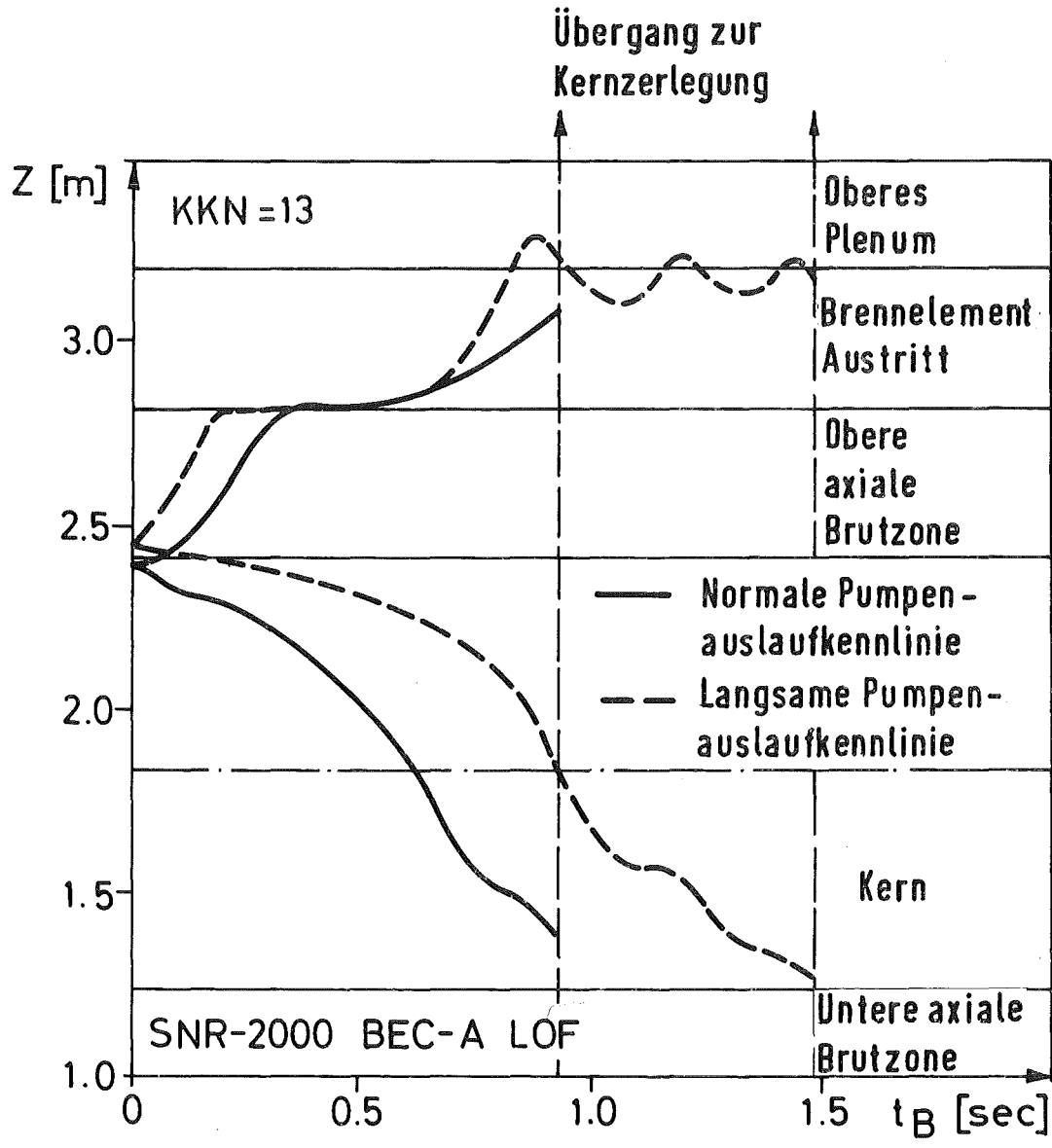


Fig. 61: Transient void front evolution in the coolant channel with the highest linear rating dependent on different mass flow reduction curves for the ULOF-accident

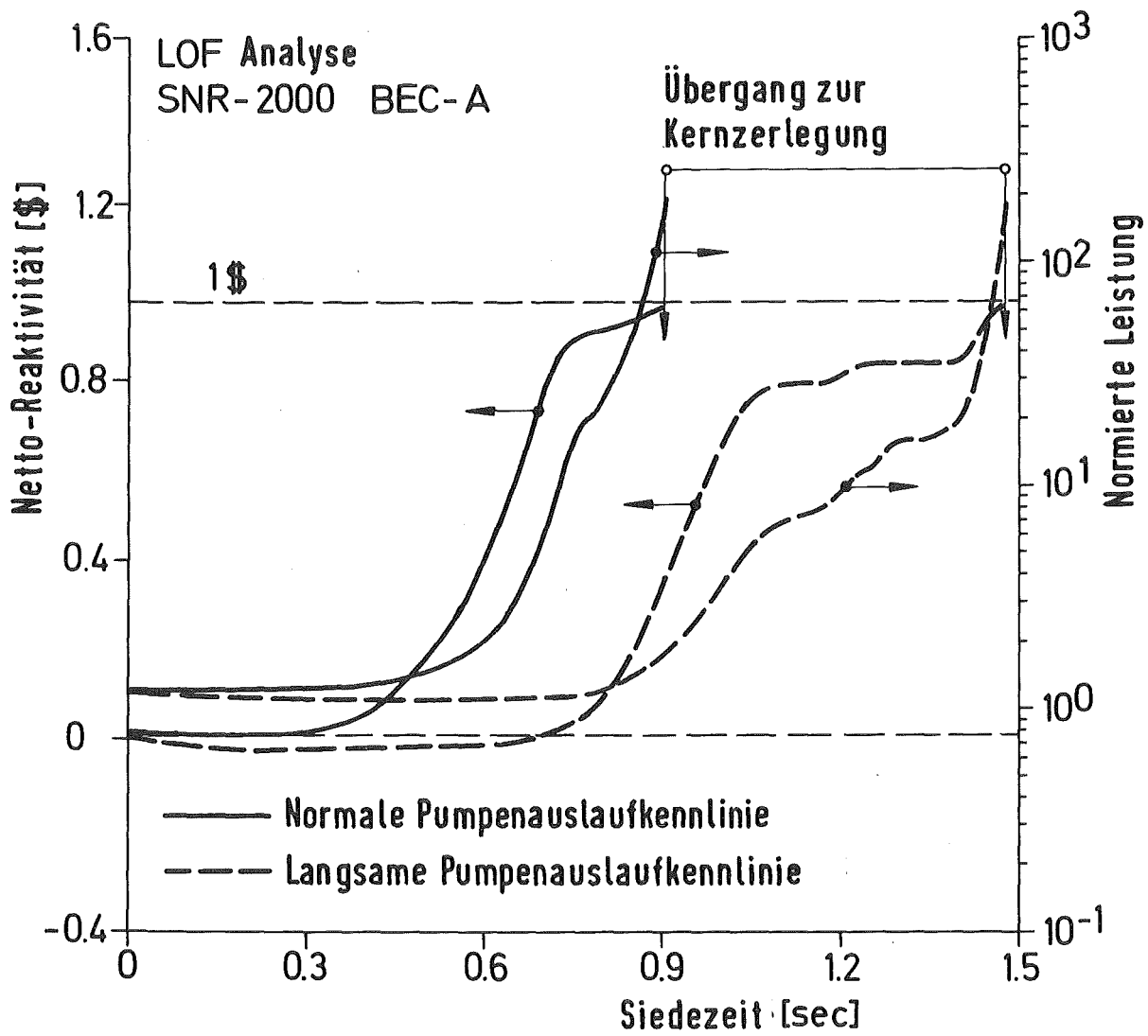


Fig. 62: Reactivity and power evolution in the BEC-A core configuration dependent on different mass flow reduction curves for the ULOF-accident

List of symbols

(Only symbols used throughout the report are listed)

A	=	Area of coolant channel cross section (m^2)
c^2	=	$(dp/d\rho)$ sound speed (m/sec)
c_p	=	specific heat (J/kg $^{\circ}C$)
D_h	=	hydraulic diameter (m)
e	=	specific internal energy (J/kg)
f	=	friction coefficient
F	=	surface area (m^2)
g	=	gravity acceleration (m/sec^2)
G	=	coolant mass flux (kg/m^2 sec)
h,H	=	specific enthalpy: (J/kg)
L	=	channel length (m)
m	=	mass flux by phase change (kg/m^2 sec)
Nu	=	Nusselt number
p	=	pressure (N/m^2)
Pr	=	Prandtl number
q,Q	=	specific power (W/m^3)
r	=	radial coordinate (m)
R	=	radius (m)
Re	=	Reynolds number
S	=	liquid film thickness (m)
t	=	time (sec)
T	=	temperature ($^{\circ}C$)
u	=	coolant velocity (m/sec)
U	=	wetted perimeter (m)
V	=	volume (m^3)
z	=	axial coordinate (m)

Greeck symbols

α	=	void fraction
α	=	heat transfer coefficient ($W/m^2 \text{ } ^\circ C$)
ζ	=	pressure drop coefficient for inlet valve
θ	=	time discretization parameter
λ	=	thermal conductivity ($W/m \text{ } ^\circ C$)
λ	=	friction coefficient
μ	=	dynamic viscosity ($kg/m \text{ sec}$)
ν	=	kinematic viscosity (m^2/sec)
ρ	=	density (kg/m^3)
Φ	=	specific power (W/m^3)
Ψ	=	friction coefficient ($\lambda = 4\Psi$)

Indices

a	=	channel outlet
B	=	fuel
ei	=	channel inlet
fg	=	fluid-vapour
h	=	time discretization
H	=	cladding
i	=	liquid-vapour interface
k	=	identifier of a vapour bubble
K	=	coolant
l	=	liquid
m	=	axial mesh zone
n	=	time discretization
r	=	iteration index
S	=	structure (hexagonal can)
v	=	vapour
w	=	wall

References

- /1/ P. Wirtz - Ein Beitrag zur theoretischen Beschreibung des Siedens unter Störfallbedingungen in natriumgekühlten schnellen Reaktoren.
KFK 1858, Oktober 1973
- /2/ C. Girard et al. - French Program on LMFBR Safety, Proc. Fast Reactor Safety Meeting, CONF-740401-P1, April 1974
- /3/ D. Struwe, M. Bottoni, W. Fries, H. Elbel, G. Angerer - Theoretical interpretation of SCARABEE Single Pin In-pile Boiling experiments.
Nuclear Engineering and Design 43 (1977) pp. 259 - 271
- /4/ G. Kessler - Zur numerischen Lösung der ortsabhängigen dynamischen Gleichungen schneller Brutreaktoren mit Hilfe eines Variationsprinzips.
KFK 781/I - EUR 3957 d, August 1968
- /5/ M. Bottoni, W. Pepler, D. Struwe - Theoretical interpretation of sodium boiling experiments in a 7-pin bundle under flow rundown conditions with the computer code BLOW-3A.
Report presented at the 7th LMBWG-Petten, 1 - 3rd June, 1977
- /6/ M. Bottoni - Calculation of temperature distribution in a melting clad with the Pekeris-Slichter series expansion method.
Nuclear Engineering and Design 43 (1977) pp. 249 - 257
- /7/ R.W. Lockhart, R.C. Martinelli - Proposed correlation of data for isothermal two-phase, two components flow in pipes
Chemical Engineering Progress 45, 1949, pp. 39 - 48
- /8/ G.B. Wallis - Use of the Reynolds flux concept for analyzing one-dimensional two-phase flow - Part I and II.
International Journal of Heat and Mass Transfer 11, 1968, pp. 445 - 458.
- /9/ U. Schumann - MAPLIB, ein Programmsystem zur Bereitstellung von Stoffdaten für Rechenprogramme.
KFK 1253, September 1970
- /10/ H. Kämpf, H. Elbel, F. Depisch - The Computer Programme SATURN-1a for fuel rods
KFK 1575, 1972 (in German)

- /11/ J. Crank, P. Nicolson - A practical method for numerical evaluation of solutions of partial differential equations of the heat-conduction type.
Proc. Cambridge Philos. Soc. 43 (1947), pp. 50-67
- /12/ D.M. Young - Iterative solution of large linear systems
Academic Press, 1971
- /13/ R.D. Richtmyer, K.W. Morton - Difference Methods for Initial-Value Problems.
Interscience Publishers, 1967
- /14/ W. Pepler - Experimentelle Untersuchungen der Siedevorgänge mit Natrium in engen Kanälen und deren Anwendung auf schnelle Reaktoren
KFK - Ext. Bericht 8/72-1, Februar 1972
- /15/ E.G. Schlechtendahl - Sieden des Kühlmittels in natriumgekühlten schnellen Reaktoren
KFK 1020, Juni 1969
- /16/ H.K. Fauske - Transient Liquid Metal Boiling and Two-Phase Flow.
Int. Seminar on Heat Transfer in Liquid Metals,
Trogir, Jugoslav, 6 - 11 Sept. 1971
- /17/ M.A. Grolmes, H.K. Fauske:
Liquid film thickness and mechanism for dryout during LMFBR Loss-of-Flow Accidents
Trans. Am. Nucl. Soc., Boston, June 13-17, 1971, pp. 743-744
- /18/ E.G. Schlechtendahl - Theoretical investigations on sodium boiling in fast reactors.
Nuclear Science and Engineering 41, 1970, pp. 99 - 114
- /19/ W.J. Woods, C. Girard, D. Struwe et al.
Thermohydraulic aspects of the interpretation of the SCARABEE fuel failure experiments.
Nuclear Engineering and Design, 59 (1980), pp. 257-273.
- /20/ G.B. Wallis
One-Dimensional Two-Phase Flow
Mc. Graw-Hill, 1969

- /21/ F.G. Hewitt, N.S. Hall-Taylor
Annular Two-Phase Flow
Pergamon Press, 1970
- /22/ A. Kaiser, W. Pepler, L. Vöröss
Untersuchungen der Stömungsform, des Druckabfalls und des kritischen
Wärmefflusses einer Zweiphasenströmung mit Natrium
KFK 2085 (April 1975)
- /23/ L.K. Brumfield, T.G. Theofanus
On the prediction of heat transfer across turbulent liquid films
Journal of heat transfer, August 1976, pp. 496-502
- /24/ J. Aberle, A.J. Brook, W. Pepler, H. Rohrbacher, K. Schleisiek
Sodium boiling experiments in a 7-pin bundle under flow run down
conditions.
KFK 2378 (November 1976)
- /25/ W. Zimmerer
PLØTCP - Ein Fortran IV-Programm zur Erzeugung von Calcomp-Plot-Zeich-
nungen.
KFK 2081 (Mai 1975)
- /26/ M. Bottoni, W. Jocham, D. Struwe
Theoretical interpretation of 7-pin out-of-pile and in-pile voiding
experiments.
Procedures of International Meeting on Fast Reactor Safety Technology,
Seattle, Washington, August 19-23, 1979.
- /27/ B. Kuczera
BREDA - Ein Rechenmodell für die Verformung des Brennstabes eines Na-
gekühlten schnellen Brutreaktors unter transienter Belastung.
KfK 1729, Dezember 1972.
- /28/ H. Kämpf, H. Elbel, F. Depisch
The computer programme SATURN 1a for fuel rods.
KfK 1575, 1972.

- /29/ D. Struwe, P. Royl et al.
CAPRI - A computer code for the analysis of hypothetical core disruptive accidents in the predisassembly phase.
CONF - 740401, p. 1525 (1974)
- /30/ M. Bottoni, D. Struwe
The heterogeneous two-phase flow model BLOW-3A and its relevance for thermal-hydraulic analysis of off-normal conditions in LMFBRs. Proc. ANS/ASME Topl. Mtg. Nuclear Reactor Thermal Hydraulics, Soratoga Springs, New York, October 5-8, 1980, Vol. III, p. 1836.
- /31/ J. Aberle, A. Kaiser, H. Rohrbacher
Boiling Instrumentation and Signal Analysis of the 7-pin Bundle Experiment
Presented at the Meeting of the LMBWG, Risley, Oct. 75
- /32/ D. Struwe
Das Verhalten des Kerns eines schnellen natriumgekühlten Brutreaktors von 2000 MW_e bei Störfällen sehr geringer Eintrittswahrscheinlichkeit.
KfK 2490 (Dezember 1977)
- /33/ Düsing, Friedel, Gering
Lokale Kühlflußstörungen KNK II-Kühlmitteleinlaufblockaden von Elementen der Test- und Treiberzone
ITB 70.670.4 (Januar 1978)
- /34/ J. Reynen et al.
EAC-European Accident Code. Proc. of the 10th LMBWG meeting, Karlsruhe (October 1982)
- /35/ D. Struwe et al.
Das dynamische Verhalten des Mark I-Kerns des SNR-300 während der Predisassembly-Phase schwerer hypothetischer Unfälle, Proc. Reaktortagung, Berlin 2-5 April, 1974, Ges. im Dt. Atomforum e.V. Leopoldshafen 1974; ZAED s. 86-89
- /36/ R. Fröhlich et al.
Analyse schwerer hypothetischer Störfälle für den SNR-300 Mark 1A - Reaktorkern, KfK 2310, (Juni 1976)

/ 37/ P. Royl et al.

Comparative Analysis of a Hypothetical Loss-of-Flow Accident in a LMFBFR using different Computer Models for a Common Benchmark Problem, EUR 5946 EN

/38/ P. Schmuck et al.

KADIS - Ein Computer Programm zur Analyse der Kernzerlegungsphase bei hypothetischen Störfällen in schnellen natriumgekühlten Brutreaktoren, KfK 2497.

Acknowledgement

The BLOW-3A programme development has been carried on for several years within the Institut für Reaktorentwicklung des Kernforschungszentrums Karlsruhe. Several scientists have contributed to this development over the years. The authors would like to acknowledge especially the contributions by the former colleagues W. Fries and W. Jocham and to thank W. Zimmerer for his continuous support in the data processing and Dr. G. Friedel from INTERATOM for his valuable criticism. Beyond that we would like to thank Mrs. Stephany for her excellent work of typing and revising the manuscript, Miss Stutz and Mrs. Oberacker for preparation of the figures.